University of California Merced

Development and Evaluation of an *in-situ* Remediation Strategy for Mercury Contamination in Aquatic Sediments

A dissertation submitted in partial satisfaction of the requirements for the degree of Doctor of Philosophy in Environmental Systems

by

Edwin Rivas Meraz

Dissertation Committee

Professor Marc Beutel (Chair)
Professor Peggy O'Day (Advisor)
Professor Thomas Harmon
Dr. Dimitri Vlassopoulos
Dr. Alexander Johs

Fall 2024

The Dissertation of Edwin Rivas Meraz is approved, and it is acceptable in quality and form for publication on microfilm and electronically:

_____

Professor Peggy O'Day, (Faculty Advisor)

_____

Professor Marc Beutel, PE (Chair)

_____

Professor Thomas Harmon

_____

Dr. Dimitri Vlassopoulos

_____

Dr. Alexander Johs

University of California Merced

Fall 2024

Table of Contents

Figures

MOMAC samples divided into **(a)** XANES (fit region 6530-6590 eV) and **(b)** EXAFS (k-range fit region of 1.5-10 $Å^{-1}$) with linear combination fits (red lines show component sum). Linear combinations were conducted with a library of Mn reference compounds. Fractions of the best-fit components, normalized to 100%, are represented by the bar plots. Tabulated values and representative deconvolution for MOMAC are given in Table A4 and Fig. A10.

Figure 1.5 Estimation of Mn oxidation states in MnOx and MOMAC through analysis of **(a)** Mn 3p peak collected with X-ray photoelectron spectroscopy (XPS) and **(b)** expanded Mn K-edge pre-edge region from X-ray absorption spectra (shown in Fig. 1.4). For XPS, non-linear least-squares curve fits were used to determine distribution of oxidation states in MnOx and MOMAC based on curves defined by analysis of reference compounds. The Mn pre-edge was fit with sets of 2 or 3 pseudo-Voigt functions (FWHM = 1.3 eV; Gaussian/ Lorentzian = 0.45; peaks shown) for reference compounds where each peak was allowed to shift ±0.1 eV. Bar plots show fractions of Mn(II), (III), and (IV) fit in each sample. Tabulated values for XPS and pre-edge fits reported in Table A5 and Table A6, respectively.

Figure 1.6 Eh-pH diagrams and measured Eh and pH as a function of time in batch screening experiments of amendments (a) mixed with artificial creek water only, or (b) homogenized with Hg-contaminated sediment and mixed with artificial creek water. Eh-pH diagrams show Mn aqueous and solid speciation (solid red lines) and S aqueous species (dashed green lines). Chemical formulas for minerals: rhodochrosite: $MnCO_3$; hausmannite: Mn_3O_4; bixbyite: Mn_2O_3; pyrolusite: MnO_2. Calculations were done using the Act2 program from Geochemist Workbench. Experimental data are plotted at the end of reaction (15 d) on the Eh-pH diagrams. Solid lines on the Eh and pH time plots represent statistical smoothing of the data calculated with a generalized additive model.

Figure 1.7 Total Hg measured in solutions of batch screening experiments after 15 d of reaction with contaminated sediment and amendment treatments (untreated control vs. amendment with MnOx, AC, or MOMAC (H)). Total Hg in sediment was 11.5±1.3 mg/kg dry weight (mean ± standard error, n = 3). Uncertainty calculated as the average percent recovery from ongoing precision and recovery samples ± 2 standard deviations from the mean (96-122%).

Figure 1.8 Illustration of MOMAC depicting Mn surface species on activated carbon. The Mn oxide species and crystal morphology found in the Mn aggregates located on the surface of the activated carbon substrate. Octahedral vacancies (marked by the empty space) or Mn(III) in octahedral sites (marked by darkened octahedra) found within δ-MnO_2 result in negative charges that are balanced by hydrated cations in the interlayers, such as Mn(II). Surface of the activated carbon with Mn(II) sorbed and/or diffused into pore spaces following equilibration with $MnCl_2{\cdot}4H_2O$ for 24 h prior to oxidation with $KMnO_4$.

Figure 2.1 Experimental setup and procedures used to investigate the effects of organic

carbon (OC) and soil saturation on net mercury (Hg)-methylation in contaminated sediments with or without *in-situ* amendments. (a) Schematic for flow-through column experiments showing upflow movement of the influent solution. The table lists major components used in column construction. (b) Flow procedure for experiments to mimic fluctuations in soil saturation. The procedure involves three phases: (1) Initial flow of artificial creek water through the sediment columns over approximately 3 days (equivalent to ~80 pore volumes), (2) A 3-day stop flow period allowing for equilibration after saturation, and (3) Resumption of flow for an additional 4 days (~100 pore volumes). (c) Overview of sediment treatments and experimental conditions applied to the sediment columns. Sediment treatments included untreated sediment, manganese oxide-modified activated carbon (MOMAC)-treated sediment, or activated carbon (AC)-treated sediment. Three separate experimental conditions were evaluated: columns with no additional OC, columns with dissolved OC (acetate and pyruvate) introduced into influent, and columns with solid OC (spirulina powder) mixed into sediment.

Figure 2.2 Average pH and redox potential (Eh) measured in column effluent**.** The pH and Eh of the influent solution are marked by the horizontal black line. The stop-flow event (3 d) is marked by the vertical blue line. Uncertainty was determined based on replicates and shown as mean ± standard error. Values with no uncertainty shown are due to single replicates.

Figure 2.3 Concentrations of redox sensitive analytes and non-purgeable organic carbon (NPOC) from filtered effluent. Concentrations for the influent solution are marked by the horizontal black line. The stop-flow event is marked by the vertical blue line. Values below detection were omitted. Detection limits are shown on Table B2. Uncertainty was determined based on replicates and shown as mean ± standard error. Values with no uncertainty shown are due to single replicates.

Figure 2.4 Concentrations of total mercury (THg) and methylmercury (MeHg) from unfiltered column effluent with calculated percent MeHg ([MeHg]/[THg] × 100%). The stopped-flow state (3 d) is marked by the vertical blue line. Values below detection were omitted. Detection limits are shown on Table B2. Note the first sample from untreated sediment is off scale at 8600±3200 ng/L. Uncertainty was determined based on replicate column experiments and shown as mean ± standard error. Values with no uncertainty shown are due to single replicate columns. For MeHg, only 1 set of samples for each column met QA/QC standards and therefore no uncertainty was calculated.

Tables

Acknowledgements

I believe that no journey or accomplishments are ever achieved alone. To my family and my partner. Words are unable to express my gratitude to you all. Without your unwavering support and constant encouragement, I would never have had strength to overcome my doubts and fears to achieve this goal. To my parents, Pedro and Esther, thank you for being amazing role models and instilling in me that a good work ethic, perseverance, and a good heart will get you far in life. Thank you for supporting my wild ambitions and for the love, faith, resources, and many meals you have given to me. To my siblings, Pedro and Daisy, thank you for lighting the path before me, allowing me to follow your footsteps and giving me the courage to dare venture into new paths, you continue to inspire me. Thank you, Sara, for your encouragement and support throughout this journey! I could not be where I am today without your guidance. To my partner, Nikki, thank you for your endless love and patience. You have motivated me to keep going at times when everything seemed bleak, listened to my complaints and fears, and cared for me when I was not caring for myself. You are a constant beacon of hope, motivation, and inspiration. You are my rock, which is a big deal coming from a geologist!

To my advisor, Dr. Peggy O'Day, I would like to express my sincerest appreciation for taking a chance on an ill-experienced geology student who had ambitions of helping the environment, without a clear path of how to get there. You gave me an incredible opportunity that I will never forget. Your mentorship, guidance, and passion for science has shaped me into the scientist I am today, and I am better for it. Thank you for helping me transition from a curious student to a young professional and providing me with a skill set to continue chasing my ambitions. To Dr. Marc W. Beutel, thank you for essentially being a second advisor, bringing me into part of your lab family, and always being available to help. To Dr. Samuel J. Traina, a fountain of knowledge, every conversation I had with you taught me something new and reinforced my curiosities as a scientist. To my other committee members Dr. Alex Johs and Dr. Dimitri Vlassopoulos, thank you for always being available to help and providing me with support and advice when I needed it. Dr. Thomas Harmon, thank you for your flexibility and willingness to jump onto my committee with no hesitation. To the many undergraduate students that I had the pleasure of working with, thank you sincerely for your help in completing these experiments, you each played an unforgettable role in this body of work. In particular, Daniel Baerwaldt, Jesus Salas Hernandez, and Pei (Erica) Lee who exemplified curiosity, passion, and an incredible work ethic with all the work we did. To my colleagues, Gökay, Kutay, Paul, Danielle, Naivy, Shelby, Stefanie, and many others, thank you for the laughs, drinks, and for overall making my graduate school experience a great one. Lastly, this work would not have been possible without the support of the Department of Energy Minority Serving Institutions Partnership Program (MSIPP), a program I am proud to have been a part of.

Abstract

Mercury (Hg) contamination in aquatic soils poses significant environmental and public health risks due to its ability to undergo microbial transformation into methylmercury (MeHg), a neurotoxin that bioaccumulates in food webs. Production of MeHg in soil is largely driven by microbial pathways associated with sulfate reduction or iron-reduction, which are active under anaerobic conditions and low redox potentials. Although MeHg is typically found with trace concentrations in soils, bioaccumulation and biomagnification of MeHg in the food web can lead to high, and often hazardous, concentrations in higher trophic levels. The complexity of the mercury cycle, involving interactions between redox conditions, microbial activity, bioaccumulation, chemical speciation, and many other factors necessitates a variety of treatment approaches to address the dynamic behavior of Hg in sediment-water systems. Among these, *in-situ* remediation strategies offer an advantage by targeting the source of Hg and Hg-methylation, limiting Hg and MeHg diffusing from soils into overlying waters and entering the food web. This dissertation explores the development and evaluation of manganese oxide-modified activated carbon (MOMAC) as an *in-situ* remediation strategy for redox-sensitive contaminants, with a focus on Hg and MeHg. MOMAC presents a novel approach, combining the redox buffering capacity of manganese oxides with the high sorption capacity of activated carbon to disfavor production of MeHg, while sequestering Hg and MeHg species in soil.

The first chapter focuses on the synthesis and characterization of MOMAC compared to homogenously precipitated manganese oxide (MnOx) and unaltered activated carbon (AC). Factors influencing sorption capacity (surface area) and redox-buffering capacity (average Mn redox state and Mn speciation) were investigated and compared for all materials using a variety of techniques including X-ray absorption spectroscopy, X-ray photoelectron spectroscopy, X-ray diffraction, electron microscopy, and surface area analysis. This chapter also included incubation experiment to show how characterized properties translated into redox buffer and sorption capacity in a system with artificial creek water or Hg-contaminated soils. Results showed a lower average oxidation state in MOMAC compared to homogenous MnOx and a lower surface area compared to unaltered activated carbon. However, while MnOx-treated sediments exhibited a large release of Hg, MOMAC was able to buffer redox potential compared to untreated or AC-treated sediments while maintaining Hg concentrations similar to AC.

The second chapter utilized flow-through column experiments to compare MOMAC treatments against untreated or AC-treated sediments. Addition of organic carbon was incorporated into these experiments to promote microbial activity by adding dissolved organic carbon into the influent solution as acetate and pyruvate or by homogenizing solid OC into sediment as powdered spirulina, lyophilized cyanobacteria. A stopped-flow state was implemented in the experiments to assess performance under saturated, stagnant conditions, reflecting flooding from precipitation events that can induce changes in redox potentials and reaction kinetics. Results showed that MOMAC

can lower production of MeHg in soils compared to untreated and AC-treated soils. However, both abiotic and biotic reductive dissolution, particularly during the stopped-flow state, can rapidly exhaust redox-buffering capacity.

The third chapter was a pilot *in-situ* field trial to assess whether MOMAC could lower MeHg in soils compared to AC or untreated soils. Soil cores were collected from two floodplain sites and two bank sites and amended with or without treatment. These soils, or soil admixtures, were aliquoted into three fine mesh bags, packed into a plastic mesh tube, and returned to point of extraction. Fine mesh bags were retrieved over the course of 11 weeks. The main Hg-species in soils across sites was analyzed using high energy resolution X-ray absorption spectroscopy. Results did not show that Hg or MeHg were significantly different across treatments but showed variability across sites, suggesting the experiment did not perturb the system sufficiently to observe changes. In contrast, the Hg species were largely similar across sites with some differences in MOMAC-treated soils, suggesting oxidative reaction with Hg-bearing analytes, such as organic associated Hg complexes.

1 Characterization of Manganese Oxide Modified Activated Carbon for Remediation of Redox-Sensitive Contaminants

*This chapter is a reproduction of a published article: Rivas Meraz, E.; Traina, S.J.; Beutel, M.W.; O'Day, P.A. Characterization of Manganese Oxide Modified Activated Carbon for Remediation of Redox-Sensitive Contaminants. *ACS Earth and Space Chemistry.* **2023**, 7, 7, 1281–1293.

1.1 Abstract

Manganese oxide-modified activated carbon (MOMAC) was synthesized as a novel *in situ* sediment and soil amendment for treatment of redox-sensitive contaminants, such as mercury (Hg), through buffering of reduction-oxidation (redox) potential and sorption. This study characterized MOMAC synthesis products at three different Mn concentrations on activated carbon (AC) surfaces and compared them with homogeneously precipitated Mn oxide (MnOx) and unmodified AC for properties influencing redox buffering and sorption capacity. Bulk spectroscopic analyses (XAS and XPS), XRD, and electron microscopy showed that homogeneous MnOx matched the local structure of vernadite (δ-Mn(IV)O_2), while MOMAC formed aggregates on the AC surface composed mostly of vernadite with fractions of manganite (γ-Mn(III)OOH) (17-46%) and sorbed Mn(II) (11-21%). Higher bulk surface area and lower Mn average oxidation state were associated with MOMAC and are attributed to the reduction of Mn(IV) by Mn(II) adsorbed on AC or diffused into AC pores. Cation exchange reactions of Na^+ and Ca^{2+} also contributed to Mn oxidation state changes by driving disproportionation of Mn(III) to Mn(II) and Mn(IV). In batch slurry experiments with and without Hg-contaminated sediment from Oak Ridge National Laboratory (TN, USA), addition of MOMAC and MnOx resulted in higher solution redox potential and lower pH compared to AC and no-amendment controls. MnOx poised solution redox at higher potential than MOMAC, but MOMAC was more effective at sorbing Hg released by the oxidation of sediment HgS(s), Hg^0, and/or organic-associated Hg. By combining redox buffering with sorption, MOMAC is a promising *in situ* amendment that may more efficiently target redox-sensitive contaminants in aquatic sediments.

1.2 Introduction

Sediments and soils within freshwater aquatic ecosystems can be sinks for hazardous organic and inorganic contaminants sourced from both anthropogenic and natural activity.[1–3] Accumulation of pollutants in sediments degrades aquatic ecosystems and poses a global threat to water quality.[2] Investigating effective remediation strategies for natural sediments remains a challenge due to the myriad of biological, chemical, and physical mechanisms that influence the fate of contaminants.[2,3] Among these, reduction-oxidation (redox) reactions and sorption processes occupy a large role in the chemical speciation, mobility, bioavailability, and toxicity of metal, metalloid, and organic compounds.[4,5]

Gaseous[6–8], aqueous[9,10], and solid-phase[11–13] amendments have been applied to

freshwater systems to target redox-sensitive contaminants with promising results. Solid phase amendments can be cost-effective, can combine redox buffering with sorption, and can be engineered to withstand diverse environmental conditions.[14,15] Manganese (Mn), commonly present as Mn(II), (III), or (IV) in environmental systems, has a rich redox chemistry where all oxidation states above Mn(II) possess strong oxidizing capabilities.[16–21] Solid Mn(IV) oxide phases are ubiquitous minerals in environmental systems that can directly influence the chemical speciation of redox-sensitive constituents and contaminants.[16,21–24] However, a potential limitation to the use of Mn oxides as a remedial amendment is rapid reductive dissolution of Mn(IV) oxides to aqueous Mn(II) in some environments. Dissolution of Mn(IV) oxides is favored at acidic pH[25] and may be accelerated by reaction with major electron donors in sediment (e.g., Fe(II), sulfide, or organic carbon) and mediated by microorganisms.[26–31] Rapid dissolution may also lead to accumulation of aqueous Mn(II), which can impair potable water treatment systems.[13,32]

Remediation approaches that promote oxidation and sorption in aquatic sediments can be utilized to: 1) provide an oxidizing barrier that buffers redox potential (Eh) at the sediment-water interface, 2) expand the zone of oxidized porewater below the sediment-water interface to impede diffusion of contaminants into the water column, and 3) sequester and oxidatively degrade contaminants, thus limiting diffusion into overlying waters. Supplementing $Mn(IV)O_2$, hereafter MnOx, with an additional high-surface area sorbent may help slow Mn(IV) reduction by adsorbing electron donors, limiting the accumulation of aqueous Mn(II) through adsorption, and/or providing additional sorption of redox-sensitive species.[32–34] Activated carbon (AC) is a commonly used sorbent for the sequestration of organic and inorganic contaminants from water and sediment.[33,35,36] However, implementing two separate media *in situ* as an amendment cap or sediment admixture is challenging, adds cost, or may be infeasible. Adhering MnOx onto the AC surface to form a manganese oxide modified activated carbon (MOMAC) potentially combines the effects of both amendments while simplifying field application.

This study characterized MOMAC prepared with three different Mn concentrations on AC particle surfaces, and compared them to MnOx homogeneously precipitated from solution and to unmodified AC (Fig. 1.1). Properties that influence the redox buffering capacity, sorption capacity, and longevity of each amendment, such as surface area, particle size, pore diameter, and Mn chemical species and oxidation states, were compared. To evaluate the ability of MOMAC and MnOx amendments to regulate Eh and pH in sediment-water systems and sorb contaminants, batch experiments were done with mercury (Hg)-contaminated sediments collected from East Fork Poplar Creek (EFPC), Oak Ridge National Laboratory, TN, USA.

Despite several large remediation efforts, discontinuous layers of high Hg concentration persist in bank sediments along EFPC.[37,38] The periodic erosion of these contaminated sediment layers introduces high amounts of Hg into EFPC where methylation can occur.[39] Redox buffering (by MnOx) or redox buffering and sorption (by MOMAC) could potentially be used to limit Hg and MeHg transport into the creek by surface or subsurface application of solid amendments to bank sediments. Additionally, the calcareous, slightly alkaline (pH ~7.8) environment at EFPC favors stability of Mn(III), (IV) oxide and Mn(II) carbonate phases, while elevated levels of nitrate from treated wastewater discharges may provide additional redox buffering and favor potential

reoxidation of Mn(II).[40]

1.3 Methods

1.3.1 Materials

Ultrapure water (18.2 MΩ cm, Millipore-Sigma Milli-Q) was utilized for all syntheses and analytical experiments. Reagent grade chemicals (Sigma Aldrich, St. Louis, MO, USA) and powder AC (Fisher Scientific, Hampton, NH, USA) were purchased and used in syntheses without further alteration. Reagent grade (β-MnO2) and trace metal grade (Mn_2O_3, MnO) Mn reference materials were purchased (Sigma Aldrich, St. Louis, MO, USA) and kept under an inert atmosphere (N_2).

1.3.2 Preparation of MnOx and MOMAC Amendments

Preparation of synthetic MnOx and MnOx surface modified AC (MOMAC) was adapted from the synthesis of poorly crystalline vernadite (δ-MnO_2)[20] as follows:

$$2\ KMnO4 + 3\ MnCl2{\cdot}4H2O + 4\ NaOH \rightarrow 5\ MnO2 + 2\ K+ + 4\ Na+ + 6\ Cl– + 10\ H2O \quad (1)$$

A 66.67 mL solution of 0.29 M $MnCl_2{\cdot}4H_2O$ was equilibrated for 24 h with (MOMAC) or without (MnOx) 13.3 g AC. A solution of 0.19 M $KMnO_4$ was slowly added to a solution of 0.38 M NaOH (66.67 ml of each). The combined solution was then added to the $MnCl_2{\cdot}4H_2O$ ± AC solution dropwise and stirred for approximately 1 h. The pH was kept above 7.0 during the synthesis process by small additions of 0.1 M NaOH. Particles were allowed to settle for 1 h before recording the final pH. Solids were separated from the reaction solution by centrifugation at 10,000 relative centrifugal force (rcf). The supernatant solution was carefully extracted, filtered through a 0.45 µm PES filter, acidified with 0.4% HCl (v/v), and stored at 4 °C until analysis. The solid was washed three times by mixing with 50 mL 1 M $CaCl_2$, shaken vigorously, vortexed for up to 30 s or until well-mixed, and then centrifuged to separate solids and solution. The supernatant solution was collected for Mn analysis as described above. The $CaCl_2$ wash was followed by three washes with 50 mL ultrapure water before drying in the oven at 55 °C for 24 h. The dried solids were stored in amber glass jars and frozen. Solution samples were analyzed for total Mn by inductively coupled plasma-optical emission spectrometry (ICP-OES) (see Text A1).[41]

1.3.3 Amendment Characterizations

Synthesized products were characterized with several spectroscopic and analytical techniques to assess differences between synthetic MnOx, unmodified AC, and MOMAC. Scanning and scanning transmission electron microscopic (SEM and STEM) imaging and energy-dispersive X-ray (EDX) spectroscopy were used to assess Mn presence and surface distribution on AC particles in MOMAC solids (see Text A2). Extractable Mn was determined by reacting 0.5 g of solid with 25 mL of 0.1 M hydroxylamine hydrochloride (HHCl) solution prepared in 0.01 M HNO_3 and placed on a rotating mixer at 40 rpm for 30 m.[42] Slurries were centrifuged at 7000 rcf to separate solid and solution, and supernatant solutions were analyzed for total Mn with ICP-OES.

Surface area was analyzed using the BET method and pore size distribution by the BJH method with a Micromeritics® Tristar II Plus (see Text A3).[43] Determination of Mn oxidation states and phases was conducted using X-ray absorption spectroscopy (XAS), X-ray photoelectron spectroscopy (XPS), and X-ray diffraction (XRD). Changes to the AC were also investigated with C1s XP spectroscopy.

1.3.3.1 X-ray Absorption Spectroscopy

Samples for XAS analysis were prepared (see Text A4) in a glovebox under a 95% N_2 and 5% H_2 to minimize changes in oxidation state. Bulk Mn K-edge XAS was conducted on beam line 4-1 at the Stanford Synchrotron Radiation Lightsource (SSRL). Spectral analyses were done using SIXpack and Athena programs.[44,45] Multiple scans (at least three and up to six) were averaged to improve signal to noise. Averaged spectra were separated using Athena to isolate the XANES and EXAFS regions for individual background subtraction to obtain uniform normalization and improve reference spectra matching for linear combination (LC) fits. Background was subtracted using a linear fit through the pre-edge region and a spline fit through the EXAFS region. Linear combination fits were conducted on XANES and EXAFS regions using a reference library of thoroughly characterized Mn compounds (Fig. A1; Table A1). To help with LC fits, a sample of Mn(II) sorbed to AC was synthesized in which 0.9 g of AC was reacted for 24 h with 30 mL of 10 mM $MnCl_2{\cdot}4H_2O$ and collected as a reference spectrum (additional information in Text A4). Components that constituted less than 5% of the LC fit of an unknown spectrum were rejected.

The pre-edge region (6530-6550 eV) was extracted from the normalized XANES spectra and modeled using Larch XAS[46] with parameters described in Farges et al. 2005.[47] An estimation of the Mn valence could be obtained from the pre-edge region within ±5% accuracy.[47] The pre-edge for 2-3 representative samples of Mn(II), (III), and (IV) oxidation states were fit. For each reference sample, the baseline was subtracted using a linear-Lorentzian curve and a least-squares fit was performed with 2-3 peaks of fixed width (FWHM = 1.3 eV) and shape (0.45 Gaussian-Lorentizan mix). The centroids of each peak for each reference sample were averaged (Fig. A2; Table A2). The averaged centroids for each peak were used to fit secondary standards and unknown samples with shifts of ± 0.1 eV allowed for each peak. Secondary standards were samples with known mixed oxidation states (Mn_3O_4 and triclinic Na-birnessite[20]) that were utilized to check reliability of AOS estimations (Fig. A3). Comparisons of the fit centroids were used as an additional estimate of Mn valency states for MnOx and MOMAC.

1.3.3.2 X-ray Photoelectron Spectroscopy

X-ray photoelectron spectroscopy (XPS) was used for estimation of MnOx oxidation states on particle surfaces of homogeneously precipitated MnOx and MOMAC.[48–51] Samples and references were ground with a CerCo Diamonite™ synthetic sapphire mortar and pestle and dispersed onto copper tape adhered on a silicon wafer (Ted Pella) for Mn3p, O1s, or C1s XPS. Data were collected with a Thermo Scientific™ Nexsa G2 X-Ray Photoelectron Spectrometer equipped with a monochromatic Al Kα source. Samples were scanned using a 400 µm spot size and 50 ms dwell time for both survey and narrow scans. Survey wide scans were collected with a 150 eV pass energy,

0.5 eV step size, and represent averages of 10-15 sweeps. Narrow scans were collected with a 20 eV pass energy, 0.1 eV step size, and represent averages of 10-15 (O 1s, C 1s) or 100 (Mn 3p) sweeps. An electron flood gun was utilized during data collection to minimize sample charging.[52] Data analysis was carried out with Thermo Avantage software. A charge correction was applied based on the observed deviation from the adventitious carbon peak (284.1 eV in this study). An iterative Shirley background subtraction was employed to account for differences in intensity across the spectrum.[53–55] A non-linear least square curve fitting approach described in Ilton et al. 2016[56] was utilized to analyze the unknown mixed oxidation states. Details of the fitting procedures to Mn3p, O1s, and C1s regions and fits with reference standards are shown in Text A5 and Fig. A4, respectively. A second set of Mn(II), (III), and (IV) reference standards was scanned and fit to assess consistency of curve shapes associated with each oxidation state (Fig. A5; Table A3). Goodness-of-fit was assessed by comparing the reduced (normalized) chi-square and Abbe criterion (see Table A5 for equation).[57] A spectrum of an Ag sample that was etched clean and collected at 80 eV pass energy was used for calibration, yielding a confidence interval at or above 90%.

1.3.3.3 Powder X-ray Diffraction

Powder X-ray diffraction (XRD) was used to verify the identity of Mn crystalline reference phases (Fig. A6) and identify any crystalline phases in either synthesized MnOx or MOMAC samples. Data were collected using a PANalytical X'pert PRO Theta diffractometer operated at 50 kV and 40 mA with a Co Kα source and an X'Celerator detector. Samples were mounted on Si zero diffraction plates and scanned from 5° to 80° 2θ angle. Data were converted to Cu Kα wavelength, stripped of $K\alpha_2$, background subtracted, and peak matched using the X'pert HighScore software and ICDD PDF-4+ library.

1.3.4 Batch Experiments

Mercury-contaminated stream sediment from EFPC was collected along a left descending bank (36° 0' 16'' N, 84° 16' 56'' W) on the Oak Ridge National Lab site. Total Hg (THg) in the sediment was measured using a Direct Mercury Analyzer (Milestone DMA-80) via thermal decomposition, amalgamation, and atomic absorbance spectrophotometry.[58] Sequential thermal desorption was used to estimate weakly and strongly bound Hg species present in sediment. Approximately 0.1 g of wet sediment was ignited sequentially at 100°C, 225°C, 325°C, 475°C, and 750°C for 480 s.[59] These measurements were supplemented with sequential selective chemical extractions that target the exchangeable fraction and organic Hg fractions in sediments.[60] Approximately 2 g of sediment was reacted with 20 mL of solvent (1 M $CaCl_2$, followed by 0.2 M NaOH, and lastly 4% (v/v) acetic acid) in a 50 mL polypropylene tube, shaken for 2 h at 150 rpm (Thermo Scientific Solaris™ Open Air Orbital Shaker), and centrifuged at 7000 rcf for 15 m. Following extractions with $CaCl_2$ and acetic acid, the sediment was rinsed twice with ultrapure water (20 mL and then 10 mL) for 15 minutes, centrifuged, and combined with the supernatant solution from the respective solvent extraction. Total Hg in the extracted solutions was measured on a MERX-T Hg system through oxidation,

purge and trap, and cold vapor atomic fluorescence spectroscopy (CVAFS) (Brooks-Rand MERX-T) following standard quality assurance/control protocols with a reporting limit of 0.2 ng/L.[61]

Batch experiments were prepared with either 0.30 g MnOx, 1.02 g MOMAC, or 0.89 g of AC to normalize for mass of Mn added and surface area of AC provided. The MnOx was added at 2% dry weight ($g_{amend}/ g_{dry\ sed}$), slightly below the dose used for *in situ* sediment remediation at Hg-contaminated sites (2.5-5%).[62] Dosing for MOMAC was normalized to the mass of Mn added in the MnOx to compare the redox buffering effect between homogeneous MnOx and Mn in MOMAC. In one set, amendments (synthetic MnOx, AC, or MOMAC with the highest Mn concentration) were mixed with 40 mL of an artificial creek water (ACW) solution designed to match the water chemistry of EFPC (Table 1.1). In another set, 15 g of EFPC wet sediment was homogenized with the amendment and mixed with 40 mL of ACW. Experiments were prepared and carried out in an N_2-filled glove box. Measurements of pH (ROSS Sure-Flow) and redox potential were taken by probe (Thermo Scientific Orion Triode) every 24 h over a 2-week period. Redox measurements were converted to Eh by correcting for the electrode potential of the reference electrode (Ag/AgCl; E_{ref} = 207 mV).[63]

1.4 Results

1.4.1 Solid Synthesis and Selective Extractions

Chemical extractions and analyses of reaction solutions were used to characterize Mn synthesis products (MnOx and MOMAC). The initial pH of each synthesis reaction solution was 1.32, 4.40, 5.30, and 5.40, and was adjusted to a final pH of 7.49, 7.68, 7.17, and 7.08 for MnOx, and MOMAC with low (L), medium (M), and high (H) Mn concentrations, respectively. The HHCl treatments to measure total extractable Mn yielded 3.1±0.05, 7.4±0.01, and 11.9±0.04 g_{Mn}/g_{MOMAC} (mean ± standard error, n = 3) in MOMAC (L), (M), and (H), respectively. The Mn concentration in $CaCl_2$ and ultrapure water wash solutions was measured as an indicator of residual Mn(II) removed from the solid via ion exchange or desorption. Low to non-detectable (< 0.1 mg/L) concentrations of Mn(II) were measured in the supernatant solutions from the MnOx and MOMAC syntheses and in subsequent washes with $CaCl_2$ (Fig. 1.2). However, higher concentrations of Mn(II) were observed in solution after the first wash, or subsequent washes, with ultrapure water rather than $CaCl_2$ solutions. The Mn(II) released by MOMAC products was much higher than from MnOx solid (Fig. 1.2).

1.4.2 Solid Characterizations

Images captured with SEM and STEM coupled with EDX showed fluorescence from both Mn and O on the surface of AC particles for MOMAC solids (Fig. 1.3). Mn oxide particles were aggregated in small areas on the AC surface rather than uniformly coated. Similarly, synthetic MnOx particle sizes ranged from nanoparticulate to larger (~20-50 μm) aggregates based on SEM images (Fig. A7). Surface areas (measured by the BET method) of synthetic MnOx (130 m^2/g) and activated carbon (958 m^2/g) were lower and higher, respectively, than BET surface areas measured from MOMAC samples, which decreased with increasing MnOx concentration (L: 785±56, M: 736±71, H: 616±47 m^2/g; mean ± standard error, n = 3) (Fig. A8). Average pore diameter (measured

by the BJH method) was lowest for AC (4.8 – 5.1 nm) and highest for MnOx (12.4 – 13.1 nm). For MOMAC samples, average pore diameter increased with increasing MnOx concentration (L:5.4 – 5.7 nm; M:5.6 – 6.0 nm; H: 7.0 – 7.4 nm). Diffractograms of synthetic MnOx and MOMAC showed no significant reflections attributed to Mn(IV)Ox minerals (Fig. A9). MOMAC samples exhibited reflections attributed to graphite with an additional reflection in the MOMAC (M) sample that matched the major reflection for feitknechtite (β-Mn(III)OOH).

1.4.3 X-ray absorption spectroscopy (XAS): XANES and EXAFS

Estimation of Mn species determined from XAS was consistent with separate analysis of the XANES and EXAFS regions (Fig. 1.4; Table A4). Linear combination (LC) fits of reference spectra to MOMAC samples were similar across concentrations and consisted of three components (Fig. A10), compared to synthetic MnOx, which was fit by one component. Fits to MnOx XANES and EXAFS regions matched best with synthetic vernadite (δ-Mn(IV)O_2); additional components did not statistically improve the fit. Fits of MOMAC samples included fractions of manganite (γ-Mn(III)OOH, 17-46%) and Mn(II) sorbed on AC (11-21%), in addition to vernadite (42-63%). The AOS estimated from LC fits of separated XANES and EXAFS regions were within 5% (Table A5).

.

1.4.4 X-ray Photoelectron Spectroscopy and X-ray Absorption Spectroscopy Pre-edge Peak

Manganese oxidation states in MnOx and MOMAC were estimated independently by analysis of XPS Mn 3p binding energy peaks and XAS Mn K-edge (1s) pre-edge peak region extracted from the total X-ray absorption spectrum (Fig. 1.5). Unlike LC fits to MnOx XANES and EXAFS, Mn 3p XPS data collected on MnOx was fit with fractions of Mn(II) (~10%) and Mn(III) (~15%) in addition to Mn(IV) (Table A6). There was little difference among MOMAC samples, but a consistently lower Mn AOS was observed in MOMAC samples compared to MnOx (Table 1.2). The MOMAC XPS data were fit with smaller fractions of Mn(IV) and contained higher fractions of low-valent Mn, mostly as Mn(II). Distinctions between MnOx and MOMAC were also seen with O1s XPS where MOMAC exhibited lower fractions of lattice oxide groups and greater fractions of hydroxl groups or sorbed H_2O (Fig. A11; Table A7). Analyses of C1s XPS data showed negligible differences between the unmodified AC and MOMAC (Fig. A12; Table A8). Among MOMAC samples, the AOS estimated from XPS agreed with analysis by XANES and EXAFS (±5%) (Table 1.2; Table A5).

Analysis of the X-ray absorption pre-edge features of the Mn K-edge was conducted as an additional indicator of Mn redox states.[47,64–66] The pre-edge features reflect electronic transitions from the 1s core level to the lowest unoccupied valence orbitals, i.e., 3d or 4p orbitals, the latter if hybridized by Mn ligands.[47,64] Peak fits to synthetic MnOx showed entirely Mn(IV) whereas MOMAC samples were fit with 32-46% Mn(III) and 15-19% Mn(II) (Table A9). The fit centroid was highest for synthetic MnOx (6541.9 eV) and lower for all MOMAC samples (6541.7 eV). The AOS of MOMAC and MnOx samples estimated with the pre-edge fits agreed with the analysis by XPS, XANES, and EXAFS (±5% and ±10%, respectively) (Table 1.2).

1.4.5 Batch Experiments with Hg-Contaminated Sediments

Batch experiments with AC, MnOx, or MOMAC amendment and ACW, with and without Hg-contaminated sediment, were monitored for solution Eh and pH to assess regulation of these parameters by each amendment. Eh-pH diagrams (Fig. 1.6) show measured Eh and pH from batch experiments plotted on equilibrium stability regions for Mn aqueous and solid species and sulfur (S) aqueous species. Total Hg in the sediment was 11.5±1.3 mg Hg/kg (mean ± standard error, n = 3) measured by thermal desorption on a DMA, with the largest fractions associated with thermal desorption at temperatures of 100 and 225 °C, which are assigned to Hg^0 and other common Hg species including $HgCl_2$ and methylmercury (Fig. A13).[59,67] Other non-mobile, compounds such as β-HgS or Hg_2Cl_2 are also associated with decomposition at 225°C. Selective extractions intended to target the exchangeable and organic fractions of sediment Hg yielded only 0.07 and 0.275 mg Hg/kg, respectively, which is ~0.007% and 0.02% of total Hg (Fig. A14).

In batch experiments with amendment and ACW (Fig. 1.6a), the pH of the control (ACW, no solid) and AC treatments decreased slightly (pH ~7.80 to 7.10) from the initial conditions (pH ~ 7.82), but Eh remained constant (~0.440 V). In contrast, a higher Eh was observed in ACW amended with MnOx (0.700 to 0.840 V) compared to the ACW control and initial conditions. However, ACW amended with MnOx also had the lowest pH of all treatments (pH ~5.40). ACW amended with MOMAC had higher Eh (~0.600 V) compared to AC and control treatments, but lower Eh than ACW with MnOx. Similarly, the pH of ACW-MOMAC solutions decreased (pH ~6.50) compared to initial conditions but remained higher than ACW-MnOx treatments.

Batch experiments with Hg-contaminated sediment (Fig. 1.6b) had similar overall trends as the ACW-amendment experiments, but differences among the three solids were much less pronounced. There were slight decreases in Eh (~0.500 to 0.400 V) and pH (~7.80 to 7.20) in the control (ACW and sediment) and AC samples compared to initial conditions (Table 1.1). Sediments treated with either MnOx or MOMAC showed an increase in Eh (~0.500 to 0.600 V), but similar pH (~7.00), over time compared to the sediment control. Measured THg in solution (by CVAFS) was similar between the control, AC, and MOMAC experiments at around 2.0-2.4 µg/L, whereas the MnOx treatment exhibited higher dissolved Hg concentrations at 6.2 µg/L (Fig. 1.7).

1.5 Discussion

1.5.1 Bulk and Surface Properties of Amendments

Results from spectroscopic characterizations identified synthetic vernadite (δ-MnO_2) as the primary Mn(IV) phase in both MnOx and MOMAC (Fig. 1.8). The absence of major reflections in XRD patterns, however, indicated that it formed as an XRD-amorphous precipitate, indicating a lack of long-range atomic structural order, both homogeneously from solution and on the AC surface. Synthetic vernadite resembles a birnessite-like layered structure with interlayer cations, but exhibit turbostratically disordered layer stacking of Mn(IV)-O_6 octahedra linked by shared edges,[18,68–70] which leads to an absence of major reflections in XRD.[68,69] Additionally, synthetic manganese

oxides that have not been annealed at high temperatures are typically disordered and amorphous to XRD.[71] MOMAC solids identified by XAS included fractions of sorbed Mn(II) (11-21%) and γ-Mn(III)OOH (17-46%) in addition to vernadite (Fig. 1.8). The presence of γ-Mn(III)OOH, or other Mn(III)OOH polymorphs, is further supported by XPS O1s fits that suggest higher fractions of hydroxyl associated with MOMAC (Fig. A11; Table A7). Fractions of Mn(II) fit in both MnOx and MOMAC were attributed to sorbed Mn(II) (Fig. 1.8). In MnOx, lower AOS observed with XPS compared to bulk XAS analyses (pre-edge, XANES, and EXAFS) could be attributed to the surface sensitivity of XPS where the surface may contain sorbed Mn(II) and can be more reduced than the bulk.[56]

Gas adsorption-desorption isotherms used to measure surface area and pore size distribution utilized N_2 as probing molecule and has previously been reported to underestimate the internal surface area of microporous structures such as MnOx.[72,73] Nitrogen gas adsorption-desorption isotherms collected on amendments indicated higher surface areas associated with MOMAC and AC compared to MnOx, and larger average pore size in MnOx and MOMAC compared to AC. High surface area is often correlated with higher contaminant sorption, while larger average pore size can prevent pore blockage from competing sorbates like dissolved organic matter.[74–76] Aggregation of MnOx particles, observed with SEM, can decrease accessible surface area and limit sorption of contaminants.[77] Images of the MOMAC solids coupled with EDX also showed Mn oxide aggregated in small areas rather than uniformly dispersed on the AC surface. Similarly, higher Mn concentrations among the three MOMAC samples corresponded to a decrease in surface area compared to unmodified AC. Decreasing surface area may indicate aggregation of Mn oxide on the AC surface onto AC. While aggregation may decrease sorption on the surface, unmodified AC surface may be beneficial as it would allow sorption of other constituents on the AC substrate.[77]

1.5.2 Role of Mn(II) and AC During Amendment Synthesis

Synthesis of MnOx and MOMAC was driven by a comproportionation reaction between $MnCl_2{\cdot}4H_2O$ and $KMn(VII)O_4$, to form $Mn(IV)O_2$, in the absence or presence of AC, respectively (reaction 1). Prior studies[78–80] have also suggested formation of nanoparticulate MnO_2 on carbonaceous surfaces, such as AC, through spontaneous surface oxidation of carbon and reduction of MnO_4^- through the following reaction:

$$4MnO_4^- + 3C + H_2O \rightleftharpoons 4MnO_2 + CO_3^{2-} + 2HCO_3^- \qquad (2)$$

The formation of CO_3^{2-} or HCO_3^- through this mechanism buffered pH during MOMAC synthesis and resulted in higher initial pH compared to homogeneous MnOx precipitation. However, no major changes in the AC characteristics were observed with C1s XP spectroscopy (Fig. A12).

For MOMAC synthesis, a $MnCl_2{\cdot}4H_2O$ solution was equilibrated with AC to promote sorption of Mn^{2+} ions prior to addition of $KMnO_4$, which could serve as nucleation sites for the oxidative precipitation of MnOx by reaction of sorbed Mn(II) with $KMnO_4$. The presence of dissolved Mn in multiple sequential washes of MOMAC after synthesis supports the hypothesis of Mn(II) diffusion into AC pores and delayed

release during washes (Fig. 1.2). Aqueous or adsorbed Mn(II) can undergo electron exchange with structural Mn(IV) and initiate reductive transformation to Mn(III)OOH by the reaction:[81–83]

$$MnO_2 + Mn^{2+} + 2H_2O \rightarrow 2MnOOH + 2H^+ \qquad (3)$$

Therefore, a fraction of MnO_2 formed on the MOMAC surface through either reaction 1 or 2 could have been reduced by surface Mn(II) form Mn(III) by reaction 3. For homogeneously precipitated MnOx, fractions of Mn(II) and (III) were observed with XPS but not by bulk XAS, which showed only Mn(IV). These results suggest that reduction of MnO_2 by reaction 3 was likely restricted mostly to the surface due to particle aggregation and lower overall surface area.[84]

1.5.3 Role of Cation Exchange During Amendment Synthesis

Synthesis of MnOx and MOMAC was followed by triplicate washes with 1 M $CaCl_2$ and ultrapure water. Results indicated that these post-synthesis steps can further alter Mn oxide solids. Synthetic vernadite commonly exhibits defect sites where Mn(IV) in octahedral layers is substituted by either Mn(III) or other trivalent cations, or may be vacant, with charge-balancing cations present above or below the vacancy site.[18,69] Substitution of Mn(IV) by Mn(III) induces charge deficits within structural birnessite layers that are balanced by the presence of interlayer hydrated cations such as Na^+, K^+, Ca^{2+}, or Mn^{2+}. Cation exchange within interlayers of Na-birnessite, such as where Na^+ is exchanged by Ca^{2+}, has been shown to change the oxidation state of octahedrally coordinated Mn(III) in structural layers.[69,85]. The exchange of Ca^{2+} for Na^+ favors a destabilization of the Mn(III)-O bond and subsequent disproportionation:[85]

$$2Mn(III) \rightarrow Mn(II) + Mn(IV) \qquad (4)$$

During synthesis of MnOx and MOMAC with NaOH, Na^+ would be incorporated initially into Mn oxide interlayers. Post-synthesis washes with 1 M $CaCl_2$ would exchange Na^+ with Ca^{2+}, driving a Ca-induced disproportionation of Mn(III) by reaction (4). Mn(II) cations produced by this reaction are too large to occupy octahedral sites in the Mn oxide layers and are instead relocated as strongly sorbed species either above or below the vacancy site, or lost to solution.[85] During the $CaCl_2$ wash steps, Mn was below detection in the extracted supernatant solutions, which indicates retention of Mn(II) on the MnOx or MOMAC solid by either relocation to vacancy sites or adsorption to other surface sites rather than released into solution.[85] In either case, sharp changes to the ionic strength and cation composition of the washing solution can cause changes in sorption (on AC in case of MOMAC) or incorporation of metals into the MnOx interlayers.[86,87] The removal of interlayer cations such as Mn(II) to solution following washes with ultrapure water may have also contributed to structural disorder observed with XRD. In addition to Mn(II) released through disproportionation of Mn(III), these washes may have also released Mn(II) diffused into AC pores during equilibration, which may account for the higher concentrations of Mn in solution from the $CaCl_2$ and ultrapure water washes of

MOMAC samples compared to homogeneous MnOx. Bulk and surface characterizations of MnOx and MOMAC suggest that changes to Mn oxidation state associated with cation exchange reactions were largely confined to the surface.

1.5.4 Role of Mn Species in Redox and pH Buffering

Results from the batch experiments suggest that solution redox buffering was affected by differences in Mn species between MnOx and MOMAC.[88] Homogeneous MnOx was matched best with synthetic vernadite by XAS analysis, which is predominantly Mn(IV), whereas MOMAC contained Mn(III) as γ-Mn(III)OOH (or other polymorphs) and sorbed Mn(II). Results from batch experiments with ACW showed that measured solution Eh was highest for MnOx amendment followed by MOMAC amendment, which was higher than unamended or AC treatments. The larger fraction of Mn(III)OOH in MOMAC likely decreased the redox buffering potential when compared to MnOx in ACW.[89] For example, Mn(III) sites within MnOx are expected to be less effective than Mn(IV) in the oxidation of contaminants such as As(III) by Mn oxides.[89,90] Although Mn(III)OOH would poise Eh at a lower equilibrium potential than Mn(IV) in synthetic vernadite (MnOx) in the ACW solution, MOMAC with both Mn(III) and Mn(IV) was shown to poise Eh higher than no-amendment controls or AC treatments.[89]

The electron configuration of Mn(II), consisting of a half-filled d-shell, generates a stable atom that does not readily oxidize other compounds in aquatic systems.[22] Rather, several studies have reported reductive transformations of birnessite (Mn(IV) oxide) to Mn(III)OOH, or mixed-valent $Mn(II,III)_3O_4$, while in the presence of aqueous Mn(II), which lowers the overall redox buffering capacity.[81,82,89] Additionally, Mn(II) can passivate reactive surface sites, block sorption sites on AC, or occupy vacancy sites on Mn oxide that can decrease total sorption capacity.[83,91,92] Reactions between Mn(III) or (IV) oxides and electron donors such as sulfide minerals or organic matter can cause reductive dissolution and generate high concentrations of aqueous Mn(II).[13] There is increasing concern about Mn contamination of drinking water, which can lead to neurotoxic health effects.[93,94] Precipitation of Mn(II) compounds such as rhodochrosite ($MnCO_3$), or oxidation to Mn(III) or Mn(III,IV) solids, may limit the concentration of Mn(II) in solution, but these processes can be kinetically slow and are strongly pH dependent.[95,96] Oxidation of Mn(II) can be catalyzed both abiotically through complexation with organic compounds or by Mn(IV) oxide mineral surfaces, and biotically through various enzymatically driven bacterial or fungal pathways.[97,98] Calcareous systems such as EFPC can promote stability of Mn(II) solids, and the presence of additional electron acceptors (e.g., nitrate) can potentially re-oxidize Mn(II) to provide additional redox buffering.[99]

Another potential consequence of applying amendments such as MnOx or MOMAC to sediment is the oxidative dissolution of sulfide minerals, such as HgS(s) or FeS(s), or oxidation of metallic Hg^0 that can introduce dissolved Hg species into the water phase.[13,100,101] Prior Hg speciation studies of EFPC sediment report HgS(s) as a dominant Hg species (~10-35%) and have also noted fractions of Hg^0 ranging from ~10-15%.[101–104] Thermal desorption gradient measurements performed on EFPC sediment in this study showed that ~6% of Hg is present as HgS and ~10% is volatilized at low (~100 °C) temperatures, suggesting the presence of a small fraction of Hg^0 in the

sediment.[59,67,104] Release of Hg to solution observed in batch experiments with MnOx may be associated with oxidation of Hg^0, HgS(s), Hg complexed with organic matter, and/or other easily exchangeable Hg. The additional sorption capacity of AC and MOMAC may have limited Hg release to solution compared with MnOx.

While oxidative dissolution may increase dissolved Hg concentrations, high redox potential should suppress the microbial transformation of Hg(II) to methylmercury. Methylmercury is a neurotoxic form of mercury that typically comprises < 1% of THg in the sediment by mass, but bioaccumulates in aquatic food webs.[6,13] Methylmercury is favored to form under low redox conditions through microbial iron-reducing or sulfate-reducing pathways[105–108] and can be disfavored through redox buffering by addition of Mn oxides.[11–13] The mobility and toxicity of other redox-sensitive contaminants in sediments, such as As(III) or Cr(III), can also be affected by addition of poorly crystalline Mn oxides.[90,91,109] For example, redox buffering by Mn oxides has been hypothesized to limit large arsenic releases from sediment in a seasonally anoxic lake by favoring oxidation to As(V) and sorption onto solid phases such as ferrihydrite.[92] Conversely, Cr(III) in soils can be oxidized by Mn oxides to the more mobile and toxic form Cr(VI).[109,110]

In addition to redox buffering, the MnOx and MOMAC amendments decreased the pH of solutions in batch experiments compared to controls and AC treatments. Solution pH is a key variable that can control the speciation and fate of MnOx-based amendments. Mn(III, IV) oxides are thermodynamically unstable at lower pH for a given Eh (Fig. 1.6).[25] Intermediate Mn(II,III) oxide phases such as hausmannite are favored to form at high pH (> ~8) and can provide additional redox buffering or limit release of aqueous Mn(II). The pH decrease observed when MnOx was mixed with ACW favors reductive dissolution to aqueous Mn(II) without the formation of intermediate phases (Fig. 1.6), particularly in slightly acidic (pH < 7) or highly reducing environments, resulting in higher aqueous Mn(II) concentrations.[13] In limestone-rich environments such as EFPC[37], high concentrations of dissolved bicarbonate can buffer pH > 7, as seen in the sediment batch experiments, while favoring stabilization of Mn(II) as $MnCO_3$, which may form given sufficient reaction time.[12] In the absence of pH buffering, reductive dissolution of Mn(IV) solids can occur rapidly and diminish redox buffering capacity[3,6].

1.6 Conclusion

Characterization of MnOx and MOMAC revealed differences in properties that impact redox buffering and sorption capacity, which are largely influenced by Mn species, Mn AOS, pore size, and surface area. Results suggest that aqueous and sorbed Mn(II) and cation exchange processes involving Na^+ and Ca^{2+} can influence Mn redox states during synthesis and, in turn, the performance of the final MOMAC product as a redox buffer. MOMAC solids contained fractions of Mn(III) as Mn(III)OOH and sorbed Mn(II) that resulted in lower solution Eh in batch experiments than MnOx (identified as amorphous synthetic vernadite, δ-Mn(IV)O_2) when applied to ACW. In treatments with sediment, solution Eh was similar for MOMAC and MnOx, but MnOx amendments released more Hg to solution, probably by oxidation of sediment Hg^0, HgS(s) and/or organic-Hg. Treatment with AC did not alter redox potential in either ACW or sediment experiments, and release of Hg into solution was similar to MOMAC and no-amendment

control, which may reflect the higher surface area and thus sorption capacity of AC and MOMAC. Experimental results suggest that the lower AOS of MOMAC resulted in less reduction in pH compared with MnOx, which is favorable due to the thermodynamic instability of Mn oxide solids at low pH. Mn AOS impacts redox buffering capacity and can affect the treatment of organic[16] and inorganic contaminants in freshwater systems.[90,91,109] Our results suggest that the Mn(III) fraction can be adjusted by altering the cation (either Na^+ or Ca^{2+}) and mass of Mn(II) used during syntheses. While changes to Mn redox states occurred during synthesis in this study, cation exchange and release of Mn(II) also commonly occur in aquatic ecosystems, and these processes can be used to inform *in situ* implementation strategies.

Application of MOMAC to sediment-water systems contaminated with redox-sensitive contaminants should consider environmental conditions that affect stability and fate of Mn oxide amendments. For example, sediment-water systems with low pH and high concentrations of sulfide, Fe(II), or other electron donors can lead to rapid reductive dissolution of Mn oxides.[13,27,29] Reductive dissolution of Mn oxides releases aqueous Mn(II), which drives an autocatalyzed reductive dissolution that further depletes the redox buffering capacity if not removed from solution through precipitation.[13] Understanding the impact of these processes on Mn-based *in situ* amendments can inform both future synthesis methods and favorable environmental conditions for implementation. Our findings suggest that applying multifaceted techniques, such as combining redox buffering and sorption, can have a compounding effect that can more effectively remediate redox-sensitive contaminants, such as Hg, compared to redox buffering or sorption alone.

1.7 Figures

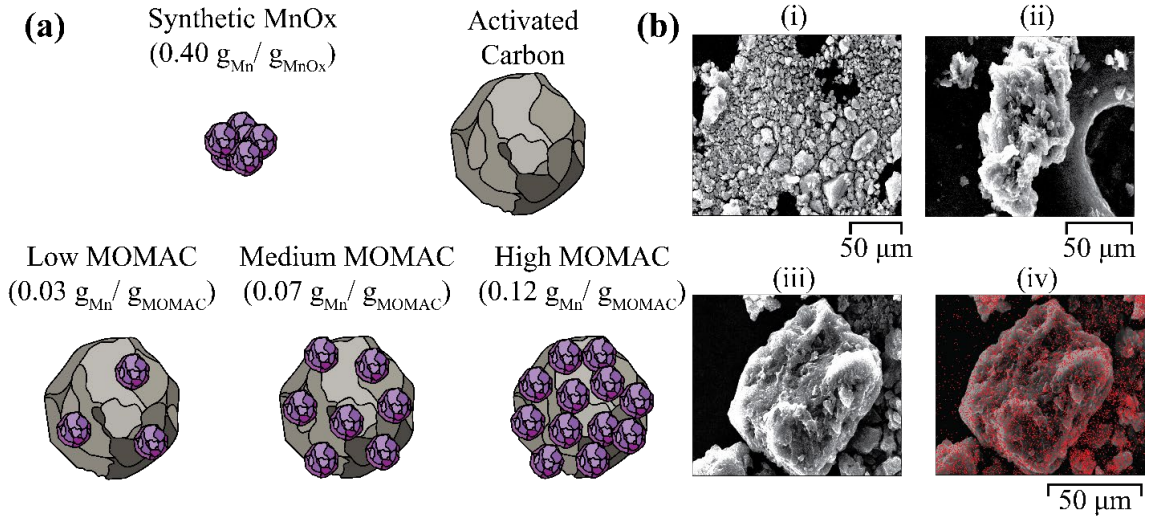

Figure 1.1 (a) Conceptual model for MnOx and MOMAC treatments showing MnOx adhered onto AC at a low, medium, and high concentrations to combine sorption and redox buffering. (b) Scanning electron microscopy images showing representative images of (i) MnOx, (ii) AC, and (iii) MOMAC solids dispersed on carbon tape with (iv) an energy

dispersive spectroscopic image showing Mn fluorescence (red) on the surface of MOMAC particles.

Table 1.1 Chemical composition of the artificial creek water solution

Species	mmol/L	mg/L
Ca^{2+}	1.2	46.8
Cl^-	1.1	40.0
NO_3^-	0.7	10.0
K^+	0.1	2.0
Mg^{2+}	0.4	10.2
SO_4^{2-}	0.4	35.0
Total alkalinity (as HCO_3^-)	1.1	50.3
Na^+	0.7	16.6
Ionic Strength (mmol/kgw) = 5.5[a]		
Total alkalinity (meq/kg) = 1.0[a]		
pH = 7.82[b]		
Eh = 0.437 V[b]		

[a] Calculated with PHREEQC[111]

[b] Initial value measured in solution

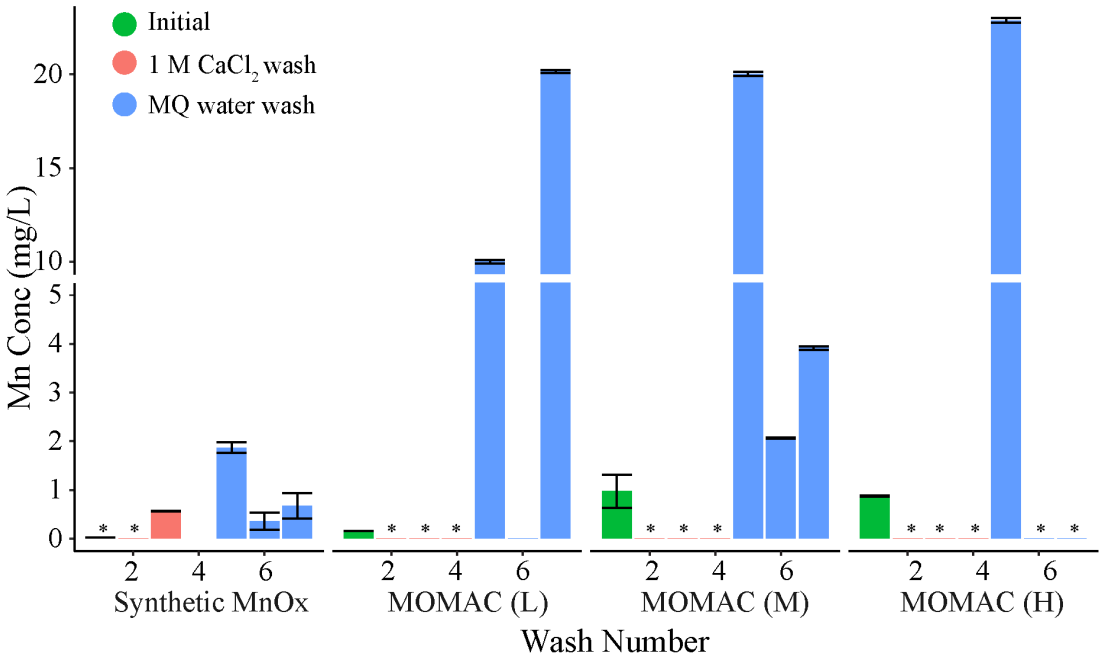

Figure 1.2 Mn concentrations in synthesis supernatant solutions of MnOx and MOMAC. Green: initial solution after synthesis; Red: washes with 1 M $CaCl_2$; Blue: washes with ultrapure water; *: Sample measurement below detection limit (2.5 µg/L). Instrumental uncertainty (2σ) from triplicate measurements of each sample is shown by the black lines. Note break in y-axis for data visualization.

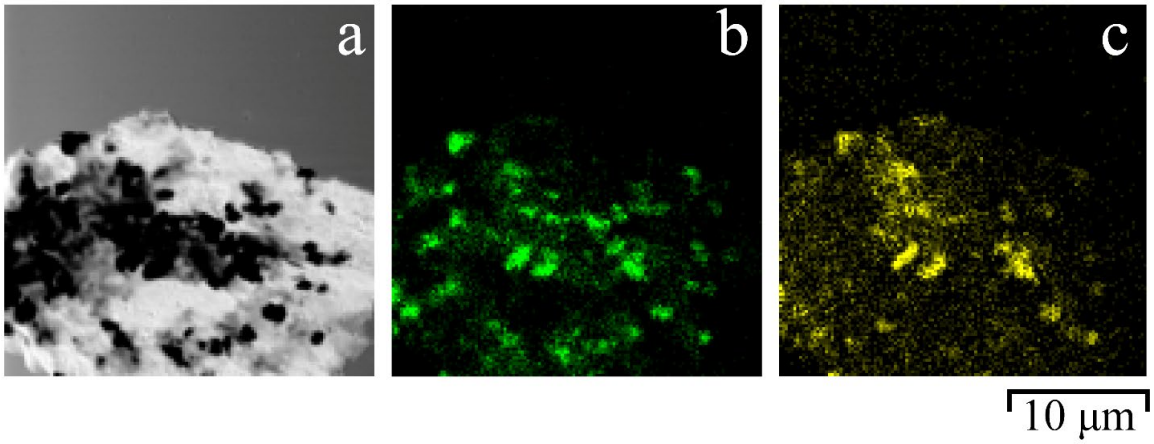

Figure 1.3 a) Image of a MOMAC particle (AC substrate with MnOx granules) captured with scanning transmission electron microscopy (STEM). Energy dispersive X-ray spectroscopy (EDX) fluorescence mapping of the same area showing the distribution of **b)** Mn and **c)** O on the AC surface.

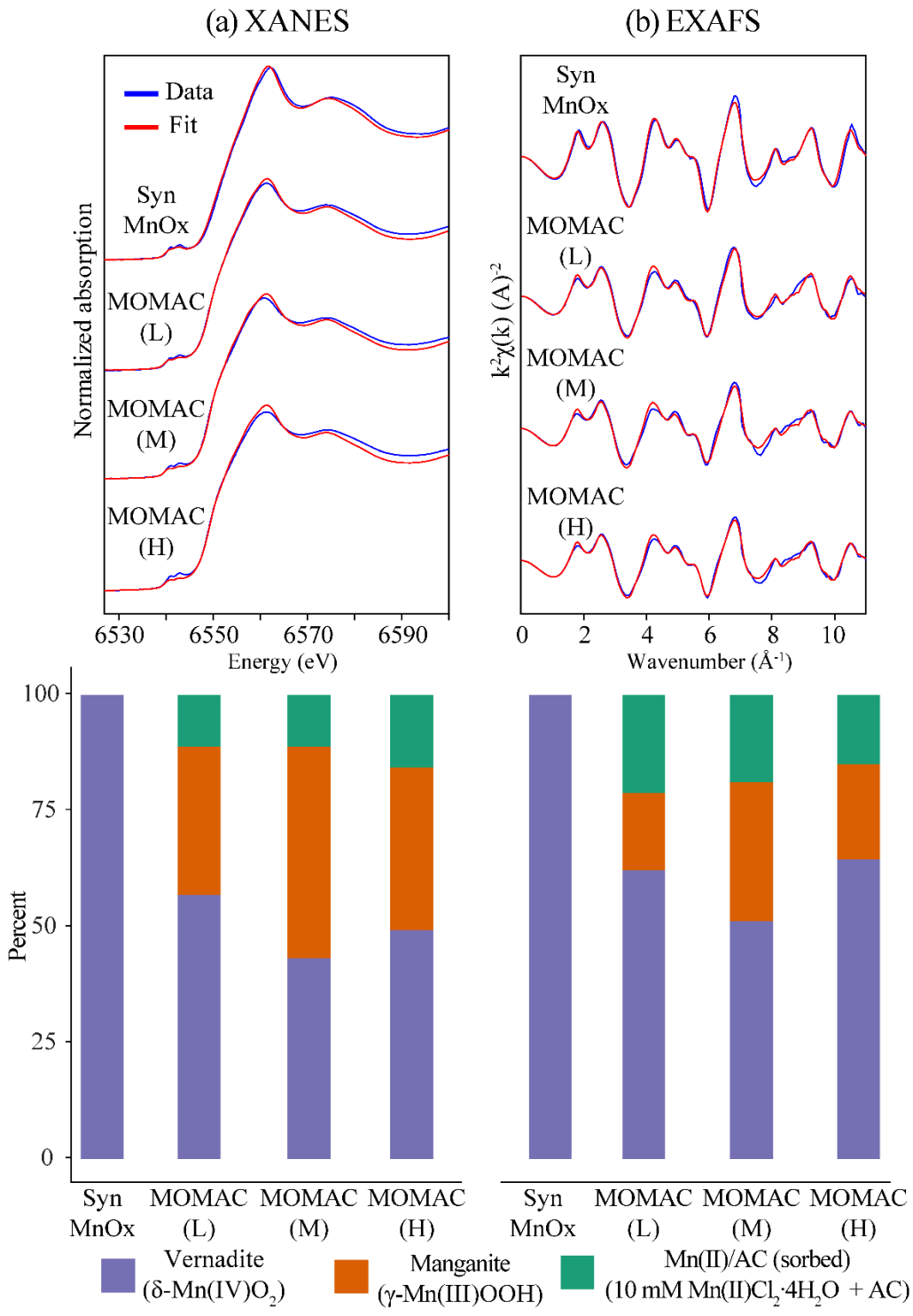

Figure 1.4. Mn K-edge X-ray absorption spectra (blue lines) of synthetic MnOx and MOMAC samples divided into **(a)** XANES (fit region 6530-6590 eV) and **(b)** EXAFS (k-range fit region of 1.5-10 $Å^{-1}$) with linear combination fits (red lines show component sum).

Linear combinations were conducted with a library of Mn reference compounds. Fractions of the best-fit components, normalized to 100%, are represented by the bar plots. Tabulated values and representative deconvolution for MOMAC are given in Table A4 and Fig. A10.

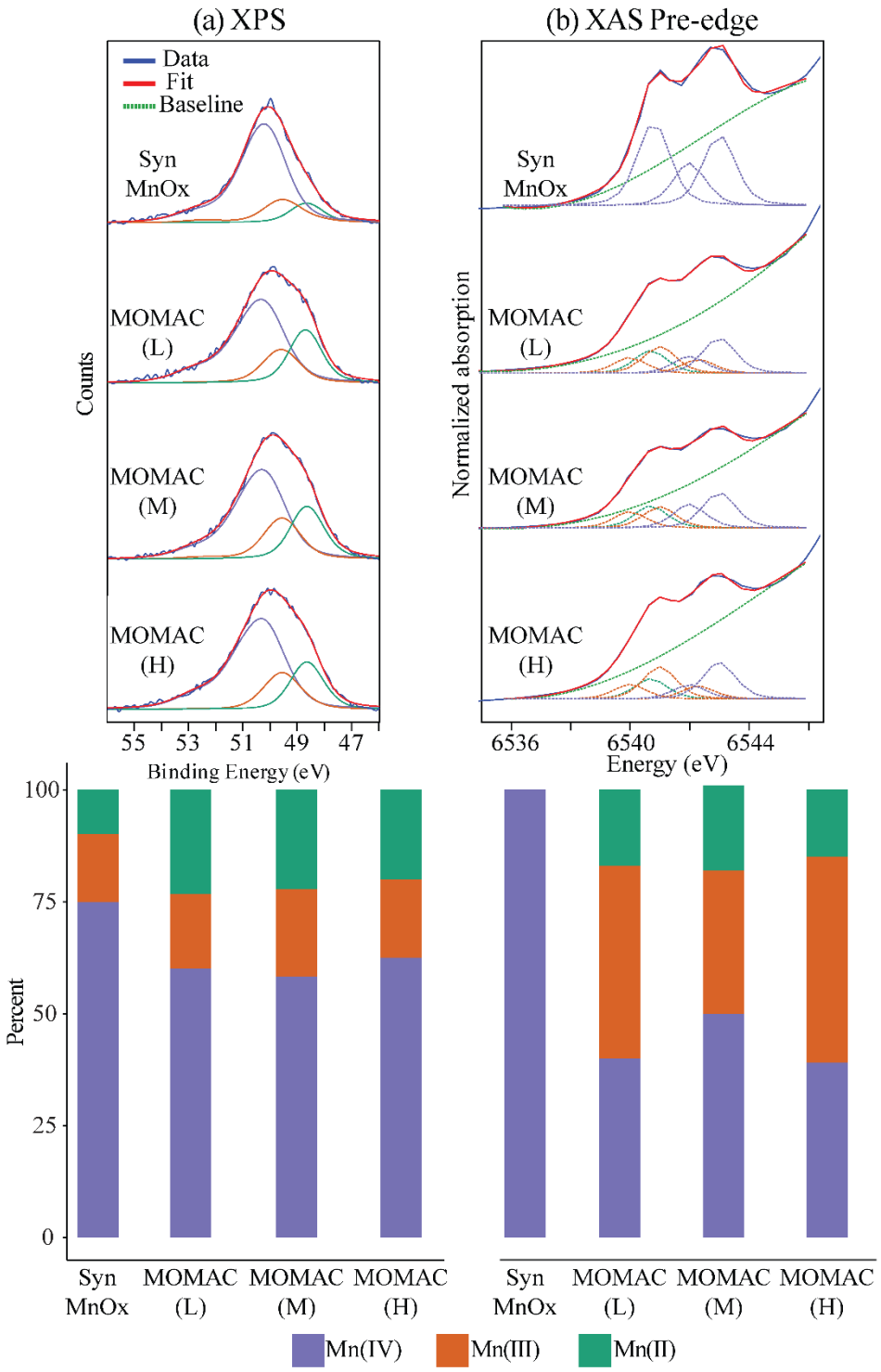

Figure 1.5. Estimation of Mn oxidation states in MnOx and MOMAC through analysis of **(a)** Mn 3p peak collected with X-ray photoelectron spectroscopy (XPS) and **(b)** expanded Mn K-edge pre-edge region from X-ray absorption spectra (shown in Fig. 1.4). For XPS, non-linear least-squares curve fits were used to determine distribution of oxidation states

in MnOx and MOMAC based on curves defined by analysis of reference compounds. The Mn pre-edge was fit with sets of 2 or 3 pseudo-Voigt functions (FWHM = 1.3 eV; Gaussian/ Lorentzian = 0.45; peaks shown) for reference compounds where each peak was allowed to shift ±0.1 eV. Bar plots show fractions of Mn(II), (III), and (IV) fit in each sample. Tabulated values for XPS and pre-edge fits reported in Table A5 and Table A6, respectively.

Table 1.2. Mean Mn average oxidation state estimated with XAS (pre-edge, XANES, and EXAFS) and XPS analysis.

Sample	Average Oxidation State[a]
Synthetic MnOx	3.91±0.26
MOMAC (L)	3.37±0.15
MOMAC (M)	3.34±0.03
MOMAC (H)	3.38±0.17

[a] Mean average oxidation state ± standard error (3×)

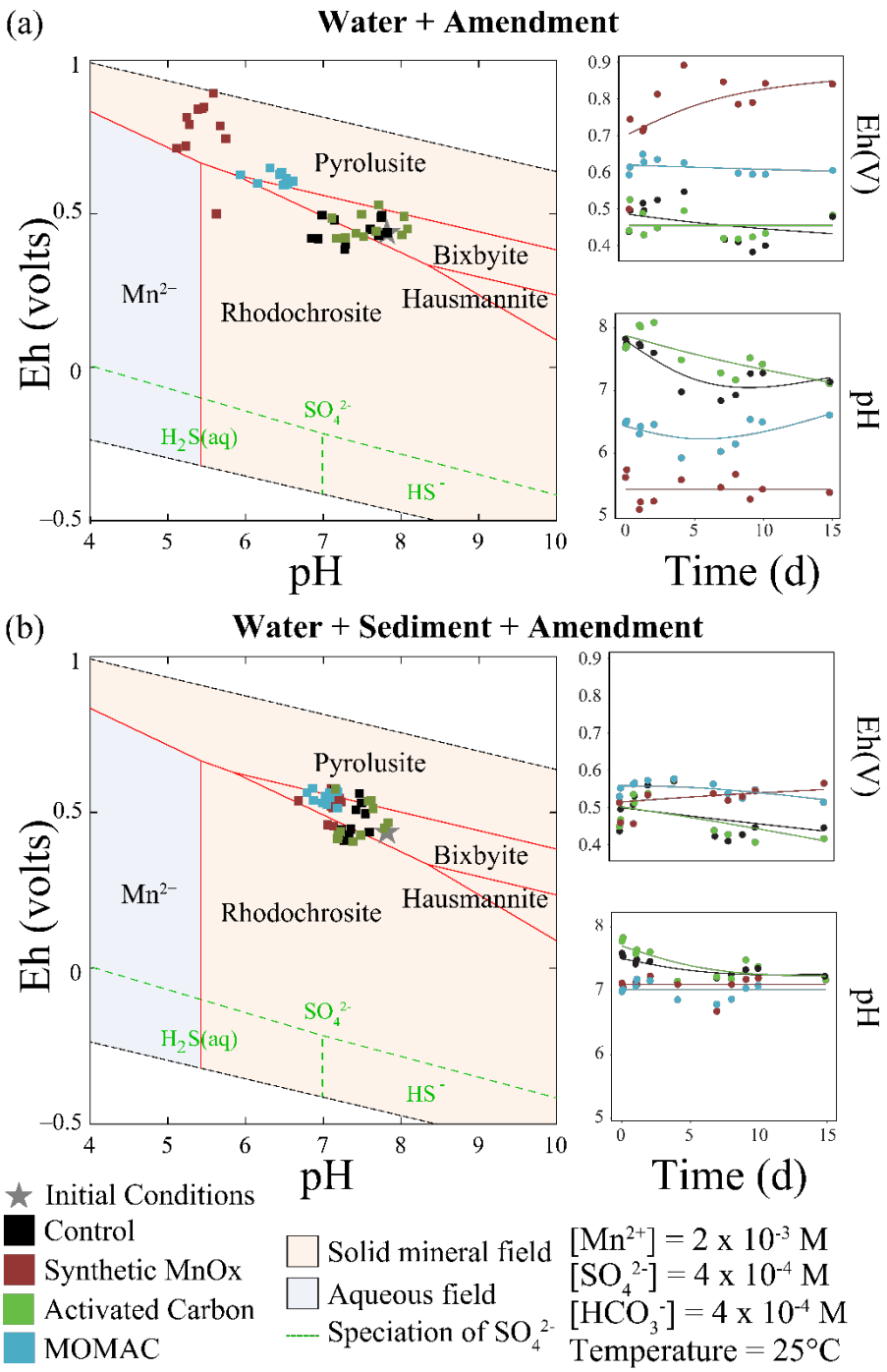

Figure 1.6. Eh-pH diagrams and measured Eh and pH as a function of time in batch screening experiments of amendments (a) mixed with artificial creek water only, or (b) homogenized with Hg-contaminated sediment and mixed with artificial creek water. Eh-pH diagrams show Mn aqueous and solid speciation (solid red lines) and S aqueous species (dashed green lines). Chemical formulas for minerals: rhodochrosite: $MnCO_3$; hausmannite: Mn_3O_4; bixbyite: Mn_2O_3; pyrolusite: MnO_2. Calculations were done using the Act2 program from Geochemist Workbench. Experimental data are plotted at the end

of reaction (15 d) on the Eh-pH diagrams. Solid lines on the Eh and pH time plots represent statistical smoothing of the data calculated with a generalized additive model.

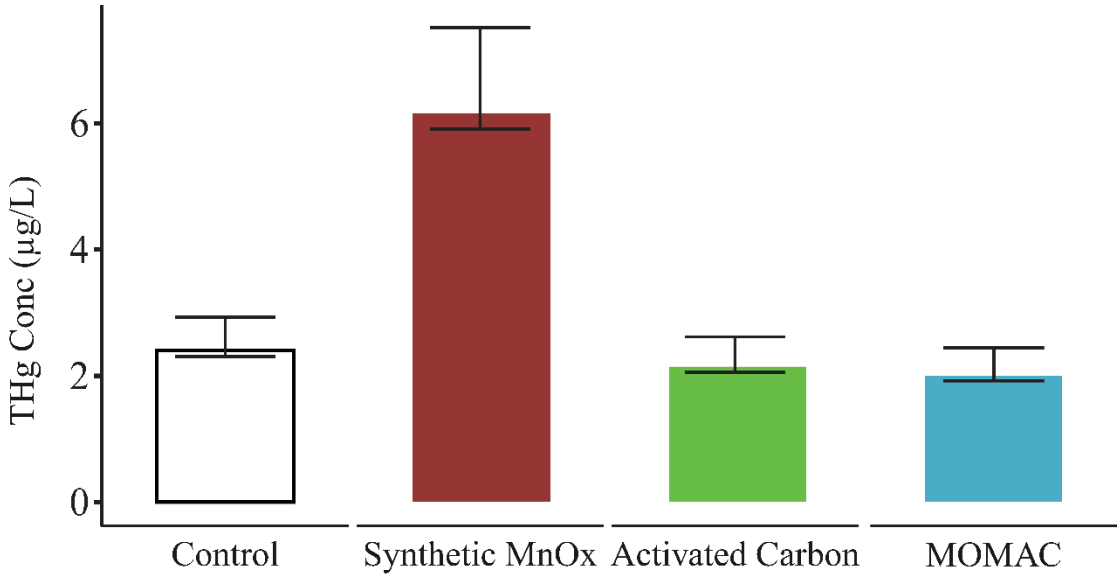

Figure 1.7. Total Hg measured in solutions of batch screening experiments after 15 d of reaction with contaminated sediment and amendment treatments (untreated control vs. amendment with MnOx, AC, or MOMAC (H)). Total Hg in sediment was 11.5±1.3 mg/kg dry weight (mean ± standard error, n = 3). Uncertainty calculated as the average percent recovery from ongoing precision and recovery samples ± 2 standard deviations from the mean (96-122%).

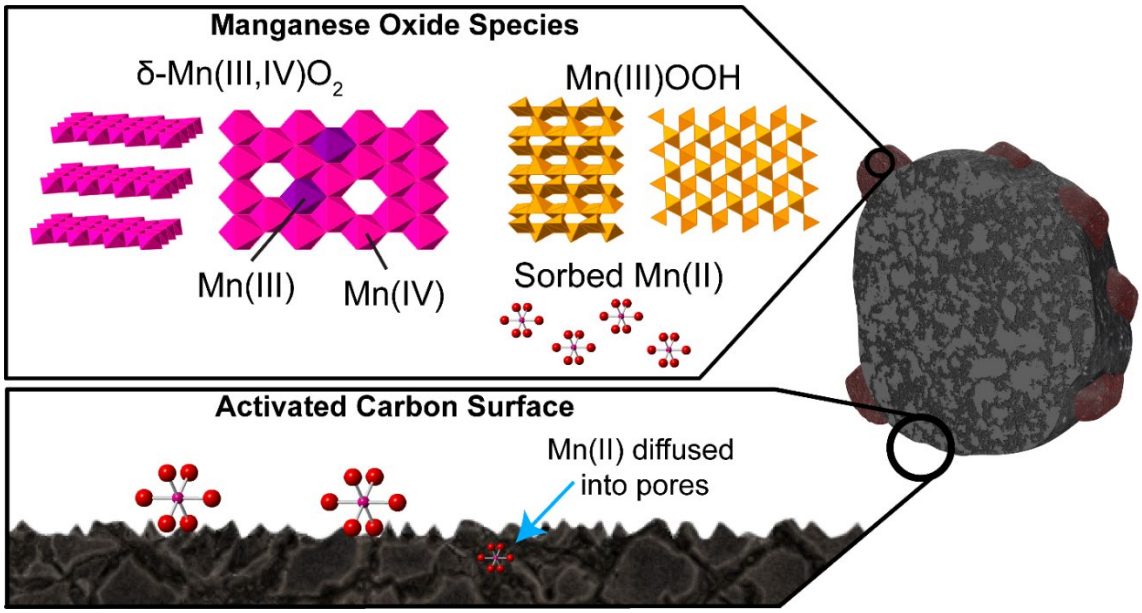

Figure 1.8. Illustration of MOMAC depicting Mn surface species on activated carbon. The Mn oxide species and crystal morphology found in the Mn aggregates located on the surface of the activated carbon substrate. Octahedral vacancies (marked by the empty space) or Mn(III) in octahedral sites (marked by darkened octahedra) found within δ-MnO_2 result in negative charges that are balanced by hydrated cations in the interlayers, such as Mn(II). Surface of the activated carbon with Mn(II) sorbed and/or diffused into pore spaces following equilibration with $MnCl_2 \cdot 4H_2O$ for 24 h prior to oxidation with $KMnO_4$.

1.8 References

(1) Perelo, L. W. Review: In Situ and Bioremediation of Organic Pollutants in Aquatic Sediments. *J Hazard Mater* **2010**, *177* (1–3), 81–89. https://doi.org/10.1016/j.jhazmat.2009.12.090.

(2) Burton, G. A. Metal Bioavailability and Toxicity in Sediments. *Crit Rev Env Sci Tec* **2010**, *40* (9–10), 852–907. https://doi.org/10.1080/10643380802501567.

(3) Peng, J.; Song, Y.; Yuan, P.; Cui, X.; Qiu, G. The Remediation of Heavy Metals Contaminated Sediment. *J Hazard Mater* **2009**, *161* (2–3), 633–640. https://doi.org/10.1016/j.jhazmat.2008.04.061.

(4) Borch, T.; Kretzschmar, R.; Kappler, A.; Cappellen, P. V.; Ginder-Vogel, M.; Voegelin, A.; Campbell, K. Biogeochemical Redox Processes and Their Impact on Contaminant Dynamics. *Environ Sci Technol* **2010**, *44* (1), 15–23. https://doi.org/10.1021/es9026248.

(5) Eggleton, J.; Thomas, K. V. A Review of Factors Affecting the Release and Bioavailability of Contaminants during Sediment Disturbance Events. *Environ Int* **2004**, *30* (7), 973–980. https://doi.org/10.1016/j.envint.2004.03.001.

(6) Seelos, M.; Beutel, M.; Austin, C. M.; Wilkinson, E.; Leal, C. Effects of Hypolimnetic Oxygenation on Fish Tissue Mercury in Reservoirs near the New Almaden Mining District, California, USA. *Environ Pollut* **2021**, *268* (Pt A), 115759. https://doi.org/10.1016/j.envpol.2020.115759.

(7) Duvil, R.; Beutel, M. W.; Fuhrmann, B.; Seelos, M. Effect of Oxygen, Nitrate and Aluminum Addition on Methylmercury Efflux from Mine-Impacted Reservoir Sediment. *Water Res* **2018**, *144*, 740–751. https://doi.org/10.1016/j.watres.2018.07.071.

(8) Beutel, M.; Dent, S.; Reed, B.; Marshall, P.; Gebremariam, S.; Moore, B.; Cross, B.; Gantzer, P.; Shallenberger, E. Effects of Hypolimnetic Oxygen Addition on Mercury Bioaccumulation in Twin Lakes, Washington, USA. *Sci Total Environ* **2014**, *496*, 688–700. https://doi.org/10.1016/j.scitotenv.2014.06.117.

(9) Todorova, S. G.; Driscoll, C. T.; Matthews, D. A.; Effler, S. W.; Hines, M. E.; Henry, E. A. Evidence for Regulation of Monomethyl Mercury by Nitrate in a Seasonally Stratified, Eutrophic Lake. *Environ Sci Technol* **2009**, *43* (17), 6572–6578. https://doi.org/10.1021/es900887b.

(10) Matthews, D. A.; Babcock, D. B.; Nolan, J. G.; Prestigiacomo, A. R.; Effler, S. W.; Driscoll, C. T.; Todorova, S. G.; Kuhr, K. M. Whole-Lake Nitrate Addition for Control of Methylmercury in Mercury-Contaminated Onondaga Lake, NY. *Environ Res* **2013**, *125*, 52–60. https://doi.org/10.1016/j.envres.2013.03.011.

(11) Vlassopoulos, D.; Kanematsu, M.; Henry, E. A.; Goin, J.; Leven, A.; Glaser, D.; Brown, S. S.; Day, P. A. Manganese(Iv) Oxide Amendments Reduce Methylmercury Concentrations in Sediment Porewater. *Environ Sci Process Impacts* **2018**, *20* (12), 1746–1760. https://doi.org/10.1039/c7em00583k.

(12) Leven, A.; Vlassopoulos, D.; Kanematsu, M.; Goin, J.; O'Day, P. A. Characterization of Manganese Oxide Amendments for in Situ Remediation of Mercury-Contaminated Sediments. *Environ Sci Process Impacts* **2018**, *20* (12), 1761–1773. https://doi.org/10.1039/c7em00576h.

(13) Seelos, M.; Meraz, E. R.; Beutel, M.; Traina, S. J.; Furhmann, B.; Burmistrova, J.; Vlassopoulos, D.; O'Day, P. A. Evaluation of Manganese Oxide Amendments for Mercury Remediation in Contaminated Aquatic Sediments. *Acs Es T Eng* **2021**. https://doi.org/10.1021/acsestengg.1c00267.

(14) O'Day, P. A.; Vlassopoulos, D. Mineral-Based Amendments for Remediation. *Elements* **2010**, *6* (6), 375–381. https://doi.org/10.2113/gselements.6.6.375.

(15) Eckley, C. S.; Gilmour, C. C.; Janssen, S.; Luxton, T. P.; Randall, P. M.; Whalin, L.; Austin, C. The Assessment and Remediation of Mercury Contaminated Sites: A Review of Current Approaches. *Sci Total Environ* **2020**, *707*, 136031. https://doi.org/10.1016/j.scitotenv.2019.136031.

(16) Remucal, C. K.; Ginder-Vogel, M. A Critical Review of the Reactivity of Manganese with Organic Contaminants. *Environ Sci Process Impacts* **2014**, *16* (6), 1247–1266. https://doi.org/10.1039/c3em00703k.

(17) Hullebusch, E. D. V.; Huguenot, D.; Pechaud, Y.; Simonnot, M.-O.; Colombano, S. *Environmental Soil Remediation and Rehabilitation, Existing and Innovative Solutions*; Springer Nature Switzerland AG, 2020. https://doi.org/10.1007/978-3-030-40348-5.

(18) Post, J. E. Manganese Oxide Minerals: Crystal Structures and Economic and Environmental Significance. *Proc National Acad Sci* **1999**, *96* (7), 3447–3454. https://doi.org/10.1073/pnas.96.7.3447.

(19) Tebo, B. M.; Bargar, J. R.; Clement, B. G.; Dick, G. J.; Murray, K. J.; Parker, D.; Verity, R.; Webb, S. M. Biogenic Manganese Oxides: Properties and Mechanisms of Formation. *Earth Planet Sci* **2004**, *32* (1), 287–328. https://doi.org/10.1146/annurev.earth.32.101802.120213.

(20) Villalobos, M.; Toner, B.; Bargar, J.; Sposito, G. Characterization of the Manganese Oxide Produced by Pseudomonas Putida Strain MnB1. *Geochim Cosmochim Ac* **2003**, *67* (14), 2649–2622. https://doi.org/10.1016/s0016-7037(03)00217-5.

(21) Petrunic, B. M.; MacQuarrie, K. T. B.; Al, T. A. Reductive Dissolution of Mn Oxides in River-Recharged Aquifers: A Laboratory Column Study. *J Hydrol* **2005**, *301* (1), 163–181. https://doi.org/10.1016/j.jhydrol.2004.06.022.

(22) Armstrong, F. A. Why Did Nature Choose Manganese to Make Oxygen? *Philosophical Transactions Royal Soc B Biological Sci* **2008**, *363* (1494), 1263–1270. https://doi.org/10.1098/rstb.2007.2223.

(23) Zhang, H.; Huang, C.-H. Oxidative Transformation of Triclosan and Chlorophene by Manganese Oxides. *Environ Sci Technol* **2003**, *37* (11), 2421–2430. https://doi.org/10.1021/es026190q.

(24) Shaikh, N.; Taujale, S.; Zhang, H.; Artyushkova, K.; Ali, A.-M. S.; Cerrato, J. M. Spectroscopic Investigation of Interfacial Interaction of Manganese Oxide with Triclosan, Aniline, and Phenol. *Environ Sci Technol* **2016**, *50* (20), 10978–10987. https://doi.org/10.1021/acs.est.6b02673.

(25) Peng, J.; Giordano, L.; Davenport, T. C.; Shao-Horn, Y. Stability Design Principles of Manganese-Based Oxides in Acid. *Chem Mater* **2022**, *34* (17), 7774–7787. https://doi.org/10.1021/acs.chemmater.2c01233.

(26) Herszage, J.; Afonso, M. dos S. Mechanism of Hydrogen Sulfide Oxidation by Manganese(IV) Oxide in Aqueous Solutions. *Langmuir* **2003**, *19* (23), 9684–9692. https://doi.org/10.1021/la034016p.

(27) Stone, A. T. Reductive Dissolution of Manganese(III/Iv) Oxides by Substituted Phenols. *Environ Sci Technol* **1987**, *21* (10), 979–988. https://doi.org/10.1021/es50001a011.

(28) Stone, A. T. Microbial Metabolites and the Reductive Dissolution of Manganese Oxides: Oxalate and Pyruvate. *Geochim Cosmochim Ac* **1987**, *51* (4), 919–925. https://doi.org/10.1016/0016-7037(87)90105-0.

(29) Postma, D.; Appelo, C. A. J. Reduction of Mn-Oxides by Ferrous Iron in a Flow System: Column Experiment and Reactive Transport Modeling. *Geochim Cosmochim Ac* **2000**, *64* (7), 1237–1247. https://doi.org/10.1016/s0016-7037(99)00356-7.

(30) Postma, D. Concentration of Mn and Separation from Fe in Sediments—I. Kinetics and Stoichiometry of the Reaction between Birnessite and Dissolved Fe(II) at 10°C. *Geochim Cosmochim Ac* **1985**, *49* (4), 1023–1033. https://doi.org/10.1016/0016-7037(85)90316-3.

(31) Stone, A. T.; Morgan, J. J. Reduction and Dissolution of Manganese(III) and Manganese(IV) Oxides by Organics. 1. Reaction with Hydroquinone. *Environ Sci Technol* **1984**, *18* (6), 450–456. https://doi.org/10.1021/es00124a011.

(32) Tobiason, J.; Bazilio, A.; Goodwill, J.; Mai, X.; Nguyen, C. Manganese Removal from Drinking Water Sources. *Curr Pollut Reports* **2016**, *2* (3), 168–177. https://doi.org/10.1007/s40726-016-0036-2.

(33) Gilmour, C. C.; Riedel, G. S.; Riedel, G.; Kwon, S.; Landis, R.; Brown, S. S.; Menzie, C. A.; Ghosh, U. Activated Carbon Mitigates Mercury and Methylmercury Bioavailability in Contaminated Sediments. *Environ Sci Technol* **2013**, *47* (22), 13001–13010. https://doi.org/10.1021/es4021074.

(34) Goñez-Rodríguez, L.; Johs, A.; Lowe, K. A.; Carter, K. E.; Löffler, F. E.; Mayes, M. A. Evaluation of Engineered Sorbents for the Sorption of Mercury from Contaminated Bank Soils: A Column Study. *Environ Sci Pollut R* **2021**, *28* (18), 22651–22663. https://doi.org/10.1007/s11356-020-12073-4.

(35) Schwartz, G. E.; Sanders, J. P.; McBurney, A. M.; Brown, S. S.; Ghosh, U.; Gilmour, C. C. Impact of Dissolved Organic Matter on Mercury and Methylmercury Sorption to Activated Carbon in Soils: Implications for Remediation. *Environ Sci Process Impacts* **2019**, *21* (3), 485–496. https://doi.org/10.1039/c8em00469b.

(36) Patmont, C. R.; Ghosh, U.; Larosa, P.; Menzie, C. A.; Luthy, R. G.; Greenberg, M. S.; Cornelissen, G.; Eek, E.; Collins, J.; Hull, J.; Hjartland, T.; Glaza, E. E.; Bleiler, J.; Quadrini, J. In Situ Sediment Treatment Using Activated Carbon: A Demonstrated Sediment Cleanup Technology. *Integr Environ Asses* **2015**, *11* (2), 195–207. https://doi.org/10.1002/ieam.1589.

(37) Brooks, S. C.; Southworth, G. R. History of Mercury Use and Environmental Contamination at the Oak Ridge Y-12 Plant. *Environ Pollut* **2011**, *159* (1), 219–228. https://doi.org/10.1016/j.envpol.2010.09.009.

(38) Southworth, G.; Mathews, T.; Greeley, M.; Peterson, M.; Brooks, S.; Ketelle, D. Sources of Mercury in a Contaminated Stream—Implications for the Timescale of Recovery. *Environ Toxicol Chem* **2013**, *32* (4), 764–772. https://doi.org/10.1002/etc.2115.

(39) Dickson, J. O.; Mayes, M. A.; Brooks, S. C.; Mehlhorn, T. L.; Lowe, K. A.; Earles, J. K.; Goñez-Rodriguez, L.; Watson, D. B.; Peterson, M. J. Source Relationships between Streambank Soils and Streambed Sediments in a Mercury-Contaminated Stream. *J Soils Sediments* **2019**, *19* (4), 2007–2019. https://doi.org/10.1007/s11368-018-2183-0.

(40) Brooks, S. C.; Lowe, K. A.; Mehlhorn, T. L.; Olsen, T. A.; Yin, X.; Fortner, A. M.; Peterson, M. J. *Intraday Water Quality Patterns in East Fork Poplar Creek with an Emphasis on Mercury and Monomethylmercury*; Oak Ridge National Laboratory ORNL/TM-2016/ 578; 2018; pp 1–88. http://www.osti.gov/scitech/.

(41) *U.S. EPA. 2014. "Method 6010D (SW-846): Inductively Coupled Plasma-Atomic Emission Spectrometry," Revision 4. Washington, DC. https://www.epa.gov/esam/epa-method-6010d-sw-846-inductively-coupled-plasma-atomic-emission-spectrometry*

(42) Chao, T. T. Selective Dissolution of Manganese Oxides from Soils and Sediments with Acidified Hydroxylamine Hydrochloride. *Soil Sci Soc Am J* **1972**, *36* (5), 764–768. https://doi.org/10.2136/sssaj1972.03615995003600050024x.

(43) Thommes, M.; Kaneko, K.; Neimark, A. V.; Olivier, J. P.; Rodriguez-Reinoso, F.; Rouquerol, J.; Sing, K. S. W. Physisorption of Gases, with Special Reference to the Evaluation of Surface Area and Pore Size Distribution (IUPAC

Technical Report). *Pure Appl Chem* **2015**, *87* (9–10), 1051–1069. https://doi.org/10.1515/pac-2014-1117.

(44) Ravel, B.; Newville, M. ATHENA, ARTEMIS, HEPHAESTUS: Data Analysis for X-ray Absorption Spectroscopy Using IFEFFIT. *J Synchrotron Radiat* **2005**, *12* (4), 537–541. https://doi.org/10.1107/s0909049505012719.

(45) Webb, S. M. SIXPack a Graphical User Interface for XAS Analysis Using IFEFFIT. *Phys Scripta* **2005**, 1011. https://doi.org/10.1238/physica.topical.115a01011.

(46) Newville, M. Larch: An Analysis Package for XAFS and Related Spectroscopies. *J Phys Conf Ser* **2013**, *430* (1), 012007. https://doi.org/10.1088/1742-6596/430/1/012007.

(47) Farges, F. Ab Initio and Experimental Pre-Edge Investigations of the Mn K-Edge XANES in Oxide-Type Materials. *Phys Rev B* **2004**, *71* (15), 155109. https://doi.org/10.1103/physrevb.71.155109.

(48) Birkner, N.; Nayeri, S.; Pashaei, B.; Najafpour, M. M.; Casey, W. H.; Navrotsky, A. Energetic Basis of Catalytic Activity of Layered Nanophase Calcium Manganese Oxides for Water Oxidation. *Proc National Acad Sci* **2013**, *110* (22), 8801–8806. https://doi.org/10.1073/pnas.1306623110.

(49) Biesinger, M. C.; Payne, B. P.; Grosvenor, A. P.; Lau, L. W. M.; Gerson, A. R.; Smart, R. S. C. Resolving Surface Chemical States in XPS Analysis of First Row Transition Metals, Oxides and Hydroxides: Cr, Mn, Fe, Co and Ni. *Appl Surf Sci* **2011**, *257* (7), 2717–2730. https://doi.org/10.1016/j.apsusc.2010.10.051.

(50) Peng, H.; McKendry, I. G.; Ding, R.; Thenuwara, A. C.; Kang, Q.; Shumlas, S. L.; Strongin, D. R.; Zdilla, M. J.; Perdew, J. P. Redox Properties of Birnessite from a Defect Perspective. *Proc National Acad Sci* **2017**, *114* (36), 9523–9528. https://doi.org/10.1073/pnas.1706836114.

(51) Nesbitt, H. W.; Banerjee, D. Interpretation of XPS Mn(2p) Spectra of Mn Oxyhydroxides and Constraints on the Mechanism of MnO2 Precipitation. *Am Mineral* **1998**, *83* (3–4), 305–315. https://doi.org/10.2138/am-1998-3-414.

(52) Baer, D. R.; Engelhard, M. H.; Gaspar, D. J.; Lea, A. S.; Windisch, C. F. Use and Limitations of Electron Flood Gun Control of Surface Potential during XPS: Two Non-homogeneous Sample Types. *Surf Interface Anal* **2011**, *33* (10-11), 781–790. https://doi.org/10.1002/sia.1454.

(53) Vegh, J. The Shirley Background Revised. *J Electron Spectrosc* **2006**, *151* (3), 159–164. https://doi.org/10.1016/j.elspec.2005.12.002.

(54) Hofmann, S. Auger- and X-Ray Photoelectron Spectroscopy in Materials Science, A User-Oriented Guide. *Springer Ser Surf Sci* **2013**. https://doi.org/10.1007/978-3-642-27381-0.

(55) Seah, M. P.; Brown, M. T. Validation and Accuracy of Software for Peak Synthesis in XPS. *J Electron Spectrosc* **1998**, *95* (1), 71–93. https://doi.org/10.1016/s0368-2048(98)00204-7.

(56) Ilton, E. S.; Post, J. E.; Heaney, P. J.; Ling, F. T.; Kerisit, S. N. XPS Determination of Mn Oxidation States in Mn (Hydr)Oxides. *Appl Surf Sci* **2016**, *366*, 475–485. https://doi.org/10.1016/j.apsusc.2015.12.159.

(57) Singh, B.; Diwan, A.; Jain, V.; Herrera-Gomez, A.; Terry, J.; Linford, M. R. Uniqueness Plots: A Simple Graphical Tool for Identifying Poor Peak Fits in X-Ray Photoelectron Spectroscopy. *Appl Surf Sci* **2016**, *387*, 155–162. https://doi.org/10.1016/j.apsusc.2016.06.070.

(58) *Method 7473: Mercury in Solids and Solution by Thermal Decomposition, Amalgamation, and Atomic Absorption Spectrophotometry* **2007**.

(59) Saniewska, D.; Bełdowska, M. Mercury Fractionation in Soil and Sediment Samples Using Thermo-Desorption Method. *Talanta* **2017**, *168*, 152–161. https://doi.org/10.1016/j.talanta.2017.03.026.

(60) Neculita, C.; Zagury, G. J.; Deschênes, L. Mercury Speciation in Highly Contaminated Soils from Chlor-Alkali Plants Using Chemical Extractions. *J Environ Qual* **2005**, *34* (1), 255–262. https://doi.org/10.2134/jeq2005.0255a.

(61) *Method 1631: Revision E: Mercury in Water by Oxidation, Purge and Trap, and Cold Vapor Atomic Fluorescence Spectrometry; US EPA: 2002.* **2002**.

(62) Use of Amendments for In Situ Remediation at Superfund Sediment Sites. *U.S. Environmental Protection Agency (EPA). OSWER Directive 9200.2-128FS* **2013**.

(63) *SESDPROC-113-R3, Field Measurement of Oxidation-Reduction Potential*.

(64) Chalmin, E.; Farges, F.; Brown, G. E. A Pre-Edge Analysis of Mn K-Edge XANES Spectra to Help Determine the Speciation of Manganese in Minerals and Glasses. *Contrib Mineral Petr* **2009**, *157* (1), 111–126. https://doi.org/10.1007/s00410-008-0323-z.

(65) Nietubyć, R.; Sobczak, E.; Attenkofer, K. E. X-Ray Absorption Fine Structure Study of Manganese Compounds. *J Alloy Compd* **2001**, *328* (1–2), 126–131. https://doi.org/10.1016/s0925-8388(01)01332-9.

(66) Visser, H.; Anxolabéhère-Mallart, E.; Bergmann, U.; Glatzel, P.; Robblee, J. H.; Cramer, S. P.; Girerd, J.-J.; Sauer, K.; Klein, M. P.; Yachandra, V. K. Mn K-Edge XANES and Kβ XES Studies of Two Mn−Oxo Binuclear Complexes: Investigation of Three Different Oxidation States Relevant to the Oxygen-Evolving Complex of Photosystem II. *J Am Chem Soc* **2001**, *123* (29), 7031–7039. https://doi.org/10.1021/ja004306h.

(67) Reis, A. T.; Coelho, J. P.; Rucandio, I.; Davidson, C. M.; Duarte, A. C.; Pereira, E. Thermo-Desorption: A Valid Tool for Mercury Speciation in Soils and Sediments? *Geoderma* **2015**, *237*, 98–104. https://doi.org/10.1016/j.geoderma.2014.08.019.

(68) Lee, S.; Xu, H.; Xu, W.; Sun, X. The Structure and Crystal Chemistry of Vernadite in Ferromanganese Crusts. *Acta Crystallogr Sect B* **2019**, *75* (Pt 4), 591–598. https://doi.org/10.1107/s2052520619006528.

(69) Post, J. E.; McKeown, D. A.; Heaney, P. J. Raman Spectroscopy Study of Manganese Oxides: Layer Structures. *Am Mineral* **2021**, *106* (3), 351–366. https://doi.org/10.2138/am-2021-7666.

(70) Grangeon, S.; Fernandez-Martinez, A.; Warmont, F.; Gloter, A.; Marty, N.; Poulain, A.; Lanson, B. Cryptomelane Formation from Nanocrystalline Vernadite Precursor: A High Energy X-Ray Scattering and Transmission Electron Microscopy Perspective on Reaction Mechanisms. *Geochem T* **2015**, *16* (1), 12. https://doi.org/10.1186/s12932-015-0028-y.

(71) Corpuz, R. D.; Juan, L. M. Z. D.; Praserthdam, S.; Pornprasertsuk, R.; Yonezawa, T.; Nguyen, M. T.; Kheawhom, S. Annealing Induced a Well-Ordered Single Crystal δ-MnO2 and Its Electrochemical Performance in Zinc-Ion Battery. *Sci Rep-uk* **2019**, *9* (1), 15107. https://doi.org/10.1038/s41598-019-51692-x.

(72) Walton, K. S.; Snurr, R. Q. Applicability of the BET Method for Determining Surface Areas of Microporous Metal−Organic Frameworks. *J Am Chem Soc* **2007**, *129* (27), 8552–8556. https://doi.org/10.1021/ja071174k.

(73) Rouquerol, J.; Llewellyn, P.; Rouquerol, F. Is the BET Equation Applicable to Microporous Adsorbents? *Stud Surf Sci Catal* **2007**, *160*, 49–56. https://doi.org/10.1016/s0167-2991(07)80008-5.

(74) Johs, A.; Eller, V. A.; Mehlhorn, T. L.; Brooks, S. C.; Harper, D. P.; Mayes, M. A.; Pierce, E. M.; Peterson, M. J. Dissolved Organic Matter Reduces the Effectiveness of Sorbents for Mercury Removal. *Sci Total Environ* **2019**, *690*, 410–416. https://doi.org/10.1016/j.scitotenv.2019.07.001.

(75) Ding, L.; Snoeyink, V. L.; Mariñas, B. J.; Yue, Z.; Economy, J. Effects of Powdered Activated Carbon Pore Size Distribution on the Competitive Adsorption of Aqueous Atrazine and Natural Organic Matter. *Environ Sci Technol* **2008**, *42* (4), 1227–1231. https://doi.org/10.1021/es0710555.

(76) Li, Q.; Snoeyink, V. L.; Mariãas, B. J.; Campos, C. Elucidating Competitive Adsorption Mechanisms of Atrazine and NOM Using Model Compounds. *Water Res* **2003**, *37* (4), 773–784. https://doi.org/10.1016/s0043-1354(02)00390-1.

(77) Zhang, H.; Xu, F.; Xue, J.; Chen, S.; Wang, J.; Yang, Y. Enhanced Removal of Heavy Metal Ions from Aqueous Solution Using Manganese Dioxide-Loaded Biochar: Behavior and Mechanism. *Sci Rep-uk* **2020**, *10* (1), 6067. https://doi.org/10.1038/s41598-020-63000-z.

(78) Lee, S. W.; Kim, J.; Chen, S.; Hammond, P. T.; Shao-Horn, Y. Carbon Nanotube/Manganese Oxide Ultrathin Film Electrodes for Electrochemical Capacitors. *Acs Nano* **2010**, *4* (7), 3889–3896. https://doi.org/10.1021/nn100681d.

(79) Zhang, X.; Sun, X.; Zhang, H.; Zhang, D.; Ma, Y. Development of Redox Deposition of Birnessite-Type MnO2 on Activated Carbon as High-Performance Electrode for Hybrid Supercapacitors. *Mater Chem Phys* **2012**, *137* (1), 290–296. https://doi.org/10.1016/j.matchemphys.2012.09.023.

(80) Jin, X.; Zhou, W.; Zhang, S.; Chen, G. Z. Nanoscale Microelectrochemical Cells on Carbon Nanotubes. *Small* **2007**, *3* (9), 1513–1517. https://doi.org/10.1002/smll.200700139.

(81) Lefkowitz, J. P.; Rouff, A. A.; Elzinga, E. J. Influence of PH on the Reductive Transformation of Birnessite by Aqueous Mn(II). *Environ Sci Technol* **2013**, *47* (18), 10364–10371. https://doi.org/10.1021/es402108d.

(82) Elzinga, E. J. Reductive Transformation of Birnessite by Aqueous Mn(II). *Environ Sci Technol* **2011**, *45* (15), 6366–6372. https://doi.org/10.1021/es2013038.

(83) Hinkle, M. A. G.; Flynn, E. D.; Catalano, J. G. Structural Response of Phyllomanganates to Wet Aging and Aqueous Mn(II). *Geochim Cosmochim Ac* **2016**, *192*, 220–234. https://doi.org/10.1016/j.gca.2016.07.035.

(84) Simanova, A. A.; Kwon, K. D.; Bone, S. E.; Bargar, J. R.; Refson, K.; Sposito, G.; Peña, J. Probing the Sorption Reactivity of the Edge Surfaces in Birnessite Nanoparticles Using Nickel(II). *Geochim Cosmochim Ac* **2015**, *164*, 191–204. https://doi.org/10.1016/j.gca.2015.04.050.

(85) Elmi, C.; Post, J. E.; Heaney, P. J.; Ilton, E. S. Effects of PH and Ca Exchange on the Structure and Redox State of Synthetic Na-Birnessite. *Am Mineral* **2021**, *106* (1), 15–27. https://doi.org/10.2138/am-2020-7112.

(86) Yu, Q.; Tanaka, K.; Kozai, N.; Sakamoto, F.; Tani, Y.; Ohnuki, T. Adsorption of Cs onto Biogenic Birnessite: Effects of Layer Structure, Ionic Strength, and Competition Cations. *Acs Earth Space Chem* **2018**, *2* (8), 797–810. https://doi.org/10.1021/acsearthspacechem.8b00042.

(87) Jones, M. R.; Tebo, B. M. Novel Manganese Cycling at Very Low Ionic Strengths in the Columbia River Estuary. *Water Res* **2021**, *207*, 117801. https://doi.org/10.1016/j.watres.2021.117801.

(88) Crago, C.; Zhong, S.; Rajupet, S.; Zhang, H.; Lacks, D. J. Charge Distributions and Oxidation States in Mn-Based Oxidants from Ab Initio Molecular Dynamics Simulation. *Chemosphere* **2021**.

(89) LaRowe, D. E.; Carlson, H. K.; Amend, J. P. The Energetic Potential for Undiscovered Manganese Metabolisms in Nature. *Front Microbiol* **2021**, *12*, 636145. https://doi.org/10.3389/fmicb.2021.636145.

(90) Lafferty, B. J.; Ginder-Vogel, M.; Sparks, D. L. Arsenite Oxidation by a Poorly Crystalline Manganese-Oxide 1. Stirred-Flow Experiments. *Environ Sci Technol* **2010**, *44* (22), 8460–8466. https://doi.org/10.1021/es102013p.

(91) Schacht, L.; Ginder-Vogel, M. Arsenite Depletion by Manganese Oxides: A Case Study on the Limitations of Observed First Order Rate Constants. *Soil Syst* **2018**, *2* (3), 39. https://doi.org/10.3390/soilsystems2030039.

(92) Ehlert, K.; Mikutta, C.; Kretzschmar, R. Impact of Birnessite on Arsenic and Iron Speciation during Microbial Reduction of Arsenic-Bearing Ferrihydrite. *Environ Sci Technol* **2014**, *48* (19), 11320–11329. https://doi.org/10.1021/es5031323.

(93) Zaitsev, G. A.; Dubrovina, O. A.; Shainurov, R. I. Iron and Manganese Migration in “Soil–Plant” System in Scots Pine Stands in Conditions of Contamination by the Steel Plant’s Emissions. *Sci Rep-uk* **2020**, *10* (1), 11025. https://doi.org/10.1038/s41598-020-68114-y.

(94) Aiken, M. L.; Pace, C. E.; Ramachandran, M.; Schwabe, K. A.; Ajami, H.; Link, B. G.; Ying, S. C. Disparities in Drinking Water Manganese Concentrations in Domestic Wells and Community Water Systems in the Central Valley, CA, USA. *Environ Sci Technol* **2023**, *57* (5), 1987–1996. https://doi.org/10.1021/acs.est.2c08548.

(95) Lebron, I.; Suarez, D. L. Mechanisms and Precipitation Rate of Rhodochrosite at 25°C as Affected by PCO2 and Organic Ligands. *Soil Sci Soc Am J* **1999**, *63* (3), 561–568. https://doi.org/10.2136/sssaj1999.03615995006300030019x.

(96) Morgan, J. J.; Schlautman, M. A.; Bilinski, H. Rates of Abiotic MnII Oxidation by O2: Influence of Various Multidentate Ligands at High PH. *Environ Sci Technol* **2021**, *55* (21), 14426–14435. https://doi.org/10.1021/acs.est.1c01795.

(97) Godwin, C. M.; Zehnpfennig, J. R.; Learman, D. R. Biotic and Abiotic Mechanisms of Manganese (II) Oxidation in Lake Erie. *Frontiers Environ Sci* **2020**, *8*, 57. https://doi.org/10.3389/fenvs.2020.00057.

(98) Duckworth, O. W.; Sposito, G. Siderophore−Manganese(III) Interactions. I. Air-Oxidation of Manganese(II) Promoted by Desferrioxamine B. *Environ Sci Technol* **2005**, *39* (16), 6037–6044. https://doi.org/10.1021/es050275k.

(99) Bartlett, R.; Mortimer, R. J. G.; Morris, K. M. The Biogeochemistry of a Manganese-Rich Scottish Sea Loch: Implications for the Study of Anoxic Nitrification. *Cont Shelf Res* **2007**, *27* (10–11), 1501–1509. https://doi.org/10.1016/j.csr.2007.01.027.

(100) Poulain, A. J.; Orihel, D. M.; Amyot, M.; Paterson, M. J.; Hintelmann, H.; Southworth, G. R. Relationship between the Loading Rate of Inorganic Mercury to Aquatic Ecosystems and Dissolved Gaseous Mercury Production and Evasion. *Chemosphere* **2006**, *65* (11), 2199–2207. https://doi.org/10.1016/j.chemosphere.2006.05.066.

(101) Demers, J. D.; Blum, J. D.; Brooks, S. C.; Donovan, P. M.; Riscassi, A. L.; Miller, C. L.; Zheng, W.; Gu, B. Hg Isotopes Reveal In-Stream Processing and Legacy Inputs in East Fork Poplar Creek, Oak Ridge, Tennessee, USA. *Environ Sci Process Impacts* **2018**, *20* (4), 686–707. https://doi.org/10.1039/c7em00538e.

(102) Southworth, G. R.; Jr, M. S. G.; Peterson, M. J.; Lowe, K. A.; Ketelle, R. H.; Floyd, S. B. Sources of Mercury to East Fork Poplar Creek Downstream from the Y-12 National Security Complex: Inventories and Export Rates. **2010**. https://doi.org/10.2172/974633.

(103) Liu, G.; Cabrera, J.; Allen, M.; Cai, Y. Mercury Characterization in a Soil Sample Collected Nearby the DOE Oak Ridge Reservation Utilizing Sequential Extraction and Thermal Desorption Method. *Sci Total Environ* **2006**, *369* (1–3), 384–392. https://doi.org/10.1016/j.scitotenv.2006.07.011.

(104) Miller, C. L.; Watson, D. B.; Lester, B. P.; Lowe, K. A.; Pierce, E. M.; Liang, L. Characterization of Soils from an Industrial Complex Contaminated with Elemental Mercury. *Environ Res* **2013**, *125*, 20–29. https://doi.org/10.1016/j.envres.2013.03.013.

(105) Hsu-Kim, H.; Kucharzyk, K. H.; Zhang, T.; Deshusses, M. A. Mechanisms Regulating Mercury Bioavailability for Methylating Microorganisms in the Aquatic Environment: A Critical Review. *Environ Sci Technol* **2013**, *47* (6), 2441–2456. https://doi.org/10.1021/es304370g.

(106) Driscoll, C. T.; Mason, R. P.; Chan, H. M.; Jacob, D. J.; Pirrone, N. Mercury as a Global Pollutant: Sources, Pathways, and Effects. *Environ Sci Technol* **2013**, *47* (10), 4967–4983. https://doi.org/10.1021/es305071v.

(107) Eagles-Smith, C. A.; Wiener, J. G.; Eckley, C. S.; Willacker, J. J.; Evers, D. C.; Marvin-DiPasquale, M.; Obrist, D.; Fleck, J. A.; Aiken, G. R.; Lepak, J. M.; Jackson, A. K.; Webster, J. P.; Stewart, A. R.; Davis, J. A.; Alpers, C. N.; Ackerman, J. T. Mercury in Western North America: A Synthesis of Environmental Contamination, Fluxes, Bioaccumulation, and Risk to Fish and Wildlife. *Sci Total Environ* **2016**, *568*, 1213–1226. https://doi.org/10.1016/j.scitotenv.2016.05.094.

(108) Parks, J. M.; Johs, A.; Podar, M.; Bridou, R.; Hurt, R. A.; Smith, S. D.; Tomanicek, S. J.; Qian, Y.; Brown, S. D.; Brandt, C. C.; Palumbo, A. V.; Smith, J. C.; Wall, J. D.; Elias, D. A.; Liang, L. The Genetic Basis for Bacterial Mercury Methylation. *Science* **2013**, *339* (6125), 1332–1335. https://doi.org/10.1126/science.1230667.

(109) Landrot, G.; Ginder-Vogel, M.; Sparks, D. L. Kinetics of Chromium(III) Oxidation by Manganese(IV) Oxides Using Quick Scanning X-Ray Absorption Fine Structure Spectroscopy (Q-XAFS). *Environ Sci Technol* **2010**, *44* (1), 143–149. https://doi.org/10.1021/es901759w.

(110) Landrot, G.; Ginder-Vogel, M.; Livi, K.; Fitts, J. P.; Sparks, D. L. Chromium(III) Oxidation by Three Poorly Crystalline Manganese(IV) Oxides. 2. Solid Phase Analyses. *Environ Sci Technol* **2012**, *46* (21), 11601–11609. https://doi.org/10.1021/es302384q.

2 Manganese Oxide Modified Activated Carbon Lowers Mercury and Methylmercury in Legacy Contaminated Sediments: A Flow-Through Column Study

2.1 Abstract

Mercury (Hg) contamination in sediments threaten aquatic ecosystems due to potential mobilization and methylation into neurotoxic methylmercury (MeHg) under anaerobic, chemically reducing conditions. For example, historical Hg use at Y-12 National Security Complex (Oak Ridge, TN) resulted in dispersal of Hg throughout East Fork Poplar Creek (EFPC). Manganese(III)/(IV) oxide-modified activated carbon (MOMAC) was synthesized as a cost-effective sediment amendment intended to lower net Hg methylation through redox control while sequestering Hg species in sediments through sorption. Bench-top flow-through column experiments compared Hg dynamics in MOMAC-treated, activated carbon-treated (AC), and untreated sediments, with dissolved organic carbon (OC) additions (acetate + pyruvate) or solid OC (spirulina powder) to stimulate microbial activity and Hg methylation. For each column, ~80 pore volumes of ACW flowed through, the flow was stopped for 3 days and flushed for ~100 pore volumes. MOMAC and AC treatments effectively reduced THg elution, demonstrating enhanced Hg sequestration even with ample OC. MeHg production was associated with lower redox states in untreated sediments with solid OC, whereas MOMAC-treated sediments maintained higher redox potential, limiting MeHg release. Redox buffering from MOMAC may decline over time due to MnOx dissolution, which is affected by higher flow rates and OC levels.

2.2 Introduction

Mercury (Hg) released from anthropogenic activities such as coal combustion, mining, waste incineration, or other industrial processes have led to contamination of aquatic sediments and soils, causing long-term adverse effects on the surrounding environment and biota.[1–4] The neurotoxic form, methylmercury (MeHg), can form in sediments through microbial pathways and bioaccumulate in aquatic food webs, posing significant health risks to humans and wildlife that consume contaminated organisms.[5–7] The 2018-2019 National Rivers and Streams Assessment conducted by the EPA sampled fish tissue across 41,099 river miles in the continental United States and found that all fish sampled contained MeHg, with 26% exceeding the EPA regulatory limit of 300 mg/kg.[8,9] A lack of improvement from the 2013-2014 assessment, which found 24% of the sampled fish exceeded regulatory standard, highlights the need for effective approaches that can limit MeHg production, bioavailability and, in turn, bioaccumulation.[10]

One prominent example of legacy Hg contamination is from the use of elemental Hg^0 for lithium isotope separation in the development of thermonuclear weaponry at the Y-12 National Security Complex (Oak Ridge, TN) during the mid-20th century, which resulted in environmental Hg contamination of East Fork Poplar Creek (EFPC).[2,11,12] Presently, legacy Hg at EFPC is found primarily along the creek banks, where erosion

processes introduce Hg into the creek, which can then be converted into MeHg and enter the aquatic food web. Prior work showed that Hg in water from EFPC was isotopically similar with Hg^0 used in industry, which indicates ongoing adverse impacts from historical use of elemental Hg.[1,13] Legacy contamination at Oak Ridge, along with many other case studies[14–19], demonstrates the necessity for innovative treatments that address Hg contamination and limit the production of MeHg in legacy contaminated soils and sediments.

Mercury in soils and sediments is generally dominated by Hg(II) bonded with sulfide, as HgS(s), or complexed with organic matter (OM), with a particularly high affinity for thiol groups (R–SH).[20–22] Competing biogeochemical interactions between Hg(II), sulfide, and OM largely govern the speciation, bioavailability, mobilization, and fate of mercury in soils and sediments.[21,23] Riparian soils, such as those at EFPC, are critical interfaces between terrestrial and aquatic systems. They control the mobility of contaminants into surface waters but exhibit fluctuating biogeochemical conditions due, in part, to their proximity to converging hydrologic flows, the influence of precipitation events, biological activity, and many other factors.[24,25] Notably, changes in redox potential (expressed as Eh), as a consequence of soil saturation and drying, is a primary control in the speciation of Hg(II) and the formation of MeHg in soils.[25] Studies have reported a redox potential window where peak MeHg production occurs under mildly reducing conditions (Eh = -200 – -300 mV), generally associated with microbial sulfate reduction or, to a lesser extent, iron-reduction.[26–31] In highly reduced environments, the presence of reduced sulfur, from dissimilatory sulfate reduction, can result in sulfide mineral precipitation that immobilizes Hg(II) as HgS(s), while methanogenesis, favored in highly reduced environments, balances methylation and demethylation microbial pathways, often neutralizing net MeHg production.[29,32,33] Aquatic environments with redox potentials above the Hg-methylation window typically favor microbial populations not highly associated with MeHg production (Mn oxide reducers, nitrate reducers, aerobic respirators).[27,34–37] Among these, solid Mn oxide can elevate redox potential directly in sediments, potentially disfavoring microbial production of MeHg at the source. Supplementing Mn oxide with an additional sorbent, such as activated carbon can further help sequester Hg and MeHg in the sediment, limiting transport to overlying water.[34,37–40]

Manganese oxide-modified activated carbon (MOMAC) is an *in-situ* amendment designed to treat redox-sensitive contaminants in soils and sediments, such as Hg and MeHg.[37] MOMAC combines the high sorption capacity of activated carbon (AC) with the redox buffering properties of manganese(III, IV) oxide (MnOx). High surface area and sorption capacity can help sequester Hg species in sediment, while MnOx poises redox at potentials that favor Mn-reducing microbial pathways above redox potentials typically associated with Hg-methylation.[34,37,41,42] However, prior studies have shown that the effectiveness of sorbents is decreased in the presence of OM due to competitive ligands occupying limited sorption sites.[43–45] Additionally, oxidation of OM in sediments by MnOx can reduce high-valent Mn and lower redox buffering capacity of MOMAC amendment.[41,46–49] Therefore, the redox control and sorption efficiency of oxidizing *in-situ* sediment amendments, such as MOMAC, depends heavily on the concentration of OM in sediments. Furthermore, altered biogeochemical conditions caused by changes in

sediment saturation and water stagnation can impact both abiotic and biotic reduction of MnOx in MOMAC, the retention of contaminants on sorbent surfaces, and overall treatment longevity. These factors should be thoroughly investigated as they pose potential obstacles for implementation of in-situ treatments.

Flow-through column experiments were used to investigate whether combining redox buffering and sorption with MOMAC can limit Hg-methylation while sequestering Hg in EFPC sediment compared to sediment treated with AC, just providing sorption, or untreated sediment (Figure 2.1). These experiments were carried out under conditions that mimic natural fluctuations in sediment saturation/ water stagnation and varying organic matter content. Organic matter was added to artificial creek water either as simple aqueous organic carbon compounds, acetate and pyruvate, or as spirulina powder, a lyophilized biomass of cyanobacteria, homogenized into sediment to stimulate microbial activity and evaluate changes in MeHg production, sorption, and redox buffering capacity of MOMAC in a system with high OM. A stopped-flow state was incorporated in each experiment to simulate flooding and stagnant porewaters that can induce transient redox conditions. Organic carbon (OC), Hg, MeHg, ions, and other metrics (pH, Eh) were measured in effluent to assess how the sediment (±treatment) responded to changes in sediment saturation and the amount of reactive organic carbon over time.

2.3 Methods

2.3.1 Materials and Equipment

Reagent grade chemicals (KCl, $CaCl_2$, $MgSO_4$, $MgCl_2$, $CaCO_3$, $NaHCO_3$, $MnCl_2{\cdot}4H_2O$, $KMnO_4$, NaOH, glacial acetic acid, sodium pyruvate) (Sigma-Aldrich, St. Louis, MO, U.S.A.), powder AC (Fisher Scientific, Hampton, NH, U.S.A.; CAS 7440-44-0), and spirulina powder (Micro Ingredients), were purchased and used without further alteration. Ultrapure water (18.2 MΩ cm, MilliporeSigma Milli-Q) was used as reagent water for all experiments. Sediment columns (7.9 x 2.0 cm ID; 22.2 cm^3) were machined from polyether ether ketone (PEEK) due to its chemically inert properties. Mercury-contaminated sediment from EFPC was collected and composited from the top 4 inches of sediment in the flowing stream, approximately ~0.5 meters from a left descending bank (36° 0′ 16″ N, 84° 16′ 56″ W), and approximately 3 kg were shipped on dry ice to UC Merced in a large bag. Upon arrival at the laboratory, the sediment transferred to an anaerobic glovebox (95% N_2; 5% H_2), aliquoted into several bags (~100 g each), and sealed. Bags were stored at –20° C until needed in an effort to limit freeze-thaw cycles between column experiments.

Manganese oxide modified activated carbon (MOMAC) was prepared as described in Rivas Meraz et al. 2023.[37] Briefly, 13.3 g of powder AC was reacted with 66.67 mL of a 0.29 M $MnCl_2{\cdot}4H_2O$ solution for 24 h. Solutions of 0.19 M $KMnO_4$ and 0.38 M NaOH (66.67 mL each) were thoroughly mixed and added dropwise to the reaction vessel for approximately 1 h. Throughout the reaction, the pH was maintained above 7.0 using 0.1 M NaOH solution. The solid was separated via centrifugation and washed three times with 1 M $CaCl_2$ followed by three times with ultrapure water. The final solid was oven dried at 55 °C for 24 h and stored in the freezer.

An artificial creek water (ACW) solution composed of the average major ion concentrations of water from EFPC[3], was prepared and used as the influent solution for

all column experiments (Table. 2.1). Nitrate was omitted from the water mixture to avoid the presence of additional redox buffers.

2.3.2 Column Packing

A day prior to packing the column, Hg-contaminated sediment from EFPC was thawed in a, and 30 g of wet sediment, with addition of MOMAC or AC as treatments homogenized into sediment, was mixed with 10 mL ACW in a 40 mL polypropylene copolymer (PPCO) tube and placed on a rotating mixer overnight. Treatment dosing was about 2% dry weight, or about 0.46 g of MOMAC and about 0.30 g of AC (~958 m^2/g) for 30 g of wet sediment. This dosing gave approximately equal bulk surface areas for both treatments (~616 m^2/g). The equilibration step with ACW was incorporated to dampen large changes in analyte concentrations associated with the initial column flush out and removal of constituents weakly sorbed to the sediment surfaces. Just before column packing, the tube was centrifuged at 18725 relative centrifugal force, the supernatant was carefully extracted and discarded, and the sediment was packed into the column. A PEEK rod was used to lightly pack and score the surface of the sediments between layers to improve hydraulic conductivity. PEEK columns were packed with an average of 30.16±1.02 g of Hg-contaminated sediment based on column mass measured after packing. At each end of the column, 4.0 – 5.0 g of quartz sand (0.5 – 0.6 cm thick) were packed above and below the sediment to help uniformly distribute flow throughout the column. A 100 µm nylon mesh was included at each end of the column to limit sediment entrainment and transport into the tubing or samples.

2.3.3 Column Experiment

The conditions used for the flow-through column experiments are summarized in Table B1. In one set, dissolved OC was added as a solution of acetate and pyruvate into the influent solution at environmentally relevant concentrations (~10 mg_{carbon}/L). A 100 mL acetate and pyruvate stock solution (~1000 mg_{carbon}/L) was prepared by adding 0.120 mL of glacial acetic acid and 152.6 mg of sodium pyruvate into 99.88 mL of ultrapure water. To prepare the influent solution, a 10 mL aliquot of the acetate and pyruvate stock was added to 990 mL of ultrapure water and pH adjusted to 7.8-8.0 using 0.1 M NaOH. In another set of experiments, solid OC was added as powdered spirulina, a lyophilized biomass of cyanobacterium at high concentration to investigate the behavior of treatments when OC is not a limiting factor for Hg-methylation. The loss on ignition (LOI) of dry sediment at 550°C, measured at 1.4 ± 0.2% OC (mean ± standard deviation; n=3), was used to estimate the OC content in untreated EFPC sediment. The spirulina powder was assumed to contain roughly 50% carbon, similar to other forms of OM.[53] To approximately double the resident organic carbon content, 0.34 g of spirulina powder was added to 30 g of wet sediment (~24 g dry sediment). Spirulina was homogenized into the sediment after extracting the supernatant solution following the equilibration step.

Before each experiment, PEEK tubing, fittings, and columns were placed in a 2% HCl bath for at least 24 h before being rinsed thoroughly with ultrapure water. PharMed BPT tubing was replaced for each column experiment. The influent solution was pumped upflow through the column using an Ismatec IPC peristaltic pump fitted with 1.52 mm (yellow-blue) PharMed BPT tubing that fed into 2 mm PEEK tubing at a rate of 0.118-

0.119 mL/min or ~1.6 sediment pore volume (PV)/hr), assuming an average pore volume of 6.68 mL. Effluent solution was collected for 3d (~80 PVs) before a stopped-flow state was initiated by turning off the pump, closing both stopcocks, and allowing the sediment and porewater to react for 3 d (Figure 2.1). Column flow was resumed, and effluent was collected for an additional 4 d (~100 PVs) before terminating the experiment.

2.3.4 Effluent Solution Collection, Processing, and Analysis

Effluent solution (~7.0 mL) was collected into 13 mm polypropylene tubes with a Spectra/Chrom CF-2 fraction collector. The empty and filled mass of each tube were recorded to measure the mass of effluent eluted for every fraction. Fractions were collected every hour and tubes were combined every 12 h (12 tubes) to constitute one sample for analysis. Total volume collected for each sample is shown in Figure B1. These volumes were used to convert eluted concentrations of select analyses (Hg, MeHg, Mn) to total mass eluted for a given sample. The cumulative masses of each sample were used to determine total mass eluted throughout the experiment. Measurements of pH (Orion ROSS Sure-flow) and redox potential (Mettler Toledo Redox Micro ORP) were collected with a probe. Redox measurements were converted to Eh by correcting for the electrode potential of the reference electrode (Ag/AgCl; E_{ref} = 207 mV).[54] Part of the combined effluent (~45 mL) was filtered through a pre-rinsed 0.7 µm GF/F filter fitted to a luer-lock plastic syringe and aliquoted into containers for various analyses. Additional details for analyses performed on effluent are discussed in Text B1, while corresponding detection limits and practical quantitation levels are shown in Table B2. Approximately 10-13 mL was filtered into a 15 mL polypropylene tube and frozen for ion chromatography analysis to measure anion concentrations (SO_4^{2-}, NO_3^-, Cl^-). For element analysis by ICP-OES, ~10 mL was filtered into a polypropylene tube, preserved with 2% (v/v) trace metal grade nitric acid, and refrigerated until analysis. Samples for non-purgeable organic carbon (NPOC) analysis were collected every 24 h where ~15 mL of filtered effluent from each sample were mixed into a 30 mL HDPE bottle, and frozen until analysis. The remaining effluent (~45 mL) was left unfiltered for total Hg (THg) and MeHg analyses. About 5 mL of effluent were stored in a Hg-free clear glass vial and preserved with 1% (v/v) BrCl for THg analysis. Total Hg was measured through oxidation, purge and trap, and cold vapor atomic fluorescence spectrometry (CVAFS). Approximately 30 – 40 mL were stored in an Hg-free amber vial and preserved with 0.4% (v/v) Optima grade HCl for MeHg analysis. The contents of the vial were decanted into a PTFE vessel, diluted to 55 mL, and distilled for 3 h at 125 °C under nitrogen-flow. Approximately 20-30 mL of distillate was placed into a new Hg-free amber vial and pH-adjusted to 4.5-5.0 using 500 µL 2M sodium acetate buffer. Dissolved Hg species in the sample were volatilized via ethylation using 50 µL of sodium tetraethylborate and measured with CVAFS. The percentage of total Hg that is present as MeHg was calculated as $[MeHg_{(aq)}]/[THg_{(aq)}]$ Additional details for Hg and MeHg analyses are described in Text B2 and associated QA/QC are shown in Table B3.

Raw data were grouped by type of organic carbon addition (no C added, Acetate + Pyruvate, Spirulina) for statistical analysis using R v4.4.1[55] and rstatix package[56]. Normality of the data was assessed using the Shapiro-Wilk test.[57] Because many groups showed distributions significantly different from normal distribution (Shapiro-Wilk p-

value < 0.05), non-parametric tests were used. Pairwise comparisons between treatments were conducted using the Wilcoxon Rank Sum test[58], and p-values were adjusted for multiple comparisons using the Bonferroni correction.[59]

2.3.5 Sediment Collection and Analysis

Total Hg in unamended sediment was measured using a Direct Mercury Analyzer (Milestone DMA-80) via thermal decomposition, amalgamation, and atomic absorption spectrophotometry.[60] At the end of each column experiment, sediment was extruded with a PEEK rod, split into lower and upper halves, each half transferred to a 20 mL amber vial, and frozen at –20° C until analysis. Sediment THg was measured by igniting 0.02-0.04 g of solid using a direct mercury analyzer (Milestone DMA-80). MeHg concentration in sediment was measured with a KOH-methanol digestion method.[61] Approximately 0.1 – 0.2 g of wet sediment was placed into a 15 mL polypropylene centrifuge tube and digested with 0.5 mL 1 N HCl in methanol for 30 minutes. Afterward, 2.5 mL of 25% KOH in methanol was added and the tubes were placed in an oven at 60°C for 4 h and vortexed every hour. The samples were diluted with 10 mL of ultrapure water and measured for MeHg. Samples were pH-adjusted to 4.5-5.0 using 300 µL of a 2 M sodium acetate buffer, volatilized via ethylation using 50 µL of sodium tetraethylborate, and measured with CVAFS. To validate results from our lab, untreated sediment samples from columns with and without spirulina and certified reference material used as a standard for our measurements (TORT 2) were sent to Brooks Applied Labs for MeHg analysis. For these two samples, both sediment halves were homogenized into one sample. Partitioning of MeHg between the aqueous and solid phase were calculated from total mass of MeHg eluted compared to total mass of MeHg in the sediment, this was shown as $\log(K_d)$ where K_d = mass $MeHg_{sed}$/mass $MeHg_{aq}$.

2.4 Results

2.4.1 Native Sediment and Artificial Creek Water Properties

The average pH, redox potential (as Eh), concentrations of major ions, OC, and inorganic C that were measured in the influent ACW solution for each set of experiments are reported in Table 2.1. The pH was slightly alkaline ranging from 7.85 to 8.03 and Eh was about 0.40 to 0.41 V. Total Hg in the native sediment was 16.1 ± 1.4 mg Hg/kg (mean ±standard error, n = 3).

2.4.2 Columns with No Organic Carbon Added

In the absence of added OC, effluent chemistry remained relatively stable across treatments, with only a few variations in analyte concentrations between MOMAC-treated and untreated sediments. Fluctuations in pH were observed in effluent from both untreated and MOMAC-treated sediments throughout the experiment but stabilized to values reflecting the influent solution by the experiment end. The redox potential measured in the effluent from MOMAC-treated sediment was significantly different (adj. p-value ≤ 0.001) compared to effluent from untreated sediment (Figure 2.2). Results for major cation concentrations measured in in solution are discussed and shown in Text B3 and Figure B2, respectively.

Concentrations of ions associated with terminal electron acceptor processes

(nitrate, dissolved Mn, dissolved Fe, sulfate) and other redox-sensitive analytes (non-purgeable organic carbon) were similar for both treatment conditions, with the exception of dissolved Mn (Figure 2.3). Although nitrate was not added to the influent and was undetectable in the stock solution, low concentrations (<1 mg/L) were measured in the effluent. Some Mn was eluted after the stopped-flow state from the MOMAC-treated sediment column but was absent in the effluent from untreated sediment columns. Sulfate and organic carbon concentrations in the effluent solution remained consistent with those in the ACW stock solution at 40 – 44 mg/L and ~0.1 mg/L, respectively. Chloride, total C, and inorganic C (calculated as TC-NPOC) are shown in Figure B3.

Total Hg eluted from sediment with no OC added was significantly lower when treated with MOMAC compared to the untreated control (adj. p-value ≤ 0.001). The Hg concentration in the initial effluent from the untreated sediment measured up to 159 ng/L and decreased gradually to toward 15 ng/L before the stopped-flow state. After the stopped-flow state, the concentration continued to decrease until stable at 8 ng/L (Figure 2.4). The Hg concentration in the initial effluent from the MOMAC-treated sediment began around 10 ng/L and slowly decreased to 5 ng/L before the stop flow. No increase in Hg was observed after the stopped-flow state and the concentration continued to decrease until remaining stable at 1-2 ng/L. Total Hg and MeHg measured in column sediments are shown in Table 2.2 as averages from bottom and top fraction and replicate columns. Individual measurements for each half are shown in Table B4. Total Hg measured from column sediment was similar to Hg in native sediment.

There were no notable differences or trends for MeHg eluted from columns. MeHg concentrations in effluent from untreated and MOMAC-treated sediments columns were similar to background concentrations measured in method blank samples (Table B2.), with averages of 0.07 and 0.04 ng/L and maxima 0.17 and 0.05 ng/L, respectively (Figure 2.4), and concentrations remained steady throughout both experiments. The %MeHg (concentrations of [MeHg]/[THg] × 100%) in untreated sediment column effluent increased slightly but remained <1%, while MOMAC-treated sediment measured between 1-2% (Figure 2.4). Table 2.2 shows extracted MeHg in sediment measured at 1.5 pg/mg as reported by Brooks Applied Labs which agreed with values from a replicate column carried out under the similar conditions, but without an equilibration step, within relative percent difference allowed for replicates based on EPA Method 1630 (35%).[62] MOMAC-treated sediments exhibited similar concentrations as untreated sediments at 0.9±0.1 pg/mg.

2.4.3 Columns with Organic Carbon Added as Acetate + Pyruvate

Compared to columns without added OC, the addition of acetate and pyruvate moderately changed the effluent chemistry and increased the concentrations of some analytes. The initial pH for the influent solution was adjusted after addition of the DOC stock and measured at 8.03 for both the untreated and MOMAC-treated columns. The initial Eh of the influent solutions was between 0.44 and 0.45 V. The pH decreased before the stopped-flow for both treatments but stabilized at values similar to the influent solution after the stopped-flow state. The Eh of the untreated sediment column remained stable and reflected the value measured in the influent whereas there was a significant increase (adj. p-value ≤ 0.001) in Eh from MOMAC-treated sediment effluent (Figure 2.2).

The concentration of ions sourced from terminal electron acceptors showed slightly varied behavior between untreated and MOMAC-treated sediment effluent (Figure 2.3). Nitrate concentrations varied between treatments, with higher concentrations detected in the effluent from MOMAC-treated sediment (1-5 mg/L) compared to untreated sediment (0.1 – 1 mg/L). Similar to columns with no OC added, Mn was only eluted from MOMAC-treated sediment, but a modest increase of Mn eluted was observed with the addition of acetate and pyruvate. Unlike columns with no OC added, Mn was detectable immediately following the stopped-flow state, rather than a delayed elution, and stabilized around 2.1 mg/L for the remainder of the experiment. Sulfate behaved conservatively, with effluent concentrations mirroring those in the influent solution. Dissolved organic carbon stock solutions ranged from 3.3 to 3.9 mg/L. Dissolved OC in the effluent from the untreated sediment column initially reflected the influent concentration, then rapidly increased to 7.6 mg/L and gradually decreased before finally stabilizing around 1.6 mg/L. In the MOMAC-treated sediment column, dissolved organic carbon concentrations reached 9.0 an average of mg/L after 26 pore volumes and then decreased, eventually dropping below detection limits soon after the stopped-flow state.

The THg eluted from the untreated sediment column was significantly higher (adj. p-value ≤ 0.01) when acetate and pyruvate were added in the influent compared to no OC being added (Figure 2.4). The initial fraction had the highest THg measured at 174 ng/L and gradually decreased between 40-60 ng/L before the stopped-flow state compared to 15 ng/L without OC. After the stopped-flow state, the concentration from the untreated sediment column began increasing again, reaching around 80 ng/L before returning to 40-60 ng/L near the experiment end. Meanwhile, the THg concentration in the effluent from the MOMAC-treated sediment was similar with or without the addition of acetate and pyruvate as OC. The THg concentration was highest initially at 24 ng/L and, without any changes after the stopped-flow state, decreased to 1.5 ng/L in the final sample collected. Total Hg in sediment was similar to native sediment.

The addition of acetate and pyruvate did not change MeHg concentrations in effluent or sediment compared to columns with no OC added (Figure 2.4). The MeHg eluted from both untreated and MOMAC treated columns were comparable to background concentrations measured from method blanks, with averages of 0.10±0.06 and 0.05±0.01 ng/L and maxima of 0.24 and 0.06 ng/L, respectively. Percent MeHg remained stable in effluent from untreated sediment but increased slightly from MOMAC-treated sediment. MeHg in sediment was similar to sediment from columns with no C added (Table 2.2).

2.4.4 Columns with Organic Carbon Added as Spirulina Powder

In spirulina-treated columns, effluent pH decreased from the influent value (~7.85) in all sediment columns, with a more significant decreases in the untreated and AC-treated columns (Figure 2.2). Before the stopped-flow state, effluent Eh decreased in all columns but decreased more in the AC-treated and untreated columns compared to the MOMAC-treated column. After the stopped-flow, Eh remained stable in the MOMAC-treated column, while it gradually increased in the AC-treated and untreated columns, approaching values similar to MOMAC-treated effluent. Overall, the Eh measured in

effluent from MOMAC-treated sediment was significantly different from untreated (adj. P-value ≤ 0.0001) and AC-treated (adj. P-value ≤ 0.001) sediment.

The response from terminal electron acceptors was more pronounced with the addition of solid OC and varied between treatments (Figure 2.3). In contrast to the prior experiments, nitrate was undetected in effluent from sediment columns mixed with spirulina powder. Unlike the other carbon addition experiments, dissolved Mn was eluted from treated and untreated columns. Dissolved Mn eluted was highest for MOMAC-treated sediment, followed by in untreated sediment, and lowest in AC-treated sediment. All columns followed similar trends for dissolved Mn which consisted of a slow initial release prior to the stopped-flow event followed by a surge of dissolved Mn immediately after the stopped-flow state. After the surge, dissolved Mn from untreated and AC treated columns decreased, but remained stable in effluent from MOMAC-treated columns. Dissolved Fe was detected in the effluent, primarily from the untreated sediment column after the stopped-flow state. Sulfate concentrations in the effluent were mostly clustered around the influent baseline concentration, with occasional deviations downward in effluent from the untreated sediment column. The introduction of spirulina powder, a solid OC source, greatly elevated the DOC concentrations. The effluent from untreated sediment consistently exhibited the highest OC concentrations throughout the experiment, while MOMAC and AC treatments showed lower concentrations, with AC maintaining slightly higher levels than MOMAC. Similar to other analytes, there was a surge of OC released immediately after the stopped-flow state, followed by a drastic decrease that was sustained for the remainder of the experiment.

Total Hg released from sediment columns mixed with solid OC increased over an order of magnitude compared to other column experiments (Figure 2.4). The initial release from untreated sediments was consistently high but varied widely between replicate columns at 8600 ± 3200 ng/L (mean ± standard error, n=3) (off scale in Figure 2.4) but quickly decreased to ~250 ng/L prior to the stopped-flow state. Sediments treated with AC exhibited a higher initial THg release compared to MOMAC-treated sediments but generally showed no significant differences (adj. P-value ≥ 0.05). After the stopped-flow state, a spike in Hg was observed from all treatments, particularly from untreated sediment columns and remained stable until the end of the experiment. Overall, the THg eluted from untreated sediment was significantly higher from AC-treated (adj. P-value ≤ 0.01) and MOMAC-treated sediment (adj. P-value ≤ 0.0001). Similarly, the total mass of Hg eluted was lowest for MOMAC-treated sediment, followed by AC-treated sediment, and highest with untreated sediment (Figure 2.5).

Addition of solid OC as spirulina powder enhanced MeHg measured in column effluent. Concentrations from untreated sediment columns quickly increased up to 12.0 ng/L prior to the stopped-flow state. However, elution behavior for MeHg was erratic, particularly after the stopped-flow, where effluent concentrations of 10.0 – 12.0 ng/L were followed by sharp decreases in concentration to 0.6–1.0 ng/L. In contrast, MeHg eluted from the MOMAC-treated sediment remained low (0.1 – 0.2 ng/L) until just before the stopped-flow period. Following the stopped-flow state, MeHg concentrations peaked at 9.3 ng/L and decreased until stabilizing at ~2.0 ng/L. The total MeHg eluted did not differ significantly between untreated and MOMAC-treated sediments overall.

However, significant differences (adjusted P-value ≤ 0.05) were observed when comparing values before the stopped-flow state.

2.5 Discussion

2.5.1 MOMAC Lowered THg and MeHg Elution in Columns

Results revealed distinct patterns in Hg and MeHg elution depending on the treatment applied or the type of OC introduced, highlighting the critical role of redox dynamics and organic matter in governing Hg mobility and methylation processes in contaminated sediments. In these experiments, native sediment Hg was the source for THg measured in effluent. However native sediment showed little to no MeHg without microbial stimulation with solid OC (Table 2.2). This indicates that redox conditions, organic matter, or microbial activity required for MeHg production were not present.

Treating sediments with a sorbent MOMAC or AC lowered THg effluent concentrations and total mass eluted across all OC additions compared to untreated sediments, demonstrating that sorption can help sequester Hg in sediment (Figure 2.4; Figure 2.5). Furthermore, THg elution was significantly higher in untreated sediments with dissolved OC compared to those without OC added, suggesting that the presence of DOC increased Hg mobility. In contrast, THg concentrations and total mass eluted in MOMAC-treated sediments did not differ significantly between columns with and without DOC, demonstrating that MOMAC effectively sequestered Hg even in the presence of dissolved OC, which has been shown to reduce sorbent effectiveness (Figure 2.4; Figure 2.5).[43]

The introduction of solid OC as spirulina powder into the sediment amplified differences in sediment chemistry, leading to MeHg production, as shown by increased sediment MeHg concentrations (Table 2.2), and pronounced variations in analyte concentrations and other parameters between MOMAC-treated, AC-treated, and untreated effluent. In untreated sediments, solid OC decreased the redox state in the sediment. This is shown by a lower redox potential in effluent, compared to MOMAC treated sediment, in addition to a lack of nitrate in effluent, presence of native Mn in effluent, and elution Fe^{2+}, suggesting nitrate reduction, Mn-reduction, and iron reduction was favored. Sediment treated with AC also exhibited lower redox potential compared to MOMAC-treated sediment, but sorption capacity likely played a role in limiting the amount of dissolved Mn and Fe^{2+} eluted as shown by lower total mass of Mn (Figure B4). The low redox potential in untreated and AC-treated sediments indicates that native Mn was not providing redox buffering capacity and was likely present as a reduced Mn(II) phase. Overall, a lower redox state corresponded to increased MeHg production in untreated sediments with sharp fluctuations in effluent concentrations (Figure 2.4). Demethylation, or degradation, of MeHg can occur through reductive and oxidative pathways from similar microbial communities associated with Hg-methylation.[63–65] Specifically, the reductive pathway, *mer*-detoxification, has been proposed to actively degrade MeHg in severely contaminated sediments (≥ 10 mg_{Hg}/kg dry wt.).[64] This pathway can help explain the sharp decreases in MeHg concentration that were preceded by samples with high MeHg concentrations (≥ 10 ng/L).

In contrast, sediments treated with MOMAC exhibited higher redox potentials in effluent, limited Fe^{2+} being eluted, and lack of changes in sulfate suggests a higher redox

state. Higher concentrations, and masses, of Mn were eluted in MOMAC-treated sediment compared to untreated or AC-treated sediments, indicating reductive dissolution of high-valent MnOx from MOMAC that provided a buffered redox state (Figure 2.3; Figure B4). Although MeHg concentrations in MOMAC-treated sediment were similar to those from untreated sediment at the end of the experiment (Table 2.2), a higher redox state likely limited production initially, resulting in a lower total mass of MeHg eluted (Figure 2.5a). Higher %MeHg in MOMAC treated sediment is due to a high mass of THg eluted from untreated sediment (Figure 2.5b). When excluding initial samples that contributed the majority of the THg mass eluted from untreated sediment, addition of MOMAC still showed lower THg and MeHg masses eluted but show a comparable %MeHg (Figure B5). Sorption likely played a role as shown by a higher partitioning coefficient for MeHg (Figure 2.5c). The surge in MeHg after the stopped-flow suggests this promoted a lower redox state that increased production or desorption, and subsequent elution of MeHg in MOMAC-treated sediments. These results show that MOMAC addition to sediment can effectively limit Hg-methylation through redox buffering and sorption, even when organic matter was abundant and microbial activity was elevated.

2.5.2 MOMAC Reductive Dissolution and Estimated Longevity

Solution pH and Eh are key variables that influence the speciation and fate of MnOx-based amendments. Average concentrations for dissolved Mn and inorganic C eluted were used to calculate an Eh-pH diagram that shows thermodynamically favored Mn aqueous and solid speciation across circumneutral pH (6.0 – 9.0) (Figure 2.6). This figure demonstrates thermodynamic stability fields under predetermined Mn^{2+} and HCO_3^- concentrations that are useful to predict the general trend of Mn stability. In practice, stability fields in Eh-pH diagrams are dynamic due to fluctuating concentrations of dissolved Mn, bicarbonate, or other reactive ions and offer no information regarding reaction kinetics. Without addition of solid OC, Eh and pH remained constant and thermodynamically favor stability of solid Mn(III) oxides, such as bixbyite (Mn_2O_3), which would limit reductive dissolution (Figure 2.6). This follows the observations in columns with no C added, or added as dissolved OC, where no dissolved Mn was eluted from untreated soils.

With addition of solid OC, however, decreases in solution pH and Eh were observed across all treatments. The reductive dissolution of Mn oxides can be driven by organic compounds acting as electron donors, though other factors such as redox potential and microbial activity also play critical roles.[50,70] In experiments with DOC or solid OC added, reactions with OC likely enhanced Mn-reduction. This is shown by an increased mass of Mn eluted when DOC was added increased compared to columns with no C added. Similarly, initial elution of OC was lower with addition of either AC or MOMAC in sediment suggesting sorption of organic molecules that may lead to reduction of MnOx. This was likely additional driver for Mn-reductive dissolution given that Mn(III, IV) oxides are thermodynamically unstable at lower pH under the solution Eh values measured (Figure 2.6).[71] Although many values fall within the stability field for rhodochrosite, precipitation kinetics are reportedly slow and strongly pH dependent.[72,73] Therefore, in the presence of excess OC, the longevity and redox buffering capacity for MOMAC can be limited.

Dissolved Mn was eluted in all sediments treated with MOMAC (Figure 2.3), suggesting Mn reductive dissolution of MnOx from MOMAC, or from native sediment. Dissolved Mn was only eluted from untreated or AC-treated sediments when mixed with solid OC, which indicated that the fraction of native Mn in sediment was recalcitrant and only mobilized when microbial activity was promoted ,when undergoing abiotic reactions with electron donors like OC, sulfide, or ferrous iron, or due to a decrease in pH that can make dissolve Mn-oxides such as rhodochrosite ($MnCO_3$).[41,66,67] The elution of dissolved Mn increased after the stopped-flow state in all treatments, which showed that many of these reactions, either biotic or abiotic, are generally favored under anaerobic conditions or under extended equilibrium times that allowed for different reaction types.[68,69] The total mass of Mn eluted shows that MOMAC-treated sediments released 0.7, 1.1, and 6.4 mg by experiment end from column experiments with no C added, DOC added, and solid OC added, respectively (Figure B4). Each MOMAC-treated sediment column received 0.46g of MOMAC that provided ~55 mg of MnOx, assuming a Mn concentration of 0.12 g_{MnOx}/g_{MOMAC}.[37] However, in the columns with spirulina, part of the Mn eluted may have been due to native Mn, meaning that the mass of MnOx lost from MOMAC may be as low as 3.1 mg. This shows that only 6 – 12% of MnOx from MOMAC was lost to solution over 172 PV.

To roughly estimate the longevity of the MOMAC amendment in the field, a range of infiltration rates were considered. Assuming a porosity of 0.30, the average porosity calculated in column experiments, and an amended area of the creek bank spanning 100 meters in length, 1 m in height, and 5 cm in depth, the total pore volume would be 1,500 liters. In the column experiment with MOMAC-treated sediment and solid OC added, 172 PV were passed, and the same number was used for comparison in the field scenario. At a low infiltration rate of 0.1 L/s, it would take approximately 30 days to pass 172 PV with complete MnOx depletion occurring between 250 and 500 days, depending on the MnOx loss rate (6-12% in 172 PV in this experiment). At a higher infiltration rate of 1 L/s, 172 pore volumes would pass in about 3 days, with total MnOx depletion occurring over 25 to 50 days. Notably, elution of dissolved Mn occurred primarily under stopped-flow conditions, which can favor reactions that require longer timescales for equilibrium.[68,69] Dissolved Mn observed in effluent from MOMAC-treated sediment after stopped-flow state may be attributed to microbially mediated reductive dissolution, abiotic reactions with electron donors such as OC, or due to mobilization of adsorbed and/ or diffused Mn(II), shown to be present in MOMAC.[37] This shows that increased flow, resulting in frequent flooding or inundation, can lower redox state of the system and drive reductive dissolution of MnOx faster than predicted. Therefore, MOMAC can continue to provide redox buffering capabilities for an extended period of time while minimizing MeHg production and elution but may vary depending on infiltration rates and precipitation events that lead to flooding.

2.6 Conclusions

This study found that MOMAC effectively lowers THg mobilization with a sorption capacity comparable to AC, as both treatments significantly decreased THg concentrations and total mass eluted compared to untreated sediments. However, MOMAC offers the added advantage of limiting MeHg production through its redox

buffering capabilities. The higher redox potential in MOMAC-treated sediments, compared to untreated or AC-treated sediments, likely maintained lower MeHg production and mobilization. The stopped-flow period played a significant role in revealing some limitations of redox buffering, as MeHg concentrations surged following the stagnant conditions. This suggests that while MOMAC can effectively control Hg mobilization under continuous flow, stagnant periods may promote MeHg remobilization or production. The long-term redox buffering capacity of MOMAC may decrease due to MnOx dissolution, either abiotically through reactions with OC, or other electron donors, or through microbial reduction processes that can be favored under transient chemically reducing conditions induced under stagnant sediment porewater. In field applications, periodic monitoring and potential reapplication may be necessary to maintain MOMAC's effectiveness in mitigating Hg and MeHg mobilization, especially considering the potential impact of flow interruptions. MOMAC presents a promising approach for controlling Hg and MeHg mobilization in contaminated sediments, though its long-term effectiveness may be challenged under conditions of prolonged stagnation or elevated OC. Field applications should consider these factors and include strategies for maintaining redox control in environments prone to flooding or high OC inputs.

2.7 Figures

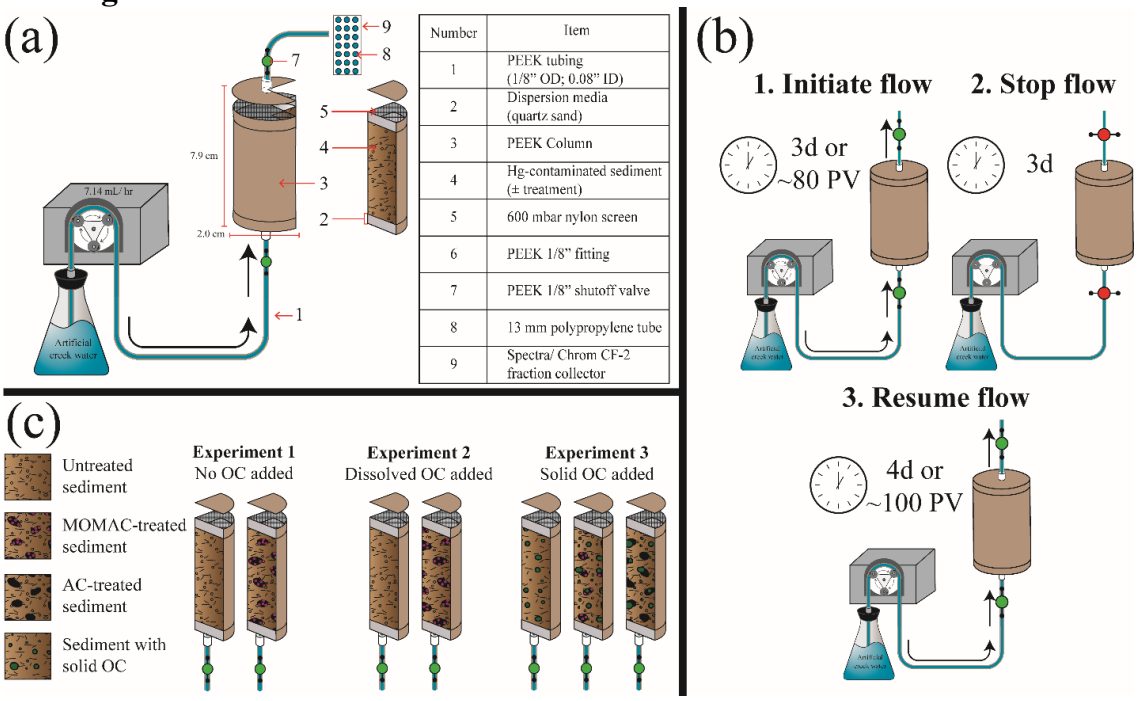

Number	Item
1	PEEK tubing (1/8" OD; 0.08" ID)
2	Dispersion media (quartz sand)
3	PEEK Column
4	Hg-contaminated sediment (± treatment)
5	600 mbar nylon screen
6	PEEK 1/8" fitting
7	PEEK 1/8" shutoff valve
8	13 mm polypropylene tube
9	Spectra/ Chrom CF-2 fraction collector

Figure 2.1. Experimental setup and procedures used to investigate the effects of organic carbon (OC) and soil saturation on net mercury (Hg)-methylation in contaminated sediments with or without *in-situ* amendments. (a) Schematic for flow-through column experiments showing upflow movement of the influent solution. The table lists major components used in column construction. (b) Flow procedure for experiments to mimic fluctuations in soil saturation. The procedure involves three phases: (1) Initial flow of artificial creek water through the sediment columns over approximately 3 days (equivalent

to ~80 pore volumes), (2) A 3-day stop flow period allowing for equilibration after saturation, and (3) Resumption of flow for an additional 4 days (~100 pore volumes). (c) Overview of sediment treatments and experimental conditions applied to the sediment columns. Sediment treatments included untreated sediment, manganese oxide-modified activated carbon (MOMAC)-treated sediment, or activated carbon (AC)-treated sediment. Three separate experimental conditions were evaluated: columns with no additional OC, columns with dissolved OC (acetate and pyruvate) introduced into influent, and columns with solid OC (spirulina powder) mixed into sediment.

Table 2.1. Composition of the Artificial Creek Water (ACW) Solution Measured from Influent Solutions

Property	ACW Properties for Columns with No Carbon Added (mean ± standard error; n=4)	ACW Properties for Columns with Dissolved Organic Carbon Added (mean ± standard error; n=2)	ACW Properties for Columns with Solid Organic Carbon Added (mean ± standard error; n=4)
pH	7.91 ± 0.02	8.03 ± 0.00	7.85 ± 0.01
Eh (V)	0.41 ± 0.00	0.41 ± 0.00	0.40 ± 0.00
Ca^{2+} (mg/L)	42.2 ± 0.8	40.7 ± 1.4	44.1 ± 2.7
Cl^- (mg/L)	82.3 ± 6.3	75.2 ± 0.0	78.4 ± 1.8
K^+ (mg/L)	2.7 ± 0.0	4.1 ± 1.2	2.2 ± 0.0
Mg^{2+} (mg/L)	12.2 ± 0.1	11.9 ± 0.0	10.6 ± 0.1
SO_4^{2-} (mg/L)	40.4 ± 0.1	40.4 ± 0.2	43.5 ± 1.1
Na^+ (mg/L)	13.19 ± 0.15	18.16 ± 0.11	12.4 ± 0.1
NO_3^- (mg/L)	-	-	-
Inorganic C (mg/L)	8.02 ± 0.24	9.28 ± 1.83	8.34 ± 0.12
Non-purgeable Organic C (mg/L)	0.18 ± 0.0	Filtered: 3.6 ± 0.04	0.17 ± 0.0

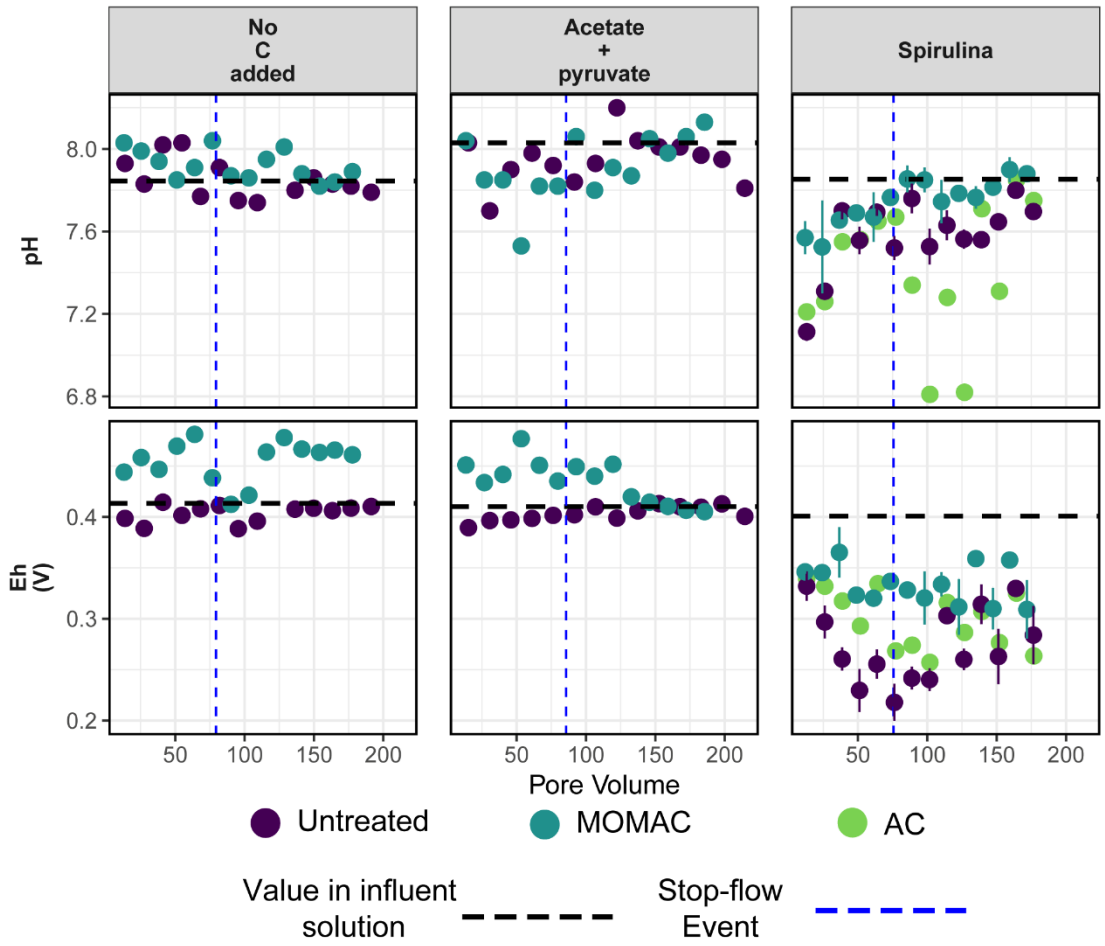

Figure 2.2. Average pH and redox potential (Eh) measured in column effluent**.** The pH and Eh of the influent solution are marked by the horizontal black line. The stop-flow event (3 d) is marked by the vertical blue line. Uncertainty was determined based on replicates and shown as mean ± standard error. Values with no uncertainty shown are due to single replicates.

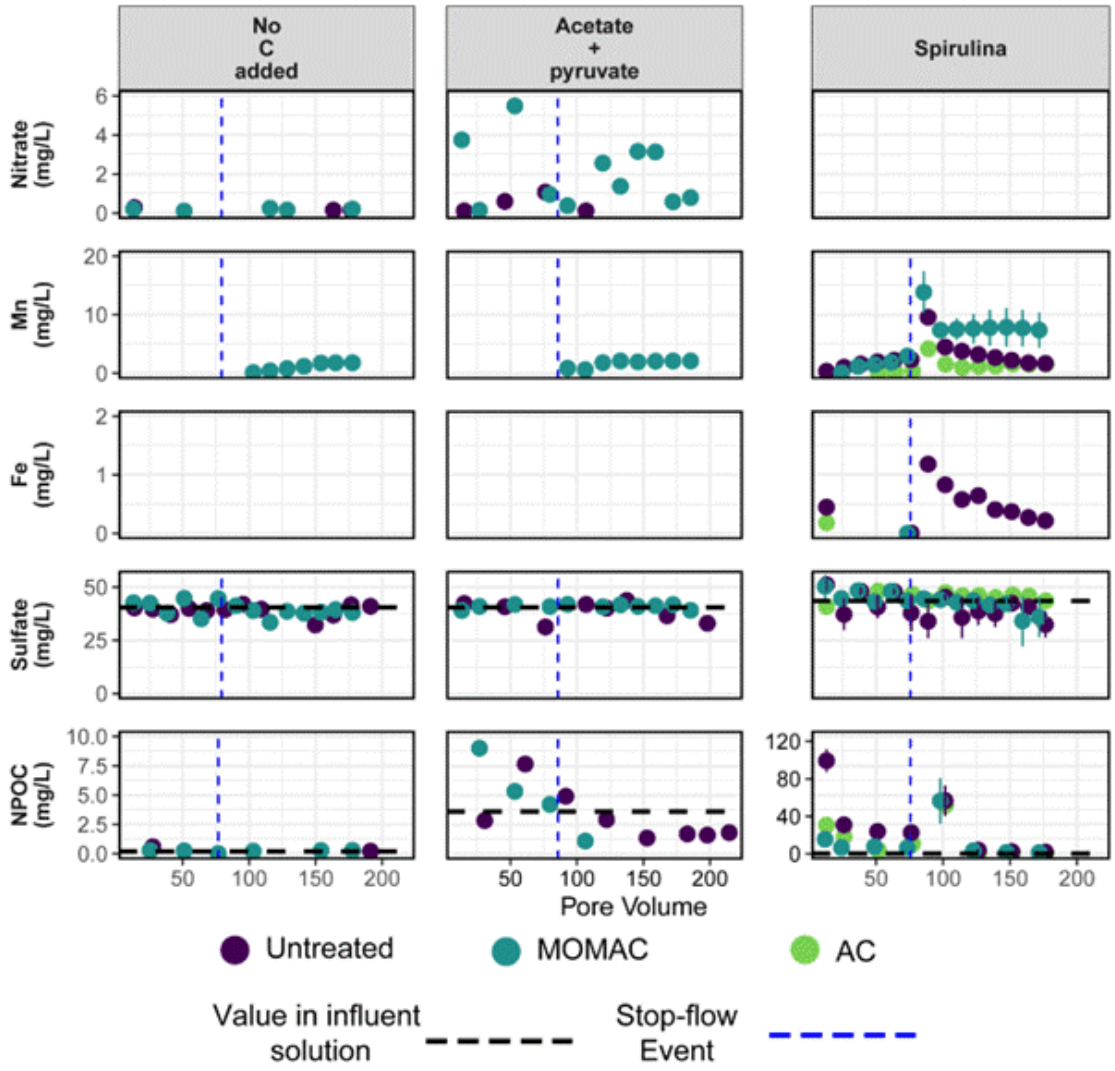

Figure 2.3. Concentrations of redox sensitive analytes and non-purgeable organic carbon (NPOC) from filtered effluent. Concentrations for the influent solution are marked by the horizontal black line. The stop-flow event is marked by the vertical blue line. Values below detection were omitted. Detection limits are shown on Table B2. Uncertainty was determined based on replicates and shown as mean ± standard error. Values with no uncertainty shown are due to single replicates.

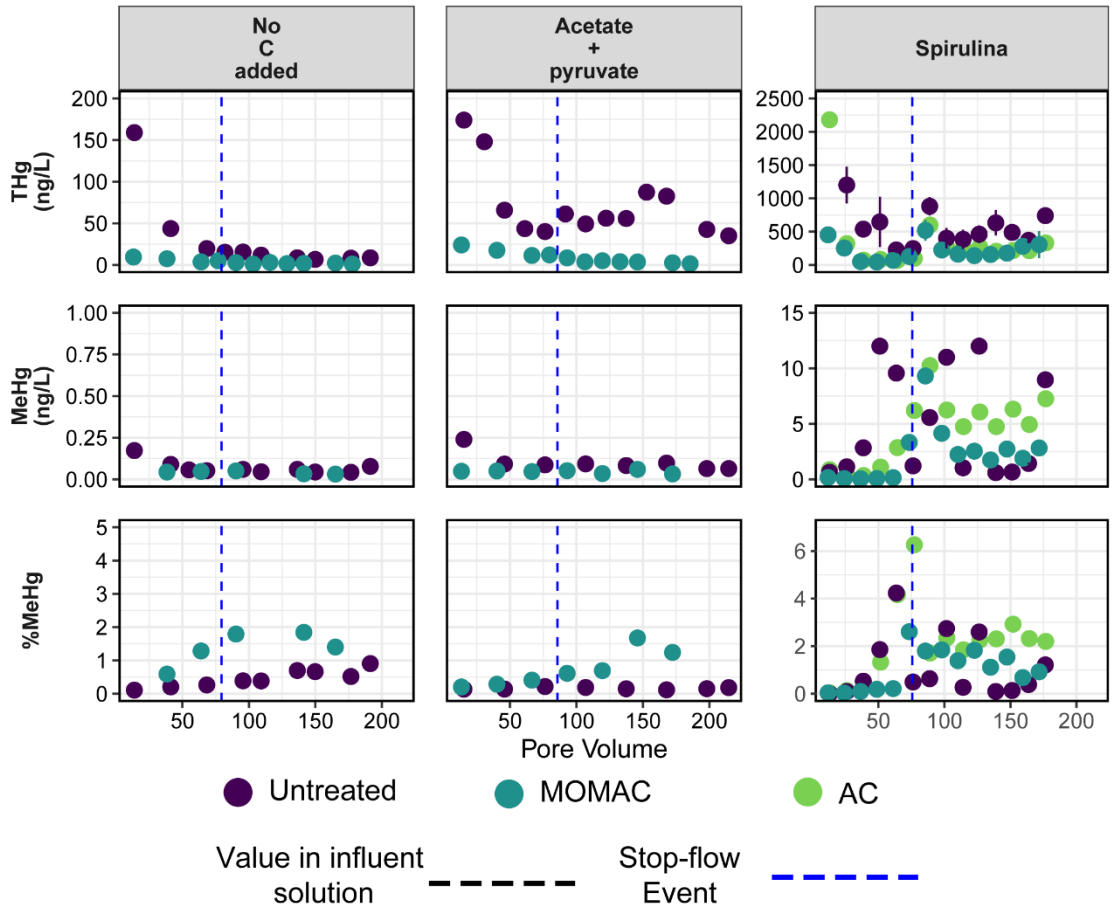

Figure 2.4. Concentrations of total mercury (THg) and methylmercury (MeHg) from unfiltered column effluent with calculated percent MeHg ([MeHg]/[THg] × 100%). The stopped-flow state (3 d) is marked by the vertical blue line. Values below detection were omitted. Detection limits are shown on Table B2. Note the first sample from untreated sediment is off scale at 8600±3200 ng/L. Uncertainty was determined based on replicate column experiments and shown as mean ± standard error. Values with no uncertainty shown are due to single replicate columns. For MeHg, only 1 set of samples for each column met QA/QC standards and therefore no uncertainty was calculated.

Table 2.2. Total Hg and MeHg Extracted from Native EPFC Sediment and After Experiment Termination

Organic Carbon Addition	Treatment	Mean THg (mg/kg)	SD THg (mg/kg)	SE THg (mg/kg)	n THg	Mean MeHg (µg/kg)	SD MeHg (µg/kg)	SE MeHg (µg/kg)	n MeHg
Native Sediment	-	16.1	2.5	1.4	3	1.0	0.2	0.1	3
No C added	Untreated	10.3	3.8	2.7	2	1.5†	-	-	1
No C added	MOMAC	14.3	1.3	0.9	2	0.9	0.1	0.1	2
Acetate + pyruvate	Untreated	16.1	0.7	0.5	2	1.2	0.4	0.3	2
Acetate + pyruvate	MOMAC	14.2	2.0	1.4	2	1.2	-	-	1
Spirulina Powder	Untreated	18.1	3.7	1.7	5	11.3	0.8	0.4	5
Spirulina Powder	MOMAC	12.6	4.9	2.4	4	19.6	4.1	1.7	4
Spirulina Powder	AC	17.5	1.2	0.8	2	not run	-	-	-

†Measured by Brooks Applied Labs

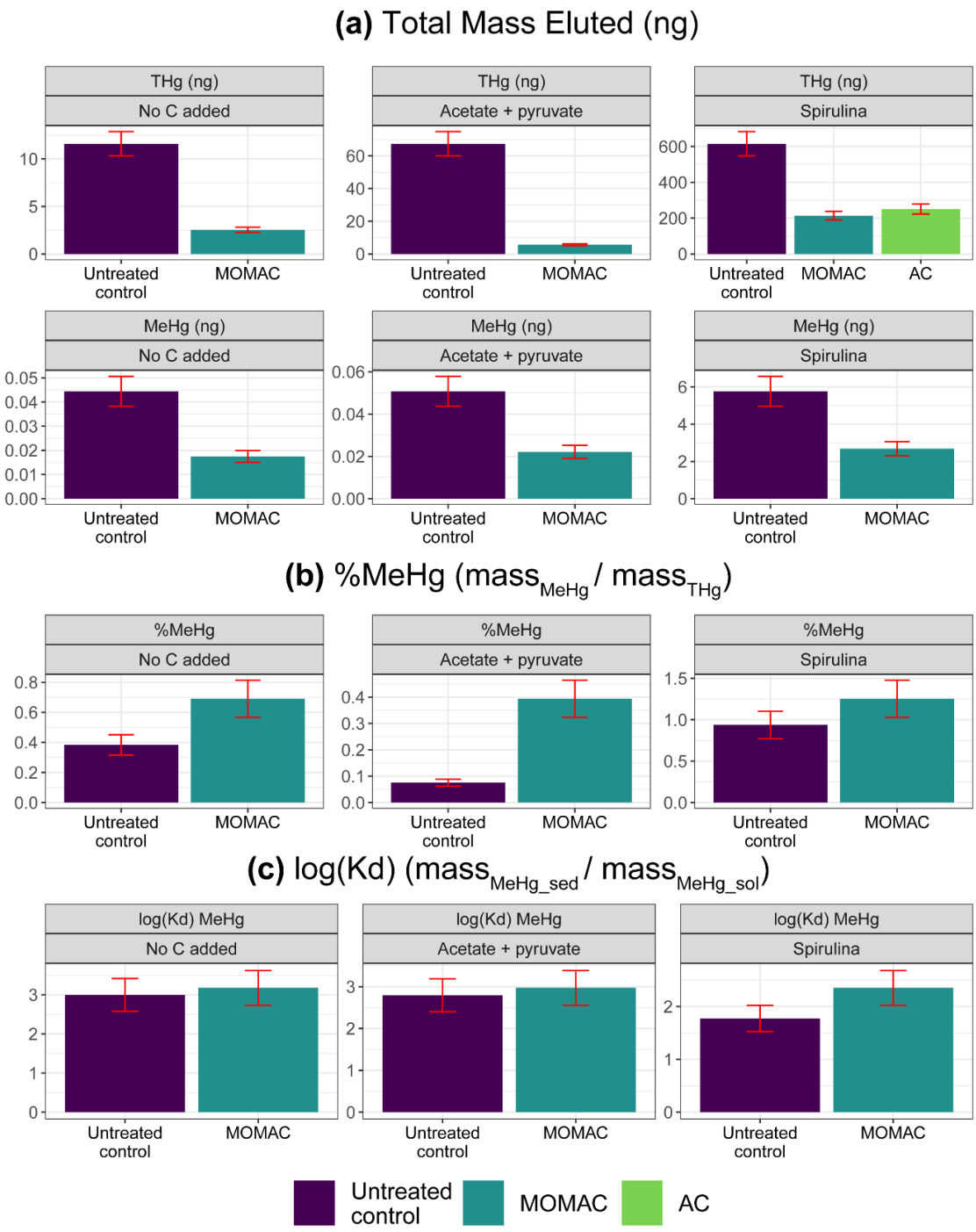

Figure 2.5. (a) Total mass of mercury (THg) and methylmercury (MeHg) eluted from column experiments. **(b)** %MeHg is ratio of MeHg mass to total Hg mass. **(c)** Log(K_d) (K_d = mass $MeHg_{sed}$/ mass $MeHg_{sol}$) represents the partitioning of methylmercury (MeHg) between the solid and aqueous phase calculated from total mass of MeHg in sediments. Comparison without accounting for initial flush out sample shown in Figure B4. Error bars are based on relative uncertainty from QA/QC samples (i.e. matrix spikes, matrix spike duplicates) measured along with unknown samples, ±11% for THg and ±14% for MeHg.

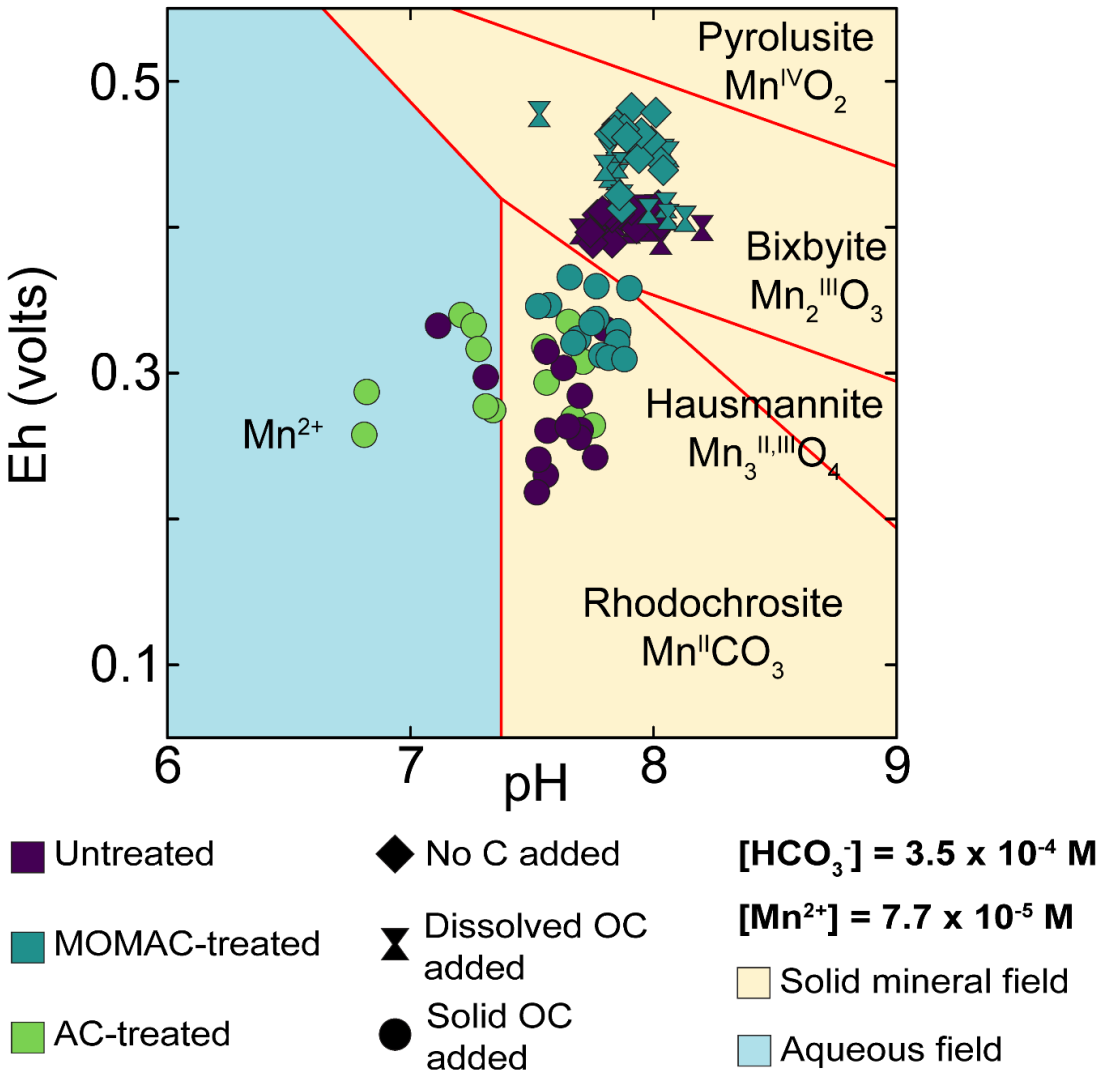

Figure 2.6. Eh−pH diagram with measured pH and Eh values of effluent from sediment flow-through column experiments. Eh−pH diagrams show Mn aqueous and solid speciation (solid red lines). Calculations were done using the Act2 program from Geochemist Workbench.

2.8 References

(1) Demers, J. D.; Blum, J. D.; Brooks, S. C.; Donovan, P. M.; Riscassi, A. L.; Miller, C. L.; Zheng, W.; Gu, B. Hg Isotopes Reveal In-Stream Processing and Legacy Inputs in East Fork Poplar Creek, Oak Ridge, Tennessee, USA. *Environ. Sci.: Process. Impacts* **2018**, *20* (4), 686–707. https://doi.org/10.1039/c7em00538e.

(2) Brooks, S. C.; Southworth, G. R. History of Mercury Use and Environmental Contamination at the Oak Ridge Y-12 Plant. *Environ Pollut* **2011**, *159* (1), 219–228. https://doi.org/10.1016/j.envpol.2010.09.009.

(3) Brooks, S. C.; Lowe, K. A.; Mehlhorn, T. L.; Olsen, T. A.; Yin, X.; Fortner, A. M.; Peterson, M. J. *Intraday Water Quality Patterns in East Fork Poplar Creek with an Emphasis on Mercury and Monomethylmercury*; Oak Ridge National Laboratory ORNL/TM-2016/ 578; 2018; pp 1–88. http://www.osti.gov/scitech/.

(4) Dickson, J. O.; Mayes, M. A.; Brooks, S. C.; Mehlhorn, T. L.; Lowe, K. A.; Earles, J. K.; Goñez-Rodriguez, L.; Watson, D. B.; Peterson, M. J. Source Relationships between Streambank Soils and Streambed Sediments in a Mercury-Contaminated Stream. *J Soils Sediments* **2019**, *19* (4), 2007–2019. https://doi.org/10.1007/s11368-018-2183-0.

(5) Marsh, D. O.; Myers, G. J.; Clarkson, T. W.; Amin-Zaki, L.; Tikriti, S.; Majeed, M. A. Fetal Methylmercury Poisoning: Clinical and Toxicological Data on 29 Cases. *Ann Neurol* **1980**, *7* (4), 348–353. https://doi.org/10.1002/ana.410070412.

(6) Driscoll, C. T.; Mason, R. P.; Chan, H. M.; Jacob, D. J.; Pirrone, N. Mercury as a Global Pollutant: Sources, Pathways, and Effects. *Environ Sci Technol* **2013**, *47* (10), 4967–4983. https://doi.org/10.1021/es305071v.

(7) Mergler, D.; Anderson, H. A.; Chan, L. H. M.; Mahaffey, K. R.; Murray, M.; Sakamoto, M.; Stern, A. H. Methylmercury Exposure and Health Effects in Humans: A Worldwide Concern
. *A Journal of the Human Environment* **2007**, *36* (1), 3–11.

(8) U.S. Environmental Protection Agency. 2023. National Rivers and Streams Assessment: The Third Collaborative Survey. EPA 841-R-22-004. U.S. Environmental Protection Agency, Office of Water and Office of Research and Development. Https://Riverstreamassessment.Epa.Gov/Webreport.

(9) U.S. Environmental Protection Agency. 2023. National Rivers and Streams Assessment 2018-2019 Technical Support Document. EPA 841-R-22-005. Office of Water and Office of Research and Development. Washington, D.C. Https://Www.Epa.Gov/National-Aquatic-Resource-Surveys/Nrsa.

(10) U.S. Environmental Protection Agency. 2020. National Rivers and Streams Assessment 2013–2014: A Collaborative Survey. EPA 841-R-19-001. Washington, DC. Https://Www.Epa.Gov/National-Aquatic-Resource-Surveys/Nrsa.

(11) Watson, D. B.; Brooks, S. C.; Mathews, T. J.; Bevelhimer, M. S.; DeRolph, C.; Brandt, C. C.; Peterson, M. J.; Ketelle, R. *Evaluation of Lower East Fork Poplar Creek Mercury Sources*; 2016. https://www.osti.gov/servlets/purl/1257903.

(12) Southworth, G.; Mathews, T.; Greeley, M.; Peterson, M.; Brooks, S.; Ketelle, D. Sources of Mercury in a Contaminated Stream—Implications for the Timescale of Recovery. *Environ Toxicol Chem* **2013**, *32* (4), 764–772. https://doi.org/10.1002/etc.2115.

(13) Sun, R.; Streets, D. G.; Horowitz, H. M.; Amos, H. M.; Liu, G.; Perrot, V.; Toutain, J.-P.; Hintelmann, H.; Sunderland, E. M.; Sonke, J. E. Historical (1850–2010) Mercury Stable Isotope Inventory from Anthropogenic Sources to the Atmosphere. *Elementa* **2016**, *4*, 000091. https://doi.org/10.12952/journal.elementa.000091.

(14) Anatone, K.; Baumann, Z.; Mason, R. P.; Hansen, G.; Chernoff, B. Century-Old Mercury Pollution: Evaluating the Impacts on Local Fish from the Eastern United States. *Chemosphere* **2020**, *259* (Mar. Pollut. Bull. 123 2017), 127484. https://doi.org/10.1016/j.chemosphere.2020.127484.

(15) Janssen, S. E.; Hoffman, J. C.; Lepak, R. F.; Krabbenhoft, D. P.; Walters, D.; Eagles-Smith, C. A.; Peterson, G.; Ogorek, J. M.; DeWild, J. F.; Cotter, A.; Pearson, M.; Tate, M. T.; Yeardley, R. B.; Mills, M. A. Examining Historical Mercury Sources in the Saint Louis River Estuary: How Legacy Contamination Influences Biological Mercury Levels in Great Lakes Coastal Regions. *Sci. Total Environ.* **2021**, *779*, 146284. https://doi.org/10.1016/j.scitotenv.2021.146284.

(16) Rudd, J. W. M.; Bodaly, R. A.; Fisher, N. S.; Kelly, C. A.; Kopec, D.; Whipple, C. Fifty Years after Its Discharge, Methylation of Legacy Mercury Trapped in the Penobscot Estuary Sustains High Mercury in Biota. *Sci. Total Environ.* **2018**, *642*, 1340–1352. https://doi.org/10.1016/j.scitotenv.2018.06.060.

(17) Deonarine, A.; Hsu-Kim, H.; Zhang, T.; Cai, Y.; Richardson, C. J. Legacy Source of Mercury in an Urban Stream–Wetland Ecosystem in Central North Carolina, USA. *Chemosphere* **2015**, *138*, 960–965. https://doi.org/10.1016/j.chemosphere.2014.12.038.

(18) Janssen, S. E.; Tate, M. T.; Krabbenhoft, D. P.; DeWild, J. F.; Ogorek, J. M.; Babiarz, C. L.; Sowers, A. D.; Tuttle, P. L. The Influence of Legacy Contamination on the Transport and Bioaccumulation of Mercury within the Mobile River Basin. *J. Hazard. Mater.* **2021**, *404* (Pt A), 124097. https://doi.org/10.1016/j.jhazmat.2020.124097.

(19) Reinfelder, J. R.; Janssen, S. E. Tracking Legacy Mercury in the Hackensack River Estuary Using Mercury Stable Isotopes. *J. Hazard. Mater.* **2019**, *375*, 121–129. https://doi.org/10.1016/j.jhazmat.2019.04.074.

(20) Manceau, A.; Lemouchi, C.; Enescu, M.; Gaillot, A.-C.; Lanson, M.; Magnin, V.; Glatzel, P.; Poulin, B. A.; Ryan, J. N.; Aiken, G. R.; Gautier-Luneau, I.; Nagy, K. L. Formation of Mercury Sulfide from Hg(II)–Thiolate Complexes in Natural Organic Matter. *Environ. Sci. Technol.* **2015**, *49* (16), 9787–9796. https://doi.org/10.1021/acs.est.5b02522.

(21) Skyllberg, U.; Bloom, P. R.; Qian, J.; Lin, C.-M.; Bleam, W. F. Complexation of Mercury(II) in Soil Organic Matter: EXAFS Evidence for Linear Two-Coordination with Reduced Sulfur Groups. *Environ. Sci. Technol.* **2006**, *40* (13), 4174–4180. https://doi.org/10.1021/es0600577.

(22) Southworth, G. R.; Jr, M. S. G.; Peterson, M. J.; Lowe, K. A.; Ketelle, R. H.; Floyd, S. B. Sources of Mercury to East Fork Poplar Creek Downstream from the Y-12 National Security Complex: Inventories and Export Rates. **2010**. https://doi.org/10.2172/974633.

(23) Manceau, A.; Lemouchi, C.; Rovezzi, M.; Lanson, M.; Glatzel, P.; Nagy, K. L.; Gautier-Luneau, I.; Joly, Y.; Enescu, M. Structure, Bonding, and Stability of Mercury Complexes with Thiolate and Thioether Ligands from High-Resolution XANES Spectroscopy and First-Principles Calculations. *Inorg. Chem.* **2015**, *54* (24), 11776–11791. https://doi.org/10.1021/acs.inorgchem.5b01932.

(24) Vidon, P.; Allan, C.; Burns, D.; Duval, T. P.; Gurwick, N.; Inamdar, S.; Lowrance, R.; Okay, J.; Scott, D.; Sebestyen, S. Hot Spots and Hot Moments in Riparian Zones: Potential for Improved Water Quality Management1. *JAWRA J. Am. Water Resour. Assoc.* **2010**, *46* (2), 278–298. https://doi.org/10.1111/j.1752-1688.2010.00420.x.

(25) Poulin, B. A.; Aiken, G. R.; Nagy, K. L.; Manceau, A.; Krabbenhoft, D. P.; Ryan, J. N. Mercury Transformation and Release Differs with Depth and Time in a Contaminated Riparian Soil during Simulated Flooding. *Geochim Cosmochim Ac* **2016**, *176*, 118–138. https://doi.org/10.1016/j.gca.2015.12.024.

(26) Rodal-Morales, N. D.; Beutel, M.; Fuhrmann, B.; Defeo, S.; Hansen, A. M.; Harmon, T.; Brower, S.; Pasek, J. Hydrology and Oxygen Addition Drive Nutrients, Metals, and Methylmercury Cycling in a Hypereutrophic Water Supply Reservoir. *Front. Water* **2024**, *6*, 1356994. https://doi.org/10.3389/frwa.2024.1356994.

(27) Seelos, M.; Beutel, M.; Austin, C. M.; Wilkinson, E.; Leal, C. Effects of Hypolimnetic Oxygenation on Fish Tissue Mercury in Reservoirs near the New Almaden Mining District, California, USA. *Environ Pollut* **2021**, *268* (Pt A), 115759. https://doi.org/10.1016/j.envpol.2020.115759.

(28) Beutel, M.; Fuhrmann, B.; Herbon, G.; Chow, A.; Brower, S.; Pasek, J. Cycling of Methylmercury and Other Redox-Sensitive Compounds in the Profundal Zone of a Hypereutrophic Water Supply Reservoir. *Hydrobiologia* **2020**, *847* (21), 4425–4446. https://doi.org/10.1007/s10750-020-04192-3.

(29) Ullrich, S. M.; Tanton, T. W.; Abdrashitova, S. A. Mercury in the Aquatic Environment: A Review of Factors Affecting Methylation. *Crit. Rev. Environ. Sci. Technol.* **2001**, *31* (3), 241–293. https://doi.org/10.1080/20016491089226.

(30) Lin, H.; Ascher, D. B.; Myung, Y.; Lamborg, C. H.; Hallam, S. J.; Gionfriddo, C. M.; Holt, K. E.; Moreau, J. W. Mercury Methylation by Metabolically Versatile and Cosmopolitan Marine Bacteria. *ISME J.* **2021**, *15* (6), 1810–1825. https://doi.org/10.1038/s41396-020-00889-4.

(31) Kerin, E. J.; Gilmour, C. C.; Roden, E.; Suzuki, M. T.; Coates, J. D.; Mason, R. P. Mercury Methylation by Dissimilatory Iron-Reducing Bacteria. *Appl. Environ. Microbiol.* **2006**, *72* (12), 7919–7921. https://doi.org/10.1128/aem.01602-06.

(32) Hamelin, S.; Amyot, M.; Barkay, T.; Wang, Y.; Planas, D. Methanogens: Principal Methylators of Mercury in Lake Periphyton. *Environ. Sci. Technol.* **2011**, *45* (18), 7693–7700. https://doi.org/10.1021/es2010072.

(33) Barnett, M. O.; Harris, L. A.; Turner, R. R.; Stevenson, R. J.; Henson, T. J.; Melton, R. C.; Hoffman, D. P. Formation of Mercuric Sulfide in Soil. *Environ Sci Technol* **1997**, *31* (11), 3037–3043. https://doi.org/10.1021/es960389j.

(34) Seelos, M.; Meraz, E. R.; Beutel, M.; Traina, S. J.; Furhmann, B.; Burmistrova, J.; Vlassopoulos, D.; O'Day, P. A. Evaluation of Manganese Oxide Amendments for Mercury Remediation in Contaminated Aquatic Sediments. *Acs Es T Eng* **2021**. https://doi.org/10.1021/acsestengg.1c00267.

(35) Matthews, D. A.; Babcock, D. B.; Nolan, J. G.; Prestigiacomo, A. R.; Effler, S. W.; Driscoll, C. T.; Todorova, S. G.; Kuhr, K. M. Whole-Lake Nitrate Addition for Control of Methylmercury in Mercury-Contaminated Onondaga Lake, NY. *Environ Res* **2013**, *125*, 52–60. https://doi.org/10.1016/j.envres.2013.03.011.

(36) Duvil, R.; Beutel, M. W.; Fuhrmann, B.; Seelos, M. Effect of Oxygen, Nitrate and Aluminum Addition on Methylmercury Efflux from Mine-Impacted Reservoir Sediment. *Water Res* **2018**, *144*, 740–751. https://doi.org/10.1016/j.watres.2018.07.071.

(37) Meraz, E. R.; Traina, S. J.; Beutel, M. W.; O'Day, P. A. Characterization of Manganese Oxide Modified Activated Carbon for Remediation of Redox-Sensitive Contaminants. *ACS Earth and Space Chemistry* **2023**, *7* (7), 1281–1293. https://doi.org/10.1021/acsearthspacechem.2c00395.

(38) Leven, A.; Vlassopoulos, D.; Kanematsu, M.; Goin, J.; O'Day, P. A. Characterization of Manganese Oxide Amendments for in Situ Remediation of Mercury-Contaminated Sediments. *Environ Sci Process Impacts* **2018**, *20* (12), 1761–1773. https://doi.org/10.1039/c7em00576h.

(39) Vlassopoulos, D.; Kanematsu, M.; Henry, E. A.; Goin, J.; Leven, A.; Glaser, D.; Brown, S. S.; Day, P. A. Manganese(Iv) Oxide Amendments Reduce Methylmercury Concentrations in Sediment Porewater. *Environ Sci Process Impacts* **2018**, *20* (12), 1746–1760. https://doi.org/10.1039/c7em00583k.

(40) O'Day, P. A.; Vlassopoulos, D. Mineral-Based Amendments for Remediation. *Elements* **2010**, *6* (6), 375–381. https://doi.org/10.2113/gselements.6.6.375.

(41) Remucal, C. K.; Ginder-Vogel, M. A Critical Review of the Reactivity of Manganese with Organic Contaminants. *Environ Sci Process Impacts* **2014**, *16* (6), 1247–1266. https://doi.org/10.1039/c3em00703k.

(42) Gilmour, C. C.; Riedel, G. S.; Riedel, G.; Kwon, S.; Landis, R.; Brown, S. S.; Menzie, C. A.; Ghosh, U. Activated Carbon Mitigates Mercury and Methylmercury Bioavailability in Contaminated Sediments. *Environ Sci Technol* **2013**, *47* (22), 13001–13010. https://doi.org/10.1021/es4021074.

(43) Johs, A.; Eller, V. A.; Mehlhorn, T. L.; Brooks, S. C.; Harper, D. P.; Mayes, M. A.; Pierce, E. M.; Peterson, M. J. Dissolved Organic Matter Reduces the Effectiveness of Sorbents for Mercury Removal. *Sci Total Environ* **2019**, *690*, 410–416. https://doi.org/10.1016/j.scitotenv.2019.07.001.

(44) Goñez-Rodríguez, L.; Johs, A.; Lowe, K. A.; Carter, K. E.; Löffler, F. E.; Mayes, M. A. Evaluation of Engineered Sorbents for the Sorption of Mercury from Contaminated Bank Soils: A Column Study. *Environ Sci Pollut R* **2021**, *28* (18), 22651–22663. https://doi.org/10.1007/s11356-020-12073-4.

(45) Schwartz, G. E.; Sanders, J. P.; McBurney, A. M.; Brown, S. S.; Ghosh, U.; Gilmour, C. C. Impact of Dissolved Organic Matter on Mercury and Methylmercury Sorption to Activated Carbon in Soils: Implications for Remediation. *Environ Sci Process Impacts* **2019**, *21* (3), 485–496. https://doi.org/10.1039/c8em00469b.

(46) Allard, S.; Gutierrez, L.; Fontaine, C.; Croué, J.-P.; Gallard, H. Organic Matter Interactions with Natural Manganese Oxide and Synthetic Birnessite. *Sci. Total Environ.* **2017**, *583*, 487–495. https://doi.org/10.1016/j.scitotenv.2017.01.120.

(47) Chorover, J.; Amistadi, M. K. Reaction of Forest Floor Organic Matter at Goethite, Birnessite and Smectite Surfaces. *Geochim. Cosmochim. Acta* **2001**, *65* (1), 95–109. https://doi.org/10.1016/s0016-7037(00)00511-1.

(48) Sunda, W. G.; Kieber, D. J. Oxidation of Humic Substances by Manganese Oxides Yields Low-Molecular-Weight Organic Substrates. *Nature* **1994**, *367* (6458), 62–64. https://doi.org/10.1038/367062a0.

(49) Trainer, E. L.; Ginder-Vogel, M.; Remucal, C. K. Selective Reactivity and Oxidation of Dissolved Organic Matter by Manganese Oxides. *Environ Sci Technol* **2021**, *55* (17), 12084–12094. https://doi.org/10.1021/acs.est.1c03972.

(50) Stone, A. T.; Morgan, J. J. Reduction and Dissolution of Manganese(III) and Manganese(IV) Oxides by Organics. 1. Reaction with Hydroquinone. *Environ Sci Technol* **1984**, *18* (6), 450–456. https://doi.org/10.1021/es00124a011.

(51) Stone, A. T. Reductive Dissolution of Manganese(III/Iv) Oxides by Substituted Phenols. *Environ Sci Technol* **1987**, *21* (10), 979–988. https://doi.org/10.1021/es50001a011.

(52) Castan, S.; Sigmund, G.; Hüffer, T.; Tepe, N.; Kammer, F. von der; Chefetz, B.; Hofmann, T. The Importance of Aromaticity to Describe the Interactions of Organic Matter with Carbonaceous Materials Depends on Molecular Weight and Sorbent Geometry. *Environ. Sci.: Process. Impacts* **2020**, *22* (9), 1888–1897. https://doi.org/10.1039/d0em00267d.

(53) Pribyl, D. W. A Critical Review of the Conventional SOC to SOM Conversion Factor. *Geoderma* **2010**, *156* (3–4), 75–83. https://doi.org/10.1016/j.geoderma.2010.02.003.

(54) *SESDPROC-113-R3, Field Measurement of Oxidation-Reduction Potential*.

(55) R Core Team. R: A Language and Environment for Statistical Computing. **2023**.

(56) Kassambara, A. Rstatix: Pipe-Friendly Framework for Basic Statistical Tests. **2023**.

(57) Shapiro, S. S.; Wilk, M. B. An Analysis of Variance Test for Normality (Complete Samples). *Biometrika* **1965**, *52* (3–4), 591–611. https://doi.org/10.1093/biomet/52.3-4.591.

(58) Wilcoxon, F. Individual Comparisons by Ranking Methods. *Biom. Bull.* **1945**, *1* (6), 80. https://doi.org/10.2307/3001968.

(59) Dunn, O. J. Multiple Comparisons Among Means. *J. Am. Stat. Assoc.* **1961**, *56* (293), 52. https://doi.org/10.2307/2282330.

(60) U.S. EPA. 1998. "Method 7473 (SW-846): Mercury in Solids and Solutions by Thermal Decomposition, Amalgamation, and Atomic Absorption Spectrophotometry," Revision 0. Washington, DC.

(61) Liang, L.; Horvat, M.; Cernichiari, E.; Gelein, B.; Balogh, S. Simple Solvent Extraction Technique for Elimination of Matrix Interferences in the Determination of Methylmercury in Environmental and Biological Samples by Ethylation-Gas Chromatography-Cold Vapor Atomic Fluorescence Spectrometry. *Talanta* **1996**, *43* (11), 1883–1888. https://doi.org/10.1016/0039-9140(96)01964-9.

(62) U.S. EPA. 1998. "Method 1630: Methyl Mercury in Water by Distillation, Aqueous Ethylation, Purge and Trap, and Cold Vapor Atomic Fluorescence Spectrometry", Washington, DC. https://www.epa.gov/cwa-methods/other-clean-water-act-test-methods-chemical

(63) Marvin-DiPasquale, M. C.; Oremland, R. S. Bacterial Methylmercury Degradation in Florida Everglades Peat Sediment. *Environ. Sci. Technol.* **1998**, *32* (17), 2556–2563. https://doi.org/10.1021/es971099l.

(64) Marvin-DiPasquale, M.; Agee, J.; McGowan, C.; Oremland, R. S.; Thomas, M.; Krabbenhoft, D.; Gilmour, C. C. Methyl-Mercury Degradation Pathways: A Comparison among Three Mercury-Impacted Ecosystems. *Environ. Sci. Technol.* **2000**, *34* (23), 4908–4916. https://doi.org/10.1021/es0013125.

(65) Eckley, C. S.; Luxton, T. P.; Knightes, C. D.; Shah, V. Methylmercury Production and Degradation under Light and Dark Conditions in the Water Column of the Hells Canyon Reservoirs, USA. *Environ. Toxicol. Chem.* **2021**, *40* (7), 1827–1837. https://doi.org/10.1002/etc.5041.

(66) Stone, A. T. Adsorption of Organic Reductants and Subsequent Electron Transfer on Metal Oxide Surfaces. *Acs Sym Ser* **1987**, 446–461. https://doi.org/10.1021/bk-1987-0323.ch021.

(67) Stone, A. T. Microbial Metabolites and the Reductive Dissolution of Manganese Oxides: Oxalate and Pyruvate. *Geochim Cosmochim Ac* **1987**, *51* (4), 919–925. https://doi.org/10.1016/0016-7037(87)90105-0.

(68) Sparks, D. L.; Fendorf, S. E.; Toner, C. V.; Carski, T. H. Methods of Soil Analysis. *SSSA Book Ser.* **1996**, 1275–1307. https://doi.org/10.2136/sssabookser5.3.c43.

(69) Amacher, M. C. Rates of Soil Chemical Processes. *SSSA Spéc. Publ.* **1991**, 19–59. https://doi.org/10.2136/sssaspecpub27.c2.

(70) Li, H.; Santos, F.; Butler, K.; Herndon, E. A Critical Review on the Multiple Roles of Manganese in Stabilizing and Destabilizing Soil Organic Matter. *Environ. Sci. Technol.* **2021**, *55* (18), 12136–12152. https://doi.org/10.1021/acs.est.1c00299.

(71) Peng, J.; Giordano, L.; Davenport, T. C.; Shao-Horn, Y. Stability Design Principles of Manganese-Based Oxides in Acid. *Chem Mater* **2022**, *34* (17), 7774–7787. https://doi.org/10.1021/acs.chemmater.2c01233.

(72) Lebron, I.; Suarez, D. L. Mechanisms and Precipitation Rate of Rhodochrosite at 25°C as Affected by PCO2 and Organic Ligands. *Soil Sci Soc Am J* **1999**, *63* (3), 561–568. https://doi.org/10.2136/sssaj1999.03615995006300030019x.

(73) Morgan, J. J.; Schlautman, M. A.; Bilinski, H. Rates of Abiotic MnII Oxidation by O2: Influence of Various Multidentate Ligands at High PH. *Environ Sci Technol* **2021**, *55* (21), 14426–14435. https://doi.org/10.1021/acs.est.1c01795.

3 Pilot Field Study of a Novel Amendment Treatment for Mercury-Contaminated Soils at East Fork Poplar Creek, TN

3.1 Abstract

East Fork Poplar Creek (EFPC), located in Oak Ridge, Tennessee, has been impacted by historical mercury (Hg) contamination originating from the Y-12 National Security Complex. Microbial methylation of Hg in anaerobic conditions leads to the formation of methylmercury (MeHg), a neurotoxin that bioaccumulates and poses significant ecological and public health risks. Manganese(III, IV) oxide modified activated carbon (MOMAC) has been shown to lower Hg and MeHg concentrations in benchtop studies but has not been tested in a field setting. This study aimed to develop and implement a pilot field trial to assess potential interactions and challenges associated with the field use of amendments such as MOMAC, particularly for remediation of mercury-contaminated EFPC soils. Soil cores were collected from floodplain and bank sites, homogenized, and packed into mesh bags before redeployment. Treatments included MOMAC and activated carbon (AC), and were compared to untreated controls. Soil samples were analyzed over an 11-week period to evaluate changes in total Hg, organic carbon (OC), reactive carbon (RC), and Hg speciation. Results from high energy resolution fluorescence detection - X-ray absorption near edge structure (HERFD-XANES) showed that most soils were dominated by Hg species similar to those found in historical release deposits (HRDs), layers with high Hg concentrations deposited during active Hg use at Y-12. Mercury species were stable throughout most treatments. Some soils treated with MOMAC showed shifts in organic matter complexes. Similarly, MOMAC-treated soils exhibited lower reactive carbon fractions, likely due to oxidation of organic matter. This study highlights the need to address oxidation of organic matter and Hg speciation with Mn oxides when considering MOMAC as a treatment for Hg-contaminated soils in EFPC.

3.2 Introduction

East Fork Poplar Creek (EFPC), located in Oak Ridge, TN, has been significantly impacted by historical use of Hg, making it an important site for understanding and mitigating Hg contamination.[1,2] The contamination at EFPC originated from historical activities tied to operations at the Y-12 National Security Complex during the mid-20th century.[3] During this time, large quantities of Hg were used at the Y-12 facility as part of lithium isotope separation processes, resulting in widespread Hg contamination. Presently, the Hg used in these processes primarily resides in clay-rich historical release deposit (HRD) soil layers along the streambanks of EFPC.[3–6] Erosion of contaminated bank soils, particularly those containing HRD layers, contribute large amounts of Hg into the stream. A key concern is the microbial conversion of inorganic Hg to neurotoxic methylmercury (MeHg), which is promoted under anaerobic or low redox conditions, occurring largely through dissimilatory sulfate or iron reduction.[7–9] The production of MeHg poses significant ecological and public health risks, as it readily bioaccumulates in aquatic organisms and magnifies up the food chain, reaching detrimental concentrations in higher trophic levels.[10–12]

Fluctuating water levels from precipitation or storm events can enhance MeHg production and mobilize both Hg and MeHg from historically contaminated floodplain and riparian soils.[13–15] After microbial oxygen consumption, periods of soil saturation due to flooding create transient anaerobic conditions that promote microbial processes responsible for Hg methylation.[13,14] Floodplain soils, often rich in organic matter (OM), create conditions that stimulate microbial activity, facilitating the conversion of inorganic Hg, or Hg-organic matter (Hg-OM) complexes, into MeHg.[15–17] The concentration of reactive carbon, measured as permanganate oxidizable carbon (POxC), is a useful indicator for the biologically active fraction of C that may be available for Hg-methylating organisms.[18] When floodwaters recede, newly formed MeHg in floodplains can be flushed into nearby water bodies.[19,20] In bank soils, elevated water levels and stronger flows from precipitation events can cause bank erosion that further contribute to Hg leaching into surface waters.[5,6] The erosion of bank soils is a major source of Hg introduced into the creek, where it can then be methylated in bottom sediments. In-stream Hg-methylation was shown as a primary contributor to MeHg inputs at EFPC.[6] This indicates that sequestering Hg in floodplain or bank soils through sorption could be an effective strategy for limiting MeHg concentrations.

Common treatment strategies used to address Hg and MeHg soil contamination in aquatic ecosystems include exercising redox control by adding oxidizing reagents to inhibit Hg-methylation pathways under anaerobic conditions[21–27], or sequestering Hg and MeHg species in the soil through the addition of sorbents.[26–30] Recently, manganese(III, IV) oxide-modified activated carbon (MOMAC) has been explored as a promising treatment to remediate Hg-contaminated soils, as it not only sequesters Hg but also promotes oxidative conditions that limit Hg-methylation.[27]

While promising in lab studies, *in-situ* application of MOMAC at a contaminated field site has yet to be tested and warrants further investigation to determine feasibility or potential obstacles when implementing this treatment. For example, environments rich in OM can reduce manganese oxide (MnOx), depleting the oxidative capacity and ability to inhibit methylation, while also reducing sorption capacity through sorption of organic compounds. Although studies directly investigating reactions of MnOx and Hg-species are limited, MnOx has been shown to release Hg from soils, potentially through oxidation of Hg(0)[31], OM complexes (e.g. Hg-OM complexes)[32–34], or HgS(s)[26]. Additionally, understanding native Hg-speciation at a contaminated site, such as those in HRD layers or in bulk soils, and as a function of treatment is critical for developing effective remediation strategies. A pilot field trial was conducted with MOMAC to assess interactions between treatments, organic carbon (OC), reactive carbon (RC), microbial populations, and Hg species to inform potential for implementing MOMAC as an *in-situ* treatment for Hg-contaminated soils at EFPC.

3.3 Methods

3.3.1 Materials

A core hole sampler (2 x 6 in), plastic liners (2 x 6 in), and plastic end caps (2”) were purchased from Art’s Manufacturing & Supply (AMS) Inc. Plastic mesh squares were formed into cylinders (2 x 6 in), bound by partially melting and fusing ends of the plastic mesh together, and reinforced with interwoven nylon wire when needed. Small

nylon mesh bags fit with a zipper (2.4 x 4 in; 150 μm mesh) were used to pack soil with or without treatment. Soil moisture sensors (Decagon EC-5; TEROS 10) and data loggers (Em5B; ZL6) were used to monitor changes in soil moisture throughout the experiment. Granular activated carbon (Filtrasorb 400) was purchased from Calgon Carbon and used without further alteration.

Manganese oxide modified activated carbon was synthesized using Filtrasorb 400 as a substrate following the procedure detailed in Rivas Meraz et al. 2023.[27] For the synthesis, 100.00 g of activated carbon were reacted with 500 mL of 0.54 M $MnCl_2 \cdot 4H_2O$ in a 2 L beaker and stirred at moderate speed with an overhead mixer overnight. Additional 500 mL solutions of NaOH (0.73 M) and $KMnO_4$ (0.36 M) were mixed in a 1 L beaker until complete dissolution of the $KMnO_4$ (~1 h). The NaOH+$KMnO_4$ solution was slowly dripped into the $MnCl_2 \cdot 4H_2O$+AC mixture for ~1 h total while stirring at moderate speed. During this time, the pH was being monitored and adjusted using 2 M NaOH to remain between 7.0-8.0. The entire solution was allowed to react for ~10 minutes after the last of the NaOH+$KMnO_4$ solution was added and the final pH was recorded. Afterward, the supernatant was decanted and the granular activated carbon that settled at the bottom was transferred to 250 mL polypropylene copolymer (PPCO) centrifuge tubes for washing. The MOMAC was washed three times with $CaCl_2$ followed by three washes with MQ water before being dried at 55°C for approximately 48 h. This process was repeated three times to supply sufficient material for field application.

3.3.2 Experiment Location and Deployment

Soils were collected at four sites along EFPC, East Fork Kilometer (EFK) 3.1, EFK 5.0, EFK 13.8, and EFK 19.1 (Figure 3.1; Table 3.1). The kilometer integer indicates the distance of that site from the confluence of EFPC with Poplar Creek. Sites were set up over the course of a week due to weather constraints that limited access. A slide hammer fit with a 2 x 6 in core sampler and plastic sleeve was used to collect the sediment. Horizontal core samples were collected from two bank sites (EFK 5.0 and 19.1) along left-descending banks near the water surface (~90 cm from ground surface). Vertical core samples were collected from the surface of two sites (EFK 3.1 and 13.8) where flooding was observed following a moderate rain event. Site EFK 13.8 was placed along a small incipient oxbow lake while samples EFK 3.1 were placed near the creek shoreline.

Two soil treatments (AC, MOMAC) were used in this study and compared against untreated soil controls. Nine soil cores were collected at each site arranged into three sets of three cores (Figure 3.1). Each set contained soil amended with AC, MOMAC, or left untreated. Within each set, the cores were spaced about 20 cm apart, and each set was positioned 0.5 – 2 meters apart. After core extraction, soil was transferred to a PPCO plastic container, and an unamended aliquot (~ 25 g) was transferred to a 20 mL scintillation vial as a field control (FC) sample. The remaining mass of soil was recorded (200-500 g), and MOMAC treatment was added at 5% dry weight (g_{amend}/g_{dry_soil}) assuming a water content (WC) of 21% from prior measurements, except for soils at EFK 13.8 where a WC of 30% was used because of higher sand content. Soils treated with AC were adjusted to provide an equal surface area as those treated with MOMAC (681 m^2/g). Consequently, the amount of AC (876 m^2/g) added was scaled down by approximately 22% before being homogenized into the soil. After

homogenization (with or without treatment), a second aliquot was transferred to a 20 mL scintillation vial for the t_0 time point. The remaining soil was packed into three fine-mesh zipper bags with approximately 70-75 g in each for the 1w, 4w, and 11w time points. The bags were packed into a plastic mesh tube, capped with plastic end caps secured by zip-ties, and returned to the extraction point (Figure 3.1a). For tubes placed along the bank, 4.37 mm (5/32") holes were drilled concentrically on the cap face to allow water to infiltrate from the creek to the mesh bags. Soil moisture sensors were installed near the soil cores at EFK 5.0 and 19.1 to monitor changes in soil moisture that may indicate precipitation or snow events and potential inundation of the sites.

3.3.3 Sample Collection and Analysis

Soil sample mesh bags were collected from each tube after 1, 4, and 11 weeks by cutting a zip-tie, extracting a fine mesh bag, and resecuring the end cap. The soil bag was returned to the lab where aliquots (30-35 g) were separated into 20 mL scintillation vials for different analyses and frozen at -80 °C. For soil DNA analysis, an aliquot (0.20-0.25 g) was thawed, and DNA was extracted using the DNeasy PowerSoil Pro Kit according to the manufacturer instructions (Qiagen, Vedbæk, Denmark), quantified using a Qubit Fluorometer (ThermoFisher), and sent to QB3 Vincent J. Coates Genomics Sequencing Laboratory to target the prokaryotic V4 region of 16S rRNA genes using dual barcoded primers (515F/806R)[35–37].

Soil samples with and without amendment were characterized by the methods below. Samples of MOMAC and AC were characterized by the same methods, and results subtracted from amended soil samples on a mass basis. Soil water content was measured by heating ~1.00 g of soil at 105°C overnight and weighing mass difference before and after heating. Total organic carbon (OC) was estimated by loss on ignition (LOI) at 550 °C. The permanganate oxidizable organic carbon (POxC) method[18] was used to estimate the fraction of organic carbon that is biologically active, or the "reactive" carbon content. A five-point standard curve was measured prior to each run consisting of an ultrapure water blank, 0.005 M, 0.01 M, 0.15 M, and 0.02 M $KMnO_4$ solutions diluted from a 0.2 M stock in 1 M $CaCl_2$. After preparation, 0.5 mL of each standard was diluted in 49.5 mL of ultrapure water and the light absorption at 550 nm was measured using a Perkin Elmer Lambda 20 UV/Vis spectrophotometer. For unknown samples, approximately 2.5 g of air-dried soil was reacted with 18 mL of ultrapure water and 2 mL of $KMnO_4$ stock solution, totaling to 20 mL of a 0.02 M $KMnO_4$ solution. The solution was reacted with the soil for 2 minutes at 120 rpm and allowed to settle for 10 minutes before sampling the supernatant. A 0.5 mL aliquot of the reaction supernatant was then diluted into 49.5 mL of ultrapure water, being careful not to entrain any solid, and the light absorption at 550 nm of the diluted solution was measured. Untreated soil from EFK 19.1 was air-dried, homogenized with a mortar and pestle, and passed through a 250-µm sieve to serve as a soil standard. This standard was used to check consistency across runs and assess variability within a given sample. A soil standard sample was included for every 12 unknown samples along with a solution standard that had no soil added. Samples consisting of MOMAC or AC alone were measured to account for interference effects from the amendments in the soil. The concentration of POxC was calculated with the following equation:

$$[0.02\ \text{mol}_{KMnO4}/\ \text{L} - (a + b \times \text{Abs})] \times (9000\ \text{mg}_C/\ \text{mol}) \times (0.02\ \text{L solution}/\ \text{Wt}) \quad (1)$$

where *a* is the y-intercept of the standard curve, *b* is the slope of the standard curve, Abs is the absorbance of the unknown sample, and Wt is the mass of the air-dried soil sample used. This calculation assumes that 1 mol of $KMnO_4$ is reduced ($Mn^{7+} \rightarrow Mn^{2+}$) in the oxidation of 0.75 mol of C (9000 mg).[18,38]

Total Hg was measured through acid digestion, volatilization, purge and trap, and cold vapor atomic fluorescence spectrometry (CVAFS) using the MERX-T automated system. Approximately 0.5-1.0 g of soil, or certified reference material (NIST 2709a[39]), was aliquoted into a 20 mL scintillation vial, digested with 8 mL of nitric acid and 2 mL of hydrochloric acid overnight, and preserved with 0.5 mL of bromine monochloride. After preservation, 0.1 mL aliquot was diluted in 39.9 mL ultrapure water, then a 0.1-1.0 mL aliquot of the diluted solution was diluted again into 23-25 mL ultrapure water and measured for THg. The initial concentrations of MeHg in soil were measured following a KOH-methanol digestion.[40] Approximately 0.1 – 0.2 g of wet sediment was placed into a 15 mL polypropylene centrifuge tube and digested with 0.5 mL 1 N HCl in methanol for 30 minutes. Afterward 2.5 mL of 25% KOH in methanol was added and the tubes were placed in an oven at 60°C for 4 h and vortexed every hour. The samples were diluted with 10 mL of ultrapure water and 150 uL of digestant was diluted into ~40 mL ultrapure water and measured for MeHg.

3.3.4 Mercury Speciation by HERFD XANES

Select soil samples were analyzed for Hg speciation with High Energy Resolution Fluorescence Detection X-ray Absorption Near Edge Spectroscopy (HERFD-XANES) measured at the Hg-L_{III} absorption edge by the Hg $L\alpha_1$ emission line at Stanford Synchrotron Radiation Lightsource (SSRL) using beamline 15-2. All soil samples scanned were from the middle of each transect (field rep 2). The beam energy was calibrated relative to the first inflection point from a gold foil at the Au L_{III} edge (11918.7 eV) and to a glitch in the Hg spectrum at 12291.5 eV, using a Si(311) double crystal monochromator. Consistency in spectra collected across runs were checked by comparing the spectrum from a $HgSO_4$ standard diluted in boron nitride collected during each run. Samples were maintained in a helium flow cryostat (Oxford instruments, Abingdon, UK) at a temperature of 10-12 K and held at a 45° angle to the incident x-ray beam. High-energy resolution X-ray fluorescence was measured using a 7-element array of spherically bent Si(555) crystal analyzers with Johann-type geometry focused on Hg $L\alpha_1$ emission[41] and measured using a single-element silicon-drift Vortex detector (Hitachi High-Technologies Science America Inc., Northridge, CA, USA). Emission energy was scanned for each sample and the maximum emission used for XANES was 9988.9±0.1 eV for all samples. HERFD X-ray spectra were collected from 12260 to 12550 eV. Unknown soil samples were scanned multiple times, at least 12 and up to 24, to improve signal-to-noise. Solid powder reference standards were diluted in boron nitride or smeared thinly on Kapton tape to lower count-rate and limit potential self-absorption effects. Aqueous Hg-ligand solutions were loaded into liquid sample holder cartridges and quench frozen in liquid N_2. No beam damage or changes in spectra were observed for soil samples during collection. In some cases, aluminum filters were positioned between the incident beam and sample chamber to maintain the count-rates within the pseudo-

linear range for the detector (< ~250,000 ct/s). Instrument control and data acquisition were carried out with the SPEC software package (Certified Scientific Software, Cambridge, Massachusetts, USA). Replicate scans were averaged with PyMCA[42], and exported to Larix[43] for data normalization and analysis. In some cases, raw scans were imported and averaged in Larix. Background was subtracted using a linear fit through the pre-edge region and post-edge regions. Sources and preparation of reference Hg compounds and species are described in Text C1. Spectra are shown in Figure C1 and summarized details are given in Table C1. Linear combination (LC) fits with reference spectra were carried out in Larch XAS over an energy range of 12270-12370 eV where components were not forced to sum to 1, no shifts in energy were allowed, components less than 5% were rejected, and goodness-of-fit were evaluated by comparing reduced chi-square values.[43] Unknown sample spectra were initially fit with a maximum of 4 components using the entire reference library. Major components (2-3) were identified, and the unknown spectrum was fit again with a maximum of 3 components. Components less than 5% were rejected as not significant.

3.4 Results

3.4.1 Soil Carbon and Water Content

There were no major trends or changes observed for estimated total OC (Figure C2), reactive C (Figure C3), or percent reactive C (Figure C4) throughout the course of the experiment (0-11w). Therefore, differences in total OC (Figure 2a), reactive C (Figure C5), and percent reactive C (% reactive C = POxC/ total OC) (Figure 2b) were compared between treatments and across sites. The average reactive carbon content of the soil standard measured at 606.2 ± 34.5 (mean ± standard deviation, n=18) showing relative uncertainty of ~6% for these measurements. Both AC and MOMAC reacted with $KMnO_4$ during measurement of reactive carbon at quantities of 765.0 ± 71.1 and 1289.0 ± 282.2 $mg_{POxC}/kg_{treatment}$ (mean ± standard error, n=4), respectively. This resulted in 4.8 ± 0.4% and 11.5 ± 1.0% (mean ± standard error, n=48) of the total $KMnO_4$ reacted in treated sediments due to the AC or MOMAC treatments, respectively. The amount of $KMnO_4$ reacted with a given treatment was accounted for when calculating POxC to determine whether there were changes in reactive C from the soil alone. The mass of amendment lost when heating the sample to determine water content and LOI were also considered for each treated soil. Treatment mass lost at 105 °C was low for AC with only 1.2 ± 0.4% while MOMAC lost 24.1 ± 3.1% (mean ± standard deviation, n=3). The majority of the remaining mass was lost at 550 °C with a 91.2 ± 0.0% loss in AC and 88.0 ± 0.2% (mean ± standard deviation, n=3) loss in MOMAC.

Soils treated with MOMAC or AC exhibited higher total OC compared to untreated soils, despite accounting for mass lost from treatments, at each field site but showed little difference in reactive carbon between soil treatments for a given field site. In contrast, AC and MOMAC treated soils exhibited a lower percent reactive carbon compared to untreated soils. In general, soils treated with MOMAC had the lowest percent reactive carbon, particularly in EFK 5.0 bank and EFK 13.8 floodplain sites (Figure 2b). Soils with the highest total OC (72 – 95 g kg^{-1}) and reactive carbon (868.6 – 938.9 mg_{POxC} kg^{-1}) measured were from floodplain site EFK 3.1. Interestingly, the total

OC of EFK 5.0 bank site was lower than the EFK 19.1 bank site across all treatments but exhibited higher reactive carbon content in comparison. Similarly, EFK 5.0 exhibited the highest percent reactive carbon among all field sites (Figure 2b). Although EFK 13.8 floodplain site was sandier than other sites, the site exhibited similar total OC as EFK 19.1 bank site for treated soils, and similar total OC to EFK 5.0 for untreated soils.

Periods of increased, and decreased, volumetric water content (VWC) were observed from the data collected by the soil moisture sensors (Figure 3.3). A moderate rain event was observed after setting up the EFK 5.0 site, which corresponded with increased VWC at EFK 5.0. This was followed by a large snow event during collection of the 1w time point samples, which corresponded with a decrease in VWC. The water contents measured from soil samples were stable throughout the experiment (Figure C6), and were similar across replicates, but differed between sites (Figure C7). EFK 13.8 floodplain site exhibited the lowest WC, ranging from 18.8 – 20.1%, followed by EFK 5.0 bank site with WC ranging from 23.9 – 24.6%, then EFK 19.1 bank site measured 25.2 – 26.4% WC, and finally EFK 3.1 floodplain site had the highest WC spanning 29.5 – 30.4 % WC.

3.4.2 Soil Total Mercury and Methylmercury

The THg extracted from the soil remained consistent throughout the experiment with few notable differences between treatment groups (Figure C8). However, there were notable differences in THg concentrations between the field sites (Figure 3.4). The EFK 5.0 bank site had the highest average THg concentrations compared to other sites, with values ranging from 37.2 to 58.6 mg_{Hg}/kg_{dry_soil}. However, there was considerable variation across the transect at EFK 5.0. Samples from the middle of the transect (replicate 2) showed higher THg concentrations, ranging from 60.2 to 165.8 mg_{Hg}/kg_{dry_soil}, compared to the upstream (replicate 1) and downstream (replicate 3) samples, which ranged from 8.7 to 23.6 mg_{Hg}/kg_{dry_soil} and 10.2 to 35.5 mg_{Hg}/kg_{dry_soil}, respectively (Figure C9). In comparison, the EFK 19.1 bank site had relatively consistent THg concentrations across all treatments, with untreated, MOMAC-treated, and AC-treated samples ranging from 23.2 to 26.6 mg_{Hg}/kg_{dry_soil}, all within similar uncertainty ranges.

The floodplain sites, EFK 13.8 and EFK 3.1, exhibited lower THg concentrations across all treatments. For EFK 13.8, THg concentrations ranged from 14.6 to 17.7 mg_{Hg}/kg_{dry_soil} across treatments, with little variability between untreated, MOMAC-treated, and AC-treated samples. The EFK 3.1 flood site displayed the lowest overall THg concentrations, with values close to 10 mg_{Hg}/kg_{dry_soil} for all treatments, showing minimal variability. Overall, the bank sites, particularly EFK 5.0, displayed higher THg concentrations compared to the floodplain sites, where concentrations were more consistent and lower across treatments.

Methylmercury was measured in the initial time points for each site and ranged from 2.8 to 14.0 µg/kg (Figure C10). Notably, bank sites with high THg did not show high MeHg concentrations. Rather floodplain soils which had lower THg concentrations exhibited higher MeHg concentrations, particularly in untreated soil. This was especially evident in EFK 3.1 which also contained the highest total OC and reactive C concentrations.

3.4.3 Mercury Speciation with High Energy Resolution Fluorescence Detection – X-ray Absorption Spectroscopy

Sample HERFD-XANES spectra, LC fits, and corresponding fractions of best-fit components are shown in Figure 5. Few differences were observed between all soil samples scanned. Samples exhibited slight variability in the first spectral feature along the rising edge between 12284.0 – 12288.0 eV. Some differences were observed in samples from MOMAC-amended bank sites at the 4w time point, which featured a peak in this region (12284.0 – 12288.0 eV) that was absent in all other samples. Linear combinations with pure reference compounds yielded poor fits. Instead, a sample collected from HRD deposits and/or residue from filtered leachate of the HRD were used in fits. The spectral signature of the residue was similar to the HRD source material (Figure C11), with a minor variation in the first spectral feature along the rising edge. These reference spectra, specifically the residue from the filtered leachate, matched well with the majority of the spectral features observed within soil samples, comprising ~72-92% of the unknown soil spectra (Figure 5). The library of Hg standards was then used to determine slight differences between samples. Unknown soils mostly fit with two components, but some samples required up to three components (Figure C12).

The fractions of reference standards fit in soil samples are shown in Table C2. Most soils fit with a combination of the HRD leachate residue and Hg-thiourea. Within some time points, distinct differences in Hg speciation were observed between treatments. At the EFK 5.0 bank site, the untreated samples across all time points (0w, 4w, 11w) showed consistent fractions of HRD soil leachate residue and Hg-thiourea. MOMAC-treated samples (4w) showed a difference by fitting with Hg-selenocysteine, while the 11w MOMAC-treated samples displayed similar distributions of Hg species compared to untreated samples. AC-treated samples (11w) at this site also exhibited similar proportions of HRD soil leachate residue and Hg-cysteine$_4$ as the untreated samples.

At the EFK 3.1 and 13.8 floodplain sites, both untreated (0w) and MOMAC-treated (4w) samples showed relatively stable distributions of HRD soil leachate residue and Hg-thiourea, with minimal variation between treatments.

At the EFK 19.1 bank site, untreated (0w and 11w) and AC-treated (11w) samples were dominated by HRD soil leachate residue with smaller fractions of Hg-thiourea. In contrast, MOMAC-treated samples at 4w did not show Hg-cysteine$_4$ but rather had an increased fraction of Hg-cysteine$_2$ and Hg-selenocysteine, while the 11w MOMAC-treated sample displayed similar distributions of Hg species compared to untreated samples.

3.5 Discussion

3.5.1 Mercury Distribution and Site-Specific Behavior

The comparison between sites revealed the localized nature of areas with Hg concentration but very similar Hg-speciation. While the EFK 19.1 bank site exhibited consistent THg concentrations, the EFK 5.0 bank site had variability across the transect. At EFK 5.0, the elevated THg concentrations in the middle of the transect (replicate 2) ranged from 60.2 to 165.8 $mg_{Hg}\,kg^{-1}{}_{drysoil}$ which suggest the presence of a Hg-laden layer, likely associated with HRDs which prior studies have shown contains approximately 157

mg kg^{-1} on average.[45,46] However, adjacent replicates 1 and 3 showed much lower concentrations (ranging from 8.7 to 35.5 mg_{Hg} $kg^{-1}_{dry\_soil}$), illustrating the large variability in Hg concentrations over short distances (1–2 m). Erosion of bank soils, especially those containing high Hg, can release significant quantities of Hg, with contributions up to 5,900 g of Hg per 100 meters per year, depending on the contamination level of the site.[5,6,45] Identifying localized hotspots of Hg contamination can facilitate a more strategic and cost-effective implementation of *in-situ* remediation with MOMAC by targeting heavily contaminated sites in conjunction with erosion prevention techniques.

Floodplain sites exhibited lower THg compared to bank sites. Differences between THg measured from bank and floodplain soils may be a factor of sampling depth. Bank soils were sampled about ~90 cm from the surface and likely captured Hg deposited during past Y-12 activities of high Hg use and release. In comparison, floodplain soils, sampled from the upper 15 cm, likely reflect more recent Hg deposition. Compared to bank sites, floodplain runoff contributes lower amounts of Hg, around 470 g of THg per year.[4–6,44] However, initial time points for MeHg digestions show higher MeHg concentrations in soil floodplain soils, particularly those rich in organic matter such as EFK 3.1 (Figure C10). While floodplain sites showed comparatively low THg concentrations to bank sites, MeHg contributions can be higher. Therefore, *in-situ* application of MOMAC through strategies such as amendment capping can keep the soil oxidized and limit MeHg production and mobilization into the stream from surface runoff.

3.5.2 Carbon Dynamics and Treatment Effects

Both AC and MOMAC treatments increased the total OC in soils compared to untreated controls at all sites, demonstrating the contribution of these carbon-based amendments to the overall organic content despite accounting for mass contributions from each amendment. However, neither amendment showed increases in reactive carbon compared to untreated soil suggesting that the organic carbon added to the system was likely not bioavailable. In contrast, amended soils exhibited a decrease in percent reactive carbon compared to untreated soils, particularly in MOMAC-treated soils, suggesting a decrease in the amount of labile OC or a shift in the carbon pool toward more recalcitrant forms. This reduction was especially evident at the EFK 5.0 bank and EFK 13.8 floodplain sites. This may be due to oxidation and destabilization of high molecular weight humic substances and other OM by MnOx, a well-established observation[33,47–51]. This reaction generally results in more aliphatic organic compounds with lower molecular weight which may have been mobilized into the stream and removed from the soil.[50] However, other studies have also reported oxidative polymerization and stabilization of low molecular weight molecules by MnOx, leading to formation of humic substances in soil which may be less reactive or already oxidized, leading to lower reactive C.[33,51,52]. By limiting the availability of reactive carbon or labile OC, treatments may mitigate one of the key factors that contribute to Hg-methylation. However, MOMAC redox buffering capacity may be consumed by reacting with OM which would lower longevity of MOMAC, particularly in sites with high OC such as EFK 3.1.

3.5.3 Mercury Speciation in Soils and Treatment Effects

The results of Hg speciation across the floodplain and bank sites provide important insights into how treatments like MOMAC and AC affect the stability and mobility of Hg. The dominant Hg species in all sampled soils was largely derived from HRDs, as indicated by the prevalence of HRD leachate residue across all sites, with a minor component of organically complexed Hg shown as Hg-thiourea, Hg-selenocysteine, or Hg-cysteine$_2$. Notably, fits with Hg-cysteine$_4$ resulted in nearly equal goodness-of-fit as Hg-thiourea, likely indicating that sulfur is a prominent ligand for Hg bound to organic matter in this system. Interestingly, the spectral signature did not change across the creek, despite varying Hg-concentrations in soil, suggesting the distribution of Hg species is largely uniform throughout the creek. This reflects the persistence of historical Hg contamination across the EFPC system that, over time, reached an equilibration with the surrounding environment into a stable Hg species. The stability of Hg speciation is further demonstrated by the similarities between the HRD layer and leachate residue which show minimal changes in the spectral signature after being mobilized by creek water (Figure C11). The Hg-thiourea component likely reflects a recalcitrant fraction of organically complexed Hg given that the fraction is stable across sites and time points throughout the experiment with some variances in MOMAC samples.

Two MOMAC-treated samples displayed slight variances compared to all other samples and were fit with Hg-selenocysteine or Hg-cysteine$_2$, or a combination thereof. Both bank soils (EFK 5.0, EFK 19.1) treated with MOMAC at 4w showed a slight change in the first spectral feature along the rising edge between 12284.0 – 12288.0 eV. An increased intensity of this absorption peak is generally associated with linearly coordinated Hg(II), found in minerals like cinnabar (α-HgS), and is dampened or disappears upon a change to the tetrahedral coordination of Hg, found in minerals such as metacinnabar (β-HgS) or tiemannite (HgSe).[52,61,63] This near edge feature was absent in nearly all samples, indicating tetrahedrally coordinated Hg may dominate but exhibited increased intensity at EFK 5.0 and 19.1. This difference is likely due to slight heterogeneity in soils of Hg complexed with various organic ligands. Alternatively, the application of oxidizing treatments, such as MOMAC, may shift the speciation of organically complexed Hg, as the two samples that were different were from MOMAC-treated soils. Reaction of MOMAC with Hg bound OM is further supported by a lower percent reactive carbon in MOMAC-treated soil averaged across the transects, but specifically for replicate 2 which was the sample scanned at the beamline (Figure C13). This oxidation could potentially favor mobilization of otherwise recalcitrant Hg.[62] However, by the 11w time point, the feature disappeared in MOMAC-treated samples indicating that the Hg had restabilized as tetrahedrally coordinated Hg or, supporting that differences observed in 4w were due to slight heterogeneity within the soil sample. Moreover, in floodplain sites EFK 3.1 and 13.8, addition of MOMAC did not appear to have an effect on speciation, further supporting that observed differences were due to heterogeneity. While MOMAC may alter OM fraction in soils, which can include Hg-OM complexes, the fraction of Hg associated with the HRD and organically complexed Hg is largely stable throughout the experiment. This indicates that despite the oxidative capacity of MOMAC, the impact on Hg speciation is minimal. However, areas with high

OM, or known Hg-OM complexes, may favor reaction which can alter Hg speciation, and, in turn, mobility and bioavailability.

Several studies have reported the dominant Hg species in bank soils as authigenic HgS, likely as metacinnabar (β-HgS) with possible structural defects or as nanoparticulates.[13,52–56] In this study, LC fits of soil samples from HRD layers, HRD residue, and bulk soils from the field trial did not fit with large fractions of either crystalline (α-HgS, β-HgS) or amorphous HgS (Figure 5). Prior studies have identified β-HgS within bulk soils, HRD layers, and leachate residue using either diffraction with a transmission electron microscope, EXAFS shell fitting, and, more recently, HERFD-XANES linear combination fits.[52–54,56]. These techniques can favor well-ordered or crystalline phases and may underestimate the fraction of Hg-OM complexes that often do not produce strong backscattering signatures or can only capture bulk properties of DOM.[57] Diffraction techniques preferentially identify the presence of crystalline or semi-crystalline inorganic Hg phases such as HgS. Similarly, studies that utilized conventional low resolution XAS tend to rely on EXAFS shell fitting, due to the relatively unfeatured absorption edge in the Hg L_{III}-edge, that may underestimate the fraction of organically complexed Hg that do not produce strong backscattering signals.[53,58] HERFD-XAS can overcome some of the limitations of traditional XAS in Hg speciation analysis by providing enhanced spectral resolution that allows for the identification and quantification of diverse Hg species, including Hg-organic complexes.[13,52,59–61] Two studies to-date have utilized HERFD-XANES linear combination fits to characterize soils from EFPC and have also identified a combination of nanoparticulate β-HgS and Hg bound to soil organic matter (Hg-SOM).[13,52] However, a critical aspect to consider is the potential presence of residual organic matter in nanoparticulate β-HgS synthesized and used as a reference standard.[52] The synthesis procedure, involving the complexation of Hg with an organic ligand (L-cysteine ethyl ester; L-Cys-OEt), may not have complete removal of organic components from the final β-HgS product, despite observing the presence of β-HgS.[52] This potential contamination introduces uncertainty into the characterization of the nanoparticulate β-HgS, as any residual organic matter could influence the spectral signature. If the nanoparticulate β-HgS reference spectrum already includes spectral contributions from organically bound Hg, this could lead to an underestimation of organically bound Hg. Furthermore, authors also noted that reference spectra for Hg-SOM might contain contributions from nanoparticulate β-HgS from abiotic reactions between sulfurized OM and Hg.[52] This further complicates the interpretation, making it challenging to deconvolve and quantify the spectral contributions of these two Hg forms accurately. Therefore, the fraction that fits with HRD leachate residue, while likely containing nanoparticulate or defected β-HgS, may also contain a notable fraction of Hg-OM complexes not entirely identified.

3.6 Conclusions

The findings from this study present some complexities for implementing MOMAC as an *in-situ* Hg remediation treatment EFPC. Due to the localized nature of HRD contamination at EFPC, implementation of *in-situ* treatments can be more cost-effective by targeting heavily contaminated sites primarily. A combination of strategies that combine MOMAC with erosion-prevention techniques may be favorable to further

stabilize contaminated soils, reduce Hg inputs into the creek through sorption, and limit the potential for Hg methylation and downstream environmental impacts. Treating with oxidizing amendments may decrease the percent of total carbon present as labile carbon that could disfavor microbial activity and Hg-methylation. However, this may result in decreased redox buffering capacity and amendment longevity. Interestingly, the distribution of Hg-species was similar throughout all sampling sites spanning ~16.1 km which shows that legacy contamination has equilibrated with the surrounding environment to reach a stable state as HgS with a smaller, but possibly underestimated, fraction of Hg-OM complexes. However, oxidation with MOMAC may react with, and potentially liberate, some of these stable Hg-species, particularly Hg-OM complexes. Investigating changes in Hg-speciation at EFPC as a consequence of oxidation with MnOx should be carefully considered prior to large-scale implementation in Hg-contaminated sites.

3.7 Figures

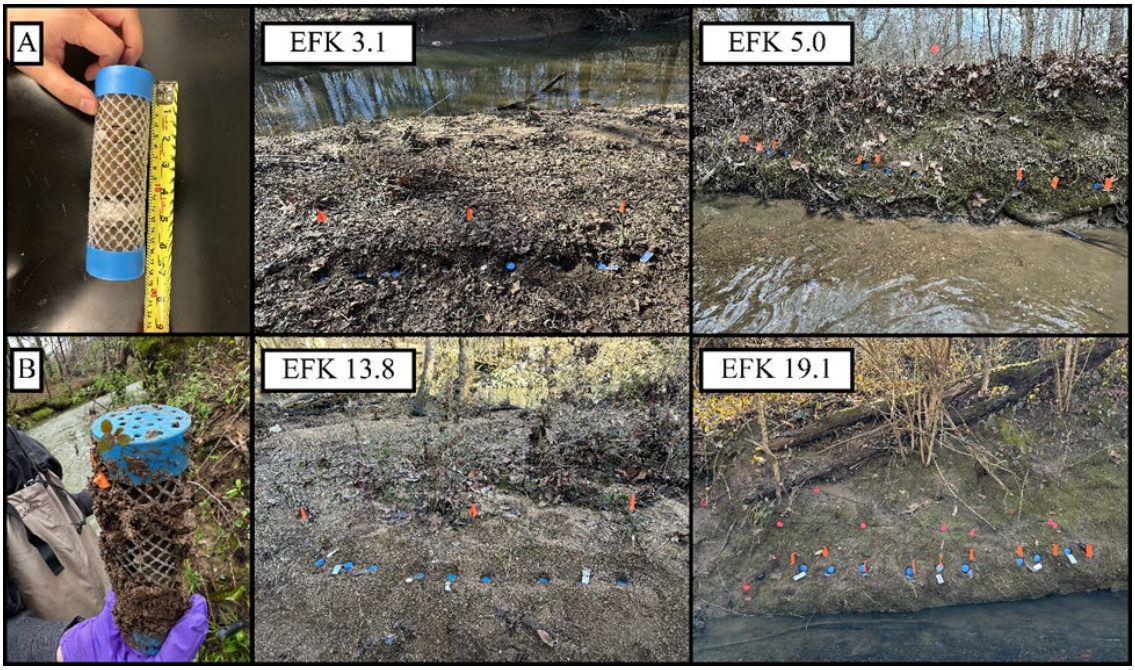

Figure 3.1. Field deployment sites along the East Fork Poplar Creek (EFPC) showing experimental setup at four different locations. Soil cores were extracted, homogenized with (or without) treatment (AC, MOMAC, or untreated controls), and placed in fine mesh bags. Bags were then packed into a plastic mesh tube and inserted back into the original extraction locations across all sites. **Picture A** shows an example plastic mesh tube packed with fine mesh bags prior to deployment while **Picture B** shows a plastic mesh tube retrieved during sample collection. At EFK 3.1, cores were positioned near the creek shoreline in a flood-prone area. At EFK 5.0 and EFK 19.1, horizontal cores were collected along left-descending banks near the water surface, with soil moisture sensors installed at both sites to monitor precipitation and potential inundation. EFK 13.8, located near a small incipient oxbow lake, featured vertical cores collected from sandy floodplain soils.

Table 3.1. Field Deployment Sites at East Fork Poplar Creek

Site[1]	Sample Location	Latitude	Longitude
EFK 3.1	Floodplain	35° 57' 22" N	84° 22' 8" W
EFK 5.0	Streambank	35° 57' 47" N	84° 21' 34" W
EFK 13.8	Floodplain	35° 59' 32" N	84° 18' 56" W
EFK 19.1	Streambank	36° 0' 33" N	84° 16' 41" W

[1] EFK – East Fork Kilometer

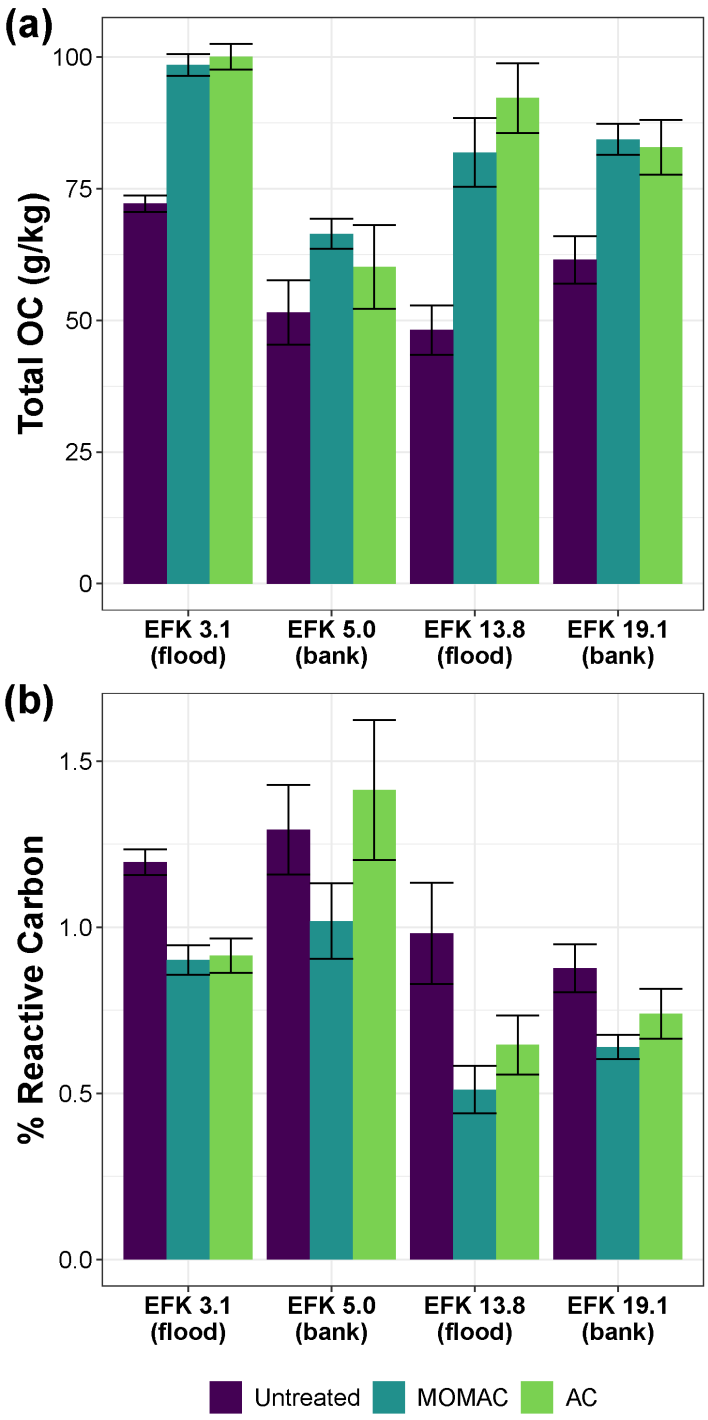

Figure 3.2. (a) Total organic carbon measured by loss on ignition at 550 °C for each sampled field site. **(b)** Percent reactive carbon calculated as the ratio of permanganate oxidizable carbon (POxC) (shown in Figure C5) to total organic carbon measured by loss on ignition at 550°C for each sampled field site. Error bars show averages from replicates across the transect and all time points (mean ± standard error; n = 12)

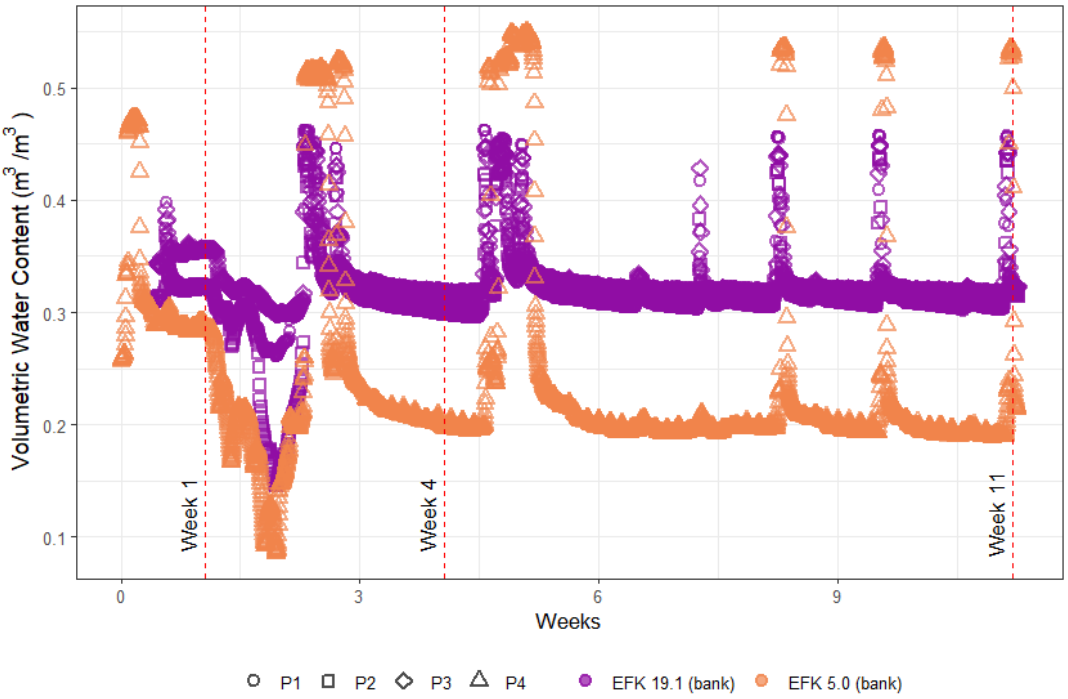

Figure 3.3. Volumetric water content measured with soil moisture sensors throughout the experiment from bank sites EFK 5.0 (P4: Decagon EC-5) and EFK 19.1 (P1-P3: TEROS 10). Sensors were placed along the same elevation as samples to indicate potential inundation following storm events. Vertical red lines indicate sampling times with respect to the start of the experiment.

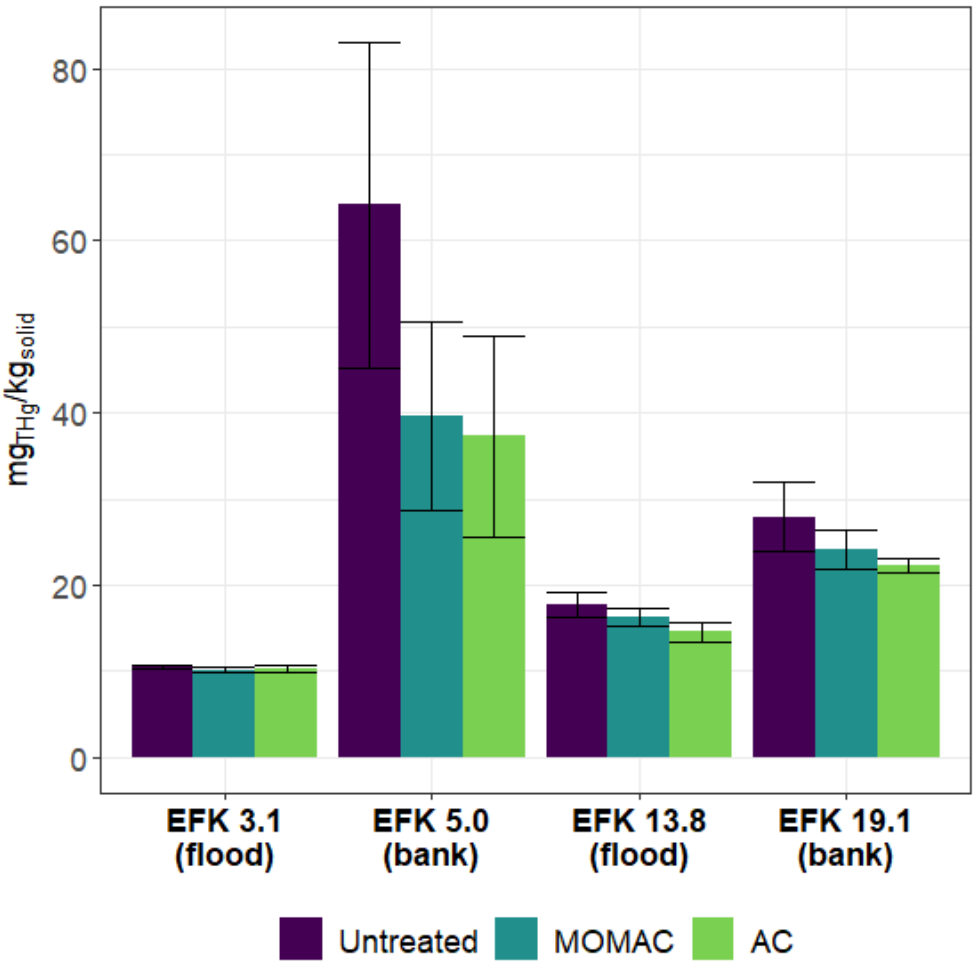

Figure 3.4. Total mercury (THg) averaged for each treatment at a given sampled field site. Error bars show averages from replicates across the transect and all time points (mean ± standard error; n = 12).

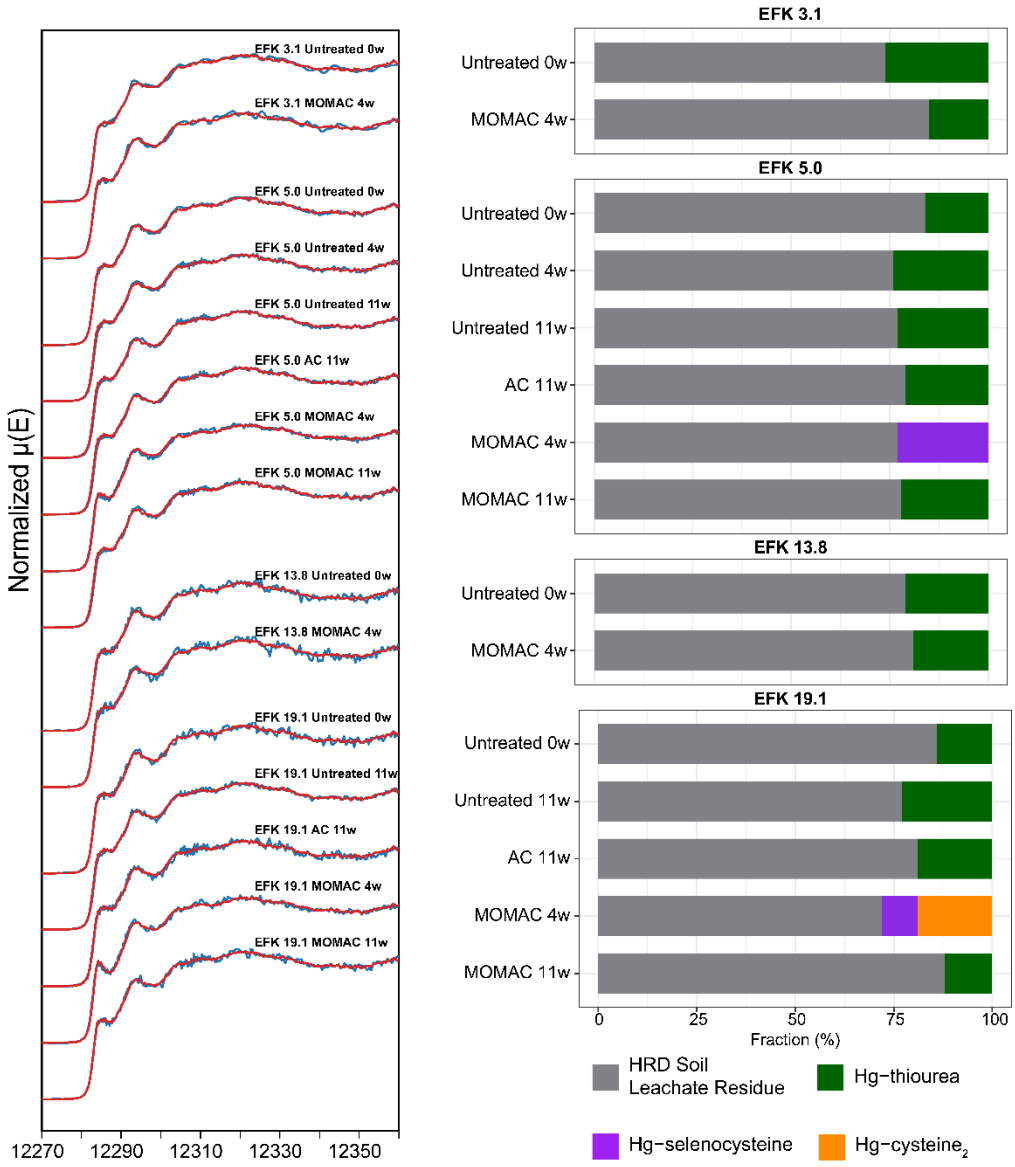

Figure 3.5. High energy resolution detected – X-ray absorption near edge spectroscopy spectra (left) of soil samples (blue lines) with linear combination fits showing component sum (red lines). Linear combinations were conducted with a library of Hg reference standards. Fractions of best-fit components, normalized to 100%, are shown in bar plots (right). Tabulated values and fit statistics are shown in Table C2.

3.8 References

(1) Loar, J. M.; Stewart, A. J.; Smith, J. G. Twenty-Five Years of Ecological Recovery of East Fork Poplar Creek: Review of Environmental Problems and Remedial Actions. *Environ Manage* **2011**, *47* (6), 1010–1020. https://doi.org/10.1007/s00267-011-9625-4.

(2) Demers, J. D.; Blum, J. D.; Brooks, S. C.; Donovan, P. M.; Riscassi, A. L.; Miller, C. L.; Zheng, W.; Gu, B. Hg Isotopes Reveal In-Stream Processing and Legacy Inputs in East Fork Poplar Creek, Oak Ridge, Tennessee, USA. *Environ. Sci.: Process. Impacts* **2018**, *20* (4), 686–707. https://doi.org/10.1039/c7em00538e.

(3) Brooks, S. C.; Southworth, G. R. History of Mercury Use and Environmental Contamination at the Oak Ridge Y-12 Plant. *Environ Pollut* **2011**, *159* (1), 219–228. https://doi.org/10.1016/j.envpol.2010.09.009.

(4) Dickson, J. O.; Mayes, M. A.; Brooks, S. C.; Mehlhorn, T. L.; Lowe, K. A.; Earles, J. K.; Goñez-Rodriguez, L.; Watson, D. B.; Peterson, M. J. Source Relationships between Streambank Soils and Streambed Sediments in a Mercury-Contaminated Stream. *J Soils Sediments* **2019**, *19* (4), 2007–2019. https://doi.org/10.1007/s11368-018-2183-0.

(5) Southworth, G.; Mathews, T.; Greeley, M.; Peterson, M.; Brooks, S.; Ketelle, D. Sources of Mercury in a Contaminated Stream—Implications for the Timescale of Recovery. *Environ Toxicol Chem* **2013**, *32* (4), 764–772. https://doi.org/10.1002/etc.2115.

(6) Watson, D. B.; Brooks, S. C.; Mathews, T. J.; Bevelhimer, M. S.; DeRolph, C.; Brandt, C. C.; Peterson, M. J.; Ketelle, R. *Evaluation of Lower East Fork Poplar Creek Mercury Sources*; 2016. https://www.osti.gov/servlets/purl/1257903.

(7) Hsu-Kim, H.; Kucharzyk, K. H.; Zhang, T.; Deshusses, M. A. Mechanisms Regulating Mercury Bioavailability for Methylating Microorganisms in the Aquatic Environment: A Critical Review. *Environ Sci Technol* **2013**, *47* (6), 2441–2456. https://doi.org/10.1021/es304370g.

(8) Parks, J. M.; Johs, A.; Podar, M.; Bridou, R.; Hurt, R. A.; Smith, S. D.; Tomanicek, S. J.; Qian, Y.; Brown, S. D.; Brandt, C. C.; Palumbo, A. V.; Smith, J. C.; Wall, J. D.; Elias, D. A.; Liang, L. The Genetic Basis for Bacterial Mercury Methylation. *Science* **2013**, *339* (6125), 1332–1335. https://doi.org/10.1126/science.1230667.

(9) Kerin, E. J.; Gilmour, C. C.; Roden, E.; Suzuki, M. T.; Coates, J. D.; Mason, R. P. Mercury Methylation by Dissimilatory Iron-Reducing Bacteria. *Appl. Environ. Microbiol.* **2006**, *72* (12), 7919–7921. https://doi.org/10.1128/aem.01602-06.

(10) Karagas, M. R.; Choi, A. L.; Oken, E.; Horvat, M.; Schoeny, R.; Kamai, E.; Cowell, W.; Grandjean, P.; Korrick, S. Evidence on the Human Health Effects of Low-Level

Methylmercury Exposure. *Environ Health Persp* **2012**, *120* (6), 799–806. https://doi.org/10.1289/ehp.1104494.

(11) Marsh, D. O.; Myers, G. J.; Clarkson, T. W.; Amin-Zaki, L.; Tikriti, S.; Majeed, M. A. Fetal Methylmercury Poisoning: Clinical and Toxicological Data on 29 Cases. *Ann Neurol* **1980**, *7* (4), 348–353. https://doi.org/10.1002/ana.410070412.

(12) Ha, E.; Basu, N.; Bose-O'Reilly, S.; Dórea, J. G.; McSorley, E.; Sakamoto, M.; Chan, H. M. Current Progress on Understanding the Impact of Mercury on Human Health. *Environ Res* **2017**, *152*, 419–433. https://doi.org/10.1016/j.envres.2016.06.042.

(13) Poulin, B. A.; Aiken, G. R.; Nagy, K. L.; Manceau, A.; Krabbenhoft, D. P.; Ryan, J. N. Mercury Transformation and Release Differs with Depth and Time in a Contaminated Riparian Soil during Simulated Flooding. *Geochim Cosmochim Ac* **2016**, *176*, 118–138. https://doi.org/10.1016/j.gca.2015.12.024.

(14) Balogh, S. J.; Nollet, Y. H.; Swain, E. B. Redox Chemistry in Minnesota Streams during Episodes of Increased Methylmercury Discharge. *Environ Sci Technol* **2004**, *38* (19), 4921–4927. https://doi.org/10.1021/es049696c.

(15) Regnell, O.; Watras, C. J.; Troedsson, B.; Helgée, A.; Hammar, T. Mercury in a Boreal Forest Stream - Role of Historical Mercury Pollution, TOC, Temperature, and Water Discharge. *Environ. Sci. Technol.* **2009**, *43* (10), 3514–3521. https://doi.org/10.1021/es802991x.

(16) Gygax, S.; Gfeller, L.; Wilcke, W.; Mestrot, A. Emerging Investigator Series: Mercury Mobility and Methylmercury Formation in a Contaminated Agricultural Flood Plain: Influence of Flooding and Manure Addition. *Environ. Sci.: Process. Impacts* **2019**, *21* (12), 2008–2019. https://doi.org/10.1039/c9em00257j.

(17) Frohne, T.; Rinklebe, J.; Langer, U.; Laing, G. D.; Mothes, S.; Wennrich, R. Biogeochemical Factors Affecting Mercury Methylation Rate in Two Contaminated Floodplain Soils. *Biogeosciences* **2012**, *9* (1), 493–507. https://doi.org/10.5194/bg-9-493-2012.

(18) Weil, R. R.; Islam, K. R.; Stine, M. A.; Gruver, J. B.; Samson-Liebig, S. E. Estimating Active Carbon for Soil Quality Assessment: A Simplified Method for Laboratory and Field Use. *Am. J. Altern. Agric.* **2003**, *18* (1), 3–17. https://doi.org/10.1079/ajaa2003003.

(19) Flanders, J. R.; Turner, R. R.; Morrison, T.; Jensen, R.; Pizzuto, J.; Skalak, K.; Stahl, R. Distribution, Behavior, and Transport of Inorganic and Methylmercury in a High Gradient Stream. *Appl. Geochem.* **2010**, *25* (11), 1756–1769. https://doi.org/10.1016/j.apgeochem.2010.09.004.

(20) Singer, M. B.; Harrison, L. R.; Donovan, P. M.; Blum, J. D.; Marvin-DiPasquale, M. Hydrologic Indicators of Hot Spots and Hot Moments of Mercury Methylation Potential along River Corridors. *Sci. Total Environ.* **2016**, *568*, 697–711. https://doi.org/10.1016/j.scitotenv.2016.03.005.

(21) Matthews, D. A.; Babcock, D. B.; Nolan, J. G.; Prestigiacomo, A. R.; Effler, S. W.; Driscoll, C. T.; Todorova, S. G.; Kuhr, K. M. Whole-Lake Nitrate Addition for Control of Methylmercury in Mercury-Contaminated Onondaga Lake, NY. *Environ Res* **2013**, *125*, 52–60. https://doi.org/10.1016/j.envres.2013.03.011.

(22) Leven, A.; Vlassopoulos, D.; Kanematsu, M.; Goin, J.; O'Day, P. A. Characterization of Manganese Oxide Amendments for in Situ Remediation of Mercury-Contaminated Sediments. *Environ Sci Process Impacts* **2018**, *20* (12), 1761–1773. https://doi.org/10.1039/c7em00576h.

(23) Duvil, R.; Beutel, M. W.; Fuhrmann, B.; Seelos, M. Effect of Oxygen, Nitrate and Aluminum Addition on Methylmercury Efflux from Mine-Impacted Reservoir Sediment. *Water Res* **2018**, *144*, 740–751. https://doi.org/10.1016/j.watres.2018.07.071.

(24) Beutel, M.; Dent, S.; Reed, B.; Marshall, P.; Gebremariam, S.; Moore, B.; Cross, B.; Gantzer, P.; Shallenberger, E. Effects of Hypolimnetic Oxygen Addition on Mercury Bioaccumulation in Twin Lakes, Washington, USA. *Sci Total Environ* **2014**, *496*, 688–700. https://doi.org/10.1016/j.scitotenv.2014.06.117.

(25) Seelos, M.; Beutel, M.; Austin, C. M.; Wilkinson, E.; Leal, C. Effects of Hypolimnetic Oxygenation on Fish Tissue Mercury in Reservoirs near the New Almaden Mining District, California, USA. *Environ Pollut* **2021**, *268* (Pt A), 115759. https://doi.org/10.1016/j.envpol.2020.115759.

(26) Seelos, M.; Meraz, E. R.; Beutel, M.; Traina, S. J.; Furhmann, B.; Burmistrova, J.; Vlassopoulos, D.; O'Day, P. A. Evaluation of Manganese Oxide Amendments for Mercury Remediation in Contaminated Aquatic Sediments. *Acs Es T Eng* **2021**. https://doi.org/10.1021/acsestengg.1c00267.

(27) Meraz, E. R.; Traina, S. J.; Beutel, M. W.; O'Day, P. A. Characterization of Manganese Oxide Modified Activated Carbon for Remediation of Redox-Sensitive Contaminants. *ACS Earth and Space Chemistry* **2023**, *7* (7), 1281–1293. https://doi.org/10.1021/acsearthspacechem.2c00395.

(28) Gilmour, C. C.; Riedel, G. S.; Riedel, G.; Kwon, S.; Landis, R.; Brown, S. S.; Menzie, C. A.; Ghosh, U. Activated Carbon Mitigates Mercury and Methylmercury Bioavailability in Contaminated Sediments. *Environ Sci Technol* **2013**, *47* (22), 13001–13010. https://doi.org/10.1021/es4021074.

(29) Schwartz, G. E.; Sanders, J. P.; McBurney, A. M.; Brown, S. S.; Ghosh, U.; Gilmour, C. C. Impact of Dissolved Organic Matter on Mercury and Methylmercury Sorption to Activated Carbon in Soils: Implications for Remediation. *Environ Sci Process Impacts* **2019**, *21* (3), 485–496. https://doi.org/10.1039/c8em00469b.

(30) Patmont, C. R.; Ghosh, U.; Larosa, P.; Menzie, C. A.; Luthy, R. G.; Greenberg, M. S.; Cornelissen, G.; Eek, E.; Collins, J.; Hull, J.; Hjartland, T.; Glaza, E. E.; Bleiler, J.; Quadrini, J. In Situ Sediment Treatment Using Activated Carbon: A Demonstrated Sediment Cleanup Technology. *Integr Environ Asses* **2015**, *11* (2), 195–207. https://doi.org/10.1002/ieam.1589.

(31) Miller, C. L.; Watson, D. B.; Lester, B. P.; Howe, J. Y.; Phillips, D. H.; He, F.; Liang, L.; Pierce, E. M. Formation of Soluble Mercury Oxide Coatings: Transformation of Elemental Mercury in Soils. *Environ. Sci. Technol.* **2015**, *49* (20), 12105–12111. https://doi.org/10.1021/acs.est.5b00263.

(32) Remucal, C. K.; Ginder-Vogel, M. A Critical Review of the Reactivity of Manganese with Organic Contaminants. *Environ Sci Process Impacts* **2014**, *16* (6), 1247–1266. https://doi.org/10.1039/c3em00703k.

(33) Li, H.; Santos, F.; Butler, K.; Herndon, E. A Critical Review on the Multiple Roles of Manganese in Stabilizing and Destabilizing Soil Organic Matter. *Environ. Sci. Technol.* **2021**, *55* (18), 12136–12152. https://doi.org/10.1021/acs.est.1c00299.

(34) Allard, S.; Gutierrez, L.; Fontaine, C.; Croué, J.-P.; Gallard, H. Organic Matter Interactions with Natural Manganese Oxide and Synthetic Birnessite. *Sci. Total Environ.* **2017**, *583*, 487–495. https://doi.org/10.1016/j.scitotenv.2017.01.120.

(35) Kozich, J. J.; Westcott, S. L.; Baxter, N. T.; Highlander, S. K.; Schloss, P. D. Development of a Dual-Index Sequencing Strategy and Curation Pipeline for Analyzing Amplicon Sequence Data on the MiSeq Illumina Sequencing Platform. *Appl. Environ. Microbiol.* **2013**, *79* (17), 5112–5120. https://doi.org/10.1128/aem.01043-13.

(36) Parada, A. E.; Needham, D. M.; Fuhrman, J. A. Every Base Matters: Assessing Small Subunit RRNA Primers for Marine Microbiomes with Mock Communities, Time Series and Global Field Samples. *Environ. Microbiol.* **2016**, *18* (5), 1403–1414. https://doi.org/10.1111/1462-2920.13023.

(37) Apprill, A.; McNally, S.; Parsons, R.; Weber, L. Minor Revision to V4 Region SSU RRNA 806R Gene Primer Greatly Increases Detection of SAR11 Bacterioplankton. *Aquat. Microb. Ecol.* **2015**, *75* (2), 129–137. https://doi.org/10.3354/ame01753.

(38) Blair, G.; Lefroy, R.; Lisle, L. Soil Carbon Fractions Based on Their Degree of Oxidation, and the Development of a Carbon Management Index for Agricultural Systems. *Crop Pasture Sci.* **1995**, *46* (7), 1459–1466. https://doi.org/10.1071/ar9951459.

(39) Mackey, E. A.; Johnson, C. S.; Lindstrom, R. M.; Long, S. E.; Marlow, A. F.; Murphy, K. E.; Paul, R. L.; Popelka-Filcoff, R. S.; Rabb, S. A.; Sieber, J. R.; Oflaz, R.; Tomlin, B. E.; Wood, L. J.; Yen, J. H.; Yu, L. L.; Zeisler, R. L.; Wilson, S. A.; Adams, M. G.; Brown, Z. A.; Lamothe, P. L.; Taggart, J. E.; Jones, C.; Nebelsick, J. Certification of Three NIST Renewal Soil Standard Reference Materials for Element Content. https://doi.org/10.6028/nist.sp.260-172.

(40) Liang, L.; Horvat, M.; Cernichiari, E.; Gelein, B.; Balogh, S. Simple Solvent Extraction Technique for Elimination of Matrix Interferences in the Determination of Methylmercury in Environmental and Biological Samples by Ethylation-Gas Chromatography-Cold Vapor Atomic Fluorescence Spectrometry. *Talanta* **1996**, *43* (11), 1883–1888. https://doi.org/10.1016/0039-9140(96)01964-9.

(41) Sokaras, D.; Weng, T.-C.; Nordlund, D.; Alonso-Mori, R.; Velikov, P.; Wenger, D.; Garachtchenko, A.; George, M.; Borzenets, V.; Johnson, B.; Rabedeau, T.; Bergmann, U. A Seven-Crystal Johann-Type Hard x-Ray Spectrometer at the Stanford Synchrotron Radiation Lightsource. *Rev. Sci. Instrum.* **2013**, *84* (5), 053102. https://doi.org/10.1063/1.4803669.

(42) Solé, V. A.; Papillon, E.; Cotte, M.; Walter, Ph.; Susini, J. A Multiplatform Code for the Analysis of Energy-Dispersive X-Ray Fluorescence Spectra. *Spectrochim. Acta Part B: At. Spectrosc.* **2007**, *62* (1), 63–68. https://doi.org/10.1016/j.sab.2006.12.002.

(43) Newville, M. Larch: An Analysis Package for XAFS and Related Spectroscopies. *J Phys Conf Ser* **2013**, *430* (1), 012007. https://doi.org/10.1088/1742-6596/430/1/012007.

(44) Southworth, G. R.; Jr, M. S. G.; Peterson, M. J.; Lowe, K. A.; Ketelle, R. H.; Floyd, S. B. Sources of Mercury to East Fork Poplar Creek Downstream from the Y-12 National Security Complex: Inventories and Export Rates. **2010**. https://doi.org/10.2172/974633.

(45) Watson, D. B.; Brooks, S. C.; Mathews, T. J.; Bevelhimer, M. S.; DeRolph, C.; Brandt, C. C.; Peterson, M. J.; Ketelle, R. Evaluation of Lower East Fork Poplar Creek Mercury Sources. https://doi.org/10.2172/1257903.

(46) Ma, D.; Wu, J.; Yang, P.; Zhu, M. Coupled Manganese Redox Cycling and Organic Carbon Degradation on Mineral Surfaces. *Environ Sci Technol* **2020**, *54* (14), 8801–8810. https://doi.org/10.1021/acs.est.0c02065.

(47) Hyun, J.-H.; Kim, S.-H.; Mok, J.-S.; Cho, H.; Lee, T.; Vandieken, V.; Thamdrup, B. Manganese and Iron Reduction Dominate Organic Carbon Oxidation in Surface Sediments of the Deep Ulleung Basin, East Sea. *Biogeosciences* **2017**, *14* (4), 941–958. https://doi.org/10.5194/bg-14-941-2017.

(48) Sunda, W. G.; Kieber, D. J. Oxidation of Humic Substances by Manganese Oxides Yields Low-Molecular-Weight Organic Substrates. *Nature* **1994**, *367* (6458), 62–64. https://doi.org/10.1038/367062a0.

(49) Trainer, E. L.; Ginder-Vogel, M.; Remucal, C. K. Selective Reactivity and Oxidation of Dissolved Organic Matter by Manganese Oxides. *Environ Sci Technol* **2021**, *55* (17), 12084–12094. https://doi.org/10.1021/acs.est.1c03972.

(50) Johnson, K.; Purvis, G.; Lopez-Capel, E.; Peacock, C.; Gray, N.; Wagner, T.; März, C.; Bowen, L.; Ojeda, J.; Finlay, N.; Robertson, S.; Worrall, F.; Greenwell, C. Towards a Mechanistic Understanding of Carbon Stabilization in Manganese Oxides. *Nat Commun* **2015**, *6* (1), 7628. https://doi.org/10.1038/ncomms8628.

(51) Jokic, A.; Wang, M. C.; Liu, C.; Frenkel, A. I.; Huang, P. M. Integration of the Polyphenol and Maillard Reactions into a Unified Abiotic Pathway for Humification in Nature the Role of δ-MnO2. *Org Geochem* **2004**, *35* (6), 747–762. https://doi.org/10.1016/j.orggeochem.2004.01.021.

(52) Manceau, A.; Lemouchi, C.; Enescu, M.; Gaillot, A.-C.; Lanson, M.; Magnin, V.; Glatzel, P.; Poulin, B. A.; Ryan, J. N.; Aiken, G. R.; Gautier-Luneau, I.; Nagy, K. L. Formation of Mercury Sulfide from Hg(II)–Thiolate Complexes in Natural Organic Matter. *Environ. Sci. Technol.* **2015**, *49* (16), 9787–9796. https://doi.org/10.1021/acs.est.5b02522.

(53) Koenigsmark, F.; Chiu, M.; Rivera, N.; Johs, A.; Eskelsen, J.; Leonard, D.; Robertson, B. K.; Szynkiewicz, A.; Derolph, C.; Zhao, L.; Gu, B.; Hsu-Kim, H.; Pierce, E. M. Crystal Lattice Defects in Nanocrystalline Metacinnabar in Contaminated Streambank Soils Suggest a Role for Biogenic Sulfides in the Formation of Mercury Sulfide Phases. *Environ. Sci.: Process. Impacts* **2023**, *25* (3), 445–460. https://doi.org/10.1039/d1em00549a.

(54) Barnett, M. O.; Harris, L. A.; Turner, R. R.; Stevenson, R. J.; Henson, T. J.; Melton, R. C.; Hoffman, D. P. Formation of Mercuric Sulfide in Soil. *Environ Sci Technol* **1997**, *31* (11), 3037–3043. https://doi.org/10.1021/es960389j.

(55) Revis, N. W.; Osborne, T. R.; Holdsworth, G.; Hadden, C. Distribution of Mercury Species in Soil from a Mercury-Contaminated Site. *Water, Air, Soil Pollut.* **1989**, *45* (1–2), 105–113. https://doi.org/10.1007/bf00208581.

(56) Barnett, M. O.; Harris, L. A.; Turner, R. R.; Henson, T. J.; Melton, R. E.; Stevenson, R. J. Characterization of Mercury Species in Contaminated Floodplain Soils. *Water, Air, Soil Pollut.* **1995**, *80* (1–4), 1105–1108. https://doi.org/10.1007/bf01189771.

(57) Chen, H.; Johnston, R. C.; Mann, B. F.; Chu, R. K.; Tolic, N.; Parks, J. M.; Gu, B. Identification of Mercury and Dissolved Organic Matter Complexes Using Ultrahigh

Resolution Mass Spectrometry. *Environ. Sci. Technol. Lett.* **2017**, *4* (2), 59–65. https://doi.org/10.1021/acs.estlett.6b00460.

(58) Gräfe, M.; Donner, E.; Collins, R. N.; Lombi, E. Speciation of Metal(Loid)s in Environmental Samples by X-Ray Absorption Spectroscopy: A Critical Review. *Anal. Chim. Acta* **2014**, *822*, 1–22. https://doi.org/10.1016/j.aca.2014.02.044.

(59) Nehzati, S.; Dolgova, N. V.; Young, C. G.; James, A. K.; Cotelesage, J. J. H.; Sokaras, D.; Kroll, T.; Qureshi, M.; Pickering, I. J.; George, G. N. Mercury Lα1 High Energy Resolution Fluorescence Detected X-ray Absorption Spectroscopy: A Versatile Speciation Probe for Mercury. *Inorg. Chem.* **2022**, *61* (13), 5201–5214. https://doi.org/10.1021/acs.inorgchem.1c03196.

(60) Isaure, M.-P.; Albertelli, M.; Kieffer, I.; Tucoulou, R.; Petrel, M.; Gontier, E.; Tessier, E.; Monperrus, M.; Goñi-Urriza, M. Relationship Between Hg Speciation and Hg Methylation/Demethylation Processes in the Sulfate-Reducing Bacterium Pseudodesulfovibrio Hydrargyri: Evidences From HERFD-XANES and Nano-XRF. *Front. Microbiol.* **2020**, *11*, 584715. https://doi.org/10.3389/fmicb.2020.584715.

(61) Manceau, A.; Lemouchi, C.; Rovezzi, M.; Lanson, M.; Glatzel, P.; Nagy, K. L.; Gautier-Luneau, I.; Joly, Y.; Enescu, M. Structure, Bonding, and Stability of Mercury Complexes with Thiolate and Thioether Ligands from High-Resolution XANES Spectroscopy and First-Principles Calculations. *Inorg. Chem.* **2015**, *54* (24), 11776–11791. https://doi.org/10.1021/acs.inorgchem.5b01932.

(62) Du, H.; Yin, X.; Gu, X.; Wang, D.; Pierce, E. M.; Gu, B. Dissolved Elemental Mercury [Hg(0)Aq] Reactions and Purgeability in the Presence of Organic and Inorganic Particulates. *Environ. Sci. Technol. Lett.* **2023**, *10* (8), 691–697. https://doi.org/10.1021/acs.estlett.3c00275.

(63) Manceau, A.; Enescu, M.; Simionovici, A.; Lanson, M.; Gonzalez-Rey, M.; Rovezzi, M.; Tucoulou, R.; Glatzel, P.; Nagy, K. L.; Bourdineaud, J.-P. Chemical Forms of Mercury in Human Hair Reveal Sources of Exposure. *Environ. Sci. Technol.* **2016**, *50* (19), 10721–10729. https://doi.org/10.1021/acs.est.6b03468.

Appendix A: Supporting Information for Characterization of Manganese Oxide Modified Activated Carbon for Remediation of Redox-Sensitive Contaminants

Contents

Text A1. Chemical analysis methods

Aqueous Mn was measured by inductively coupled plasma – optical emission spectrometry (ICP-OES; Perkin-Elmer Optima 5300DV).[1] Calibration check standards (0.1, 0.5, 1.0, 2.5, and 5.0 mg/L) and blanks (ultrapure water; 18.2 MΩ cm, Millipore-Sigma Milli-Q) were prepared and analyzed with a relative standard deviation of <5%. Five mL aliquots were removed from batch samples and filtered with a 0.45 μm PES filter, preserved with 12 M trace metal grade HCl (4% (v/v)), and stored for analysis.

The remaining supernatant solutions from batch samples were transferred to Hg-free glass vials, oxidized with bromine chloride overnight (1% (v/v)), and analyzed for total Hg on a MERX-T Hg system (Brooks Rand Labs, Seattle, WA, USA) using cold vapor atomic fluorescence spectroscopy (CVAFS). Instrument calibration was performed using an 8-point calibration from 0 to 1000 pg using mercury chloride standards with accepted recoveries between 75-125%. A pre-reduction step with 100 μL of hydroxylamine hydrochloride was performed to reduce halogens that cause trap degradation. Subsequently, 100 μL of stannous chloride was added to reduce Hg(II) to Hg(0) and analyzed using CVAFS. Method blanks using ultrapure water were prepared in parallel to samples. An ongoing precision and recovery sample containing 200 pg Hg was included in the run and deemed acceptable within 77-123%.[2]

Text A2. Electron microscopy

Scanning and scanning transmission electron microscopic (SEM and STEM) imaging coupled with energy-dispersive X-ray spectroscopy (EDX) was used to assess Mn presence and surface coverage on AC particles in MOMAC solids. Approximately 1 mg of solid sample was mixed with 10 mL ethanol and placed in an ultrasonic bath to disaggregate particles. For SEM, approximately 100 µL of this solution was drop cast onto carbon tape adhered onto an aluminum stub and imaged using an FEI Quanta 200 SEM. For STEM, 3-5 µL of solution was drop cast onto a copper grid with a holey carbon support film and imaged with a Talos F200C G2 TEM. The EDX detector for STEM was cooled with liquid nitrogen.

Text A3. Surface area and pore size analysis

Nitrogen gas (N_2) adsorption-desorption isotherms were collected on MnOx, AC, and MOMAC samples to evaluate changes in the surface area (BET method) and pore size distribution (BJH method).[3] Approximately 0.2-0.5 g of solid was weighed on a semi-micro analytical balance (readability 0.01 mg) and added into a sample tube (1.27 cm OD). The solid was degassed with N_2 overnight (> 16 hours) prior to data collection. Isotherms were collected on a Micromeritics® TriStar II at 77.4 K and data were analyzed using Micromeritics software V3.03.

Text A4: Expanded methods for collection and analysis of XAS

The MnOx and MOMAC samples were diluted 1:10 or 1:1 by mass with sucrose. Samples were homogenized in an agate mortar and pestle, mounted in Al holders, and sealed with sulfur-free tape. Samples were held in a liquid N_2 cryostat and analyzed in fluorescence using a 30-element Ge detector. Energy was calibrated using a Mn foil standard with the inflection point of the initial edge rise set to 6539 eV. In linear combination fits of unknown spectra with reference spectra (Fig. A1), negative components were rejected, components were not forced to sum to 1 for all fits, and goodness of fit was evaluated using reduced chi-square values. Components constituting less than 5% of the fit were rejected. The accuracy of linear combination fits to determine average valence state of Mn oxides is estimated to be within 0.04 valence units.[4] However, lower accuracies can be associated with birnessites (0.05 – 0.08 valence units), and particularly Mn oxides with greater than ~15% Mn(II) due to a larger variability in the shape of Mn^{2+} spectra.[4]

A reference standard of Mn(II) sorbed onto activated carbon was prepared where 0.9 g of AC was reacted for 24 h with 30 mL of 10 mM MnCl2·4H2O at circumneutral pH (6-7). While the pre-edge feature and initial edge rise in the Mn(II)AC spectrum are consistent with Mn(II), comparison against hydrated Mn(II) reference standards (i.e. aqueous Mn^{2+}) showed some changes in the coordination of Mn(II) when sorbed to AC.

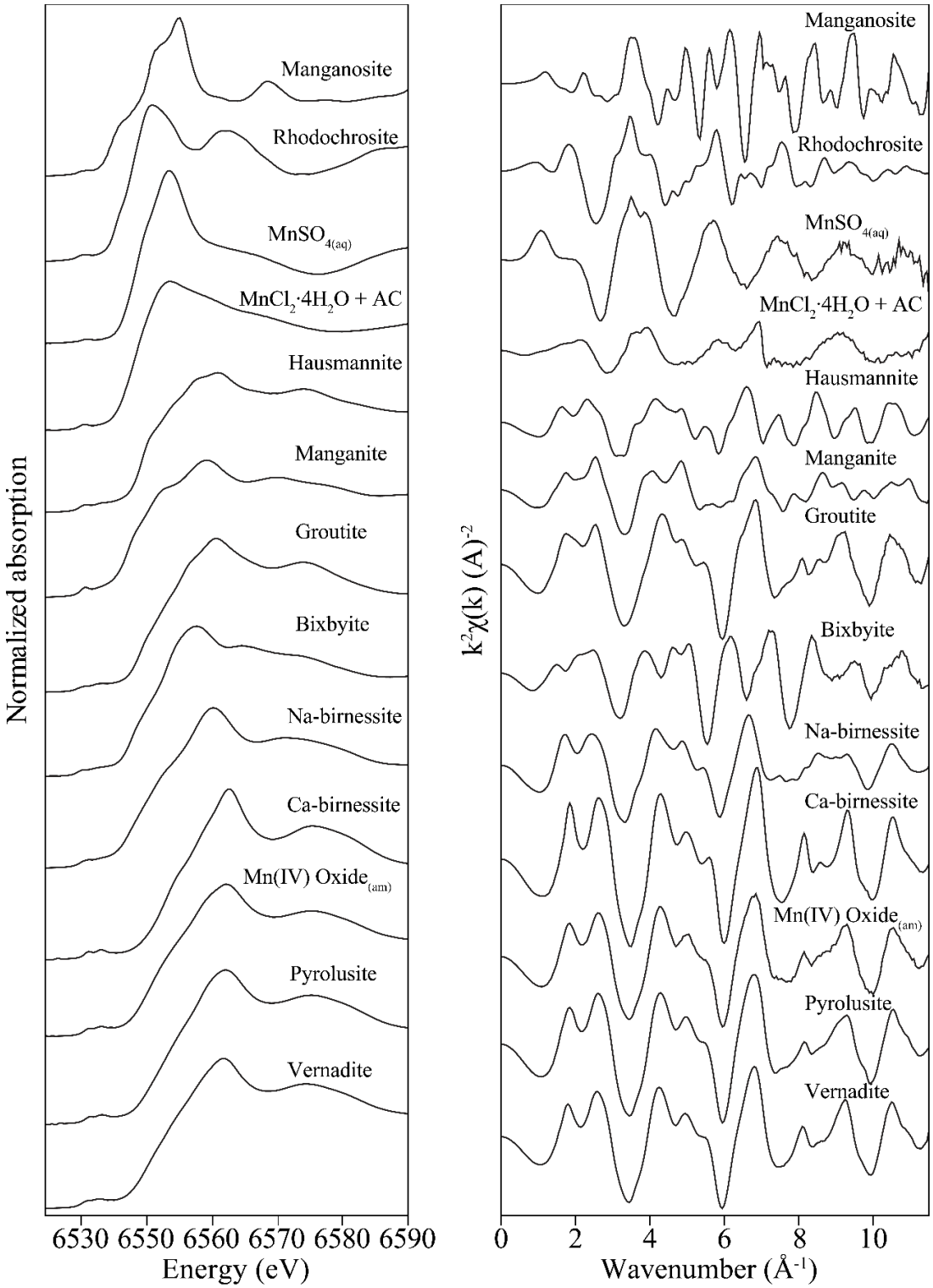

Figure A1. XANES and EXAFS reference spectra used for linear combination fits of MnOx and MOMAC amendments. Chemical formulas for reference compounds are found in Table A1.

Table A1. Manganese reference compound spectra used in XANES and EXAFS linear combination fits.

Sample	Description	Origin[a]	Collection Method	Temp[b]	Reference[c]
Pyrolusite	β-$Mn^{IV}O_2$	Syn	Transmission	LN	1
$Mn^{IV}O_2$	Amorphous $Mn^{IV}O_2$	Com	Fluorescence	LN	2
Vernadite	δ-$Mn^{IV}O_2$	Syn	Fluorescence	RT	3
Na-birnessite	$Na_{0.26}(Mn^{IV}_{0.27}Mn^{III}_{0.26})O_2$	Syn	Fluorescence	LN	3
Ca-birnessite	$Ca_{0.12}Mn^{IV}O_{1.81}\cdot 0.72H_2O$	Syn	Fluorescence	LN	4
Bixbyite	$Mn^{III}_2O_3$	Nat	Fluorescence	RT	5
Manganite	γ-$Mn^{III}OOH$	Nat	Transmission	RT	6
Groutite	α-$Mn^{III}OOH$	Nat	Fluorescence	RT	7
Hausmannite	$(Mn^{II}, Mn^{III}_2)O_4$	Syn	Transmission	RT	8
Rhodochrosite	$Mn^{II}CO_3$	Nat	Transmission	RT	9
$Mn^{2+}_{(aq)}$	10 mM $Mn^{II}SO_{4(aq)}$	Syn	Fluorescence	RT	10
$Mn^{2+}_{(sorbed)}$	10 mM $Mn^{II}Cl_2\cdot 4H_2O$ + activated carbon	Syn	Fluorescence	LN	This study
Manganosite	$Mn^{II}O$	Com	Fluorescence	LN	This study

[a] Syn: synthetic; Nat: natural; Com: commercial

[b] RT: room temperature; LN: sample holder placed in liquid nitrogen cryostat

[c] (1) Birkner & Navrotsky 2012[5]; (2) Seelos et al. 2021[6]; (3) Villalobos et al. 2003[7]; (4) Birkner & Navrotsky 2017[8]; (5) Ironton, MT, USA, collection of L. Garvie; (6) Navajo County, AZ, USA, collection of L. Garvie; (7) Thomas Mountain, UT, USA, collection of L. Garvie; (8) Bargar et al. 2005[9]; (9) Catamarca Province, Argentina, Ward's Scientific; (10) Villinski et al. 2001[10]

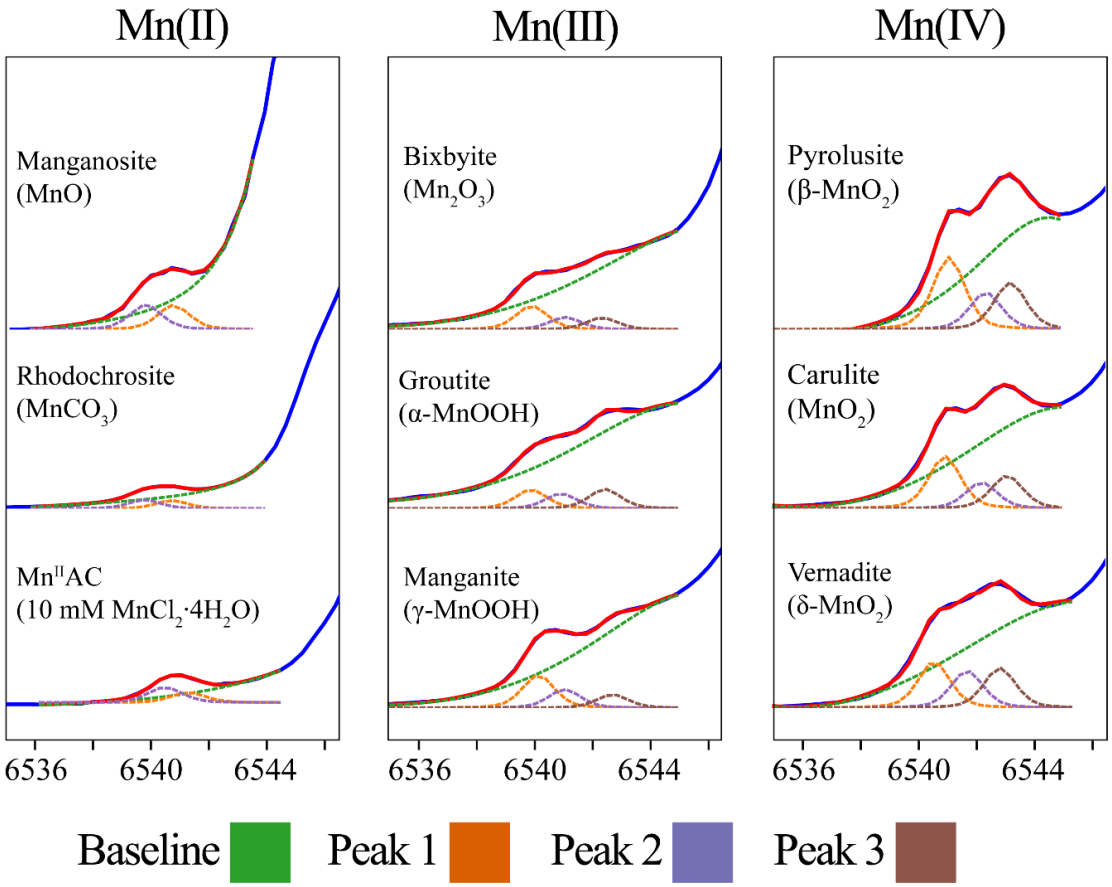

Figure A2. Pre-edge peak fits of Mn(II), Mn(III), and Mn(IV) with two or three peaks (L/G = 0.45; FWHM = 1.3). Parameters collected from these standards are shown in Table A2 along with fits to secondary standards and unknown compounds.

Table A2. XAS pre-edge fitting parameters for Mn reference materials (see Text A5 for fitting approach).

Sample	Energy (eV)[a]	Integrated Area	Fit Centroid (eV)	Total Integrated Area	Estimated AOS
$Mn^{II}O$ (Manganosite)	6539.8	0.07	6540.3	0.14	2.00
	6540.8	0.07			
$Mn^{II}CO_3$ (Rhodochrosite)	6539.8	0.03	6540.2	0.05	2.00
	6540.7	0.02			
$Mn^{II}AC$ (10 mM Mn(II) + activated carbon)	6540.0	0.03	6540.4	0.06	2.00
	6541.0	0.03			
$(Mn^{II},Mn_2^{III})O_4$ (Hausmannite)	6540.2	0.05	6540.7	0.11	2.60
	6540.8	0.06			
	6542.3	0.02			
γ-$Mn^{III}OOH$ (Manganite)	6540.2	0.10	6541.0	0.20	3.00
	6541.1	0.06			
	6542.7	0.04			
α-MnOOH Groutite	6539.9	0.06	6541.2	0.16	3.00
	6541.0	0.04			
	6542.5	0.06			
$Mn_2^{III}O_3$ (Natural Bixbyite)	6540.0	0.07	6540.9	0.14	3.00
	6541.1	0.04			
	6542.4	0.03			
$Mn_2^{III}O_3$ (Synthetic Bixbyite)	6540.2	0.07	6540.9	0.17	3.00
	6540.9	0.06			
	6542.4	0.04			
Na-Birnessite	6540.4	0.05	6541.5	0.27	3.52
	6541.6	0.12			
	6543.0	0.10			
β-$Mn^{IV}O_2$ (Pyrolusite)	6541.1	0.21	6542.0	0.45	4.00
	6542.4	0.11			
	6543.2	0.13			
δ-$Mn^{IV}O_2$ (Vernadite)	6540.6	0.14	6541.7	0.37	4.00
	6541.7	0.11			
	6542.9	0.12			
Amorphous $Mn^{IV}O_2$	6541.0	0.16	6541.9	0.34	4.00
	6542.2	0.08			
	6543.1	0.10			
Averages[b]	**Oxidation State**	**P1**	**P2**	**P3**	
	Mn(II)	**6539.9**	**6540.8**		
	Mn(III)	**6540.1**	**6541.0**	**6542.5**	
	Mn(IV)	**6540.9**	**6542.1**	**6543.1**	

[a] Each reference sample was fit with 2-3 pseudo-Voigt peaks (FWHM = 1.3 eV; G/L: 0.45)
[b] Fit centroids were calculated from the average position of peaks defined by pseudo-Voigt functions, weighted by their respective integrated areas after baseline subtraction.[11]
[c] The first (P1), second (P2), and third (P3) peak positions from fits of each oxidation state were averaged to fit samples with known (Fig. A3) and unknown (Fig. 1.5) oxidation states.

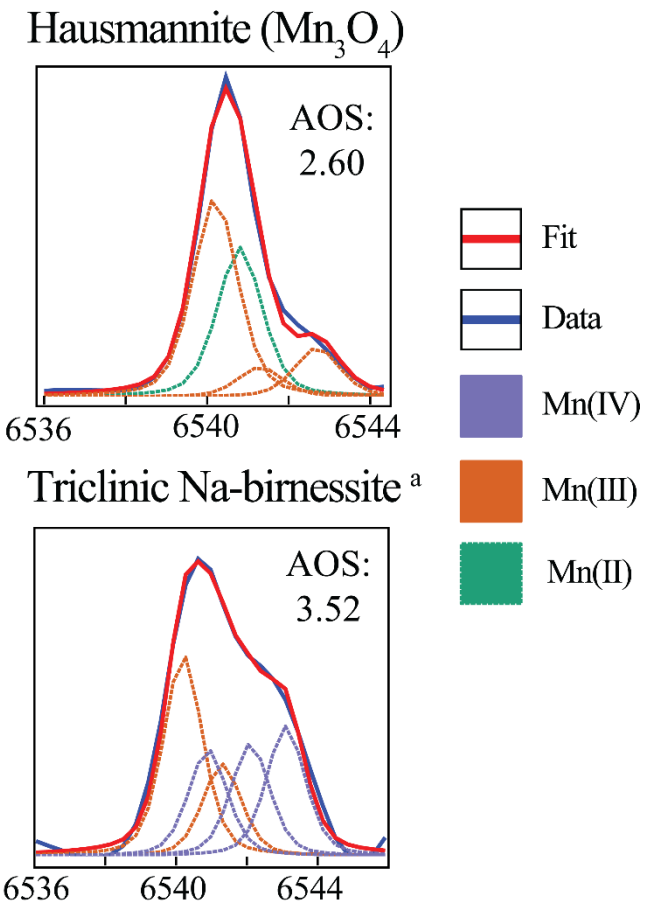

Figure A3. Fits of the pre-edge region of X-ray absorption spectra for a natural hausmannite sample (Bargar et al, 2005)[9] and triclinic Na-birnessite (Villalobos et al. 2003)[7]. The average oxidation state (AOS) was estimated from peak fits. Ideal AOS for hausmannite is 2.66 and AOS for Na-birnessite was reported as 3.57 (Villalobos et al. 2003).[7]

Text A5: Expanded methods for collection and analysis of XPS

The Mn2p region (632 – 660 eV), specifically the $Mn2p_{3/2}$ peak, generally exhibits the highest intensity in Mn XPS.[12] Among Mn species with the same oxidation state, however, the bonding environment has a greater influence on the $Mn2p_{3/2}$ peak shape than on the Mn3p peak, leading to inconsistencies or systematically lower estimates when used to determine oxidation state.[13–15] Conversely, the Mn3p region (40 – 60 eV) is less sensitive to bonding environment and has been shown to exhibit consistent peak shapes and parameters across Mn species with the same oxidation state, and therefore was chosen in this study to estimate Mn oxidation states of MnOx and MOMAC. To minimize error associated with charge correction[16], charge deviations greater than ±0.5 eV from the adventitious carbon peak were discarded and recollected at a different point that exhibited less charging.

The Mn 3p region was fit with a non-linear least squares curve fitting technique described in Ilton et al. 2016.[13] Reference compounds that corresponded to Mn(II), (III), or (IV) oxide were scanned as described in Section 2.3.2 (main text) and analyzed with the Thermo Avantage software. An iterative Shirley background subtraction was employed to account for differences in intensity across the spectrum.[17–19] First, the Mn(II)O, $Mn(III)_2O_3$, and MnO_2 samples were fit with approximately 3-4 pseudo-Voigt (G/L = 30) peaks to define curves for each oxidation state (Fig. A4; Table A3). Without changing the fit parameters, these curves were compared against a secondary set of Mn reference standards that included: $Mn(II)CO_3$ (rhodochrosite), $CaMn(III)_2O_4$ (marokite), and an amorphous commercial Mn(IV) oxide (Carulite 400®) with an EXAFS spectrum that matched the local structure of synthetic vernadite (Fig. A1).[6] Fits to Mn(III) Mn3p curves for both sets of standards were similar (Fig. A5).[13]There were slight differences in fit parameters between the Mn(II) standards, Mn(II)O and $Mn(II)CO_3$, and the Mn(IV) standards, pyrolusite and amorphous Mn(IV) oxide. Similar differences were observed by Ilton et al. 2016.[13] The fit to amorphous Mn(IV) oxide was improved by including additional fit parameters for Mn(III), which yielded a small (5%) fraction of Mn(III) in the solid. Assuming the solid was entirely Mn(IV), this fraction may be interpreted as uncertainty in AOS estimated with these fits. These parameters were used to empirically fit MnOx and MOMAC spectra and estimate relative fractions of Mn(II), (III), and (IV) oxidation states. In fitting unknown spectra, the FWHM and binding energy (BE) values were initially fixed to those shown on Table 3. Then for each oxidation state the peaks from fits to the reference spectra were merged into a curve. Subsequently, each curve was allowed to shift BE and FWHM as linked parameters rather than separate independent variables. Goodness-of-fit was assessed with normalized chi-square and Abbe criterion tests.

The O1s peak was fit qualitatively to binding energies of oxide species associated with Mn oxides (lattice oxide, hydroxyl, sorbed H_2O) for MnOx and MOMAC samples (Fig. A6).[12] After employing a Shirley background subtraction, the O1s peak was compared with three pseudo-voigt peaks where the FWHM and BE was not constrained between samples. However, the FWHM of the hydroxyl and sorbed water peaks were forced to be equal during each fit. Although unconstrained during the fits, the BE for the first two fitted peaks were within ±0.1 eV between all samples and varied only slightly in the final peak. Interestingly, the second peak, which was attributed to hydroxide, was larger in the

MOMAC samples. This excess hydroxide may further indicate a higher fraction of MnOOH in the MOMAC samples compared to synthetic MnOx.

The C1s region of unaltered activated carbon and MOMAC samples was fit qualitatively with binding energies of 3 peaks associated with C-C bonds, 3 oxygenated carbon peaks, and a $\pi \rightarrow \pi^*$ transition peak following parameters reported in Smith et al. 2016[20] (Fig. A12; Table A8). The BE of the C-$C_{primary}$ peak was constrained from 284.2 – 284.8 eV and assigned to aromatic C-C/C-H bonds. The C-C_{high} and C-C_{low} peaks were assigned to defective carbon structures at a slightly higher (285.0 – 285.4) or lower (283.4 – 284.0 eV) BE compared to the primary peak. The FWHM for each C-C peak was allowed to range from 0.9 – 2.0 eV but forced to be equal during the fit. The G/L ratio was constrained between 0 and 0.3 but also forced to be equal for each C-C peak. An additional satellite peak constrained to binding energies of 291.0 – 293.0 eV and FWHM of 2 – 3 eV was assigned to $\pi \rightarrow \pi^*$ transitions for the primary C-C peak. Satellite features can occur in XPS when an outgoing core electron excites a valence electron and consequentially loses kinetic energy, resulting in satellite structures several eV lower than the core level position.[21,22] Three peaks with BE constrained to 285.9 – 286.6, 286.7 – 287.5, and 288.3 – 288.9 eV were used to estimate fractions of carbon associated with a single oxygen bond (e.g. hydroxyl: C-OH), two oxygen bonds (e.g. carbonyl: C=O), or three oxygen bonds (e.g. carboxyl: COOH), respectively.[20] The FWHM was constrained from 1.8 – 2.2 eV during the fit but forced to be equal for each oxygenated carbon peak. The G/L ratio was constrained between 0 and 0.1 for each oxygenated carbon peak but forced to be equal during the fit. There were no significant differences between unmodified AC and MOMAC using C1s XPS. Notably, the C-C_{low} fraction, which is absent in unmodified AC, increases slightly with increasing Mn concentration. which may be a result of high-valent Mn(IV), or Mn(VII) used during synthesis, reacting with the AC surface (Fig. A12; Table A8).

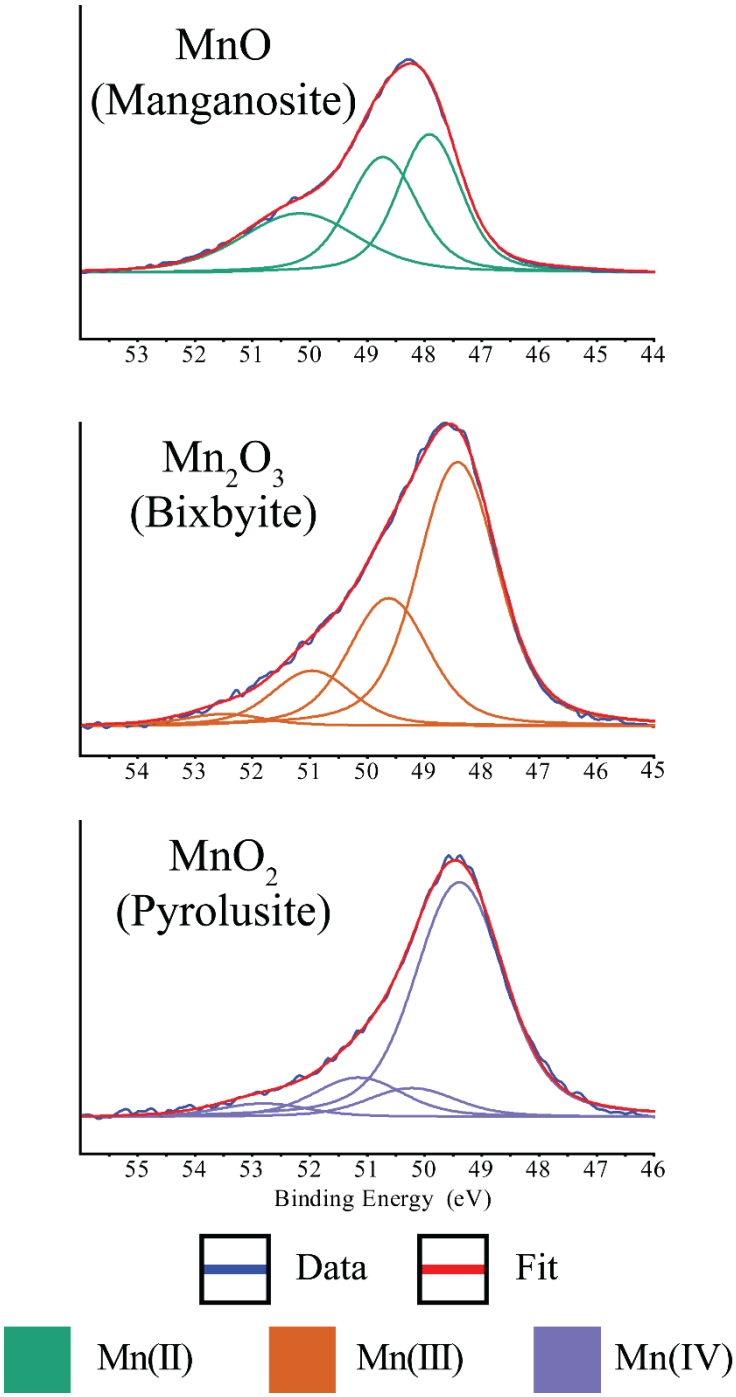

Figure A4. Reference standards for Mn(II), (III), and (IV) oxidation states used in XPS empirical fits for the quantification of Mn oxidation states in synthetic MnOx and MOMAC samples. Values for peak parameters are reported in Table A4.

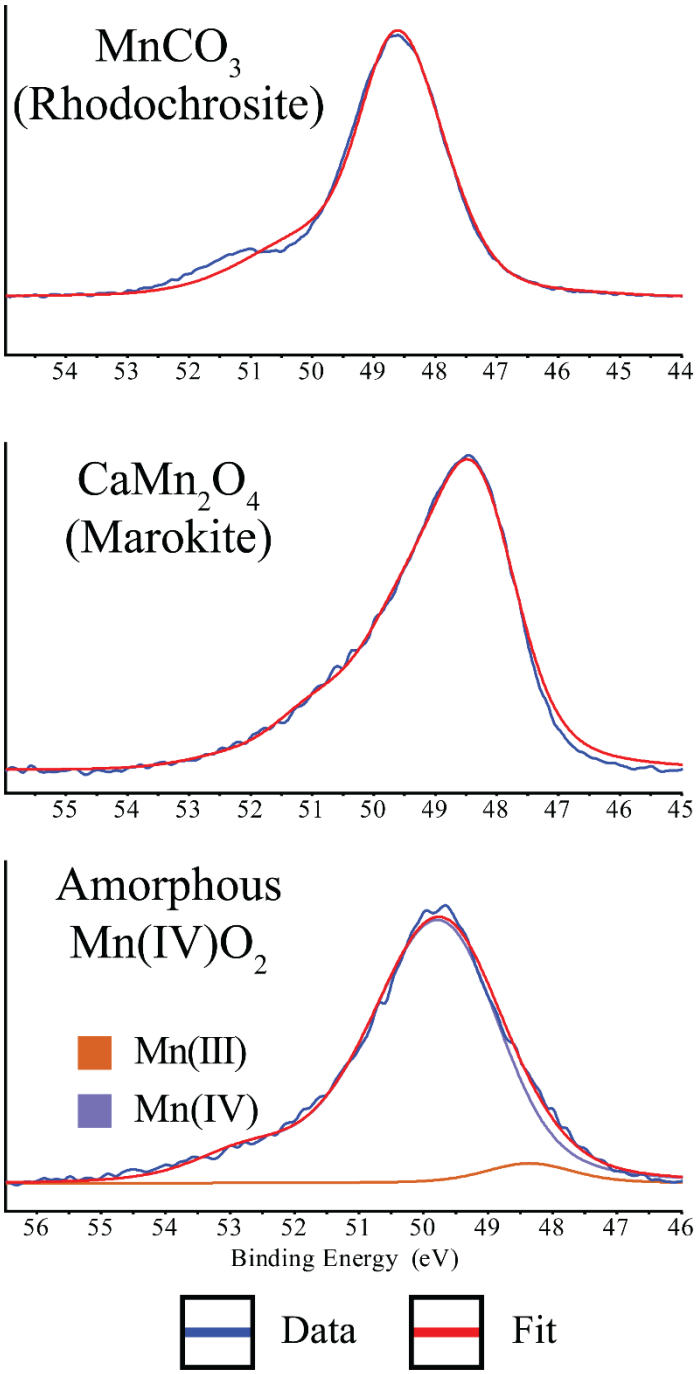

Figure A5. Test set of Mn(II), (III), and (IV) oxidation state secondary reference standards fit with the parameters from the reference set (Table A3) to evaluate consistency of curve shapes for different Mn species with the same oxidation state. A commercial amorphous Mn(IV) oxide (Carulite 400) was fit with the parameters for pyrolusite and a small fraction (5%) of Mn(III), which may be used to estimate uncertainty in the fitting procedure.

Table A3. XPS Mn 3p peak parameters from Mn reference compounds.

Sample	Peak 1	Peak 2	Peak 3	Peak 4
MnO (Manganosite)				
BE (eV)	47.9	48.7	50.2	
FWHM (eV)	1.31	1.42	2.39	
L/G	30	30	30	
Mn_2O_3 (Bixbyite)				
BE (eV)	48.4	49.6	51.0	52.5
FWHM (eV)	1.64	1.64	1.64	1.64
L/G	30	30	30	30
MnO_2 (Pyrolusite)				
BE (eV)	49.4	50.2	51.2	52.8
FWHM (eV)	1.83	1.83	1.83	1.83
L/G	30	30	30	30

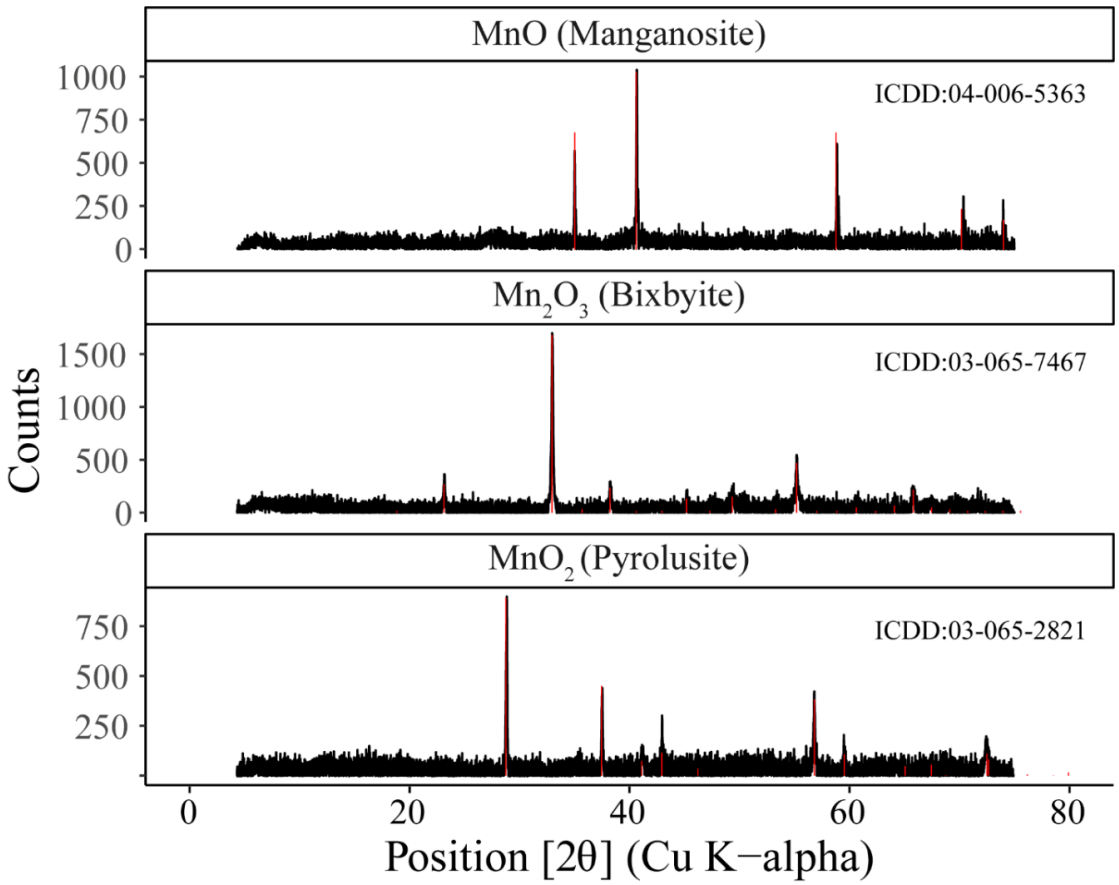

Figure A6. X-ray diffraction patterns of Mn(II), (III), and (IV) oxide reference compounds. Red lines show major reflections associated with each mineral from the PDF 4+ database.

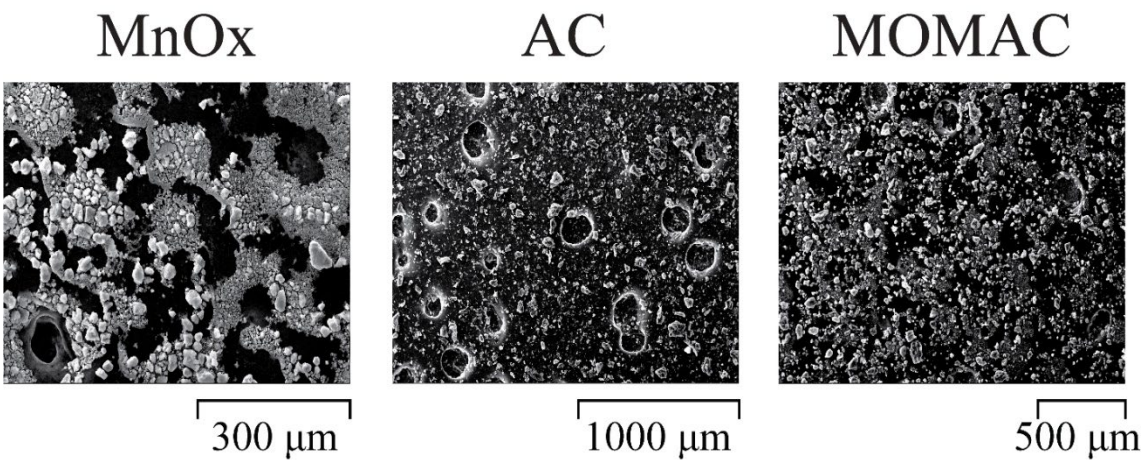

Figure A7. Low resolution SEM images of MnOx, AC, and MOMAC powder dispersed onto carbon tape. Particle sizes range widely (< 1 um to ~50 um) but are generally smaller for homogeneously precipitated MnOx than for AC. MOMAC has a mixture of large AC particles with surface Mn, MnOx not associated with AC grains, and grains of AC.

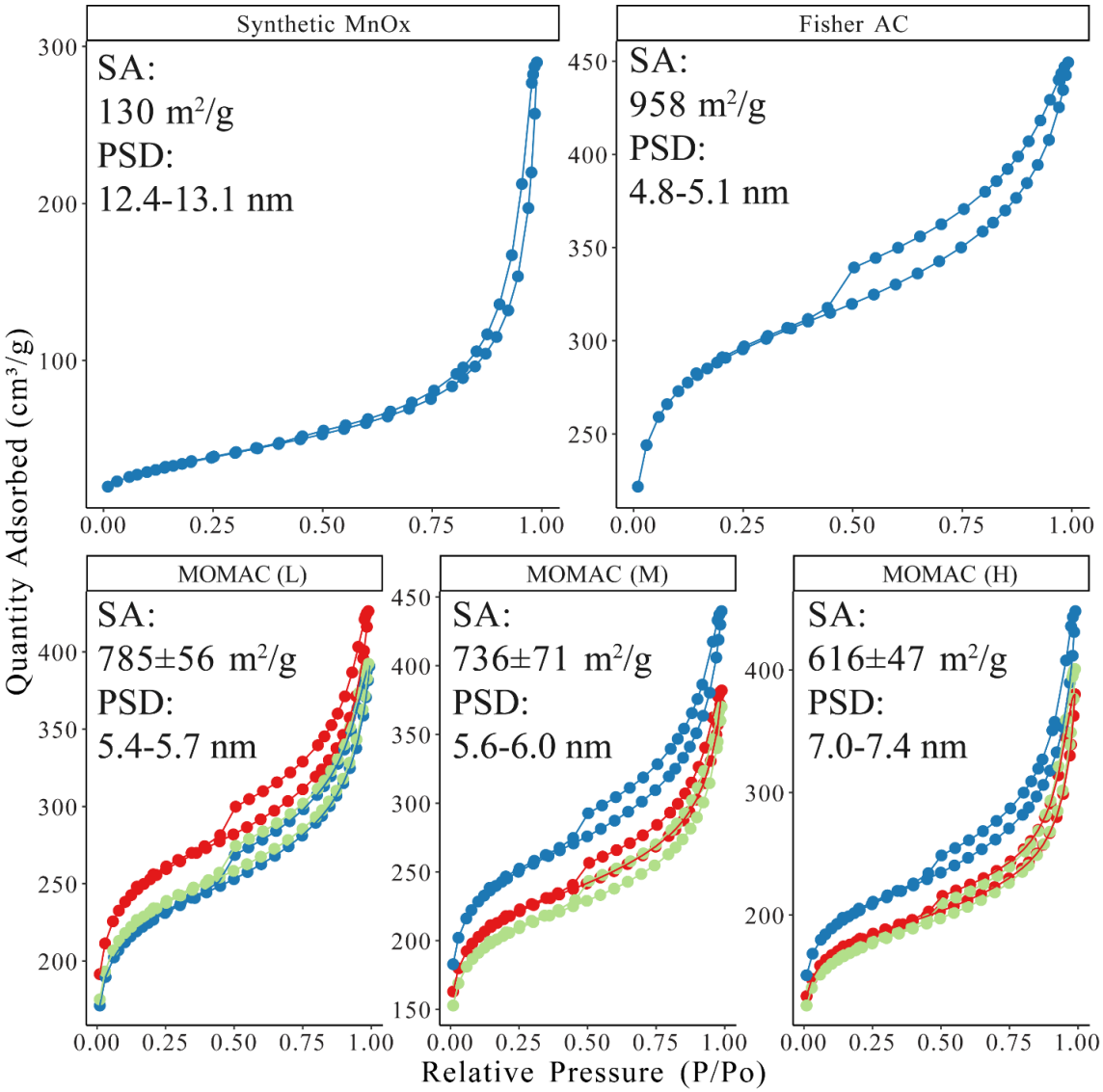

Figure A8. Nitrogen adsorption and desorption isotherms collected for AC, MnOx, and MOMAC samples to determine differences in surface area (BET method) and pore size distribution (BJH method). Samples for MOMAC were run in triplicate (runs shown by red, green, and blue lines). Surface area (SA) obtained from BET analysis of the data show decreasing surface area with increasing Mn concentration for low (L), medium (M), and high (H) MOMAC samples. Pore size distributions (PSD) showed the opposite trend and increased with increasing Mn concentrations in MOMAC samples.

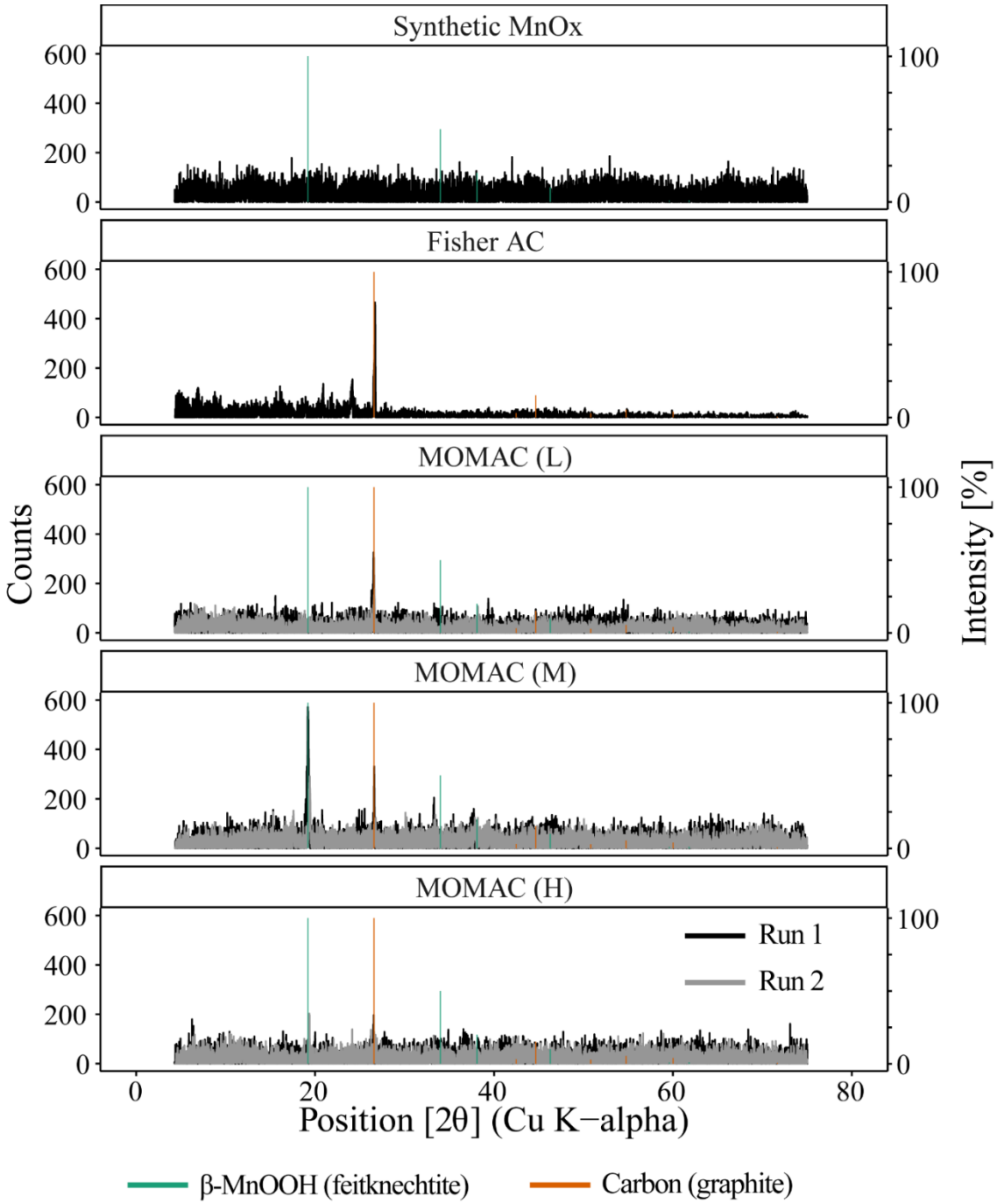

Figure A9. X-ray diffraction patterns for activated carbon, homogeneously precipitated MnOx, and MOMAC samples. A reflection is present in the MOMAC (M) sample that matched a dominant reflection for feitknechtite, shown by the green lines.

Table A4. Summary results and statistics from XANES and EXAFS linear combination fits to MnOx and MOMAC samples using Mn reference spectra.

Region	Sample[a]	Vernadite (δ-$Mn^{IV}O2$)[b]	Manganite (γ-$Mn^{III}OOH$)[b]	Mn(II)/AC (sorbed) (10 mM $MnCl_2 \cdot 4H_2O$ + activated carbon)[b]	Sum	R-factor[c]	Reduced $\chi 2$[d]
XANES	Synthetic MnOx	98 (2) **100**	0	0	98	0.0017	0.0004
	MOMAC (L)	57 (3) **57**	32 (5) **32**	11 (2) **11**	100	0.0012	0.0003
	MOMAC (M)	42 (3) **43**	45 (5) **46**	11 (2) **11**	98	0.0016	0.0003
	MOMAC (H)	49 (5) **49**	35 (7) **35**	15 (3) **16**	99	0.0030	0.0006
EXAFS	Synthetic MnOx	100 (0) **100**	0	0	100	0.0170	0.0100
	MOMAC (L)	63 (1) **62**	17 (3) **17**	22 (3) **21**	102	0.0220	0.0067
	MOMAC (M)	50 (2) **51**	29 (3) **30**	19 (3) **19**	98	0.0360	0.0090
	MOMAC (H)	55 (1) **65**	18 (2) **21**	13 (2) **15**	85	0.0210	0.0049

[a] See Table A1 for the complete Mn reference compound library used in fits.
[b] Uncertainty in fits reported in parentheses; bold values are fit percentages normalized to 100%.
[c] R-factor = $\sum$(data-fit)2 /$\sum$(data)2 normalized sum of squared residuals of the fit.
[d] Reduced $\chi 2$ = (F-factor) / (# of points - # of variables)

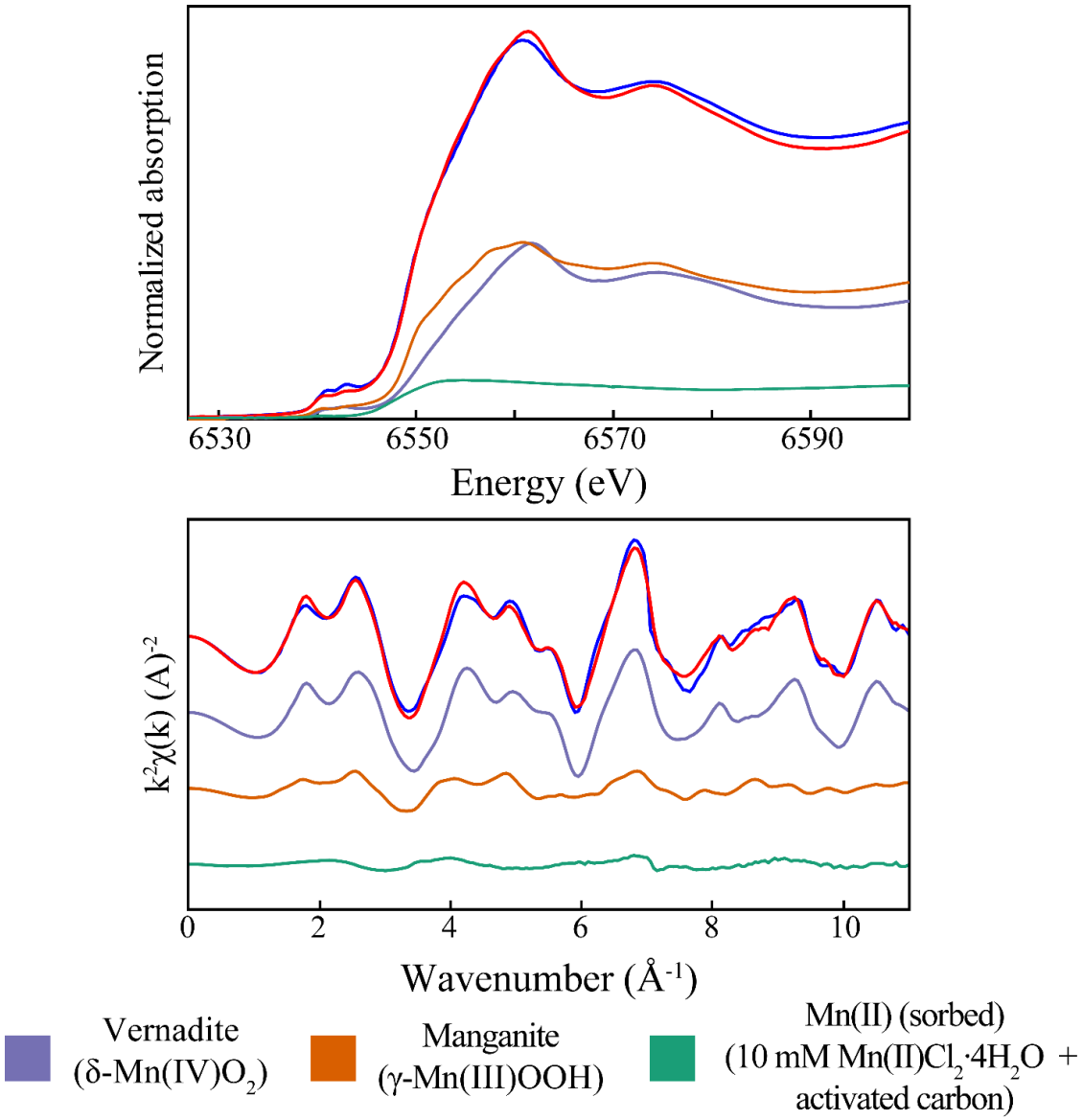

Figure A10. Mn K-edge X-ray absorption spectra divided into **(a)** XANES (6530-6590 eV) and **(b)** EXAFS (k-range of 2-10 $Å^{-1}$) showing a representative deconvolution of the linear combination fits to MOMAC using a library of Mn reference compounds shown in Fig. A1.

Table A5. Average oxidation states estimated from spectroscopic analyses of MnOx and MOMAC samples.

Method	Sample	Average Oxidation State
XANES	Synthetic MnOx	4.00
	MOMAC (L)	3.46
	MOMAC (M)	3.32
	MOMAC (H)	3.34
EXAFS	Synthetic MnOx	4.00
	MOMAC (L)	3.41
	MOMAC (M)	3.32
	MOMAC (H)	3.50
Pre-edge	Synthetic MnOx	4.00
	MOMAC (L)	3.23
	MOMAC (M)	3.34
	MOMAC (H)	3.24
XPS	Synthetic MnOx	3.65
	MOMAC (L)	3.37
	MOMAC (M)	3.36
	MOMAC (H)	3.43

Table A6. Summary results and statistics from Mn3p XPS non-linear least squares combination fits of MnOx and MOMAC samples to estimate relative fractions of Mn oxidation states.

Method	Sample	Mn(II)	Mn(III)	Mn(IV)	Normalized $\chi 2$[a]	Abbe Criterion[b]
XPS Fits	Synthetic MnOx	10	15	75	1.8	0.46
	MOMAC (L)	23	17	60	1.2	0.83
	MOMAC (M)	22	20	58	1.3	0.71
	MOMAC (H)	20	17	63	1.5	0.65

[a] Reduced $\chi 2$ = (F-factor) / (# of points - # of variables)

[b] Abbe $= \frac{1}{2}\sum_{i=1}^{N-1}\frac{[R(i+1)-R(i)]^2}{\sum_{i=1}^{N}[R(i)]^2}$; R(i)= residuals of the fit at the i^{th} data point

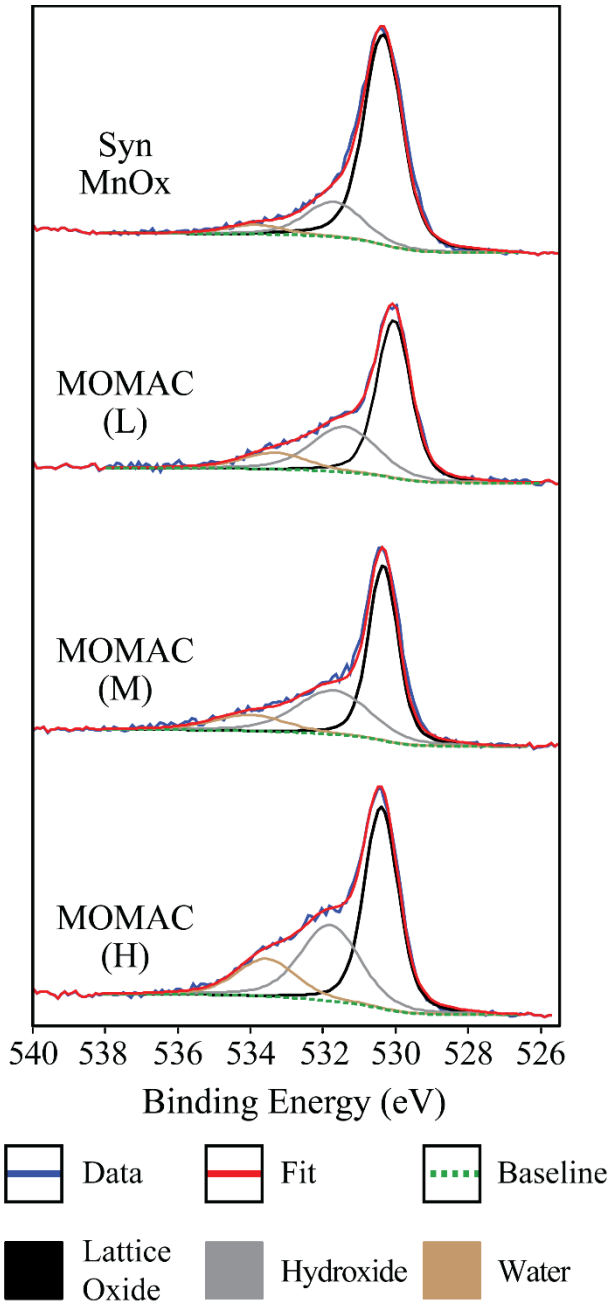

Figure A11. O1s XPS fits for synthetic MnOx and MOMAC samples showing a larger fraction of hydroxide among the MOMAC samples than for MnOx. Fit results reported in Table A7.

Table A7. Results of O1s peak fits for synthetic MnOx and MOMAC samples showing relative fractions of lattice oxygen, hydroxyl groups, and sorbed water.[1]

Sample	Lattice Oxide	Hydroxl Groups	Sorbed Water
Synthetic MnOx	77	18	5
BE (eV)	530.0	531.4	533.6
FWHM (eV)	1.36	1.90	1.90
L/G	30	30	30
MOMAC (L)	57	32	11
BE (eV)	530.1	531.4	533.3
FWHM (eV)	1.10	2.12	2.12
L/G	30	30	30
MOMAC (M)	56	32	12
BE (eV)	530.0	531.5	533.8
FWHM (eV)	1.08	2.45	2.45
L/G	30	30	30
MOMAC (H)	51	33	16
BE (eV)	530.0	531.5	533.3
FWHM (eV)	1.16	2.01	2.01
L/G	30	30	30

[1] Values modeled from pseudo-voigt peak fits (L/G:30) in Biesinger et al. 2011[12] where the FWHM and BE of the peaks was allowed to vary between samples. However, the FWHM of the hydroxyl and sorbed water peaks were forced to be equal during the fit.

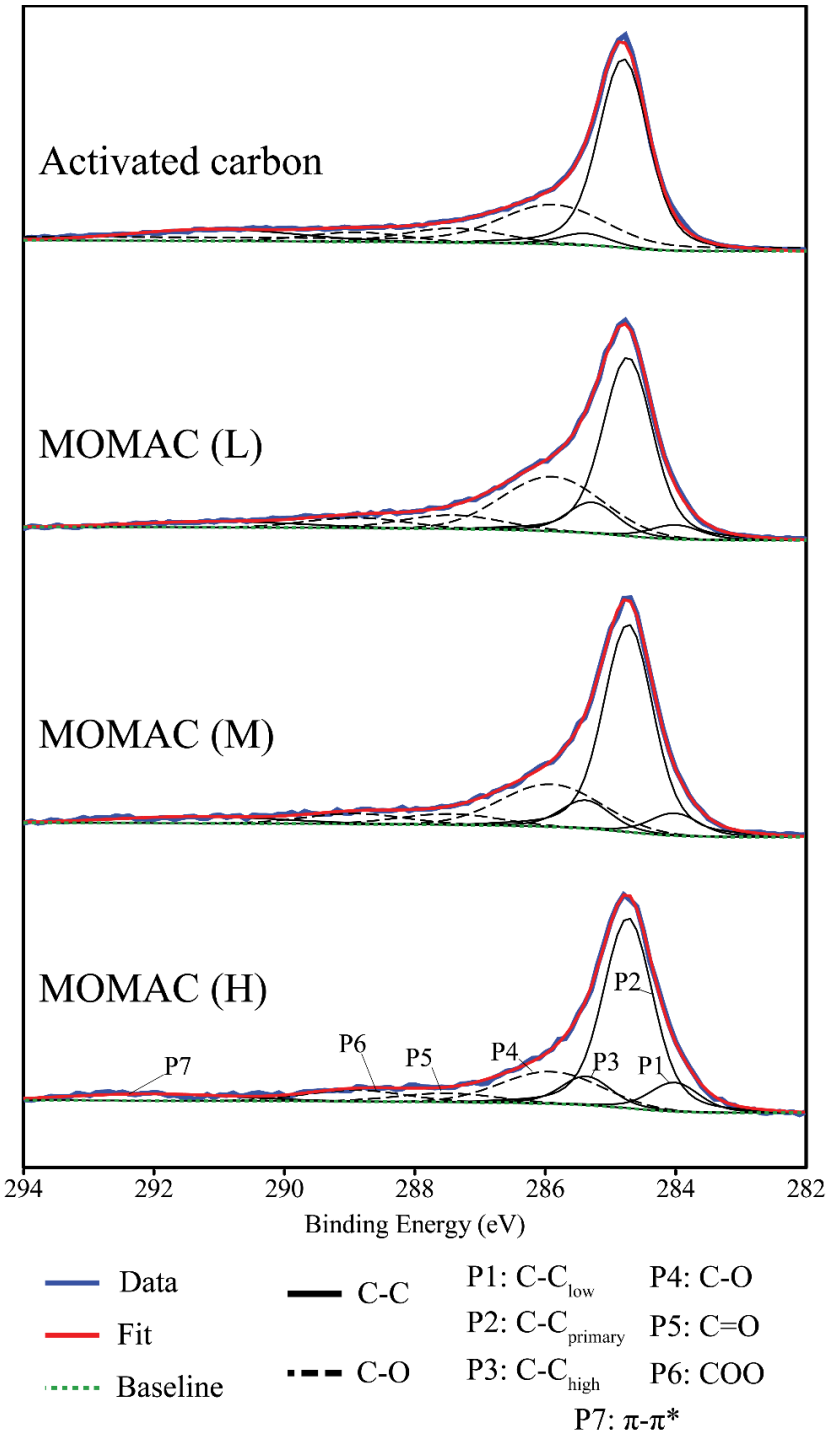

Figure A12. C1s XPS fits to unaltered AC and MOMAC samples where P2 represents the primary aromatic C-C/C-H bonds, P1 and P3 are considered C-C defect peaks, and P7 represents π-π* transitions for the primary C-C peak. Three peaks are used to estimate fractions of oxygenated peaks where carbon is bonded to either a single oxygen bond (e.g. hydroxyl: C-OH) (P4), two oxygen bonds (e.g. carbonyl: C=O) (P5), or three oxygen bonds (e.g. carboxyl: COOH) (P6).[20]

Table A8. Results of C1s peak fits for unaltered activated carbon and MOMAC samples showing deconvolutions with C-C and C-O peaks.[1]

Sample	$C\text{-}C_{low}$	$C\text{-}C_{primary}$	$C\text{-}C_{high}$	C-O	C=O	COO	π-π*
Activated carbon	0	54	3	19	7	5	10
BE (eV)	284.0	284.8	285.4	285.9	287.4	288.9	291.1
FWHM (eV)	0.90	0.90	0.90	1.80	1.80	1.80	3.00
L/G	30	30	30	0	0	0	0
MOMAC (L)	3.7	46	8	26	7	5	5
BE (eV)	284.0	284.7	285.3	285.9	287.4	288.9	291.1
FWHM (eV)	0.90	0.90	0.90	1.80	1.80	1.80	3.00
L/G	30	30	30	0	0	0	0
MOMAC (M)	5.7	53	7	20	5	5	5
BE (eV)	284.0	284.7	285.4	285.9	287.5	288.9	291.3
FWHM (eV)	0.90	0.90	0.90	1.80	1.80	1.80	3.00
L/G	30	30	30	0	0	0	0
MOMAC (H)	8	53	8	16	4	6	6
BE (eV)	284.0	284.7	285.4	285.9	287.5	288.9	291.9
FWHM (eV)	0.90	0.90	0.90	1.80	1.80	1.80	3.00
L/G	30	30	30	0	0	0	0

[1] Parameters for BE, FWHM, and L/G adapted from Smith et al. 2016[20] are discussed in Text A5.

Table A9. Summary results and statistics from XAS pre-edge peak fits of MnOx and MOMAC samples to estimate relative normalized fractions of Mn oxidation state.

Method	Sample	Mn(II)	Mn(III)	Mn(IV)	Fit Centroid (eV)[a]	Reduced $\chi 2(\times 10^{-5})$[b]
Pre-edge Fits	Synthetic MnOx	0	0	100	6541.9	7.5
	MOMAC (L)	17	43	40	6541.7	1.3
	MOMAC (M)	19	32	50	6541.7	1.7
	MOMAC (H)	15	46	39	6541.7	2.1

[a] Fit centroids were calculated from the average position of peaks defined by pseudo-Voigt functions, weighted by their respective integrated areas after baseline subtraction.[11]
[b] Reduced $\chi 2$ = (F-factor) / (# of points - # of variables)

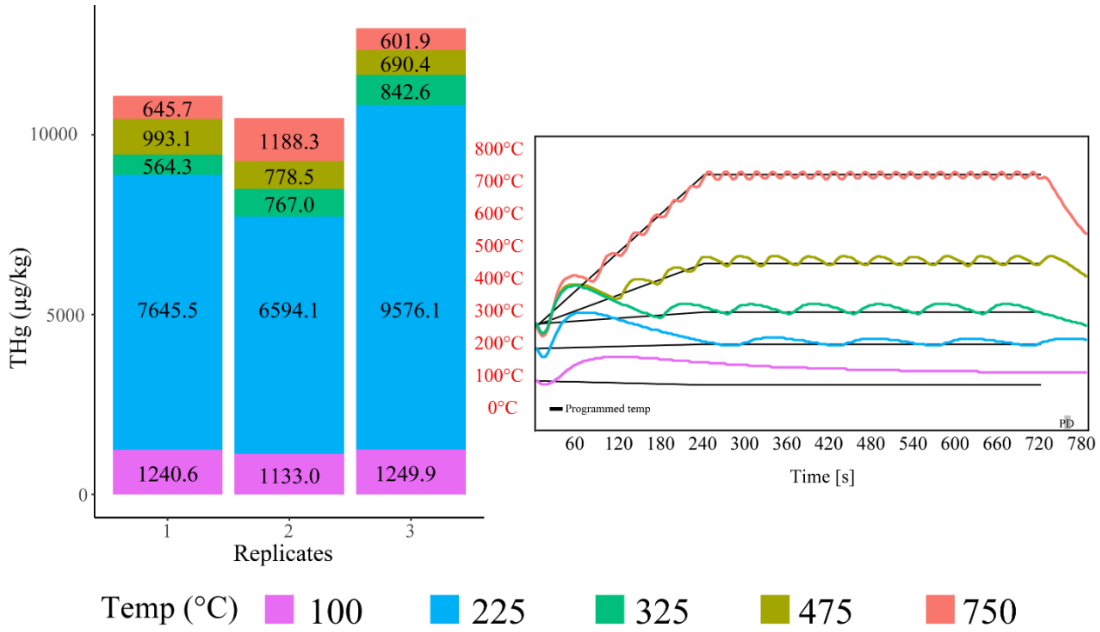

Figure A13. Thermal desorption gradient from the Direct Mercury Analyzer (Milestone DMA-80) used to determine total Hg in EFPC sediments and estimate Hg species. Species estimated from each temperature step, as reported by Saniewska & Beldowska (2017)[23] and others[24] are as follows: **100 °C** – Hg^0, **225 °C** – $HgCl_2$, Hg_2Cl_2, $Hg(ClO_4)_2$, $HgBr_2$, HgI_2, $CH_3(COO)_2Hg$, $Hg(CN)_2$, $Hg(SCN)_2$, $Hg(NO3)_2$, β-HgS, methylmercury and humus-like substance, **325 °C** – α-HgS, **475 °C** – HgO(red), HgSO4, HgF_2, and **750 °C** Hg strongly bound to minerals. Temperature fluctuations observed when heating the sediment shown on the right with the programmed temperature. Note slight overheating from 100°C step may overestimate Hg^0 fraction along with a brief ~60 second overlap between 225°C and 325°C.

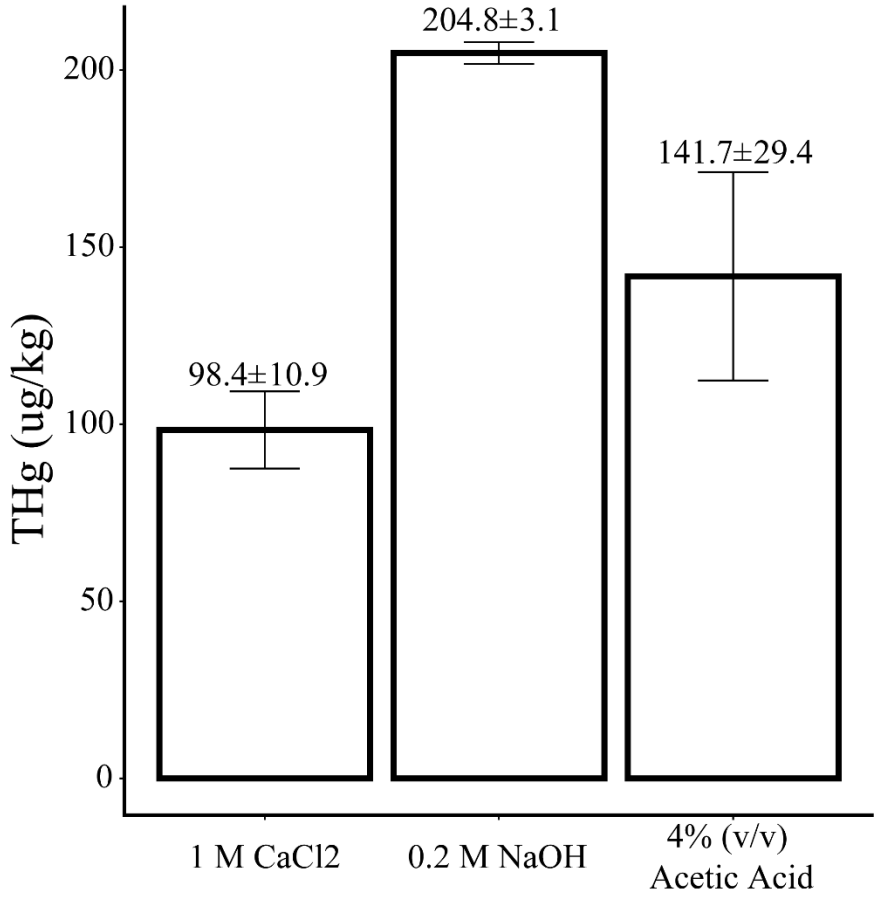

Figure A14. Chemical sequential extraction of Hg conducted in triplicate on EFPC sediments. Extractions with 1 M CaCl2 are representative of exchangeable Hg while 0.2 M NaOH and 4% (v/v) acetic acid are used to determine the fraction of organic-associated Hg.[25]

References

(1) *Method 6010D: Inductively Coupled Plasma — Optical Emission Spectrometry*.

(2) *Method 1631: Revision E: Mercury in Water by Oxidation, Purge and Trap, and Cold Vapor Atomic Fluorescence Spectrometry; US EPA: 2002.* 2002.

(3) Thommes, M.; Kaneko, K.; Neimark, A. V.; Olivier, J. P.; Rodriguez-Reinoso, F.; Rouquerol, J.; Sing, K. S. W. Physisorption of Gases, with Special Reference to the Evaluation of Surface Area and Pore Size Distribution (IUPAC Technical Report). *Pure Appl. Chem.* **2015**, *87* (9–10), 1051–1069.

(4) Manceau, A.; Marcus, M. A.; Grangeon, S. Determination of Mn Valence States in Mixed-Valent Manganates by XANES Spectroscopy. *Am. Min.* **2012**, *97* (5–6), 816–827.

(5) Birkner, N.; Navrotsky, A. Thermodynamics of Manganese Oxides: Effects of Particle Size and Hydration on Oxidation-Reduction Equilibria among Hausmannite, Bixbyite, and Pyrolusite. *Am Min.* **2012**, *97* (8–9), 1291–1298.

(6) Seelos, M.; Meraz, E. R.; Beutel, M.; Traina, S. J.; Furhmann, B.; Burmistrova, J.; Vlassopoulos, D.; O'Day, P. A. Evaluation of Manganese Oxide Amendments for Mercury Remediation in Contaminated Aquatic Sediments. *ACS Environ. Sci. Technol. Eng.* **2021**, 1, 12, 1688–1697.

(7) Villalobos, M.; Toner, B.; Bargar, J.; Sposito, G. Characterization of the Manganese Oxide Produced by Pseudomonas Putida Strain MnB1. *Geochim. Cosmochim. Acta* **2003**, *67* (14), 2649–2622.

(8) Birkner, N.; Navrotsky, A. Thermodynamics of Manganese Oxides: Sodium, Potassium, and Calcium Birnessite and Cryptomelane. *Proc. Natl. Acad. Sci.* **2017**, *114* (7), E1046–E1053.

(9) Bargar, J. R.; Tebo, B. M.; Bergmann, U.; Webb, S. M.; Glatzel, P.; Chiu, V. Q.; Villalobos, M. Biotic and Abiotic Products of Mn(II) Oxidation by Spores of the Marine Bacillus Sp. Strain SG-1. *Am. Min.* **2005**, *90* (1), 143–154.

(10) Villinski, J. E.; O'Day, P. A.; Corley, T. L.; Conklin, M. H. In Situ Spectroscopic and Solution Analyses of the Reductive Dissolution of MnO2 by Fe(II). *Environ. Sci. Technol.* **2001**, *35* (6), 1157–1163.

(11) Chalmin, E.; Farges, F.; Brown, G. E. A Pre-Edge Analysis of Mn K-Edge XANES Spectra to Help Determine the Speciation of Manganese in Minerals and Glasses. *Contrib. Min. Petr.* **2009**, *157* (1), 111–126.

(12) Biesinger, M. C.; Payne, B. P.; Grosvenor, A. P.; Lau, L. W. M.; Gerson, A. R.; Smart, R. S. C. Resolving Surface Chemical States in XPS Analysis of First Row Transition Metals, Oxides and Hydroxides: Cr, Mn, Fe, Co and Ni. *Appl. Surf. Sci.* **2011**, *257* (7), 2717–2730.

(13) Ilton, E. S.; Post, J. E.; Heaney, P. J.; Ling, F. T.; Kerisit, S. N. XPS Determination of Mn Oxidation States in Mn (Hydr)Oxides. *Appl. Surf. Sci.* **2016**, *366*, 475–485.

(14) Cerrato, J. M.; Knocke, W. R.; Hochella, M. F.; Dietrich, A. M.; Jones, A.; Cromer, T. F. Application of XPS and Solution Chemistry Analyses to Investigate Soluble Manganese Removal by MnO x (s)-Coated Media. *Environ. Sci. Technol.* **2011**, *45* (23), 10068–10074.

(15) Cerrato, J. M.; Hochella, M. F.; Knocke, W. R.; Dietrich, A. M.; Cromer, T. F. Use of XPS to Identify the Oxidation State of Mn in Solid Surfaces of Filtration Media Oxide

Samples from Drinking Water Treatment Plants. *Environ. Sci. Technol.* **2010**, *44* (15), 5881–5886.

(16) Greczynski, G.; Hultman, L. X-Ray Photoelectron Spectroscopy: Towards Reliable Binding Energy Referencing. *Prog. Mater. Sci.* **2019**, *107*, 100591.

(17) Vegh, J. The Shirley Background Revised. *J. Electron Spectros. Relat. Phenomena* **2006**, *151* (3), 159–164.

(18) Hofmann, S. Auger- and X-Ray Photoelectron Spectroscopy in Materials Science, A User-Oriented Guide. *Springer. Ser. Surf. Sci.* **2013**.

(19) Seah, M. P.; Brown, M. T. Validation and Accuracy of Software for Peak Synthesis in XPS. *J. Electron Spectros. Relat. Phenomena* **1998**, *95* (1), 71–93.

(20) Smith, M.; Scudiero, L.; Espinal, J.; McEwen, J.-S.; Garcia-Perez, M. Improving the Deconvolution and Interpretation of XPS Spectra from Chars by Ab Initio Calculations. *Carbon* **2016**, *110*, 155–171.

(21) Manne, R.; Åberg, T. Koopmans' Theorem for Inner-Shell Ionization. *Chem. Phys. Let.* **1970**, *7* (2), 282–284.

(22) Bagus, P. S.; Nelin, C. J.; Brundle, C. Richard.; Crist, B. V.; Ilton, E. S.; Lahiri, N.; Rosso, K. M. Main and Satellite Features in the Ni 2p XPS of NiO. *Inorg. Chem.* **2022**, *61* (45), 18077–18094.

(23) Saniewska, D.; Bełdowska, M. Mercury Fractionation in Soil and Sediment Samples Using Thermo-Desorption Method. *Talanta* **2017**, *168*, 152–161.

(24) Reis, A. T.; Coelho, J. P.; Rucandio, I.; Davidson, C. M.; Duarte, A. C.; Pereira, E. Thermo-Desorption: A Valid Tool for Mercury Speciation in Soils and Sediments? *Geoderma* **2015**, *237*, 98–104.

(25) Neculita, C.; Zagury, G. J.; Deschênes, L. Mercury Speciation in Highly Contaminated Soils from Chlor-Alkali Plants Using Chemical Extractions. *J Environ Qual* **2005**, *34* (1), 255–262.

Appendix B: Supporting Information for Manganese Oxide Modified Activated Carbon Lowers Mercury and Methylmercury in Legacy Contaminated Sediments: A Flow-Through Column Study

Contents:

Table B1: Experimental Design Parameters

Soil Treatment	Treatment dosing (%dry wt)	Carbon addition	Carbon dose	Replicates
Untreated	0	None	None	n = 1
MOMAC	2			n = 1
Untreated	0	Carbon added as acetate+pyruvate to feed water	~10 mg/L in influent soln.	n = 1
MOMAC	2			n = 1
Untreated	0	Carbon added as spirulina powder to sediment	Roughly double native OC in sediment	n = 3
MOMAC	2			n = 2
AC	1.3			n = 1

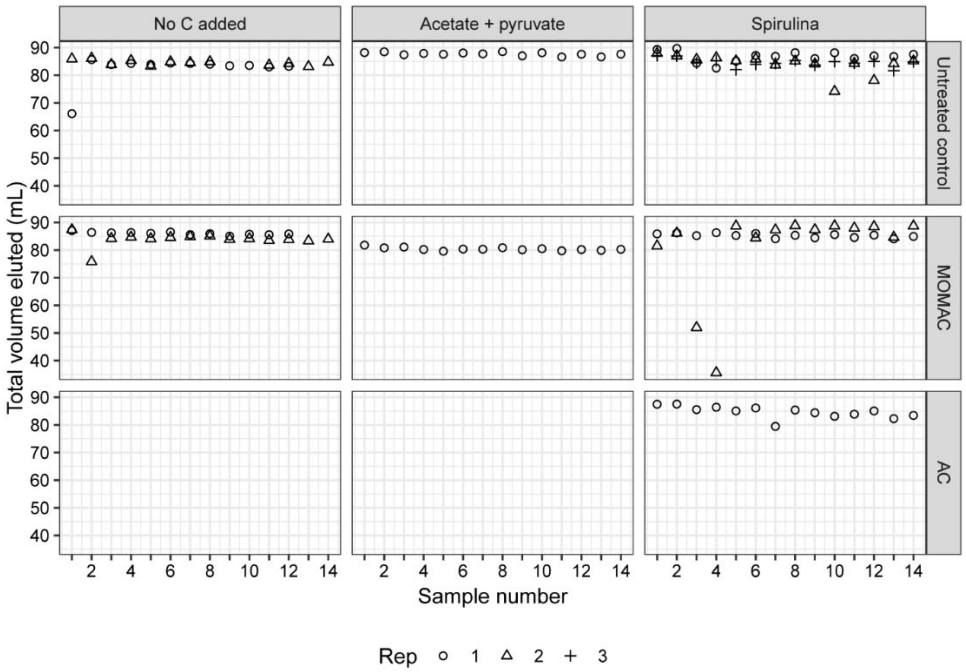

Figure B1. Total volume eluted and combined for each sample. Fractions were collected over 12 h intervals and combined to constitute one sample.

Text B1: Additional Sample Processing Details for Dissolved Ions, Total Carbon and Organic Carbon Analyses.

Aqueous cations (Na^+, Ca^{2+}, K^+, Mg^{2+}, Fe, Mn) were measured by inductively coupled plasma – optical emission spectrometry (ICP-OES; Perkin-Elmer Avio 550 Max).[1] Calibration check standards (**Na^+, Ca^{2+}, K^+, Mg^{2+}:** 0, 1.0, 5.0, 10.0, 25.0, 50.0, 100 mg/kgw; **Fe and Mn:** 0, 0.1, 0.5, 1.0, 2.5, 5.0, 10.0 and 25.0 mg/kgw) and blanks (ultrapure water; 18.2 MΩ cm, Millipore-Sigma Milli-Q) were prepared and analyzed with a relative standard deviation of <5% for check standards. Effluent aliquots (~10 mL) were stored in 15 mL polypropylene tubes, preserved with 2% (v/v) tracemetal grade nitric acid, and refrigerated until analysis.

Inorganic aqueous anions (Cl^-, NO_3^-, SO_4^{2-}) were measured on a Dionex ICS-2000 Ion Chromatograph.[2] Samples were preserved by freezing at -20°C. Prior to running, samples were thawed at 4 °C overnight. Calibration check standards (1.0, 5.0, 10.0, 25.0, 50.0 and 125 mg/L) and blanks (ultrapure water; 18.2 MΩ cm, Millipore-Sigma Milli-Q) were prepared and analyzed with a relative standard deviation of <5% for check standards.

Dissolved carbon (non-purgeable organic carbon – NPOC, total carbon – TC, and inorganic carbon – IC) were measured on a Shimadzu TOC-L instrument.[3] Samples were preserved by freezing at -20°C and thawing overnight prior to running. Inorganic carbon was calculated as TC-NPOC.

Table B2: Methods, Instruments, and Detection Limits for Analyses Performed Mercury, Methylmercury, Ions, and Dissolved Organic Carbon.

Analysis	Method	Instrument	Instrument DL; PQL (DL*3.0)	RSD
Hg	EPA Method 1631	MERX-T	0.2 ng/L	Table S3
MeHg	EPA Method 1630	MERX-M	0.02 ng/L	Table S3
Ca^{2+}	EPA Method 200.7	Avio 550 Max ICP-OES	30 µg/L; 90 µg/L	< 5%
Na^{+}				
Cl^{-}			30 µg/L; 90 µg/L	
K^{+}			30 µg/L; 90 µg/L	
Mg^{2+}			80 µg/L; 240 µg/L	
Fe			6 µg/L; 18 µg/L	
Mn			2 µg/L; 6 µg/L	
Cl-	EPA Method 300.0	Dionex ICS-2000 Ion Chromatograph	0.1 mg/L	≤ 5%
SO_4^{2-}			0.1 mg/L	
NO_3^{-}			0.1 mg/L	
Non-purgeable Organic C	EPA Method 415.3	Shimadzu TOC-L	0.1 mg/L	< 5%
Inorganic C				

Text B2: Detailed Methods for Hg and MeHg analyses

Samples for total mercury (Hg) were preserved with BrCl to oxidize all Hg forms within sample to Hg(II). Samples were analyzed on a MERX-T Hg system (Brooks Rand Labs, Seattle, WA, USA) using cold vapor atomic fluorescence spectrophotometry (CVAFS).[4] Depending on expected sample Hg concentration, 0.5 – 1.0 g of sample were diluted with 23.0 – 25.0 g with ultrapure water. Instrument calibration was performed using an 8-point calibration from 0 to 1000 pg Hg using Hg chloride standards with accepted recoveries between 75-125%. Hydroxylamine hydrochloride was used (100 uL) to neutralize BrCl and pre-reduce Hg. Stannous chloride was used to reduce Hg(II) to Hg(0), which was subsequently sparged with ultra-high purity N_2 and carried with ultra-high purity Ar to CVAFS detector. Every 12-sample batch contained two method blanks (MB), one matrix spike (MS), one matrix spike duplicate (MSD), and two ongoing precision and recovery (OPR) samples. Acceptable recoveries for MS/ MSD and OPR samples were 71-125% and 77-123%, respectively.

Samples were analyzed for methylmercury (MeHg) on a MERX-M automated Hg system (Brooks Rand Labs, Seattle, WA, USA) using cold vapor atomic fluorescence spectrophotometry (CVAFS).[5] Approximately 25.0-35.0 g of effluent were transferred to a Teflon-vial and diluted to 55 mL with ultrapure water and distilled at 125 °C for 3 h under nitrogen flow. After distillation, 20 g of distillate were transferred to amber Hg-free vials and diluted to with ~20 g of ultrapure water. Diluted samples were pH-adjusted with 300 µL of acetate buffer, volatilized via ethylation with 50 µL sodium tetraethylborate, and analyzed using a MERX-M instrument (purge and trap followed by CVAFS). Each 12-sample batch of samples contained contained two method blanks (MB), one matrix spike (MS), one matrix spike duplicate (MSD), and two ongoing precision and recovery (OPR) samples. Recoveries of the MS/MSD and OPR samples must be 75-125%, and the MB sample must contain <0.1 ng/L. Results from these quality control/ quality assurance samples are shown in Table B3.

Total Hg in unamended sediment was measured using a Direct Mercury Analyzer (Milestone DMA-80) via thermal decomposition, amalgamation, and atomic absorption spectrophotometry.[6] Methylmercury in sediment was measured with a KOH-methanol digestion.[7] Approximately 0.1 – 0.2 g of wet sediment was measured into a 15 mL polypropylene centrifuge tube, 0.5 mL 1 N HCl in methanol was added, and tubes were placed on a shaker table at 200 rotations per minute for 30 minutes. Afterward, 2.5 mL of 25% KOH in methanol was added and the tubes were placed in an oven at 60°C for 4 h and vortexed every hour. The samples were diluted with 10 mL of ultrapure water and measured for MeHg. Samples were pH-adjusted to 4.5-5.0 using 300 µL of a 2 M sodium acetate buffer, volatilized via ethylation using 50 µL of sodium tetraethylborate, and measured with CVAFS on a MERX-M instrument.

Table B3: QA/QC Statistics for Hg and MeHg Analyses

Matrix	Analyte	Method or Instrument Detection Limit	MB	MS/ MSD	OPR/ CRM
			ng/L (mean ± SD)	% Recovery (mean ± SD)	
Effluent	Hg	0.2 ng/L	0.91 ± 0.66	87.2 ± 11.3	96.4 ± 7.3
	MeHg	0.02 ng/L	0.03 ± 0.01	91.1 ± 14.1	93.6 ± 10.0
Sediment	Hg	0.01 ng	not detected	N/A	99.7 ± 0.4
	MeHg	0.02 ng/L	not detected	87.9 ± 2.7	100.8 ± 3.5

Text B3: Results for Major Cations Measured in Effluent

Text B3.1. Columns with no Organic Carbon added

In the column effluent, most cations measured (Na^+, K^+, Mg^{2+}) remained stable, mirroring the concentrations in the ACW influent solution (Figure C2). However, an initial flush of Ca^{2+} was observed, particularly from sediment treated with MOMAC.

Text B3.2. Columns with Organic Carbon Added as Acetate and Pyruvate

In the effluent from both untreated and MOMAC-treated sediment columns, most major cations behaved similarly (Figure C2). Na^+ and Mg^{2+} concentrations in the effluent closely matched those in the influent solution. However, Ca^{2+} concentrations were slightly elevated in the effluent compared to the influent, particularly in the initial fractions. The K^+ concentration in the influent was higher in solutions containing acetate and pyruvate compared to those without. For both untreated and MOMAC-treated columns, K^+ concentrations in the effluent were elevated compared to the influent, with further increases observed after the stopped-flow state in the MOMAC-treated sediment, while the untreated sediment showed no increase.

Text B3.3. Columns with Organic Carbon Added as Spirulina

The major cations in the effluent from sediment homogenized with spirulina powder exhibited less conservative behavior compared to columns without added OC or with OC added as acetate and pyruvate (Figure C2). Despite this, the elution trends for each cation were similar across all treatments. Before the stopped-flow state, monovalent cations (Na^+, K^+) sharply decreased until stabilizing at approximately 15-17 mg/L for Na^+ and around 2 mg/L for K^+ after the stopped-flow event. Prior to the stopped-flow, divalent cation ($Ca^{2+,}$ Mg^{2+}) concentrations in the effluent were higher than the influent solution but stabilized to values consistent with the ACW solution. An exception was observed with Ca^{2+} in MOMAC-treated columns, where concentrations were slightly lower but gradually increasing (36-39 mg/L). Immediately following the stopped-flow event, a surge in Ca^{2+}, Mg^{2+}, and K^+ concentrations occurred before stabilizing at concentrations similar to the ACW.

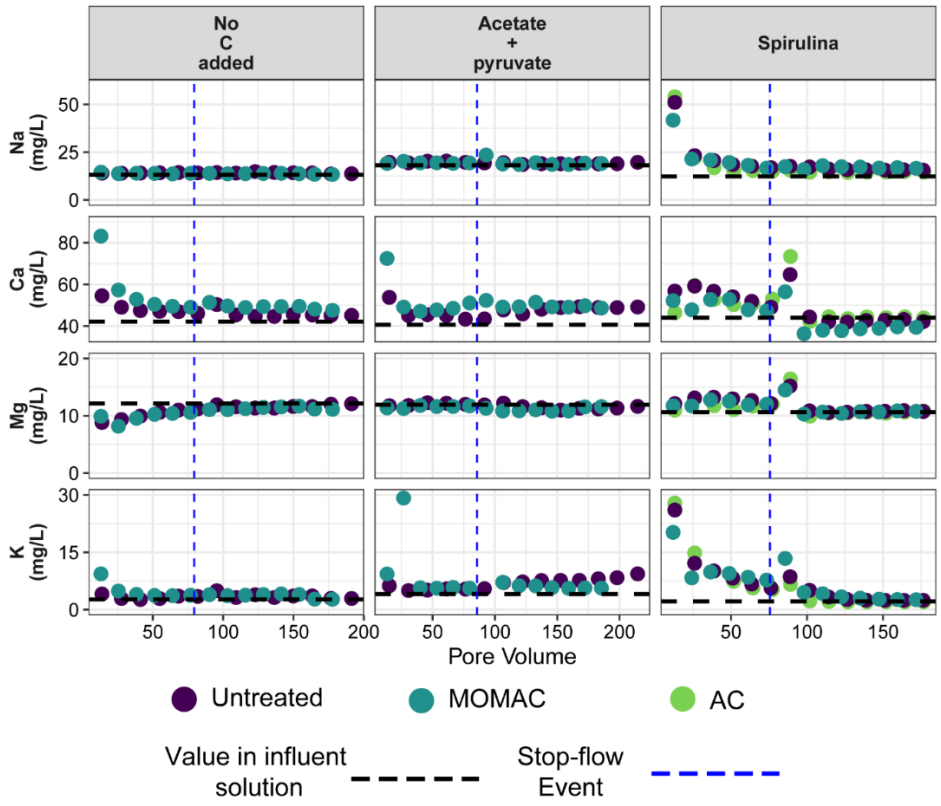

Figure B2. Concentrations of major cations measured from filtered column effluent. Concentrations for the influent solution are marked by the horizontal black line. The stopped-flow event is marked by the vertical blue line. Values below detection were omitted. Detection limits are shown on Table B2. Uncertainty was determined based on replicates and shown as mean ± standard error. Values with no uncertainty shown are due to single replicates.

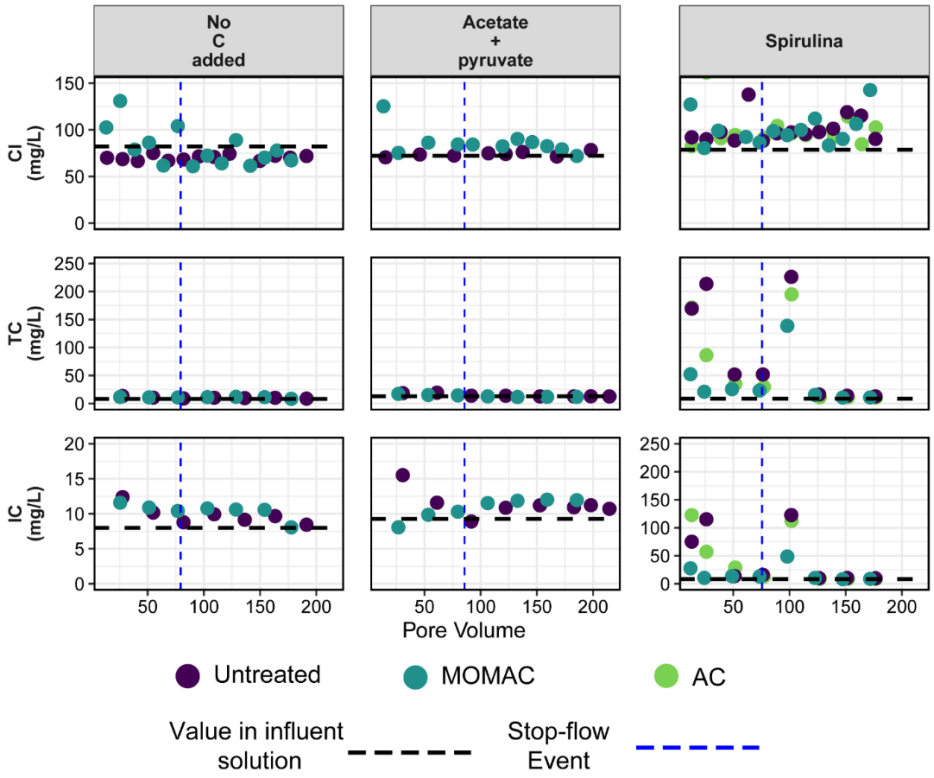

Figure B3. Concentrations of chloride, total carbon (TC), and inorganic carbon (IC) measured from filtered column effluent. Concentrations for the influent solution are marked by the horizontal black line. The stopped-flow event is marked by the vertical blue line. Values below detection were omitted. Detection limits are shown on Table B2. Uncertainty was determined based on replicates and shown as mean ± standard error. Values with no uncertainty shown are due to a single column replicate.

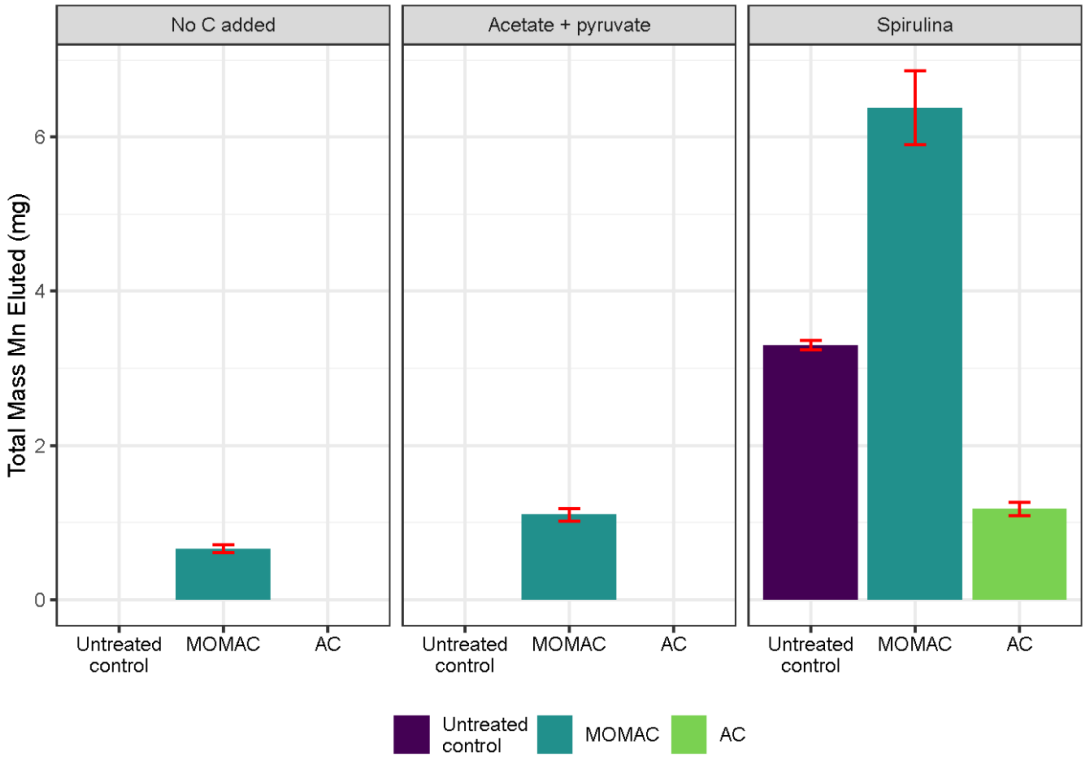

Figure B4. Total mass (mg) of dissolved manganese eluted from column experiments. Error bars are based on propagated uncertainty of Mn mass eluted from replicate columns experiments. Column experiments with 1 replicate (No C added – MOMAC; Acetate + pyruvate – MOMAC; Spirulina – AC) used relative uncertainty from Spirulina – MOMAC column (± 7.6%).

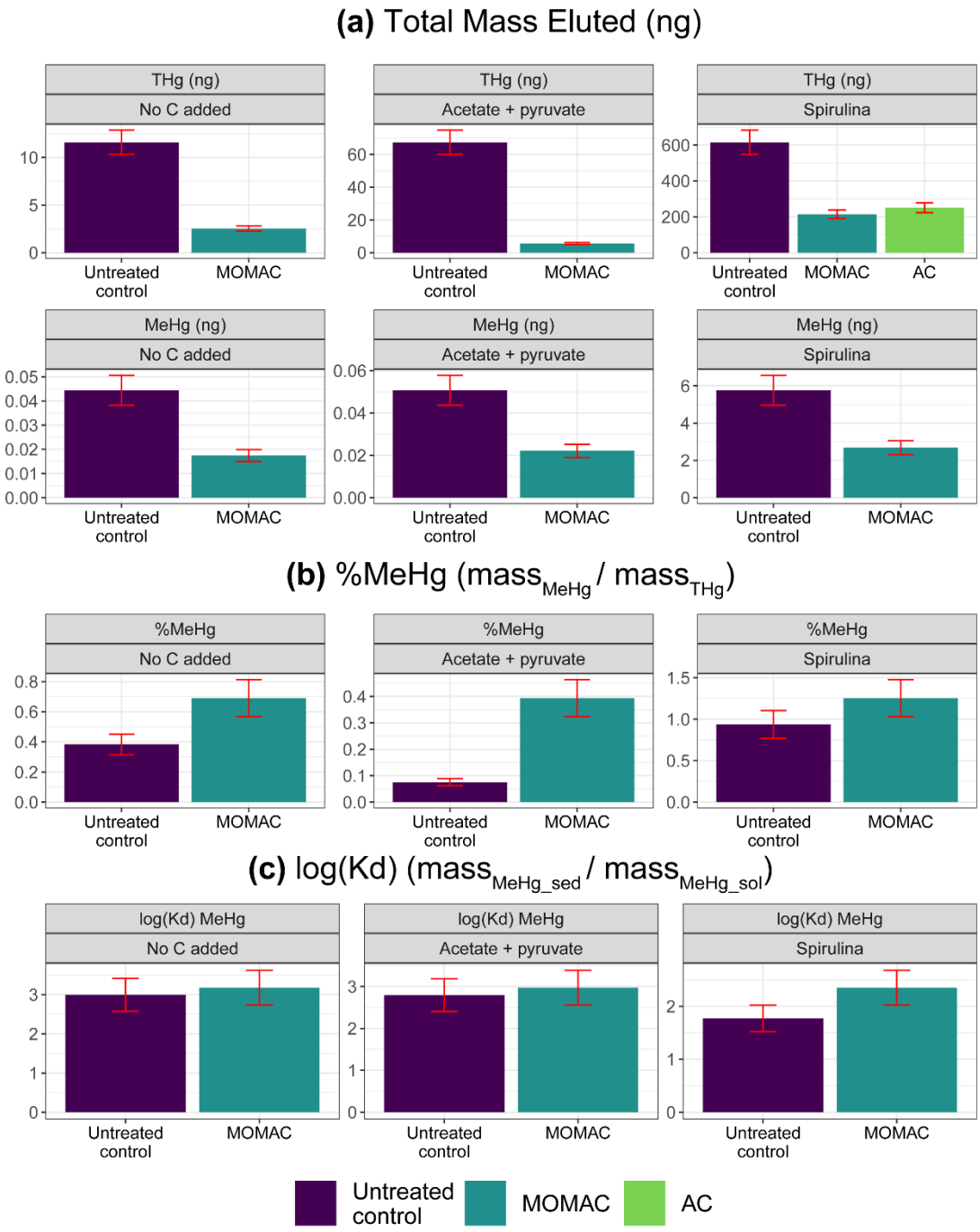

Figure B5. Comparison to Figure 5 without initial sample included in calculations **(a)** Total mass of mercury (THg) and methylmercury (MeHg) eluted from column experiments. **(b)** %MeHg is ratio of MeHg mass to total Hg mass. **(c)** Log(K_d) (K_d = mass $MeHg_{sed}$/ mass $MeHg_{sol}$) represents the partitioning of methylmercury (MeHg) between the solid and aqueous phase calculated from total mass of MeHg in sediments. Error bars are based on relative uncertainty from QA/QC samples (i.e. matrix spikes, matrix spike duplicates) measured along with unknown samples, ±11% for THg and ±14% for MeHg.

REFERENCES

(1) *Method 6010D: Inductively Coupled Plasma — Optical Emission Spectrometry*.

(2) EPA Method 300.0 - Determination of Inorganic Anions by Ion Chromatography.

(3) EPA Method 415.3 - Measurement of Total Organic Carbon, Dissolved Organic Carbon and Specific UV Absorbance at 254 Nm in Source Water and Drinking Water.

(4) *Method 1631: Revision E: Mercury in Water by Oxidation, Purge and Trap, and Cold Vapor Atomic Fluorescence Spectrometry; US EPA: 2002.* **2002**.

(5) EPA Method 1630: Methyl Mercury in Water by Distillation, Aqueous Ethylation, Purge and Trap, and Cold Vapor Atomic Fluorescence Spectrometry.

(6) *Method 7473: Mercury in Solids and Solution by Thermal Decomposition, Amalgamation, and Atomic Absorption Spectrophotometry* **2007**.

(7) Liang, L.; Horvat, M.; Cernichiari, E.; Gelein, B.; Balogh, S. Simple Solvent Extraction Technique for Elimination of Matrix Interferences in the Determination of Methylmercury in Environmental and Biological Samples by Ethylation-Gas Chromatography-Cold Vapor Atomic Fluorescence Spectrometry. *Talanta* **1996**, *43* (11), 1883–1888. https://doi.org/10.1016/0039-9140(96)01964-9.

Appendix C: Supporting Information for Pilot Field Study of a Novel Amendment Treatment for Mercury-Contaminated Soils at East Fork Poplar Creek, TN

Contents:

Text C1: Preparation of Mercury Reference Standards

Reference spectra collected and tested in linear combination fits to unknown spectra are listed in Table C1 and shown in Figure C1. When available, Hg reference standards were purchased from commercial sources such as Acros (α-HgS, $HgSO_4$), Alfa Aesar (HgSe), or American Elements (Hg^0). A sample of a historical release deposit (HRD) layer near EFK 18.2 was acquired from Oak Ridge National Laboratory, courtesy of Dr. Alex Johs and Danielle Jones. A portion of the HRD sample was leached using an artificial creek water solution in batch reactions (5 g HRD to 1L artificial creek water) and reacted for 48h to remove weakly sorbed Hg. The leachate was filtered with a 0.45 μm filter and the residue remaining on the filter was isolated and scanned as a reference standard. Aqueous reference standards were prepared using deoxygenated ultrapure water (sparged with N_2 or Ar gas overnight) and solutions of $Hg(NO_3)_2$ in 2% nitric acid. Solutions of 1 M NaOH or HCl, prepared in deoxygenated water, were used to adjust pH of aqueous solutions.

Amorphous HgS was precipitated by mixing 5 mL of 20 mM $Hg(NO_3)_2$ with 5.5 mL of 20 mM NaHS inside a nitrogen-filled glove box.[2] The solution was aliquoted into multiple 2 mL centrifuge tubes and centrifuged at 15,000 relative centrifugal force (rcf) to isolate the solid. The supernatant was carefully removed, solids were aggregated into a single tube, and the solid was quenched with liquid nitrogen.

Aqueous standards of Hg bound to cysteine in either a linear ($Hg\text{-}cysteine_{2(aq)}$) or tetrahedral ($Hg\text{-}cysteine_{4(aq)}$) coordination were prepared in a glovebox following the methods described in Thomas et al. 2019[3] and Manceau et al. 2016[4]. Solutions of 0.5 mM or 5 mM $Hg(NO_3)_2$ were mixed with L-cysteine at a metal-to-ligand ratio of 1:2 (1 mM cysteine) or 1:10 (50 mM cysteine), and adjusted to either pH 2.2 ($Hg\text{-}cysteine_2$) or 11.6 ($Hg\text{-}cysteine_4$) with 1 M HCl or NaOH.

Aqueous standards of Hg bound to glutathione were prepared by mixing 5 mL of a 10 mM $Hg(NO_3)_2$ solution with 2.5 mL of a 40 mM L-glutathione solution in an amber vial and increasing pH to 7.44.

An aqueous solution standard for Hg-selenocysteine was adapted from methods for synthesis of solid methylmercury-selenocysteinate monohydrate.[5,6] Initially, 4.18 mg of seleno-L-cystine was dissolved in approximately 10 mL of deoxygenated water in an anaerobic glovebox. Separately, 98.94 mg of sodium borohydride ($NaBH_4$) was transferred into the glovebox and dissolved in deoxygenated water to prepare a 10 mL solution of 0.26 M $NaBH_4$. The solution pH of seleno-L-cystine increased to ~12 using a pellet of NaOH. Then 4 mL of 0.26M $NaBH_4$ was added and stirred for ~5 minutes to reduce cystine to cysteine. Concentrated (~2 M) HCl was added to lower solution pH to ~4 to destroy excess $NaBH_4$. A 1.67 mL aliquot of a 7.5 mM $Hg(NO_3)_2$ solution was added and pH was slowly brought to 7.4 with small aliquots of NaOH, and then diluted to 25 mL resulting in 0.5 mM Hg:1 mM Se. The amber vial was sealed in an anaerobic chamber and stored at 4°C until analysis.

Preparation for an aqueous solution of Hg-selenomethionine was adapted from Gilsanz et al. 2011.[7] A 25 mL solution was prepared in a Hg-free amber vial by dissolving 4.90 mg of seleno-L-methionine in ~15 mL, adding 1.67 mL of a 7.5 mM $Hg(NO_3)_2$ solution, adjusting pH with NaOH to 7.4, and diluting to 25 mL with deoxygenated water. The final solution contained 1 mM Se and 0.5 mM Hg after dilution to 25 mL.

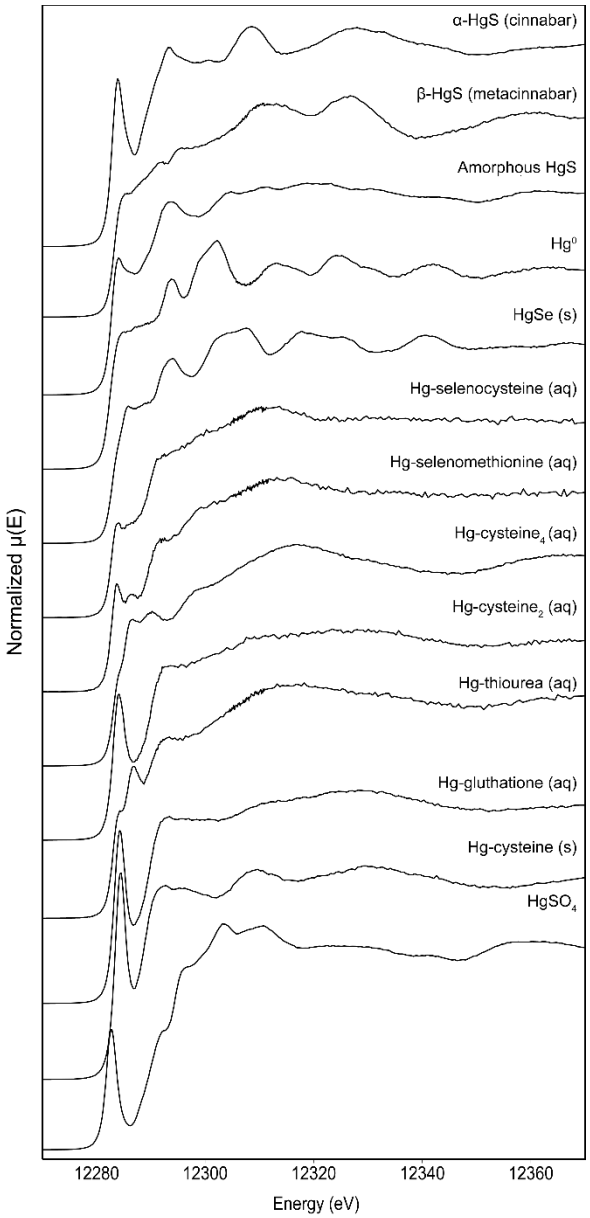

Figure C1. High energy resolution fluorescence detected – XANES reference spectra used for linear combination fits of unknown soil samples. Details (source, chemical formula – if applicable, preparation summary) are shown in Table C1 and discussed in Text C1.

Table C1. Library and details of Hg-reference spectra used in HERFD-XAS fits.

Liquid	**Source**	**Molecular Formula**	**# scans**	**Details**
Hg^0	American Elements	Hg	2	CAS: 7439-97-6
Solid	**Source**	**Molecular Formula**	**# scans**	**Details**
Mercury(II) sulfate	Acros	$HgSO_4$	6	CAS: 7783-35-9
Hg-cysteine	O'Day Lab	Hg-L-cysteine	10	
HgSe	Alfa Aesar	HgSe	6	CAS: 20601-83-6
HgS (amorphous)	Prepared in lab	HgS	3	20 mM $HgNO_3$•H_2O + 10% excess 20 mM $NaHS^-$
Cinnabar	Acros	α-HgS	20	CAS: 1344-48-5
Metacinnabar	Smithsonian National Museum of Natural History	β-HgS	5	Mineral sample
Aqueous Solutions	**Source**	**Ligand**	**# scans**	**Details**
Hg-thiourea	ORNL Lab	L-thiourea	5	0.83 mM Hg(II) + 4.2 mM L-thiourea
Hg-glutathione	Prepared in lab	L-glutathione	6	5 mM $HgNO_3$•H_2O + 10 mM L-glutathione; pH 7.4
$Hg(cysteine)_2$	Prepared in lab	L-cysteine	12	0.5 mM $HgNO_3$•H_2O + 1 mM L-cysteine; pH 2.5
$Hg(cysteine)_4$	Prepared in lab	L-cysteine	10	5 mM $HgNO_3$•H_2O + 50 mM L-cysteine; pH 11.6
Hg-selenomethionine	Prepared in lab	L-selenomethionine	4	0.5 mM $HgNO_3$•H_2O + 1 mM seleno-L-methionine; pH 7.4
Hg-selenocysteine	Prepared in lab	L-selenocystine	4	0.5 mM $HgNO_3$•H_2O + 1 mM seleno-L-cystine; pH 7.4

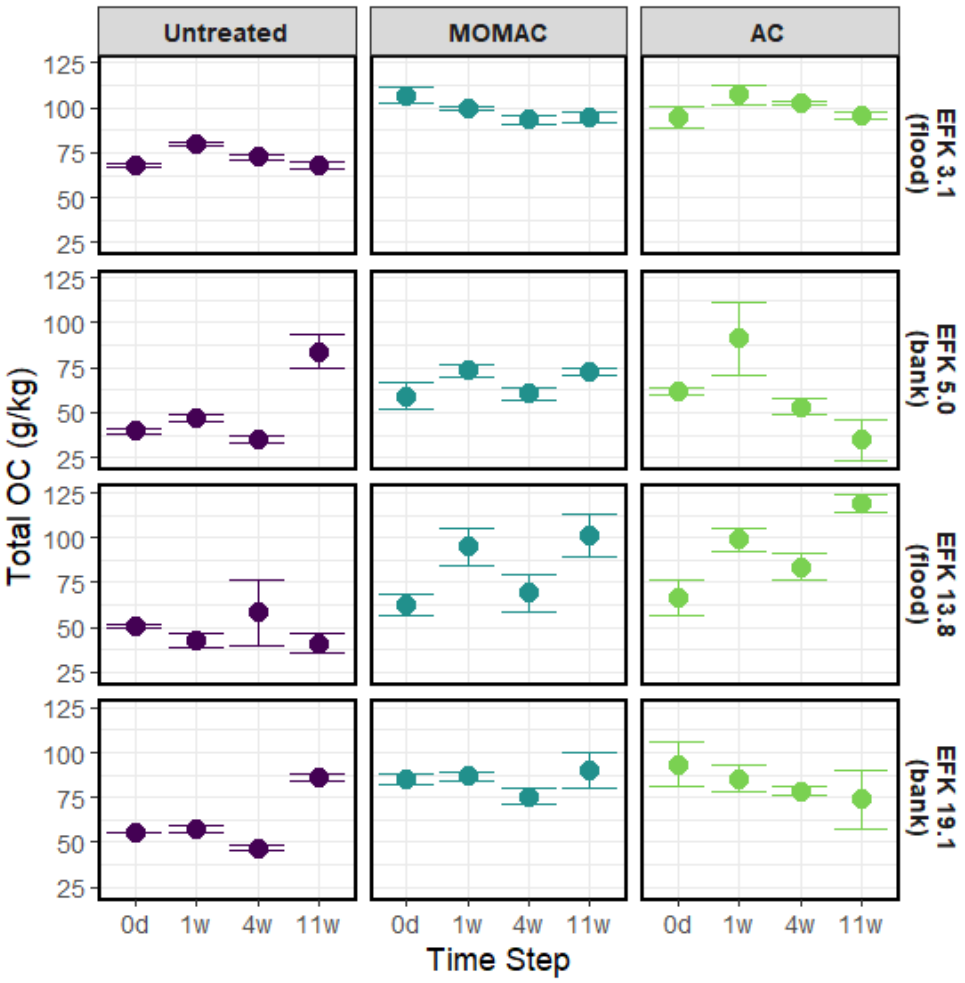

Figure C2. Total organic carbon in soil measured by loss on ignition at 550 °C from each sampling site over the course of the experiment (0-11 weeks). Error bars show average from replicates across the transect (mean ± standard error; n = 3).

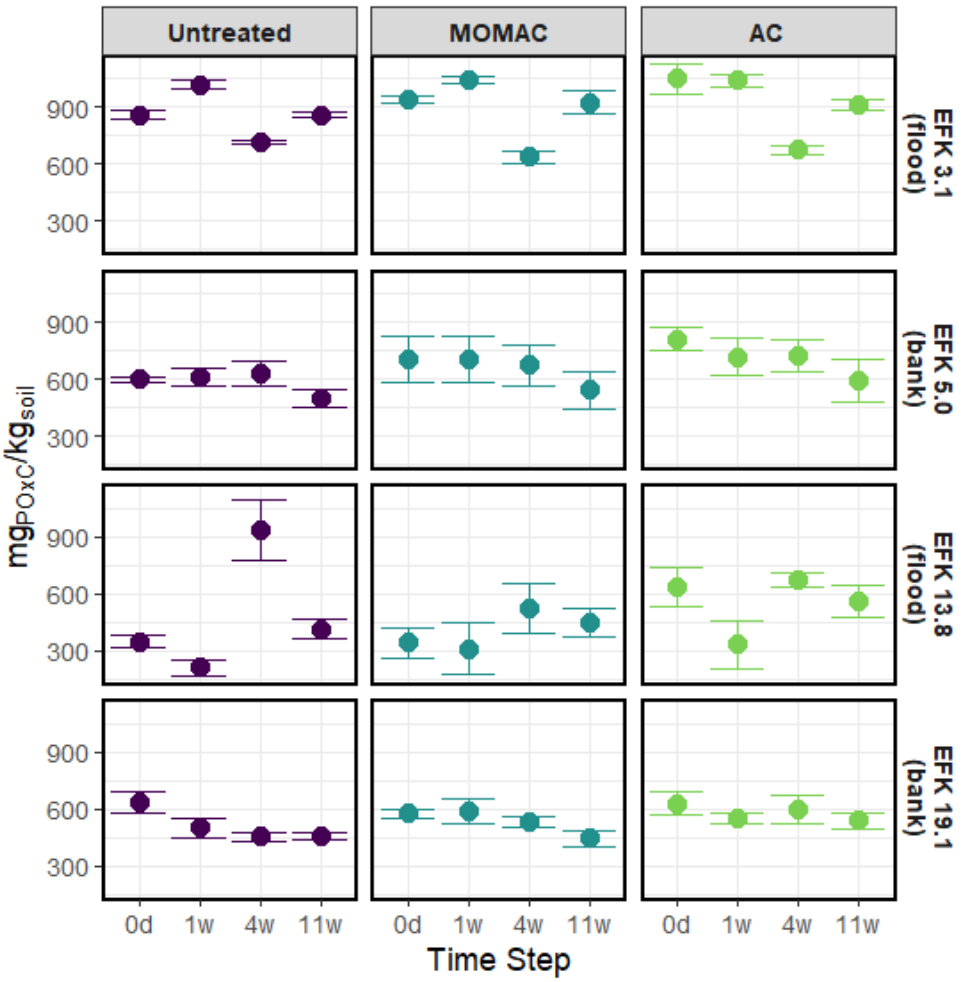

Figure C3. Reactive carbon content measured in soil as permanganate oxidizable carbon from each sampling site over the course of the experiment (0-11 weeks). Error bars show average from replicates across the transect (mean ± standard error; n = 3)

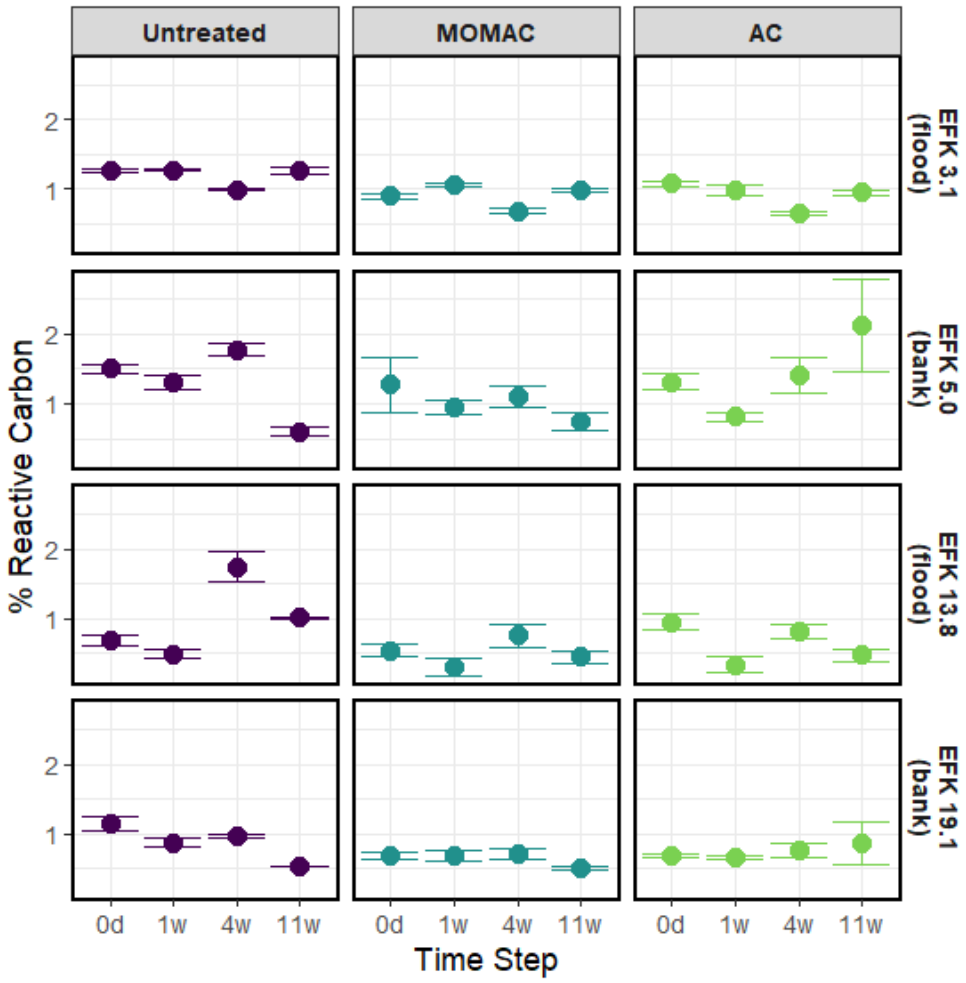

Figure C4. Percent reactive carbon measured in soil as the ratio between permanganate oxidizable carbon and total organic carbon ([POxC]/[Total OC]) from each sampling site over the course of the experiment (0-11 weeks). Error bars show average from replicates across the transect (mean ± standard error; n = 3).

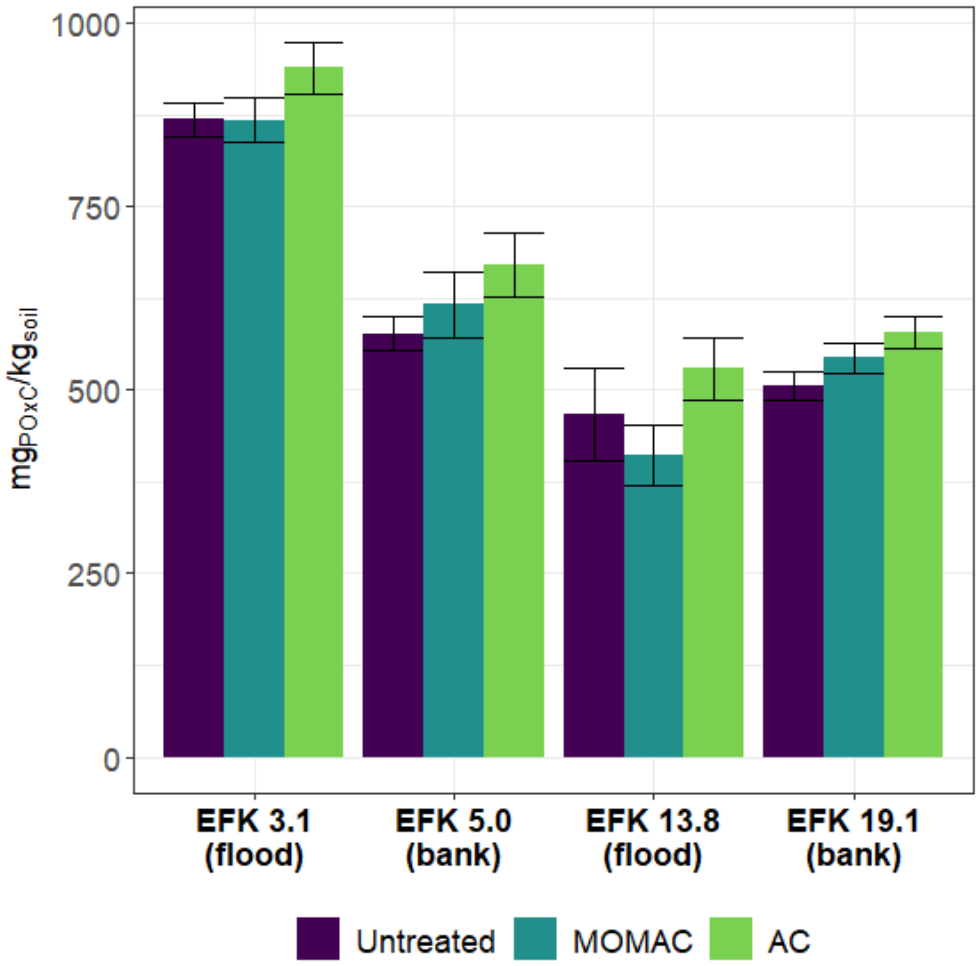

Figure C5. Total reactive carbon measured as permanganate oxidizable carbon (POxC) for each sampled field site. Error bars show averages from replicates across the transect and all time points (mean ± standard error; n = 12).

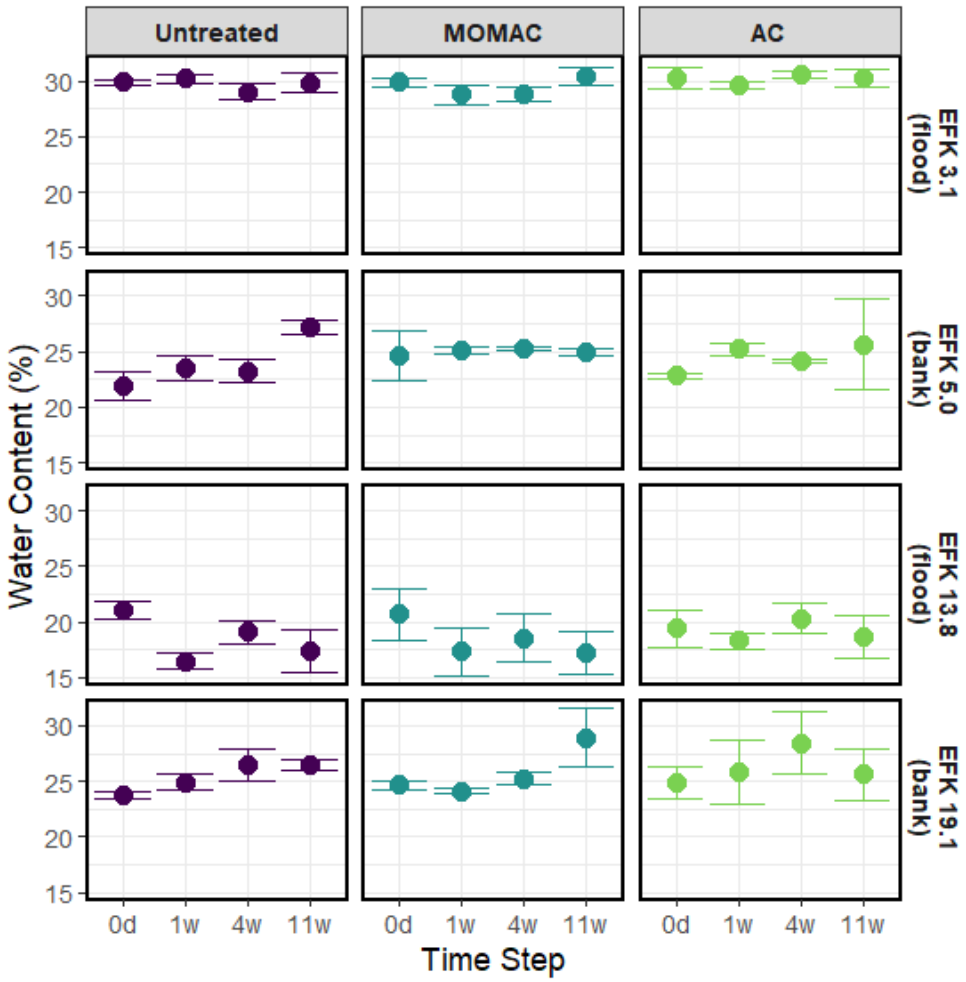

Figure C6. Soil water content measured by heating soil at 105°C overnight at each field site over the course of the experiment (11 weeks). Error bars show average from replicates across the transect (mean ± standard error; n = 3)

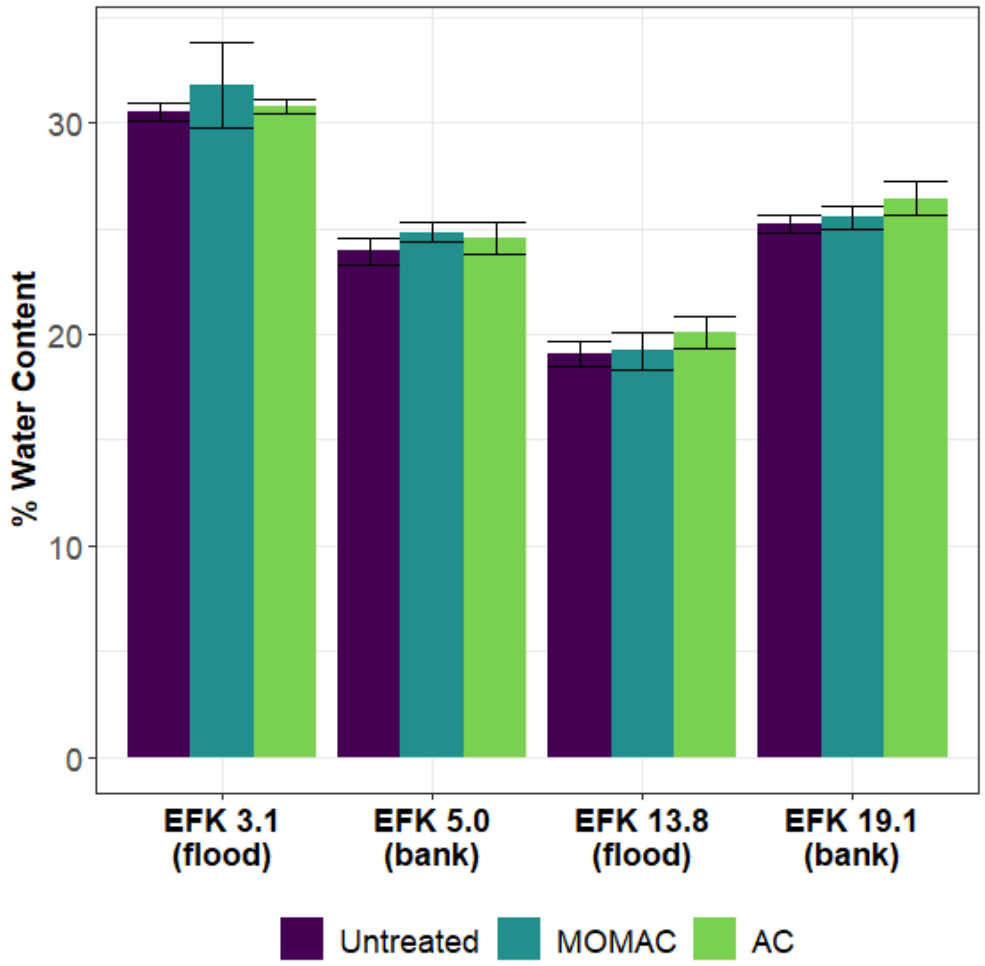

Figure C7. Soil water content measured by heating soil at 105°C for each sampled field site. Error bars show averages from replicates across the transect and all time points (mean ± standard error; n = 12).

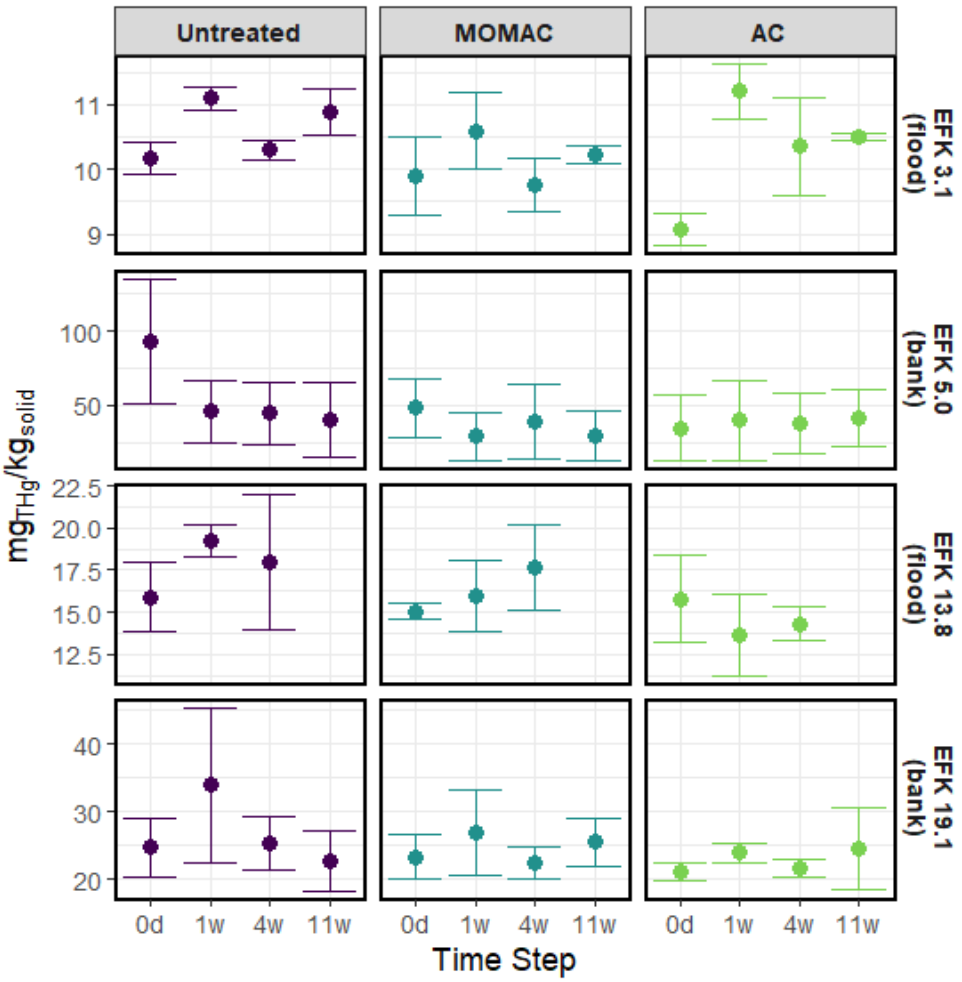

Figure C8. Total Hg measured in soil digested in aqua regia at each field site over the course of the experiment (11 weeks). Error bars show average from replicates across the transect (mean ± standard error; n = 3).

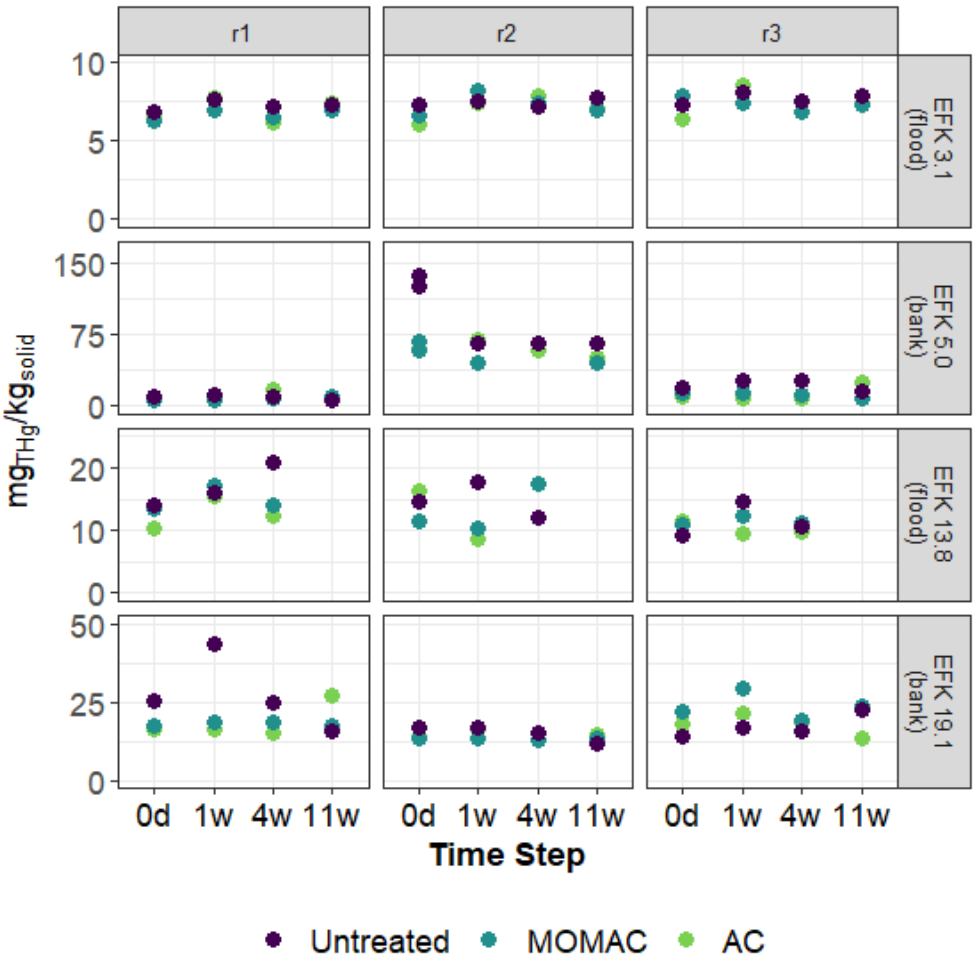

Figure C9. THg measured across the transect (replicates (r1, r2, r3) by digesting soil in aqua regia over the course of the experiment (0-11 weeks). Due to single measurements no error bars are shown.

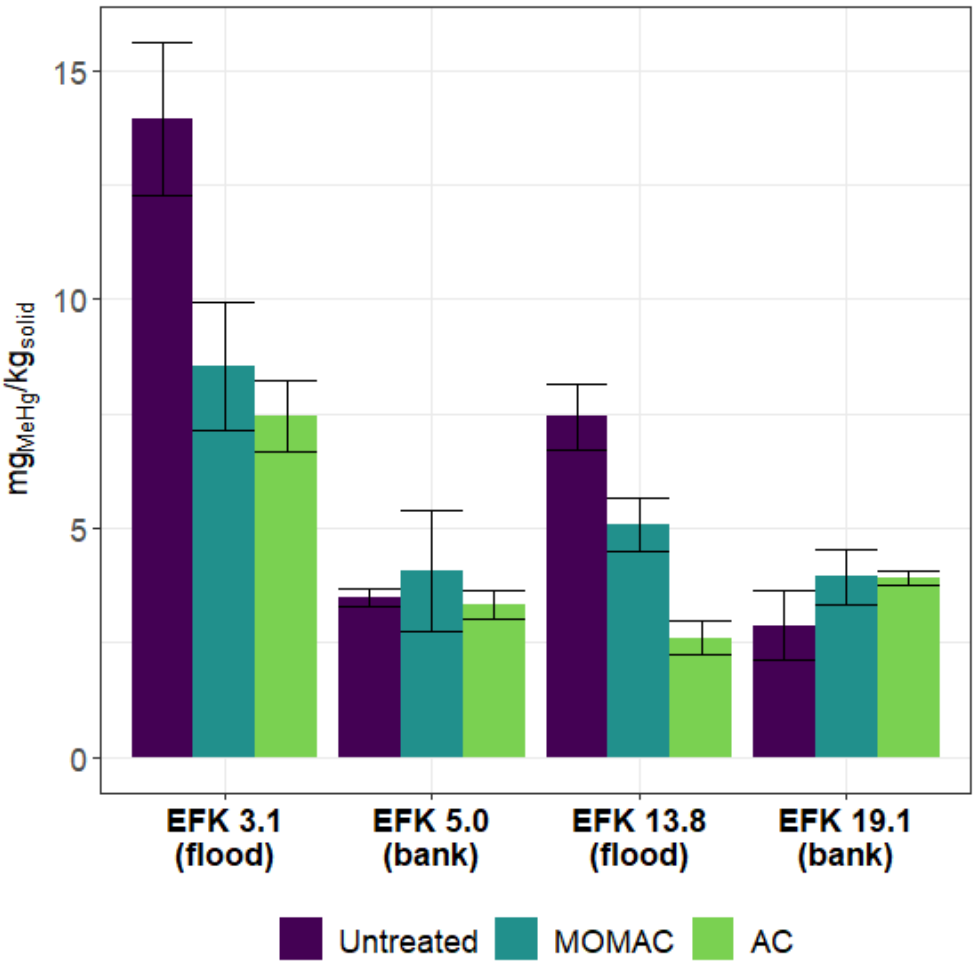

Figure C10. Methylmercury extracted from soil through a KOH-methanol digestion for the initial (t_0) time point. Error bars show averages from replicates across the transect (mean ± standard error; n = 3).

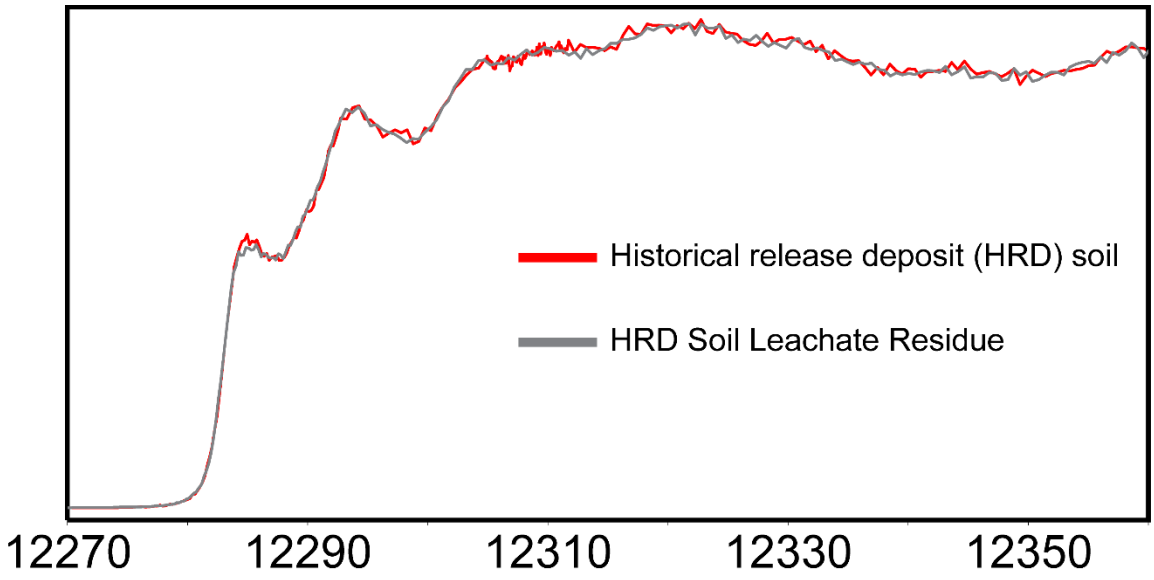

Figure C11. Sample spectra for historical release deposit layers (green) and leachate residue (blue) collected with high energy resolution fluorescence detection – X-ray absorption near edge structure. For the leachate residue an artificial creek water solution was pumped through the HRD soil, and the effluent was filtered through 0.2 µm and the residue was collected and analyzed.

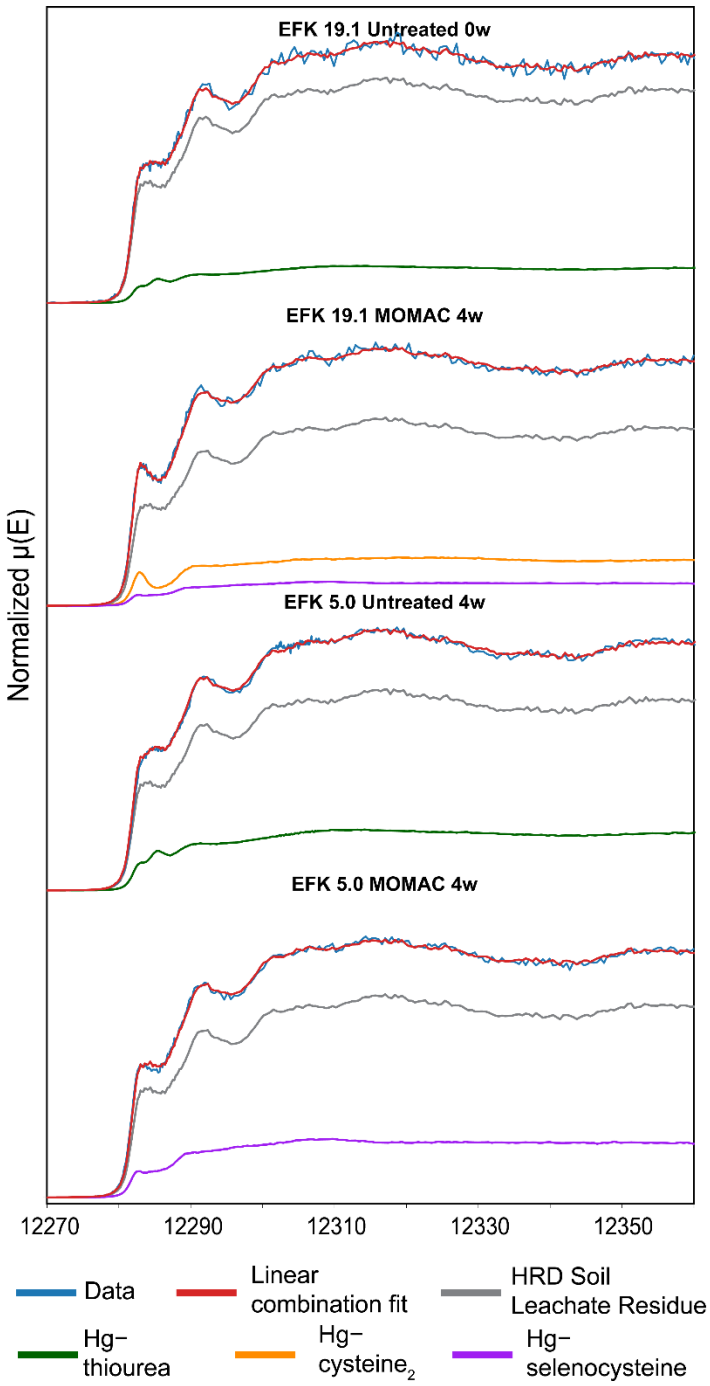

Figure C12. Representative deconvolutions of linear combination fits for spectra from soil samples, using reference standards shown in Figure C1. Spectra were collected using High Energy Resolution Fluorescence Detection X-ray Absorption Near Edge Spectroscopy (HERFD-XANES) at the Hg-L_{III} absorption edge, measured at the Lα1 emission line.

Table C2. Summary results and statistics from HERFD-XANES linear combination fits to unknown soil samples

Field Site	Sample[a]	HRD Soil Leachate Residue	Hg-cysteine$_2$ (pH 2.2)	Hg-thiourea (pH 7.0)	Hg-Selenocysteine (pH 7.4)	Sum	R-factor[c]	Reduced $\chi 2$[d]
EFK 3.1 Floodplain	Untreated 0w	74 (±2) **74**	-	26 (±2) **26**	-	100	2.34E-04	1.71E-04
	MOMAC 4w	85 (±3) **85**	-	15 (±3) **15**	-	100	3.28E-04	2.26E-04
EFK 5.0 Bank	Untreated 0w	84 (±2) **84**	-	16 (±2) **16**	-	100	1.53E-04	1.11E-04
	Untreated 4w	77 (±2) **76**	-	24 (±2) **24**	-	101	2.19E-04	1.74E-04
	Untreated 10w	77 (±2) **77**	-	23 (±2) **23**	-	100	2.30E-04	1.83E-04
	MOMAC 4w	77 (±2) **77**	-	-	23 (±2) **23**	100	2.71E-04	1.85E-04
	MOMAC 10w	78 (±2) **78**	-	22 (±2) **22**	-	99	2.42E-04	1.90E-04
	AC 10w	80 (±2) **79**	-	21 (±2) **21**	-	101	1.99E-04	1.58E-04
EFK 13.8 Floodplain	Untreated 0w	80 (±3) **79**	-	21 (±3) **21**	-	101	4.58E-04	3.39E-04
	MOMAC 4w	81 (±4) **81**	-	19 (±4) **19**	-	100	6.75E-04	4.95E-04
EFK 19.1 Bank	Untreated 0w	86 (±3) **86**	-	14 (±3) **14**	-	100	4.76E-04	3.50E-04
	Untreated 10w	77 (±2) **77**	-	23 (±2) **23**	-	100	2.01E-04	1.60E-04
	MOMAC 4w	72 (±2) **72**	19 (±2) **19**	-	9 (±2) **9**	100	2.89E-04	2.10E-04
	MOMAC 10w	89 (±3) **88**	-	12 (±3) **12**	-	101	3.29E-04	2.66E-04
	AC 10w	80 (±3) **81**	-	19 (±3) **19**	-	99	4.23E-04	3.31E-04

[a] See Table C1 for the complete Mn reference compound library used in fits.
[b] Uncertainty in fits reported in parentheses; bold values are fit percentages normalized to 100%.
[c] R-factor = $\sum$(data-fit)2 /$\sum$(data)2 normalized sum of squared residuals of the fit.
[d] Reduced $\chi 2$ = (F-factor) / (# of points - # of variables)

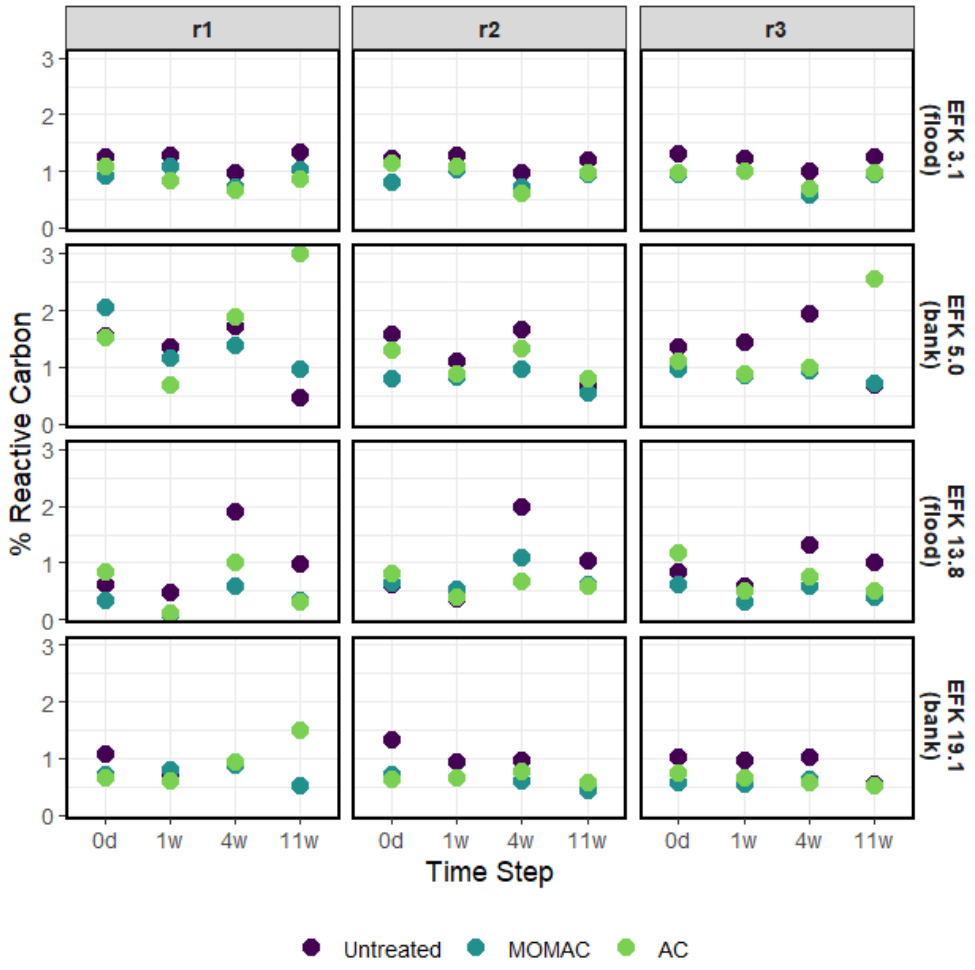

Figure C13. Percent reactive carbon in soil across transect replicates (r1, r2, r3) calculated as the ratio between permanganate oxidizable carbon, or reactive carbon, and total organic carbon ([POxC]/[Total OC]). Due to single measurements no error bars are shown.

REFERENCES

(1) Jew, A. D.; Kim, C. S.; Rytuba, J. J.; Gustin, M. S.; Brown, G. E. New Technique for Quantification of Elemental Hg in Mine Wastes and Its Implications for Mercury Evasion Into the Atmosphere. *Environ. Sci. Technol.* **2011**, *45* (2), 412–417. https://doi.org/10.1021/es1023527.

(2) Charnock, J. M.; Moyes, L. N.; Pattrick, R. A. D.; Mosselmans, J. F. W.; Vaughan, D. J.; Livens, F. R. The Structural Evolution of Mercury Sulfide Precipitate: An XAS and XRD Study. *Am. Miner.* **2003**, *88* (8–9), 1197–1203. https://doi.org/10.2138/am-2003-8-903.

(3) Thomas, S. A.; Catty, P.; Hazemann, J.-L.; Michaud-Soret, I.; Gaillard, J.-F. The Role of Cysteine and Sulfide in the Interplay between Microbial Hg(Ii) Uptake and Sulfur Metabolism†. *Metallomics* **2019**, *11* (7), 1219–1229. https://doi.org/10.1039/c9mt00077a.

(4) Manceau, A.; Enescu, M.; Simionovici, A.; Lanson, M.; Gonzalez-Rey, M.; Rovezzi, M.; Tucoulou, R.; Glatzel, P.; Nagy, K. L.; Bourdineaud, J.-P. Chemical Forms of Mercury in Human Hair Reveal Sources of Exposure. *Environ. Sci. Technol.* **2016**, *50* (19), 10721–10729. https://doi.org/10.1021/acs.est.6b03468.

(5) Pickering, I. J.; Cheng, Q.; Rengifo, E. M.; Nehzati, S.; Dolgova, N. V.; Kroll, T.; Sokaras, D.; George, G. N.; Arnér, E. S. J. Direct Observation of Methylmercury and Auranofin Binding to Selenocysteine in Thioredoxin Reductase. *Inorg. Chem.* **2020**, *59* (5), 2711–2718. https://doi.org/10.1021/acs.inorgchem.9b03072.

(6) Carty, A. J.; Malone, S. F.; Taylor, N. J.; Canty, A. J. Synthesis, Spectroscopic, and X-Say Structural Characterization of Methylmercury-d , l -Selenocysteinate Monohydrate, a Key Model for the Methylmercury(II)-Selenoprotein Interaction. *J. Inorg. Biochem.* **1983**, *18* (4), 291–300. https://doi.org/10.1016/0162-0134(83)85044-2.

(7) Gilsanz, C.; Gusmão, R.; Chekmeneva, E.; Serrano, N.; Díaz-Cruz, J. M.; Ariño, C.; Esteban, M. Electroanalysis of the Binding and Adsorption of Hg2+ with Seleno Aminoacids by Differential Pulse and Elimination Voltammetry at the Au-Disk Electrode. *Electrochimica Acta* **2011**, *56* (17), 5988–5992. https://doi.org/10.1016/j.electacta.2011.04.102.